

**A Theoretical investigation of Embedded  
Scintillator Optical Fibre Sensors for Use in Real-  
Time X-ray and  $\gamma$ -ray Dosimetry**



**Liang Ding**

School of Engineering  
Cardiff University

This dissertation is submitted for the degree of  
*Doctor of Philosophy*

October 2017

## Abstract

This thesis reports on an inorganic scintillator embedded optical fibre dosimeter (ISOFD) sensor designed and optimised using a Monte-Carlo (MC) simulation method. The major factors that hinder the application of ISOFD are: the low coupling efficiency between the scintillation-domain and the optical fibre, the incident energy dependent response, and the lack of theoretical evaluation of the sensor performance. Regarding these problems, a MC simulation method was developed in this thesis to investigate the key factors that determine the radiation sensitivity, leading to an optimized sensor design. The radiation energy absorption by the scintillator material  $\text{Gd}_2\text{O}_2\text{S}$  and optical light transmission inside the ISOFD were simulated with respect to diagnostic X-rays and therapeutic  $\gamma$ -rays separately.

The MC simulation method of ISOFD models for X-ray detection integrated the simulation of photon interactions and the ray-tracing simulation of light-rays. The simulation confirmed that the energy-dependence of ISOFDs is caused by the photon interaction cross sections of  $\text{Gd}_2\text{O}_2\text{S}$  for different incident energies. The packing density of the scintillation-domain has been identified the most prominent parameter that enhances the energy absorption efficiency. A thorough analysis of light reflection and transmission at boundaries showed that the coupling efficiency can be improved by decreasing the refractive index (RI) difference between the scintillation-domain and surrounding materials.

The simulation method of the  $\gamma$ -ray detection further included the MC simulation of electron and positron interactions. The theoretical calculation of the photon interactions in  $\text{Gd}_2\text{O}_2\text{S}$  showed that the electron energy attenuation by scintillators contributes to the overall energy absorption of  $\gamma$ -rays. The simulated parameters of electron interactions are in good agreement with the ESTAR database. The simulation of the electron transport in a single  $\text{Gd}_2\text{O}_2\text{S}$  particle model verified that the electron energy is attenuated via inelastic collisions; meanwhile the energy deposition inside the particle is determined by the average size of the scintillator-particle.

## **Acknowledgement**

First of all, I would like to express my sincere heartfelt thanks to my supervisors, Dr. Ricahrd M Perks, Dr. Hanxing Zhu and Prof. Porch, who guided me during the PhD degree learning period. Especially, I would thank Richard and Hanxing. Richard has offered me consistent help for my dissertation writing, and lots of valuable suggestions. Hanxing has always been kind and patient to me and willing to help.

I would also like to thank China Scholarship Council and Cardiff Engineering School for their generous sponsorship that gave me a chance to study and live in Cardiff, this beautiful city.

My thanks also go to Dr. Chris Yang, and Dr. Emiliano Sepzi, who gave me precious advices regarding my research. Finally, my grateful thanks must go to my families and my wife, who have always been supporting and encouraging me. You are strongest motivation.

## Contents

Acknowledgement .....	3
List of Figures .....	1
Symbols .....	7
Abbreviations .....	10
Chapter 1—Introduction .....	12
Chapter 2—Review of scintillator coupled optical fibre dosimeters .....	19
2.1 Introduction .....	19
2.2 Fundamentals of inorganic scintillation materials .....	21
2.2.1 Organic scintillators .....	22
2.2.2 Inorganic scintillators .....	23
2.3 Important characteristics of scintillators for SOFDs .....	26
2.4 Scintillation materials for ISOFD fabrication .....	30
2.4.1 Electronic transitions of PL excitation and emission process .....	32
2.4.2 The PL excitation and emission spectra of $Gd_2O_2S:RE$ .....	35
2.4.3 The X-ray luminescence (XRL) spectra of $Gd_2O_2S:RE$ .....	39
2.4.4 Temperature dependence of $Gd_2O_2S:RE$ .....	41
2.4.5 X-ray energy dependence .....	45
2.5 Introduction to SFODs .....	47
2.5.1 Plastic scintillator coupled optical fibre dosimeters (PSOFDs) .....	48
2.5.2 Inorganic scintillator coupled optical fibre dosimeters .....	51
2.5.3 Multi-point SOFDs (MPSOFDs) .....	55
2.5.4 The Cherenkov effect .....	60
2.6 Conclusion .....	62
Chapter 3—Theory and Monte-Carlo simulation algorithms for photon interactions .....	64
3.1 Introduction to photon interaction simulation .....	64
3.2 X-ray photon interactions .....	69
3.2.1 Photon cross-section and partial mass attenuation coefficient .....	70
3.2.2 Photoelectric effect .....	74
3.2.3 Incoherent scattering (or Compton scattering) .....	77
3.2.4 Coherent scattering .....	84
3.2.5 Electron-positron pair production .....	86
3.3 Detailed Monte-Carlo simulation of photon interactions with media .....	89

3.3.1	The attenuation of the X-/ $\gamma$ -ray photon.....	89
3.3.2	Photoelectric interaction .....	90
3.3.3	Incoherent scattering (Compton scattering).....	93
3.3.4	Coherent scattering .....	96
3.3.5	Electron-positron pair production .....	97
3.4	Generation of random tracks of X-ray photons.....	99
3.5	Summary .....	102
Chapter 4	—The Monte-Carlo simulation method of diagnostic X-ray detection with ISOFDs.....	104
4.1	Introduction to ISOFD modelling .....	104
4.2	Coordinate system.....	105
4.3	Geometry of the ISOFD model and material properties .....	108
4.3.1	Basic geometry of a single scintillation-domain.....	109
4.3.2	Properties of materials .....	110
4.3.3	Models with different configurations.....	115
4.4	Required input data for Monte-Carlo simulation .....	117
4.5	Simulation of diagnostic X-ray photon absorption .....	117
4.6	Simulation of Light-ray production and transport .....	122
4.7	Output parameters.....	125
4.8	Summary .....	129
Chapter 5	—Simulation of ISOFDs for diagnostic X-ray detection: results and analysis .....	131
5.1	Introduction.....	131
5.2	The influence of the mean radius of the scintillator particles .....	131
5.2.1	Result of the simulation with respect to different $r_p$ .....	132
5.2.2	Discussion regarding the effect of particle size on radiation sensitivity.....	134
5.3	Packing density $\eta_{pk}$ of SD.....	135
5.3.1	Result of the simulation with respect to different $\eta_{pk}$ .....	136
5.3.2	Discussion regarding the effect of the packing density $\eta_{pk}$ .....	138
5.4	Response to incident photons of different initial energies 10~80 KeV .....	139
5.4.1	Simulation result with respect to different initial photon energies .....	140
5.4.2	Discussion regarding the simulation results for variable initial energies.....	146
5.5	The simulation of models of different scintillator embedding depths $D_{em}$ .....	147
5.5.1	Simulation result of models with different scintillator embedding depths .....	147
5.5.2	Discussion of models with different embedding depth.....	150
5.6	The effect of the location of the port.....	151

5.6.1 Simulation result of models with different locations of the port.....	151
5.6.2 Discussion regarding the effect of the port location .....	153
5.7 The effect of the adjacent SD.....	156
5.8 Error analysis .....	159
5.9 Conclusion of simulation with respect to X-rays.....	163
Chapter 6—Review: theory and MC simulation algorithms of electron interactions .....	166
6.1 Introduction.....	166
6.2 Theory of electron and positron interactions .....	170
6.2.1 Elastic scattering .....	170
6.2.2 Inelastic collisions.....	171
6.2.3 Radiative losses (Bremsstrahlung emission).....	174
6.2.4 Positron annihilation .....	176
6.3 The mixed MC method of electron/positron interaction.....	177
6.3.1 Step lengths of hard events .....	178
6.3.2 Energy loss and angular deflection of soft event .....	179
6.3.3 Generation of random tracks.....	180
6.4 Summary .....	182
Chapter 7—The Monte-Carlo simulation of ISOFD for therapeutic $\gamma$ -ray detection .....	184
7.1 Introduction.....	184
7.2 The simulation of $\gamma$ -ray absorption and the electron/positron generation.....	185
7.2.1 The mean free path length of $\gamma$ -ray photons.....	186
7.2.2 Compton scattering (incoherent scattering) in $Gd_2O_2S$ .....	188
7.2.3 Electron-positron pair production in $Gd_2O_2S$ .....	193
7.2.4 Conclusion of the simulation of the $\gamma$ -ray photon interactions .....	196
7.3 Mean free path length for electron/positron interactions .....	197
7.3.1 The elastic scattering of electrons .....	199
7.3.2 The inelastic collisions between electrons and $Gd_2O_2S$ .....	202
7.3.3 Bremsstrahlung emission in $Gd_2O_2S$ .....	205
7.3.4 Positron annihilation .....	208
7.3.5 The mean free path length for general electron interactions .....	209
7.3.6 Conclusion of the electron/positron interactions theoretical calculation .....	211
7.4 The simulation of the electron transport in a single scintillator particle .....	211
7.4.1 The simulation method.....	212
7.4.2 The simulation result and discussion .....	214

7.4.3 Conclusion of the electron transport .....	216
7.5 Conclusions.....	216
Chapter 8 — Conclusion and future work.....	218
Conclusion .....	218
Reference .....	224

## List of Figures

Figure 2.1 A simple schematic of the radiation detection process using SOFD.....	19
Figure 2.2 Energy levels and most intense electronic transitions of $\text{Pr}^{3+}$ , $\text{Eu}^{3+}$ , $\text{Gd}^{3+}$ , and $\text{Tb}^{3+}$ ions in $\text{Gd}_2\text{O}_2\text{S}$ . The position of the ground $4f^n$ states of ions is assumed to be zero[70] .....	34
Figure 2.3 The PL excitation (a) and emission (b) spectra of the $\text{Gd}_2\text{O}_2\text{S}:\text{Pr}$ from the article of Lian et al[73].....	36
Figure 2.4 Excitation (a) and emission (b) spectra of the $\text{Gd}_2\text{O}_2\text{S}:\text{Eu}$ hollow spheres[71]	37
Figure 2.5 The PL excitation ( $\lambda_{\text{em}}=544$ nm) and emission ( $\lambda_{\text{ex}}=266$ nm) spectra of $\text{Gd}_2\text{O}_2\text{S}:\text{Tb}$ doped with different $\text{Tb}^{3+}$ content[72] .....	38
Figure 2.6 The XRL emission spectra of $\text{Gd}_2\text{O}_2\text{S}$ doped with different RE ions: the spectra of $\text{Gd}_2\text{O}_2\text{S}:\text{Pr}$ (a), $\text{Gd}_2\text{O}_2\text{S}:\text{Eu}$ (b) and $\text{Gd}_2\text{O}_2\text{S}:\text{Tb}$ (c) respectively. The spectra data were required from Phosphor Technology Ltd., UK [64]. .....	40
Figure 2.7 Temperature dependence of $\text{Gd}_2\text{O}_2\text{S}:\text{Pr}$ (Ce) reported by Blahuta S et al [79]: evolution with temperature of (a) the total luminescence intensity (area under the XRL spectra over the 400–900 nm region); (b) the intensity of the $^3P_0 \rightarrow ^3H_4$ (at 514 nm) and $^1D_2 \rightarrow ^3H_4$ (at 630 nm) emissions. ....	42
Figure 2.8 The temperature dependence of the individual emission bands (peaks) of $\text{Gd}_2\text{O}_2\text{S}:\text{Tb}$ ceramics before (a) and after heat treatment (b), reported by Gorokhova E et al [80]. 1—416 nm ( $^5D_3 \rightarrow ^7F_5$ ) 545 nm ( $^5D_4 \rightarrow ^7F_5$ ) luminescence lines. ....	44
Figure 2.9 X-ray energy fluence spectra of the X-ray tube at different voltages (a), and X-ray energy absorption efficiency for the $\text{Gd}_2\text{O}_2\text{S}:\text{Eu}$ screens in the mammographic energy range.[82] .....	45
Figure 2.10 A water-equivalent PSOFD developed by Beddar et al.[20]. The plastic scintillator is coupled to a bundle of plastic optical fibres, and a reference fibre is used to remove the Cherenkov effect. ....	49

Figure 2.11 Diagrams of the radiation sensitive probe of ISOFDs: (a) The single-crystal NaI: Tl based SOFD reported by Swinth et al.[63]. (b) The fibre optic radiation dosimeter sensor design reported by McCarthy et al.[86] .....	52
Figure 2.12 Embedded structure of an SOFD. (a) The SOFD (photograph) presented by O’Keeffe et al.[36]. (b) The SOFD (schematic representation).....	54
Figure 2.13 The MPSOFD presented by Takada et al.[28]: (a) The system for the time-of-flight (TOF) measurement. (b) A schematic of a sensing region. (c) Result of the TOF measurements of radiation with a new optical fibre.....	56
Figure 2.14 Details of the two-points PSOFD and three-points PSOFD construction[31]..	58
Figure 3.1 The photon cross-sections (mass partial attenuation coefficients) of different photon interactions with the Gd <sub>2</sub> O <sub>2</sub> S compound in (a) the diagnostic X-ray energy range 2–90 KeV, and (b) a zoom in on the energy range 20–90 KeV.....	72
Figure 3.2 The photon cross-sections of the Gd <sub>2</sub> O <sub>2</sub> S compound in the therapeutic energy range 2–24 MeV.....	72
Figure 3.3 A schematic of the photoelectric absorption .....	75
Figure 3.4 Compton scattering of a photon with energy $h\nu_0$ from a bound electron .....	78
Figure 3.5 A schematic of the coherent scattering of a photon by the target atom.....	84
Figure 3.6 A schematic of the pair production of a photon in the nucleus field.....	87
Figure 4.1 The coordinate systems: a fixed Cartesian coordinate $(x, y, z)$ system in origin point $O$ ; a local coordinate system $(x', y', z')$ and a spherical system $(r, \theta, \varphi)$ which move with particle. The local Cartesian coordinate system is parallel to the fixed one.....	106
Figure 4.2 The rotation of the motion vector from $\mathbf{d}$ to $\mathbf{d}'$ .....	107
Figure 4.3 (a) 3D image of MPISOFD, (b) The 2D diagram of the scintillation-domain, (c) the cross section of optical fibre.....	109
Figure 4.4 (a) The linear attenuation coefficients $\mu$ , and (b) the mean free path lengths $\lambda$ of the material H <sub>2</sub> O, SiO <sub>2</sub> , ER and Gd <sub>2</sub> O <sub>2</sub> S for X-ray photons. ....	112
Figure 4.5 the models of ISOFD to be simulated, 3 models are simulated: Model 1 in which the cladding layer is removed while the fibre core is intact; Model 2 in which the fibre cladding and outer layer of fibre core is removed; Model 3 with two SDs ‘A’ and ‘B’ embedded into fibre cladding layer.....	116

Figure 4.6 The flow-chart of Monte-Carlo simulation of diagnostic X-ray photon transport in a single-domain ISOFD .....	119
Figure 4.7 Schematic of the orientation of the scintillator particle upon collision by the X-ray photon .....	121
Figure 4.8 The cross section of SD (Model 1) is divided into 21 layers: $L_0$ — $L_{20}$ . The grey area (layer $L_1$ — $L_{20}$ ) is the scintillator, while $L_0$ is the fibre core. ....	127
Figure 5.1 The mean free path length $l_{\text{mean,ER}}$ and the overall photon interaction probability $p_{\text{int}}$ (a), and the overall scintillation efficiency $\eta_{\text{sc}}$ (b) as simulated corresponding to different particle sizes from 1.5—4.0 $\mu\text{m}$ . ....	133
Figure 5.2 The transmission efficiency $\eta_{\text{trans}}$ (a), and the overall X-ray detection efficiency $\eta_{\text{de}}$ as simulated with respect to different particle sizes (b) .....	133
Figure 5.3 The mean free path length $l_{\text{mean,ER}}$ and the overall photon interaction probability $p_{\text{int}}$ (a), and the scintillation efficiency $\eta_{\text{sc}}$ (b) as simulated corresponding to different packing density from 0.7%—30% vol.....	136
Figure 5.4 The transmission efficiency $\eta_{\text{trans}}$ and the energy loss at the outer surface of SD (a), and the overall X-ray detection efficiency $\eta_{\text{de}}$ (b) as simulated using models (based on Model 1) of different SD packing densities.....	137
Figure 5.5 (a) The primary interaction probability $p_{\text{int}}$ and (b) the overall scintillation efficiency $\eta_{\text{sc}}$ under incident X-ray radiation of initial energies in the interval 10~80 KeV .....	140
Figure 5.6 (a) The transmission efficiency $\eta_{\text{trans}}$ and (b) the overall X-ray detection efficiency as simulated under radiation in the energy interval 10~80 KeV.....	142
Figure 5.7 (a) The normalised distribution probability of X-ray track termination locations under X-ray radiation of 10 KeV, 20 KeV, 51 KeV and 60 KeV, and (b) the normalised distribution probability of light generation locations along the radial direction of SD. ....	144
Figure 5.8 The schematic showing the cross section of the scintillation domain, and a relative size of $D_{\text{em}}$ with reference to the position of interfaces between different parts of the optical fibre. ....	147
Figure 5.9 (a) The interaction probability and (b) the scintillation efficiency of an ISOFD with different embedding depths: 100 $\mu\text{m}$ , 110 $\mu\text{m}$ , 120 $\mu\text{m}$ , and 125 $\mu\text{m}$ .....	148

Figure 5.10 The transmission efficiency (a) and the detection efficiency of an ISOFD with different SD embedding depths (b) .....	149
Figure 5.11 The photon interaction probability $p_{\text{int}}$ (a), and the overall scintillation efficiency $\eta_{\text{sc}}$ of Model 1 (b) for different values of port-TSD distance $l_{\text{port-TSD}}$ .....	152
Figure 5.12 (a) The transmission efficiency $\eta_{\text{trans}}$ and (b) the overall detection efficiency $\eta_{\text{de}}$ of Model 1 for different port-TSD distances $l_{\text{port-TSD}}$ .....	153
Figure 5.13 The reflection and transmission of light-rays incident at the inner interfaces of ISOFD. The inner interfaces including: ①ER—core, ②core—cladding and ③ ER-cladding.....	154
Figure 5.14 Diagram of the double SD-ISOFD model. It is noted that the ratio of different parts in this figure does not coincide with the real size of the model. ....	157
Figure 5.15 The stopping power $S(E)$ of the electron in different media .....	161
Figure 7.1 The mass partial interaction coefficients and total mass attenuation coefficients of (a) $\text{Gd}_2\text{O}_2\text{S}$ , (b) $\text{SiO}_2$ , (c) epoxy resin (ER) and (d) water ( $\text{H}_2\text{O}$ ).....	186
Figure 7.2 The linear attenuation coefficient (a), and (b) mean free path of $\text{Gd}_2\text{O}_2\text{S}$ , $\text{SiO}_2$ , ER and $\text{H}_2\text{O}$ calculated with corresponding total mass attenuation coefficient.....	187
Figure 7.3 The photon energy and the kinetic energy of recoil electron (created by Compton scattering by GOS molecule) with respect to the polar angular deflection of the scattered photon relative to the direction of the initial photon movement, for the initial photon energies of (a, b) 4 MeV, (c, d) 12 MeV and (e, f) 24 MeV. ....	190
Figure 7.4 The normalized PDF of polar deflection $\cos\theta$ for the photon incoherently scattered by $\text{Gd}_2\text{O}_2\text{S}$ molecules .....	192
Figure 7.5 The modified photon cross section of pair-production for the elements Gd, S and O in the scintillator $\text{Gd}_2\text{O}_2\text{S}$ .....	194
Figure 7.6 The normalized PDF of the electron reduced energy produced by pair-production of the initial photon energy 4~24 MeV by the Gd element.....	195
Figure 7.7 The 2D illustration of an electron/positron travelling in SD and the optical fibre .....	198
Figure 7.8 (a) The mean free path length $\lambda_{\text{col}}$ , and (b) energy stopping power $S(E)$ of the electron inelastic collision in the media $\text{Gd}_2\text{O}_2\text{S}$ and ER for electron kinetic energy in the interval 4~24 MeV. ....	203

Figure 7.9 The ratio $S(E)/\rho$ (MeV · cm <sup>2</sup> /g) calculated with the oscillator model (dot) and those acquired from the ESTAR library (line) for electrons transport in the media Gd <sub>2</sub> O <sub>2</sub> S and ER.....	204
Figure 7.10 The energy stopping power $S(E)/\rho$ of radiative energy loss (i.e., the Bremsstrahlung emission) for electrons and positrons in Gd <sub>2</sub> O <sub>2</sub> S.....	206
Figure 7.11 The mean free path lengths of 'hard' radiative event for electrons ( $\lambda_{e,rad}^{(h)}$ ) and positrons ( $\lambda_{p,rad}^{(h)}$ ) travelling in Gd <sub>2</sub> O <sub>2</sub> S.....	207
Figure 7.12 The mean free path length $\lambda_{an}$ for positron annihilation in media Gd <sub>2</sub> O <sub>2</sub> S and ER.....	208
Figure 7.13 The mean path length for general practical and 'hard' electron scattering event for electrons with kinetic energy of 5~24 MeV in Gd <sub>2</sub> O <sub>2</sub> S material. ....	210
Figure 7.14 A schematic of an electron moving in the arbitrary direction inside a scintillator particle.....	213

## List of Tables

Table 2.1 A survey of the characteristics of certain scintillator materials[54], [56], [59], [67], [68].	25
Table 3.1 The parameters of the analytical approximation of Equation (3.37) to $F(q, Z)$ ..	97
Table 4.1 Materials used in ISOFD models ..	111
Table 4.2 The outer radii of all layers along fibre axis ..	127
Table 5.1 The photon interaction probabilities of first-order photoelectric absorption, first-order incoherent scattering, the K-X-ray emission probability for each incident photon and the reabsorption probability of K-X-rays.	142
Table 5.2 The critical angles at the different interfaces ..	156
Table 5.3 The simulation result of the double scintillation domain ISOFD ..	158
Table 5.4 The photoelectric cross-sections of the elements Gd, O, and S, which are modified by the elemental weight ratio in the compound $Gd_2O_2S$ ..	160
Table 7.1 The minimum energy of scattered photon and the maximum kinetic energy of the recoil electron after Compton scattering event in a gadolinium atom. ....	193
Table 7. 2 The energy limit of the secondary photon generated by pair-production .....	196
Table 7. 3 the mean free paths of elastic scattering .....	202
Table 7.4 The mean free path length of inelastic collision ( $\lambda_{col,GOS}$ , $\lambda_{col,GOS}^{(h)}$ ) for electrons and positrons transport in the medium $Gd_2O_2S$ . ....	205
Table 7.5 The average energy loss, and average numbers of electron scattering events ...	215

## Symbols

$\alpha = \frac{e^2}{\hbar c} \cong 1/137$	Fine-structure constant
$A_w$	The atomic weight of the material
$c \equiv 2.9979 \times 10^8 \text{ ms}^{-1}$	The speed of light in a vacuum
$D_{em}$	Embedding depth of the scintillation-domain
$\vec{d}$	The direction unit vector
$E_0$	Initial photon energy in KeV or MeV units
$e = 1.602 \times 10^{-19} \text{ C}$ $= 1.5189 \times 10^{-14} \text{ m}^{3/2}\text{kg}^{1/2}\text{s}^{-1}$	Elementary charge
$E_C$	the Compton line
$h = 6.62607004 \times 10^{-34} \text{ m}^2 \text{ kg s}^{-1}$	Planck's constant
$\hbar = \frac{h}{2\pi}$	Reduced Planck's constant or Dirac's constant
K-X-ray	K-shell characteristic X-ray
$l_{\text{mean},ER}$	Mean free path length of photon in <i>ER</i>
$l_{\text{port-SBT}}$	Distance between the port and the terminal of the scintillator-bulk
$l_{tr}$	Transmission distance
$m_e = 9.109534 \times 10^{-31} \text{ kg}$	Electron rest mass
$m_e c^2 = 5.11 \times 10^5 \text{ eV}$ $= 0.511 \text{ MeV}$	Electron rest mass energy
$N = N_A \rho / A_w$	The number of atoms per unit volume
$N_A = 6.022140857 \times 10^{23}$	Avogadro's number

$p$	Momentum of a particle
$P_{\text{int}}$	Sum of the probabilities of all photon interactions for each incident photon
$P_K$	the probability of K-shell ionisation
$P_K$	the probability of K-shell ionisation
$p_{\text{ph},1}$	Probability of photoelectric absorption of the incident photon
$p_{\text{KX-ab}}$	Probability of photoelectric absorption of the K-X-ray
$q$	the modulus of the momentum transfer vector
$r$	The position of a particle
$r_e = 2.8179 \times 10^{-15} \text{ m}$	Classical electron radius
$r_p$	Radius of the scintillator particle
$S(E)$	Energy stopping power for electron in $\text{cm}^2/\text{g}$
$S_{\text{SD}}$	The cross-section area of the scintillation-domain
$u = 1.6605402 \times 10^{-24} \text{ g}$	Atomic mass unit
$U_i$	The electron binding energy of the $i$ th shell
$W$	Energy loss
$Z$	Atomic number of the element
$Z_{\text{eff}}$	Effective atomic number
$\alpha = \frac{e^2}{\hbar c} \cong 1/137$	Fine-structure constant
$\beta$	Speed of the particle in the unit of light speed $c$
$v$	speed of the particle in the unit m/s
$\xi$	Pseudo-random value uniformly distributed in the interval (0, 1)

$\pi$	Constant (3.14159)
$\rho$	Density of the material
$\sigma$	Cross section in $\text{cm}^2/\text{atom}$ units
$\eta_c$	Intrinsic scintillation efficiency
$\eta_{de}$	Overall detection efficiency
$\eta_{pk}$	Scintillator packing density of the scintillation-domain
$\eta_{sc}$	Overall scintillation efficiency
$\eta_{trans}$	Transmission efficiency of light
$\theta$	Polar angular deflection
$\kappa = \frac{E_0}{m_e c^2}$	Photon energy in the units of the electron rest mass energy mass energy
$\lambda_{mean}$	Mean free path length in $\mu\text{m}$ unit
$\mu$	Linear attenuation coefficient in $/\text{cm}$ units
$\mu/\rho$	Mass attenuation coefficient of photon interactions in $\text{g}/\text{cm}^2$ units
$\varphi$	Azimuth angular deflection
$w_i$	Element weight ratio in compound
$\omega_K$	K-fluorescent yield
$\Omega$	Solid angle

## Abbreviations

an	Positron annihilation
CB	Conduction band
CIED	Cardiac implanted electronic device
coh	Photon coherent scattering
col	Inelastic collision for electron
CS	Cross section
CT	Computed tomography
DCS	Differential cross section
DDCS	Double differential cross section
el	Elastic scattering for electron
EPID	Electronic portal imaging devices
<i>ER</i>	Epoxy resin
FWHM	Full width at half maximum
GOS	Gd <sub>2</sub> O <sub>2</sub> S
HO	H <sub>2</sub> O
HDR	High dose radiation
IA	Relativistic impulse approximation
IC	Ionization chamber
incoh	Photon incoherent scattering
ISOFD	Inorganic scintillator coupled optical fibre dosimeter
LED	Light Emitting Diode
MC	Monte-Carlo

MPSOFD	Multi-point scintillator optical fibre dosimeter
MOSFET	Metal–oxide–semiconductor field effect transistors
PDF	probability distribution function
PL	photoluminescence
PMT	Photomultiplier tube
pp	Electron-positron pair production
PSOFD	Plastic optical fibre dosimeter
QA	Quality assurance
rad	Radiative energy loss
RE	Rare-earth element
RI	Refractive index
SD	Scintillation domain, which is the scintillator bound with adhesive like epoxy resin
SOFD	Scintillation optical fibre dosimeter
SO	SiO <sub>2</sub>
TLD	Thermoluminescence dosimeter
TPS	Treatment planning system
TSD	Terminal of scintillation domain
UV	Ultraviolet
VB	Valence band
VIS	visible
XRL	X-ray luminescence

## Chapter 1—Introduction

Radiotherapy dosimetry is a fundamental process for radiotherapy. It is the measurement, calculation and assessment of the ionizing radiation dose delivered to the area needing treatment, ensuring that the radiation dose is safely and correctly delivered to the malignant abnormalities. There are many types of dosimeters, such as ionization chambers (ICs), thermoluminescence dosimeters (TLDs), diodes and metal–oxide–semiconductor field effect transistors (MOSFETs), electronic portal imaging devices (EPIDs) and scintillation based optical fibre dosimeters (SOFDs). The dosimeter for radiotherapy treatment should be cautiously chosen according to the radiotherapy technique applied and radiation dose delivery plan designed. Currently, the radiotherapy dosimetry faces the challenges from the fast rapid scientific and clinical development of radiotherapy. Novel techniques applied in radiotherapy treatment, such as intensity-modulated radiotherapy (IMR), stereotactic ablative radiotherapy (SBRT) and magnetic resonance imaging (MRI), while providing better treatment opportunities for cancer patients, increase the complexity of dose delivery. Although there are well established safety and quality system of traditional radiotherapy treatment techniques [1]–[4], the sophistication of these advanced new technology introduce new possibilities of errors, and some accidents have been reported concerning wrong dose delivered during radiation treatment utilizing these new radiotherapy techniques [5], [6]. It has aroused concerns over the lag of existing dosimetric equipment behind the development of the treatment techniques [7]–[9]. Developing radiation dosimeters capable of in-vivo, real-time, dose monitoring is important to find solution to these difficulties.

On another hand, the complexity of treatment plan system (TPS) and dosimetry also increases due to the growing population of patients with cardiac implanted electronic devices (CIEDs) receiving radiotherapy treatment [10]. Modern CIEDs, using complementary metal

oxide semiconductor (CMOS), have advantages of greater reliability and low power consumption, however, they are also sensitive to the ionizing radiation, including either electromagnetic interference (EMI) under indirect radiation, or the damage to the circuit from direct radiation beam [11]. The accidents of CIEDs malfunction during radiotherapy treatment have been reported[12]–[15]. The malfunction types vary from inappropriate triggering, device reprogramming to device failure. The effects of radiation on CIEDs were well studied and reviewed by researchers as Last A[11], Makkar A et al[16], Lillicrap S C et al[1], and Lester, J. F et al[10], the code of practise treating patients with CIEDs were proposed. Even if the CIEDs are at or beyond the edge of the radiation field, it is necessary to monitor the dose rate and accumulated dose deposited on CIEDs, and secure the normal function of CIEDs and safety of the patients. In this case, the multi-points dosimeter capable of real-time, in-vivo dose rate monitoring will be of great help to detect the radiation dose delivered to the lead and circuits of CIEDs, and prevent possible malfunction accidents.

To meet the challenge from the growing complexity of radiotherapy treatment, it is necessary to update existing dosimeters, and develop new ones as well. Current dosimeters of different types used in radiation oncology have their own advantages and disadvantages. ICs for example, are capable of real-time measuring accumulated dose. They are the oldest and most widely used dosimeter, and are considered as the ‘golden stand’ for quality assurance (QA) procedure. However, ICs are operated with vacuum chamber under relatively high voltages. The size and fragility hinder the utility of ICs for real-time in-vivo dosimetry. The TLD is a robust, chip, small type of detector which measures accumulated dose, but can’t monitor the real-time dose rate. MOSFET and diodes dosimeter have the merits of good sensitivity, excellent spatial resolution, good mechanical stability, linear response and direct read out of real-time dose. However, the MOSFET is commercially expensive, angular dependent and unsatisfying durability, while diodes dosimeter is sensitive to accumulated dose

and temperature and is angular dependent as well. EPIDs have a promising capability of providing two-dimensional and three-dimensional information of the actual dose delivered to a patient. Currently, the most widely used commercial EPID is an amorphous silicon (a-Si) photodiode based flat panel detector [17]. It has a linear response to integrated dose and is independent of dose rate. The disadvantages of its use as a dosimeter are oversensitivity to photons of lower energy and “ghosting,” i.e., the continued signal after the irradiation ceased.

Scintillator coupled optical fibre dosimeter (SFOD) is a relatively new type of dosimeter compared to other dosimeters. Currently there is only one commercial scintillation optical fibre dosimeter (the Standard Imaging Exradin W1 Scintillator[18]). Although the report of using a scintillator coupled optical fibre dosimeter for intracavitary dosimetry was dated back as early as 1969 [19], the fast development of SOFD only started from 1990s owing to the inspiring research of Beddar et al on plastic scintillator optical fibre dosimeters (PSOFDs) [20]–[23], and since then, SOFDs attracted more and more research attention in the recent couple of decades [24]–[37]. The coupling of scintillator to optical fibre endows SOFD attractive merits such as passive detection, small in size, linear response to dose rate, energy independent, immunity to EMI, good mechanical robust, capability of multiplexing, et cetera. The research shows that the SOFDs have potential dosimetric application in small field radiotherapy treatment such as brachytherapy and stereotactic radiosurgery treatments [8], [26], [38], [39]. As more and more research efforts are paid to the development of SOFDs, it is reasonable to assume that this type of dosimeter would provide promising solutions to the problems introduced by the dosimetric complexity of state-of-art radiotherapy techniques and patients with CIEDs receiving radiation treatment.

Despite so many advanced characteristics of SOFDs, there are still some issues to be addressed for the wide commercial and clinic application of SOFDs. Taking the most widely investigated PSOFDs for example, they use materials with refractive indices close to water

(plastic scintillator and plastic optical fibre), thus gain favourable water-equivalent property[20]. Except from scintillation (radio-luminescent) light signal, the ionizing radiation incident on SOFDs will also introduce stem effect signals including Cerenkov Effect and fluorescence [21][40]. The magnitude of scintillation signal from plastic scintillators is not large enough to neglect stem effect signal, thus the photon signal generated under ionizing radiation need calibration to remove the stem effect interference [41], [42]. The relatively low light yield of PSOFDs may also limit its application for low dose detection [43]. Another drawback of the PSOFD is that the dose response of some plastic scintillators is temperature dependent[44]–[46], which cannot be neglected and will complicate the calibration procedure of PSOFDs.

Compared to plastic scintillators, inorganic scintillators normally have higher atomic number ( $Z$ ), contributing to higher light yield, better sensitivity to low dose radiation and larger signal-to-noise ratio. However, due to the predominant interaction mechanisms difference at different energy ranges, the absorption of the ionizing photon beam changes in accordance with energy of the incident beam[47]. The research of O'Keeffe et al [34] and Woulfe et al [48] have verified the energy dependence of a  $Gd_2O_3:S:Tb$  scintillator coupled plastic fibre optical detector. As a result, the energy-dependent-coefficient should be introduced to the calibration of inorganic SOFDs. The coupling efficiency between the scintillation part and optical fibre (i.e. the light photon collection and transmission part) is another important factor to be improved. As light photons generated in scintillator are emitted in arbitrary directions, the reflection at the scintillation domain (SD)\* and the optical fibre terminal interface, and the limit of fibre optic aperture cause significant photon energy loss. To improve the coupling efficiency, researchers utilized a variety of methods such as reflector coating on scintillator[49][50],

---

\* The scintillation domain (SD) in this thesis refers to the scintillation part in ISOFD and is comprised of inorganic scintillator particles bound by epoxy resin.

embedding the scintillator into the cladding layer of optical fibre[28], and embedding the scintillator into the core of optical fibre[36], [37].

Beside the aim of improving sensitivity and coupling efficiency of SOFDs, the multi-point SOFD (MPSOFD) is another aspect worthy of further research. The normal SOFD configuration of one scintillator tip coupled with one optical fibre has limitation for large scale radiation dose monitoring. In practical application, it is inconvenient to measure the radiation distribution by moving the sensor head. The combination of multiple single-domain SOFDs for radiation distribution measurement is cumbersome and expensive. In the context of the drawback of the single-domain SOFD, the MPSOFD, which integrates multiple scintillator sensing parts within a single optical fibre, provide a possible way to achieve the in-vivo, real-time radiation distribution monitoring.

The aim of this thesis is to design an inorganic scintillator coupled optical fibre dosimeter (ISOFD) for in-vivo, real time X-ray (and  $\gamma$ -ray) radiation dose monitoring. This is done in the context of improving the radiation detection efficiency through Monte-Carlo simulation of the X-ray and  $\gamma$ -ray detection process. The simulation investigates the coupling between the scintillation-domain and the optical fibre, the photon interaction process within the scintillator material at diagnostic and therapeutic radiation energy ranges, and secondary electrons and positrons transport inside the scintillator material. The simulation will provide an insight into the physical process of photon energy absorption and light transmission, and further assist in the optimization of ISOFD design.

The remainder of this dissertation is as follows.

The Chapter 2 introduces the background of SOFDs. The dosimeters of various types are reviewed regarding the key factors as the efficiency of scintillator materials, the coupling

design between scintillators and optical fibres, the energy dependence, angular dependence and signal processing procedure.

The chapter 3 focuses on the theory of photon interaction. The mechanisms of primary photon interactions are introduced, including photoelectric effect, incoherent scattering, coherent scattering, and pair-production. The Monte-Carlo simulation algorithms of the photon interactions involving the sampling the energy loss, angular deflection and secondary particle emission are reviewed. The method of simulating the transport and attenuation process of ionizing photons in the medium is proposed.

In chapter 4, the Monte-Carlo simulation method of ISOFD (scintillator:  $\text{Gd}_2\text{O}_2\text{S}$ ) for diagnostic X-ray detection is proposed. The properties of the materials, and the X-ray interaction related physical coefficients are discussed. After that, three different ISOFD models based on different sensor configurations are introduced. The Monte-Carlo simulation method, which integrates the X-ray transport history generation process and ray-tracing of scintillation light, is given. In chapter 5, the simulation result of diagnostic X-ray photons detection process modelling was obtained. The output data demonstrates that optimization of the sensor configurations can be made from the aspects of the scintillator-bulk packing density, the mean particle size of the inorganic scintillator, the embedding depth of the scintillator-bulk, etc. The photon energy dependence of the detection efficiency for diagnostic X-ray monitoring is also revealed.

For therapeutic  $\gamma$ -rays, since the interactions between  $\gamma$ -ray and the scintillator particles will generate electrons and positrons with high kinetic energies, in chapter 6, the theory and algorithms of Monte-Carlo simulation of electron interactions are reviewed. The ‘detailed’ simulation method and ‘condensed’ simulation method to generate electron transport history are introduced. Later, in chapter 7, the process of  $\gamma$ -ray detection with ISOFD is simulated from the aspects of  $\gamma$ -ray photon and electrons/positron interactions with the scintillator. Firstly, two

dominant photon interactions, i.e., Compton scattering and electron-positron pair production, were simulated in detail. The result gave an energy distribution of secondary electrons and positrons. Secondly, the electron interactions with the material constituting ISOFD were studied and the important parameters such as mean free path length and energy stopping power in scintillator material were investigated. In the final part of this chapter, the electron transport inside a single  $\text{Gd}_2\text{O}_2\text{S}$  scintillator particle was simulated with respect to variable electron kinetic energies. The feasibility of two types of simulation methods is tested.

Chapter 9 draws the conclusion of this research and discusses the contribution it makes for the development of ISOFDs. It also gives suggestions for further possible work from the aspects of refining the simulation and sensor fabrication.

## Chapter 2—Review of scintillator coupled optical fibre dosimeters

### 2.1 Introduction

Radiation dosimetry concerns the quantitative measurement of radiation doses. It facilitates dose calibration as well as the monitoring of dose delivery for radiotherapy treatment. Scintillator optical fibre dosimeters (SOFDs) achieve these goals by means of converting high energy ionising beams into light photons that can be detected and analysed. The intensity of the light spectrum changes in a linear fashion according to the dose rate of the radiation energy deposited on the sensor's surface.

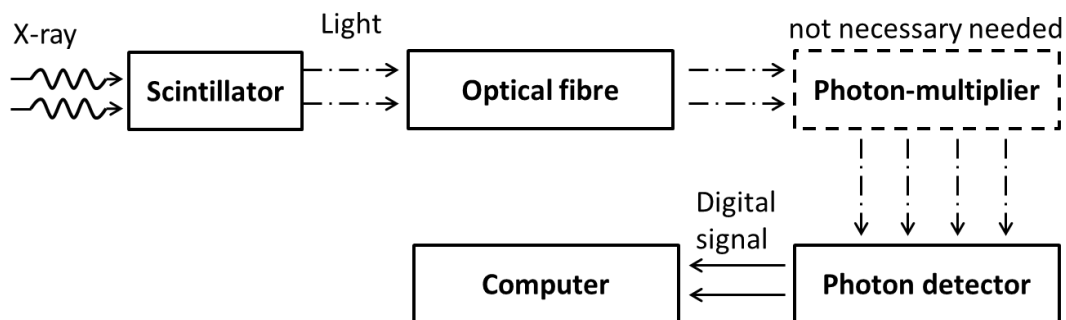


**Figure 2.1** A simple schematic of the radiation detection process using SOFD

The regular SOFD configuration involves the coupling of a piece of scintillation material to an optical fibre, which is then remotely connected to a photomultiplier and a photon detector (e.g. a spectrometer or a charge-coupled device [CCD] camera). A simple illustration of the sensing mechanism of a SOFD is presented in Figure 2.1. The scintillator will undergo the luminescence process when irradiated by a high energy ionising beam. The light generated in the scintillator is collected and transmitted by an optical fibre. This light signal will be enhanced by a photon-multiplier (although this

device may not necessarily be needed) and then remotely converted into a digital signal (usually a light spectrum) by the photon detector. The output spectrum can be analysed on a distal computer terminal. The most significant feature of any optical fibre dosimeter is the fact that the dose information is transmitted using optical signals rather than electrical signals[51]. Consequently, optical fibres are immune to electrical and electromagnetic interference, which renders an SOFD the perfect sensor to use in a harsh radiation environment. SOFDs also have other advantages, including a low cost, capacity for remote radiation monitoring, robustness, small size (high resolution) and the ability to carry multiplexed signals (time and wavelength multiplexing), which is important for the measurement of radiation distribution. Owing to these attractive features, SOFDs are gradually becoming a popular research topic. Hence, considerable research efforts have been expended in this area in relation to aspects such as plastic/inorganic scintillator optical fibre dosimeters' fabrication and optimisation[20], [33], [36], [49], removing noise signals (mainly the Cherenkov and luminescent signals generated in optical fibres)[22], [23], [41], [42], [52], and multi-point SOFDs for radiation dose distribution measurement[24], [28], [31], [53]. The dosimeters' design and fabrication methods, characterisation method, and signal processing and calibration methods as proposed in these previous works will be reviewed in section 2.3, following a brief introduction to the inorganic scintillation materials.

The performance of a SOFD is determined by several key factors, including the radiation sensitivity of the scintillator material to different incident photon energy ranges, the response dependence to radiation energy, the linearity of the radiation dose

rate, the coupling efficiency between the scintillator domain and the optical fibre, the signal-to-noise ratio, the spatial resolution, and the coupling efficiency between the radio-luminescent peaks of the scintillator and the photon detector. Focusing on these aspects, the different inorganic scintillator materials are briefly introduced in the next section. The feasibility of the different scintillator materials for utilisation in SOFDs is then discussed based on their light yield, absorption and emission peaks, and decay time. After that, the history and background of SOFDs are reviewed.

## **2.2 Fundamentals of inorganic scintillation materials**

The mechanism of radiation detection is based on the phenomenon whereby scintillation or phosphorous material is capable of converting ionising radiation into detectable light. A material with this capability is known as a phosphor or scintillator. Although the radio-luminescent mechanisms of phosphors and scintillators are almost identical, their applications are different and lots of materials can be used as both a phosphor and a scintillator. To avoid any misunderstanding, here we use the definition proposed by Nikl[54] to distinguish a scintillator from a phosphor, namely ‘materials are called phosphors when used in the applications using photon integrating (steady-state) mode detection, while scintillators are employed in the (x-/γ-ray) photon counting regime.’ As the radiation detector studied in this thesis aims to monitor the diagnostic and therapeutic x-/γ-radiation dose in real time instead of in a steady-state mode, a scintillator would be most appropriate for the description of the radio-luminescent material reviewed in this section.

Due to the long history and consistent research efforts concerning developments in this area, there are numerous types of scintillators available. These scintillators can be sub-divided into two major groups, namely organic and inorganic scintillators. Scores of articles and books have systematically reviewed and illustrated the work conducted on scintillator development and the application of scintillators for radiation detection[54]–[61]. In this chapter, we will briefly review some typical scintillators based on their characteristics, for example, the photon mass absorption coefficient, light yield, X-ray stopping power, scintillation response-decay time and radiation resistance. The principal focus will be on inorganic scintillators.

### **2.2.1 Organic scintillators**

Organic scintillators are composed of aromatic hydrocarbons and can be further divided into plastic scintillators and liquid scintillators. Plastic scintillators currently represent the most popular type of scintillation material employed for SOFD fabrication. They offer a number of attractive advantages, such as their water-equivalent property, prompt linear response to the radiation dose and independence of the radiation energy range. The water-equivalent property results from the fact that plastic scintillators are mainly composed of hydrocarbon molecules, and they hence have similar effective atomic numbers ( $Z_{\text{eff}}$ ), densities and mass energy absorption coefficients to those of water and human tissues. As a result, the water-equivalent detector will induce only minimal interference to the radiation dose distribution and, in theory, the PSOFDs should require no correction factors when being used for ionising photon detection. However, this water-equivalent property can also cause problems. Due to the low effective atomic

number and density, a plastic scintillator exhibits lower scintillation efficiency (about 2.5% [61]) when compared to that (10–15%) of a scintillation material with a high  $Z_{\text{eff}}$  factor and density (e.g. inorganic scintillators), while its sensitivity may be insufficient for low dose detection applications [43]. More importantly, radiation will induce a stem effect (fluorescence and Cherenkov effect) in the optical fibre, which emits photons in the UV/VIS energy range with a non-linear response to the radiation dose. As the intensity of the scintillation light signal generated in a plastic scintillator is not strong enough that the stem effect noise signal can be neglected, PSOFDs usually require output signal processing for the calibration of the error induced by the stem effect.

### **2.2.2 Inorganic scintillators**

Inorganic scintillators are comprised of materials with relatively high effective atomic numbers ( $Z_{\text{eff}}$ ) and densities; thus, their energy absorption coefficients and light yields are higher than those of plastic scintillators. They also have broad band gaps where electrons can jump up to higher energy levels by means of excitation through ionising radiation or down to lower energy levels via de-excitation through the emission of (visible) photons. The scintillation process can be divided into three stages [62][54], which include a) primary photon interaction, ionization of atoms, relaxation and thermalization of secondary particles, b) transport of electrons and holes and further relaxation, and c) luminescence. In stage a), the ionising photons interact with the scintillator via primary photon interactions (will be introduced in detail in Chapter 3) which including photoelectric absorption, Compton scattering, electron-positron pair production and coherent scattering. These primary photon interactions ionize the atoms,

and, in the case of high energetic photon radiation (e.g. therapeutic  $\gamma$ -rays), secondary electrons with high kinetic energies will also be created. After that, through relaxation and thermalization, the energies of the resulting electrons and holes will be gradually reduced to the band-gap energy  $E_g$ . During this process, many  $e^-—h^+$  pairs are created and thermalized in the conduction band (CB) and valence bands (VBs) respectively. In stage b), the electrons and holes transport in matter cause further relaxation and thermalization, eventually create excitons. The repeated trapping and nonradiative combination of electrons and holes cause energy loss and delay of this migration process. In stage c), the electrons and holes are trapped by the luminescence centre (defect or dopant activator, for example,  $Mn^{2+}$ ,  $Sn^{2+}$ ,  $Eu^{3+}$  and  $Ti^{4+}$ ), and contribute to radiative recombination (ultra-violet/visible light emission).

The inorganic scintillators commonly used for radiation detection can be divided into two major types, namely single crystals and polycrystalline ceramics. The characteristics of some inorganic scintillators are shown in Table (2.1). The typical single crystal scintillators include alkali halides (e.g. thallium doped caesium iodide and sodium iodide CsI:Tl, NaI:Tl),  $CdWO_4$  and  $Bi_4Ge_3O_{12}$ . Both NaI:Tl and CsI:Tl have a relatively high light output and low production, which means they have been widely used as high energy beam detectors in the field of medical imaging (e.g. X-ray computed tomography, positron emission tomography). In addition to their utility in medical imaging, attempts have been reported concerning the fabrication of ISOFDs by coupling these single crystal scintillators with a bundle of optical fibres[49][63]. Although single crystal scintillators show a good sensitivity and linearity for the

radiation response, their application in the fabrication of ISOFDs is still hampered by the difficulty of controlling the geometry of the crystal and restraining the fabrication methods when coupling the scintillator with optical fibres.

Polycrystalline scintillators represent a new class of scintillator. When compared to a traditional scintillator, they can be tailor-made for use in both medical and industrial X-ray detectors for CT-scanning applications[60]. Besides the relatively high energy conversion efficiency and radiation resistance, the powder form polycrystalline scintillators offer great flexibility for X-ray detector manufacturing. For example, Tb-doped gadolinium oxysulphide ( $Gd_2O_2S:Tb$ ) has a high density of  $7.3 \text{ g}\cdot\text{cm}^{-3}$  and an energy scintillation efficiency of 15%. The mean particle diameter of the available commercial  $Gd_2O_2S:Tb$  ranges from 2.5 nm to 25 nm[64]. The powder form  $Gd_2O_2S:Tb$  can be forged into a condensed packed X-ray phosphor layer by means of sintering[65] or the solution evaporation fabrication method[66]. It can also be coated onto the optical fibre surface with an epoxy resin adhesive for SOFD fabrication[33]. In light of this flexibility in terms of fabrication, the powder form inorganic scintillator is a promising scintillation material for ISOFD fabrication.

**Table 2.1** A survey of the characteristics of certain scintillator materials[54], [56], [59], [67], [68]

Phosphor	Density ( $\text{g}\cdot\text{cm}^{-3}$ )	Efficiency $\eta$ (%)*	Light yield photons/MeV	Emission maximum (nm)	Decay time (ns)	Afterglow
$Lu_2SiO_5:Ce$	7.4	9.7	26000	420	40	Low
$Gd_2O_2S:Tb$	7.3	16	60000	540	$6\times 10^5$	Very low
$Gd_2O_2S:Eu$	7.3	12	45000	626	$\sim 10^6$	Low

Phosphor	Density ( $\text{g}\cdot\text{cm}^{-3}$ )	Efficiency $\eta$ (%)*	Light yield photons/MeV	Emission maximum (nm)	Decay time (ns)	Afterglow
Gd <sub>2</sub> O <sub>2</sub> S: Pr	7.3	15	56000	513	$\sim 7 \times 10^3$	Very low
Lu <sub>2</sub> O <sub>3</sub> : Eu	9.4	$\sim 8$	30000	611	$\sim 10^6$	Medium
NaI:Tl	3.67	11.3	41000	410	230	High
CsI:Tl	4.51	13.7	66000	550	800	High
CaWO <sub>4</sub>	6.1	5	20000	420	$6 \times 10^3$	Very low*

### 2.3 Important characteristics of scintillators for SOFDs

There are several important characteristics that must be considered in relation to SOFD detector fabrication[54]:

- (1) The scintillation efficiency  $\eta$ .
- (2) The photon attenuation coefficient  $\mu$  (or the stopping power when the impinging radiation is electrons) corresponding to the specific photon energy range and density ( $\rho$ ) of the material.
- (3) The scintillation response-decay time and afterglow.
- (4) The matching efficiency between the emission peak of the scintillation

---

\* The scintillation efficiency  $\eta$  measures the ratio of scintillation light intensity and the energy absorbed by the scintillator. The light yield also represents the scintillation efficiency in the form of number of photons per unit of absorbed energy (usually MeV), which will be illustrated in detail in section 2.3 (Page 26). Scintillation decay time is the time required for scintillation emission to decrease to 1/e of its maximum, and afterglow describes the visible light emission phenomenon of scintillators after the excitation source been cut off and leaven in darkness, and these two parameters are also illustrated in section 2.3 (Page 27).

spectrum and the photon-detector sensitivity.

- (5) The material's stability (chemical stability and radiation resistance).
- (6) The linearity of the scintillation light response with the incident X-/γ- radiation intensity and dose rate.

Other characteristics of scintillators that are taken into account when fabricating SOFDs include the particle size, refractive index, and commercial expense and availability.

The scintillation efficiency  $\eta$  is the most important parameter of all scintillators. It represents the efficiency of transforming the absorbed radiation energy into visible photons, and it is given by [59] and [62] as

$$\eta = \frac{\text{Total energy of scintillation light}}{\text{Total energy absorption}} \quad (2.1)$$

In many cases, the light yield  $N_{ph}$  is also used to evaluate this parameter  $\eta$ , which is measured as the number of photons per MeV of the absorbed radiation. Assuming that the average energy of a scintillation light photon is  $E_\lambda$  (unit is eV), the light yield  $N_{ph}$  (in the unit  $\text{MeV}^{-1}$ ) is given by

$$N_{ph} = \frac{\eta\% \cdot 10^6 \text{ eV}}{E_\lambda} \quad (2.2)$$

The scintillation efficiency depends on the properties of the scintillator material, the type of incident particles, the energy of the particle and the temperature.

The photon attenuation coefficient  $\mu$  measures how fast the intensity of the photon flux is attenuated when the photon is travelling in the material. The attenuation relationship between the flux intensity  $I$  and the path length  $x$  is given by the exponential attenuation law

$$I = I_0 \exp(-\mu x) \quad (2.3)$$

where  $I_0$  is the intensity of the incident photon flux. For a single photon particle, the possibility  $P$  of the photon being absorbed after traveling a distance of  $x$  in the mass can also be expressed using  $\mu$  according to the following equation

$$P = \exp(-\mu x) \quad (2.4)$$

Here,  $\mu$  is the linear mass attenuation coefficient, which is the product of the total mass attenuation coefficient  $[(\mu/\rho)_{tot}]$ , in the unit  $\text{cm}^2 \cdot \text{g}^{-1}$  and the density ( $\rho$ , in the unit  $\text{g} \cdot \text{cm}^{-3}$ ) of the material

$$\mu = (\mu/\rho)_{tot} \cdot \rho \quad (2.5)$$

$\mu$  depends on the mass density  $\rho$  and the effective atomic number of the material  $Z_{eff}$ , which is calculated according to the equation given by Ishii et al.[58]. Materials with higher mass densities normally has higher electron densities, and also, for the photon absorption and attenuation of ionizing photons with energy higher than a few KeV, the corresponding total mass attenuation coefficient  $(\mu/\rho)_{tot}$  is also higher for materials of large mass densities, therefore, a scintillator material with a high  $\rho$  has a high linear photon attenuation coefficient  $\mu$ .

The scintillation decay time, which refers to the exponential decay component, is defined as the time that must pass before the luminance decreases to 1/e of its initial luminance subsequent to an excitation, while the afterglow quantifies the non-exponential components and is defined as a residual light intensity at some time (typically a few ms) after the excitation is cut off[54]. For application in real-time dose rate measurement, a short decay time and low afterglow are necessary.

The match between the phosphor/scintillator emission spectrum and the photodetector spectral sensitivity dependence is an important necessity, and UV-blue is the optimal choice for a photomultiplier detector, while green-red is optimal for a photodiode[54].

The chemical stability mainly concerns the hygroscopicity of a material. It is an important parameter for scintillators or phosphors that are to be used in the open air (e.g. NaI:Tl, CsI:Na, LaBr<sub>3</sub>:Ce phosphor screen), although in the case of SOFDs, the inorganic scintillation material usually has no direct contact with the surrounding environment, so the chemical stability should not be a concern. Radiation resistance, however, determines the performance of a radiation detector under the accumulated radiation dose. It mainly concerns the changes and performance instabilities due to the induced absorption resulting from the material irradiation and colour centre creation.

The linearity of light responses with the energy and intensity of the incident ionising photon are important parameters of real-time radiation detectors such as SOFDs. The linearity of the response to the incident photon intensity ( $I_0$ ) mainly concerns saturation or stability related issues. However, the physical phenomenon underlying the linearity of the response with the energy of the incident photon ( $h\nu$ ) is more intriguing. It depends on the partial mass attenuation coefficients ( $\mu/\rho$ ) of the predominant photon interactions as well as the light yield corresponding to the energy of the incident photon. Although persistent response linearity is always required over a vast photon energy range, this parameter is actually energy dependent, which is due to the change in the partial mass attenuation coefficients (which will be discussed in detail

in chapter 3) and the non-equal conversion efficiency of the photoelectric and Compton scattering effects. Thus, in terms of actual application, good response linearity can be achieved with X-/  $\gamma$  -ray flux intensity or a dose rate over a certain energy range.

Table (2.1) details the aforementioned parameters of several common scintillators. Comparing the different materials, we can see that none of the scintillators are ‘perfect’ in terms of every aspect of the scintillation characteristics. For example, traditional  $\text{CaWO}_4$  has a short scintillation decay time and a very low afterglow, although it also has quite a poor light yield and scintillation coefficient. Single crystal  $\text{CsI: Tl}$  has the largest light yield and a short decay time, but the afterglow is high, and it is not flexible for SOFD sensor fabrication. Thus, the relative importance of each characteristic of a scintillator must be determined based on the specific radiation detection requirements.

#### **2.4 Scintillation materials for ISOFD fabrication**

As this study aims to develop an ISOFD for the real-time detection of the medical x-/ $\gamma$ -radiation dose, the inorganic scintillator material employed should have a short decay time, a low afterglow and a linear response to the radiation dose. The material should also have a high density ( $\rho$ ) and an effective atomic number ( $Z_{\text{eff}}$ ) so as to acquire a large photon attenuation coefficient (i.e. large absorption efficient). On the other hand, the possibility of fabricating MPSOFD with inorganic scintillators to achieve in-vivo, real-time radiation dose distribution monitoring is also investigated in this thesis. To meet this goal, the scintillators employed in different locations on the optical fibre

should have distinguishable emission peaks, so that the intensity of the emission peak corresponds to the deposited radiation dose.

Taking into account both the physical properties and the commercial availability, we chose different rare-earth (RE) ions-doped  $\text{Gd}_2\text{O}_2\text{S}$  as the scintillator materials for investigation as well as the scintillator for the SOFD simulation presented in the next chapter. The RE ions doped are lanthanum ions  $\text{Tb}^{3+}$ ,  $\text{Eu}^{3+}$  and  $\text{Pr}^{3+}$ , which exhibit strong photoluminescence (PL). One common appealing characteristic of these three ions doped  $\text{Gd}_2\text{O}_2\text{S}$  are their strong scintillation efficiencies (cf. Table (2.1), 12%, 15% and 16% for  $\text{Gd}_2\text{O}_2\text{S}:\text{Eu}$ ,  $\text{Gd}_2\text{O}_2\text{S}:\text{Pr}$  and  $\text{Gd}_2\text{O}_2\text{S}:\text{Tb}$ , respectively), and they all have high densities which are almost the same as that of  $\text{Gd}_2\text{O}_2\text{S}$  ( $7.3 \text{ g} \cdot \text{cm}^{-3}$ ). Moreover, they have short decay time and low afterglow. As it shown in Table (2.1), The decay time of  $\text{Gd}_2\text{O}_2\text{S}:\text{Pr}$  is the shortest, about  $7 \mu\text{s}$ , while  $\text{Gd}_2\text{O}_2\text{S}:\text{Tb}$  has a longer decay time of about  $0.6 - 0.7 \text{ ms}$ , and the decay time of  $\text{Gd}_2\text{O}_2\text{S}:\text{Eu}$  is a little bit longer than  $\text{Gd}_2\text{O}_2\text{S}:\text{Tb}$  (about  $1 \text{ ms}$ ), which is acceptable for applications that do not involve high framing rates and a relatively low sampling frequency. The commerciality is also considered. As the scintillation mechanisms and fabrication methods of the RE-ions doped  $\text{Gd}_2\text{O}_2\text{S}$  have been well explored, these three types of scintillators have good commercial availability. For example,  $\text{Gd}_2\text{O}_2\text{S}:\text{RE}$  (where 'RE' is the rare earth element Tb, Eu or Pr) provided by Phosphor Technology Ltd., UK [64] have stable PL performances and various median particle sizes in the range ( $2.5 \sim 25$ ) nm with respect to different products. In sum,  $\text{Gd}_2\text{O}_2\text{S}:\text{Pr}$ ,  $\text{Gd}_2\text{O}_2\text{S}:\text{Eu}$  and  $\text{Gd}_2\text{O}_2\text{S}:\text{Tb}$  are idea materials for the ISOFD fabrication and following discussion of this thesis.

In the following sub-sections of section 2.4, the PL mechanisms of the scintillators  $\text{Gd}_2\text{O}_2\text{S}:\text{RE}$  ('RE'=Pr, Eu or Tb) will be reviewed with respect to their electronic configurations and the electronic transitions evolved in PL excitation and emission processes. Then, the PL excitation and emission spectra of these scintillators will be introduced. After that, the X-ray luminescence (XRL) spectra of the commercial  $\text{Gd}_2\text{O}_2\text{S}:\text{RE}$  from Phosphor Technologies [64] are described. At last, the dependence of incident radiation (X-rays) absorption efficiency on temperature and X-ray energy level will be discussed with respect to specific scintillators.

#### **2.4.1 Electronic transitions of PL excitation and emission process**

Last paragraph gave a brief introduction to the advantages of RE-ion doped  $\text{Gd}_2\text{O}_2\text{S}$ . In this paragraph, the scintillation mechanisms of  $\text{Gd}_2\text{O}_2\text{S}:\text{RE}$  will be reviewed with respect to the excitation and emission processes of PL. The general scintillation process has been introduced in section 2.2.2. Under X-rays, the  $\text{Gd}_2\text{O}_2\text{S}:\text{RE}$  scintillator first absorbs incident photons and a considerable number of electrons and holes are created. Through a cascade of relaxation and thermalization interactions, the  $e^-—h^+$  pairs are captured by the scintillation center — doped lanthanide ions, where they recombine, and visible photons are then emitted. The excitation and emission characteristics (shown as excitation and emission spectra) of the  $\text{Gd}_2\text{O}_2\text{S}:\text{RE}$  are determined by the migration of electrons and holes between different energy levels of ions and ligands. The doped lanthanide ions serve as activators, by introducing medium energy levels into the band gap of  $\text{Gd}_2\text{O}_2\text{S}$ .

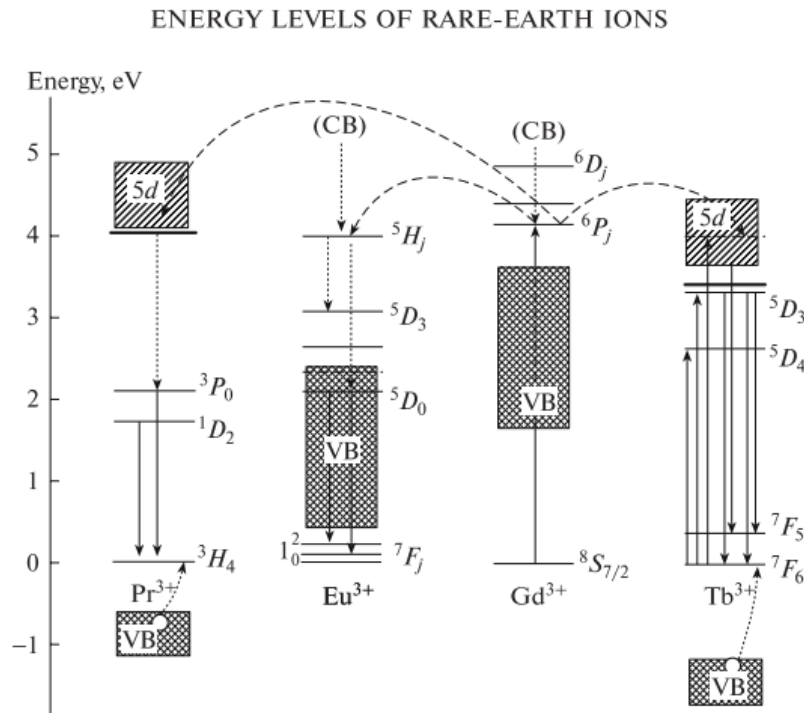
Pr, Eu, Gd, and Tb all belong to lanthanides. For the excitation and luminescence processes, lanthanide ions display three types of electronic transitions. First, the forbidden and faint intraconfiguration  $f \rightarrow f$  transitions (i.e.  $4f \rightarrow 4f$ ). The second kind of transitions involves the promotion of a  $4f$  electron into the  $5d$  subshell ( $4f \rightarrow 5d$  transitions). Finally, charge-transfer transitions, both ligand-to-metal and metal-to-ligand, constitute the third kind of electronic transitions[69]. The electronic configurations and of the doped ions ( $\text{Pr}^{3+}$ ,  $\text{Eu}^{3+}$ , and  $\text{Tb}^{3+}$ ) and the host lattice is the key factor to understand the specific electronic transitions in PL excitation and emission processes. The general electronic configuration of the lanthanide atom is  $[\text{Xe}] 4f^n 5d^1 6s^2$ , where  $n$  is between 0~14, and  $[\text{Xe}]$  represents the electronic configuration of a xenon atom. The most stable oxidation state of the lanthanide ion is +3 with a  $[\text{Xe}] 4f^n$  configuration, and the electronic configurations of  $\text{Pr}^{3+}$ ,  $\text{Eu}^{3+}$ ,  $\text{Gd}^{3+}$ , and  $\text{Tb}^{3+}$  ions are  $[\text{Xe}]4f^2$ ,  $[\text{Xe}]4f^6$ ,  $[\text{Xe}]4f^7$ , and  $[\text{Xe}]4f^8$ , respectively. The corresponding ground energy states of the  $\text{Pr}^{3+}$  ( $[\text{Xe}]4f^2$ ),  $\text{Eu}^{3+}$  ( $[\text{Xe}]4f^6$ ),  $\text{Gd}^{3+}$  ( $[\text{Xe}]4f^7$ ), and  $\text{Tb}^{3+}$  ( $[\text{Xe}]4f^8$ ) are  $^3H_4$ ,  $^7F_0$ ,  $^8S_{7/2}$ , and  $^7F_6$ , respectively\*.

Figure 2.2 gives the energy levels and most intense electronic transitions of  $\text{Pr}^{3+}$ ,  $\text{Eu}^{3+}$ ,  $\text{Gd}^{3+}$ , and  $\text{Tb}^{3+}$  ions in  $\text{Gd}_2\text{O}_2\text{S}$ , which is sourced from the article of Rodnyi[70]. For the convenience of illustration, the energy levels of the ground  $4f^n$  energy states of all ions are assumed to be zero in Figure 2.2. For  $\text{Gd}_2\text{O}_2\text{S}$  host, the common

---

\* The electronic configuration only gives a very crude description of the electronic energy levels of an atom. The state (also known as multiplet or term) of a lanthanide ion, on the other hand, gives more specific information of the electron energy states and considers the values of the orbital and the spin angular momentum (L and S, respectively), as well as the spin-orbit coupling effect (J). The state is expressed as  $^{2S+1}L_J$ . The basic knowledge of L-S coupling has been described in Ref [149].

excitation transitions include the VB→CB transition and  $f \rightarrow f$  transitions ( $^8S_{7/2}$ - $^6P_j$   $Gd^{3+}$  transitions) as shown in Figure 2.2. The final state of the  $Gd^{3+}$  relaxation is the lower  $^6P_j$  multiplets. The life time of  $^6P_j$  is relatively long, and the excitation energy can be transferred to the activator ions ( $Pr^{3+}$ ,  $Eu^{3+}$  or  $Tb^{3+}$ ). Then the excitation is transferred from  $Gd^{3+}$  to the activator (dashed arrows in Figure 2.2). As for the doped ions in the  $Gd_2O_2S$  matrix, the intense electronic transitions during the excitation process include  $4f \rightarrow 5d$  transitions of  $Pr^{3+}$  and  $Tb^{3+}$  ions, and charge transfer between  $Eu^{3+}$  and ligand.



**Figure 2.2** Energy levels and most intense electronic transitions of  $Pr^{3+}$ ,  $Eu^{3+}$ ,  $Gd^{3+}$ , and  $Tb^{3+}$  ions in  $Gd_2O_2S$ . The position of the ground  $4f^n$  states of ions is assumed to be zero[70].

The electronic transitions during PL emission process varies with respect to the doped ions as shown in Figure 2.2. For  $Pr^{3+}$  doping, the actual emission spectrum is comprised of peaks corresponding to  $^3P_j \rightarrow ^3H_j$  transitions of  $Pr^{3+}$ . Among them the

most intense transitions listed in Figure 2.2 are  ${}^3P_0 \rightarrow {}^3H_4$  (513 nm). Under certain conditions,  ${}^1D_2 \rightarrow {}^3H_4$  transition can also be intensive. For  $\text{Eu}^{3+}$  doping, the emission spectrum of  $\text{Gd}_2\text{O}_2\text{S}:\text{Eu}$  includes a series of lines which are due to  ${}^5D_0 \rightarrow {}^7F_j$  transitions of  $\text{Eu}^{3+}$ . Upon excitation, the higher excited levels like  ${}^5H_j$  and  ${}^5D_3$  will first relax to lower  ${}^5D_0$  state, then the  $\text{Eu}^{3+}$  ions relax to  ${}^7F_j$  multiplets through photon emissions. The strongest emission peaks correspond to  ${}^5D_0 \rightarrow {}^7F_2$  (near 626 nm) and  ${}^5D_0 \rightarrow {}^7F_1$  (near 590 nm). As for  $\text{Tb}^{3+}$  doped  $\text{Gd}_2\text{O}_2\text{S}$ , the lines or peaks of  $\text{Gd}_2\text{O}_2\text{S}:\text{Tb}$  emission spectrum are due to a series of  ${}^5D_i \rightarrow {}^7F_j$  (where ‘ $i$ ’= 3 or 4, and ‘ $j$ ’ is the integer between 3 and 6) transitions of  $\text{Tb}^{3+}$ . The most characteristic transition are the  ${}^5D_4 \rightarrow {}^7F_5$  (near 545 nm) transition and  ${}^5D_3 \rightarrow {}^7F_5$  (416 nm), and they have different temperature dependences, which will be discussed in section 2.4.4.

#### **2.4.2 The PL excitation and emission spectra of $\text{Gd}_2\text{O}_2\text{S}:\text{RE}$**

Last section gives a brief review of the electronic configurations of lanthanide ions (Eu, Pr, Gd and Tb) and some intense electronic transitions evolved in PL excitation and emission processes. In this section, the PL excitation and emission of three types of scintillators  $\text{Gd}_2\text{O}_2\text{S}:\text{Pr}$ ,  $\text{Gd}_2\text{O}_2\text{S}:\text{Eu}$  and  $\text{Gd}_2\text{O}_2\text{S}:\text{Tb}$  will be introduced in detail based on the experimental results reported by other researchers[71]. It is noted that, the intensities of the band and lines in PL excitation and emission spectra will change according to the concentration of the doped RE ions, fabrication methods[72], and sometimes even temperature. To make the following contents easy to understand, unless otherwise noted, the PL excitation and emission spectra referenced from other researchers’ articles are assumed to be tested under room temperature.

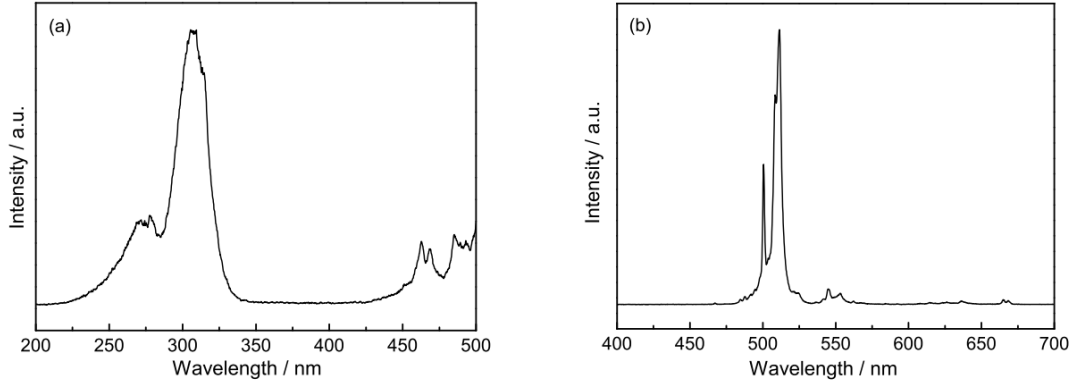


**Figure 2.3** The PL excitation (a) and emission (b) spectra of the  $\text{Gd}_2\text{O}_2\text{S}:\text{Pr}$  from the article of Lian et al[73].

$\text{Gd}_2\text{O}_2\text{S}:\text{Pr}$  exhibits green emission near 513 nm. The PL excitation spectrum of  $\text{Gd}_2\text{O}_2\text{S}:\text{Pr}$  (0.03 % mol \*) as shown in Figure 2.3 (a)[73], include two broad bands at 270 nm and 309 nm. The broad band at 270 nm is originated from the band gap self-absorption of  $\text{Gd}_2\text{O}_2\text{S}$  host lattice ( $E_g = 4.6$  eV). The stronger band at 309 nm is attributed from  $4f \rightarrow 5d$  transition of  $\text{Pr}^{3+}$  ions. In addition, the band in the 450–500 nm region corresponds to the  ${}^3H_j \rightarrow {}^3P_j$ ,  ${}^1I_6$  of transitions of  $\text{Pr}^{3+}$  ions. As for the PL emission process, the emission spectrum (Figure 2.3 (b)) shows that the  ${}^3P_j \rightarrow {}^3H_j$  transitions of  $\text{Pr}^{3+}$  contribute to different emission peaks. The dominant emission peak is at 511 nm, which corresponds to the  ${}^3P_0 \rightarrow {}^3H_4$  transition of the  $\text{Pr}^{3+}$  ions. The sharp peak around 500 nm belongs to the  ${}^3P_1 \rightarrow {}^3H_4$  transition of  $\text{Pr}^{3+}$ . The weak peaks located at 549 nm and 557 nm are attributed to the  ${}^3P_1 \rightarrow {}^3H_5$  and  ${}^3P_0 \rightarrow {}^3H_5$  transitions of  $\text{Pr}^{3+}$  respectively[74]. The further research of Lian et al[74] shows that the PL emission intensities of  $\text{Gd}_2\text{O}_2\text{S}:\text{Pr}$  microspheres depend on the concentration of  $\text{Pr}^{3+}$  ions. The  $\text{Gd}_2\text{O}_2\text{S}:\text{Pr}$  sample with 1.0% mol  $\text{Pr}^{3+}$  exhibits strongest luminescence intensity.

\* the  $\text{Pr}^{3+}$  concentration 0.03 % mol means that 1 mol  $\text{Gd}_2\text{O}_2\text{S}:\text{Pr}$  contains 0.03% mol  $\text{Pr}^{3+}$  ions.

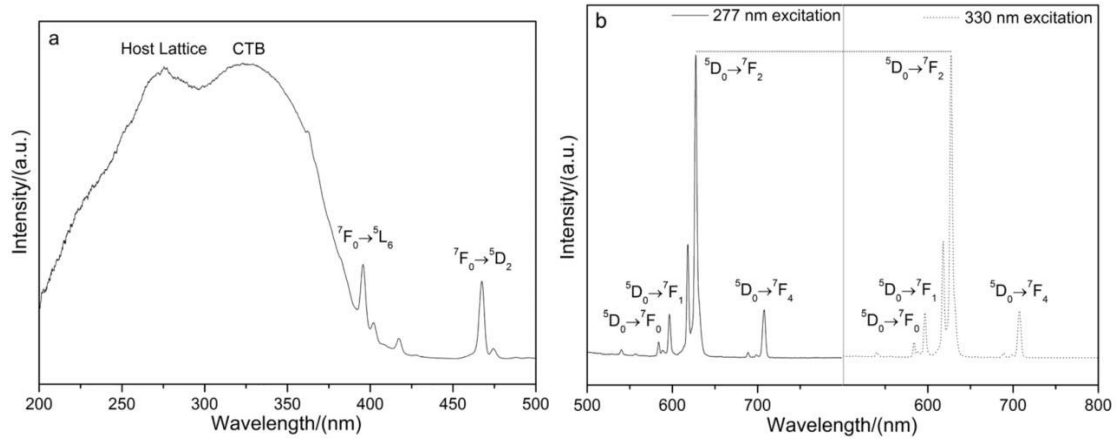


**Figure 2.4** Excitation (a) and emission (b) spectra of the  $\text{Gd}_2\text{O}_2\text{S}:\text{Eu}$  hollow spheres[71]

$\text{Gd}_2\text{O}_2\text{S}:\text{Eu}$  exhibits characteristic red luminescence under radiation. According to the research of Hang T et al[71], The PL excitation spectrum (Figure 2.4 (a)) of  $\text{Gd}_2\text{O}_2\text{S}:\text{Eu}$  (5%mol) shows two broad bands centered at 270 nm and 330 nm, which correspond to the  $\text{Gd}_2\text{O}_2\text{S}$  matrix absorption (band gap of  $\text{Gd}^{3+}$ ) and charge transfer (CT) transition ligand ( $\text{O}^{2-}/\text{S}^{2-}$ ) $\rightarrow\text{Eu}^{3+}$  respectively. The weak narrow peaks (395 nm and 465 nm) beyond UV range is attributed to the  $f \rightarrow f$  transition of  $\text{Eu}^{3+}$ . The peak located at 395 nm corresponds to  ${}^7F_0 \rightarrow {}^5L_6$  of  $\text{Eu}^{3+}$  ions while the peak at 465 nm corresponds to  ${}^7F_0 \rightarrow {}^5D_2$  of  $\text{Eu}^{3+}$ . As for the emission spectrum of  $\text{Gd}_2\text{O}_2\text{S}:\text{Eu}$ , the PL performance under 2 different excitation wavelengths (277 nm and 330 nm) were compared by Hang T et al. The emission spectra demonstrate the  ${}^5D_0 \rightarrow {}^7F_j$  ( $j = 0, 1, 2, 3, 4$ ) transitions of  $\text{Eu}^{3+}$  ions. The most intensive emission peak (628 nm) and a side peak (615 nm) corresponds to  ${}^5D_0 \rightarrow {}^7F_2$  transition of  $\text{Eu}^{3+}$ . Other weaker emission peaks are assigned to the  ${}^5D_0 \rightarrow {}^7F_0$  (581 nm),  ${}^5D_0 \rightarrow {}^7F_1$  (586, 594 nm), and  ${}^5D_0 \rightarrow {}^7F_4$  (703 nm) transitions of  $\text{Eu}^{3+}$  ions, respectively. The emission spectra under two different excitation wavelengths (277 nm and 330 nm) show minor difference.

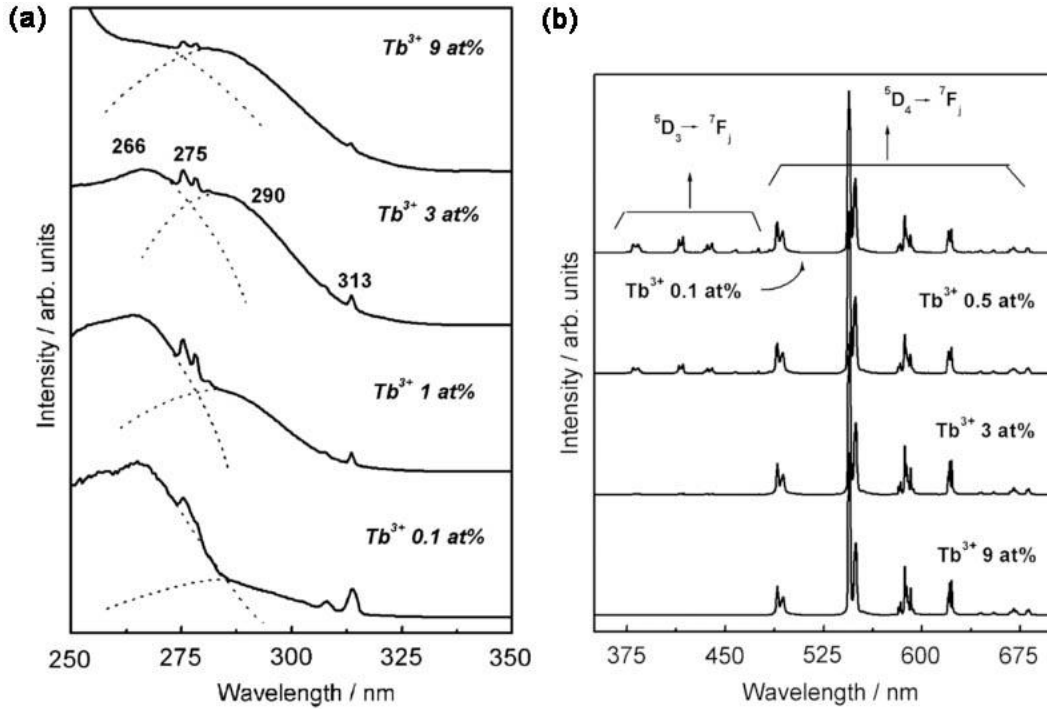


**Figure 2.5** The PL excitation ( $\lambda_{em}=544$  nm) and emission ( $\lambda_{ex}=266$  nm) spectra of  $Gd_2O_2S:Tb$  doped with different  $Tb^{3+}$  content [72]

$Gd_2O_2S:Tb$  exhibits green luminescence under radiation, and the wavelength of the green emission peak ( $\sim 540$  nm) is longer than that of  $Gd_2O_2S:Pr$  (511 nm). Figure 2.5 from Ref [72] shows the PL excitation and emission spectra of  $Gd_2O_2S:Tb$  doped with different  $Tb^{3+}$  content. The excitation spectra were obtained at the most intensive 544 nm emission wavelength ( $\lambda_{em}=544$  nm). Two broad bands were observed at 266 nm and 290 nm, which correspond to the  $Gd_2O_2S$  matrix absorption ( $VB \rightarrow CB$ ) and  $4f \rightarrow 5d$  transition of  $Tb^{3+}$  respectively. There are also two sets of lines at 275 nm and 313 nm, which are ascribed to  ${}^8S_j \rightarrow {}^6I_{3/2}$  and  ${}^8S_j \rightarrow {}^6P_j$  transitions ( $4f \rightarrow 4f$ ) of the  $Gd^{3+}$  ions respectively. Comparing the excitation spectra of the samples doped with different  $Tb^{3+}$  content, the result shows that the intensity of the broadband at 290 nm increases with respect to higher  $Tb^{3+}$  concentration, while no change is observed on the 266 nm

band. The PL emission spectra of  $\text{Gd}_2\text{O}_2\text{S:Tb}$  demonstrate the dependence on the concentration of the  $\text{Tb}^{3+}$  ions. At low  $\text{Tb}^{3+}$  concentration,  ${}^5D_3 \rightarrow {}^7F_j$  (blue) and  ${}^5D_4 \rightarrow {}^7F_j$  (green) transitions of  $\text{Tb}^{3+}$  ions can be observed. The most intensive emission line is ascribed to  ${}^5D_4 \rightarrow {}^7F_5$  transition. As the  $\text{Tb}^{3+}$  concentration is increased, the blue emission corresponding to  ${}^5D_3 \rightarrow {}^7F_j$  transitions vanish, and only  ${}^5D_4 \rightarrow {}^7F_j$  (green) emission remain in the spectrum. This  $\text{Tb}^{3+}$  concentration dependent behavior is due the cross-relaxation processes[75].

### 2.4.3 The X-ray luminescence (XRL) spectra of $\text{Gd}_2\text{O}_2\text{S:RE}$

In above sections, the PL excitation and emission spectra and related electronic transitions have been described. However, for  $\text{Gd}_2\text{O}_2\text{S:RE}$  based sensors used for X-ray detection, the XRL emission spectra of scintillators should be considered. due to the different excitation mechanisms of the UV and X-ray radiation excitation for the  $\text{Gd}_2\text{O}_2\text{S:RE}$ . The XRL spectra of commercial  $\text{Gd}_2\text{O}_2\text{S:RE}$ , which provided by Phosphor Technology Ltd., UK [64], will be introduced. Then the difference between PL and XRL emission spectra will be briefly illustrated.

The  $\text{Gd}_2\text{O}_2\text{S:RE}$  samples include UKL59/N-R1 ( $\text{Gd}_2\text{O}_2\text{S:Pr}$ ), UKL63/N-R1 ( $\text{Gd}_2\text{O}_2\text{S:Eu}$ ) and UKL65/N-R1 ( $\text{Gd}_2\text{O}_2\text{S:Tb}$ ). As shown in Figure 2.6, all these three different types of samples exhibit characteristic emission lines and peaks of the corresponding doped RE ions. The XRL spectrum of  $\text{Gd}_2\text{O}_2\text{S:Pr}$  in Figure 2.6(a) shows green emission with a dominant emission peak at 513 nm due to the  ${}^3P_0 \rightarrow {}^3H_4$  transition of  $\text{Pr}^{3+}$  ions, and a second strongest emission peak at 672.2 ascribed to the  ${}^5P_0 \rightarrow {}^3F_2$  of  $\text{Pr}^{3+}$  ions. The XRL emission spectrum of  $\text{Gd}_2\text{O}_2\text{S:Eu}$  (Figure 2.6(b)) shows red

emission. The dominant emission peak at 626.0 nm and a side peak at 616 nm are both due to  $^5D_0 \rightarrow ^7F_2$  transition of  $\text{Eu}^{3+}$  ions. As for the XRL spectrum of  $\text{Gd}_2\text{O}_2\text{S}:\text{Tb}$  shown in Figure 2.3(c) has a dominant emission peak at 544 nm due to the  $^5D_4 \rightarrow ^7F_5$  transition of  $\text{Tb}^{3+}$  ions.

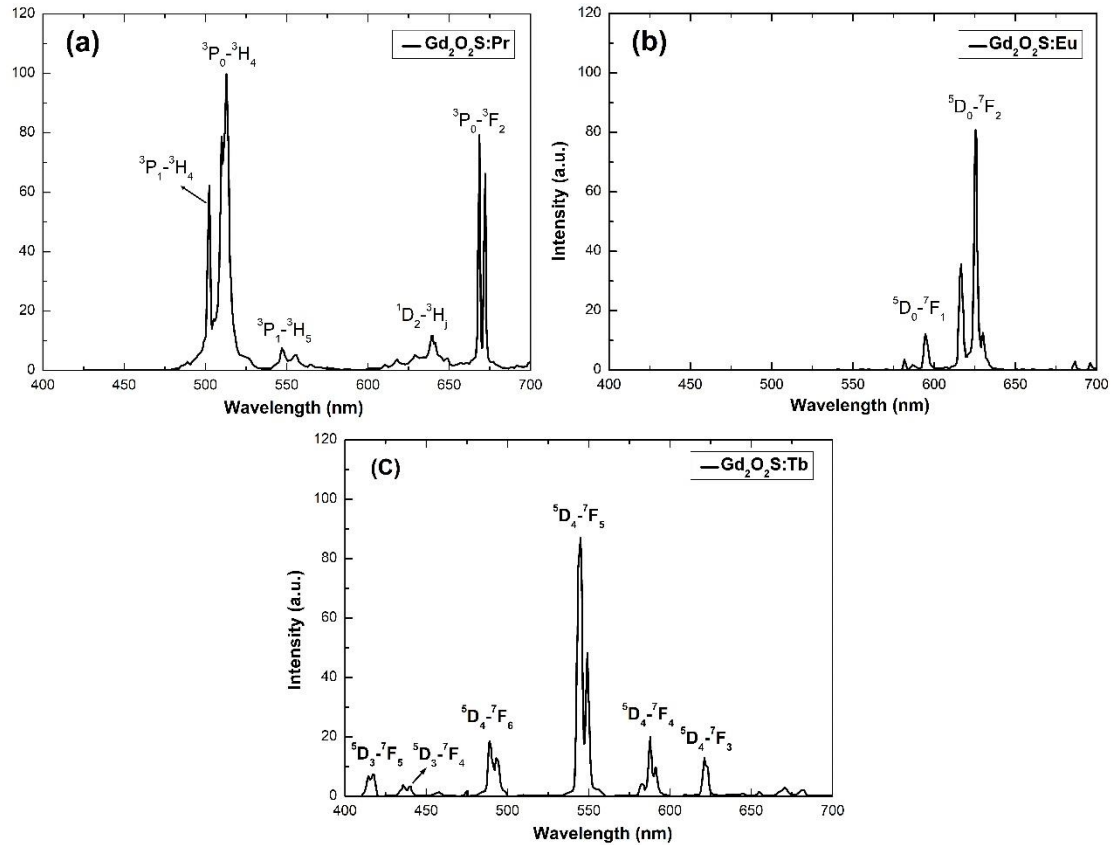


**Figure 2.6** The XRL emission spectra of  $\text{Gd}_2\text{O}_2\text{S}$  doped with different RE ions: the spectra of  $\text{Gd}_2\text{O}_2\text{S}:\text{Pr}$  (a),  $\text{Gd}_2\text{O}_2\text{S}:\text{Eu}$  (b) and  $\text{Gd}_2\text{O}_2\text{S}:\text{Tb}$  (c) respectively. The spectra data were required from Phosphor Technology Ltd., UK [64].

According to the reported research on the fabrication and characterization of  $\text{Gd}_2\text{O}_2\text{S}:\text{RE}$ [76]–[78], the XRL (using the X-ray source) and PL (using the UV light source) emission spectra share lots of similarities, the luminescence peaks both show the characteristic emission of doped RE element. However, the comparison of the XRL and PL spectra of the same sample show some differences in terms of the peak intensity,

Full Width at Half Maximum (FWHM), and even the emission peak locations. For example, the  $\text{Gd}_2\text{O}_2\text{S}:\text{Pr}$  scintillation ceramics reported by Wang et al[76], has different integrated emission peak intensity ratio\* under X-ray compared to those under UV excitation source ( $\lambda_{\text{ex}}=300$  nm). For XRL, the sample still exhibits the dominant green emission peak at 513 nm due to  ${}^3P_0 \rightarrow {}^3H_4$  transition of  $\text{Pr}^{3+}$  ions, the emission peak at 665 nm (the  ${}^3P_0 \rightarrow {}^3F_2$  transition) shows apparently stronger intensity ratio ( ${}^3P_0 \rightarrow {}^3F_2 / {}^3P_0 \rightarrow {}^3H_4$ ) compared to that of PL emission. The PL and XRL emission spectra of  $\text{Gd}_2\text{O}_2\text{S}:\text{Tb}$  also show differences in terms of FWHM and locations of emission peaks. The reason behind this phenomenon might due to the different excited mechanism between UV and X-ray excitation. The UV excitation is a simple process in which the UV photon reacts directly with the activator (doped RE ions). While the X-ray excitation and emission process, as it has been described in section 2.2.2 and 2.4.1, is a more complicated process, which is comprised of three steps[62][54]. The activator is excited by the capturing of  $e^- - h^+$  pairs which resulting from the X-ray interaction with the  $\text{Gd}_2\text{O}_2\text{S}$  matrix and furtherly secondary electron interaction with the matrix.

#### **2.4.4 Temperature dependence of $\text{Gd}_2\text{O}_2\text{S}:\text{RE}$**

The XRL excitation mechanism of  $\text{Gd}_2\text{O}_2\text{S}:\text{RE}$  determines that emission peaks of the XRL spectrum correspond to the characteristic electronic transitions of doped RE ions, thus the location of the emission peaks and lines will remain the same regardless of the energy level and intensity of the X-ray radiation source, and the intensity of the

---

\* the integrated peak ratio means the ratio of integrated intensity of two different peaks in the spectrum.

emission peak changes accordingly with the intensity of the incident radiation. However, the normalized intensity of the emission peak is determined by not only energy level of the incident X-ray, but also the X-ray absorption efficiency. In some cases, the XRL emission performance of the scintillator is also influenced by the environment temperature. In this section, the influence the environmental temperature on the XRL performance of scintillators  $\text{Gd}_2\text{O}_2\text{S:RE}$  will be discussed.

The temperature dependence of the scintillator measures the XRL of the scintillator at various temperatures. The thermal stability of scintillator is one of the important issues. For the practical application. To be utilized for medical X-ray dosimetry, the scintillator should have a good thermal stability and a consistent radio-luminescent performance. In the following paragraphs, this property will be discussed with respect to  $\text{Gd}_2\text{O}_2\text{S: Pr (Ce)}$  and  $\text{Gd}_2\text{O}_2\text{S:Tb}$ .

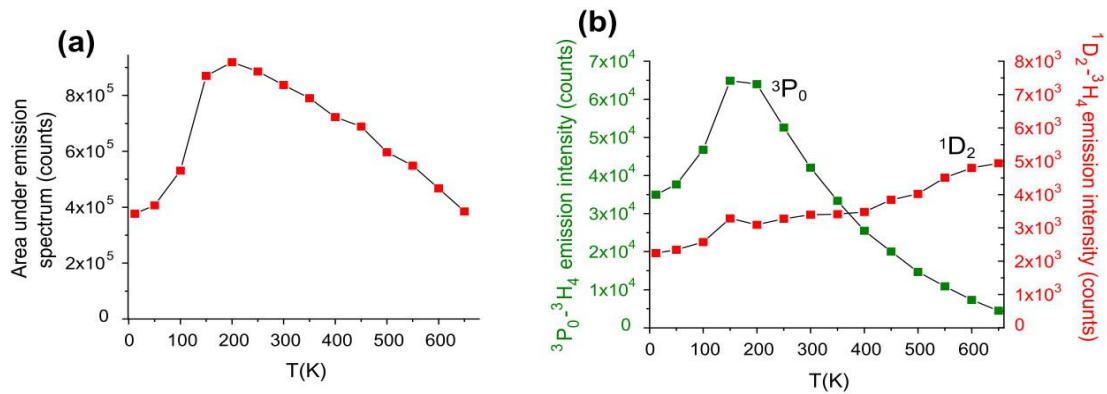


**Figure 2.7** Temperature dependence of  $\text{Gd}_2\text{O}_2\text{S:Pr (Ce)}$  reported by Blahuta S et al [79]: evolution with temperature of (a) the total luminescence intensity (area under the XRL spectra over the 400–900 nm region); (b) the intensity of the  $^3P_0 \rightarrow ^3H_4$  (at 514 nm) and  $^1D_2 \rightarrow ^3H_4$  (at 630 nm) emissions.

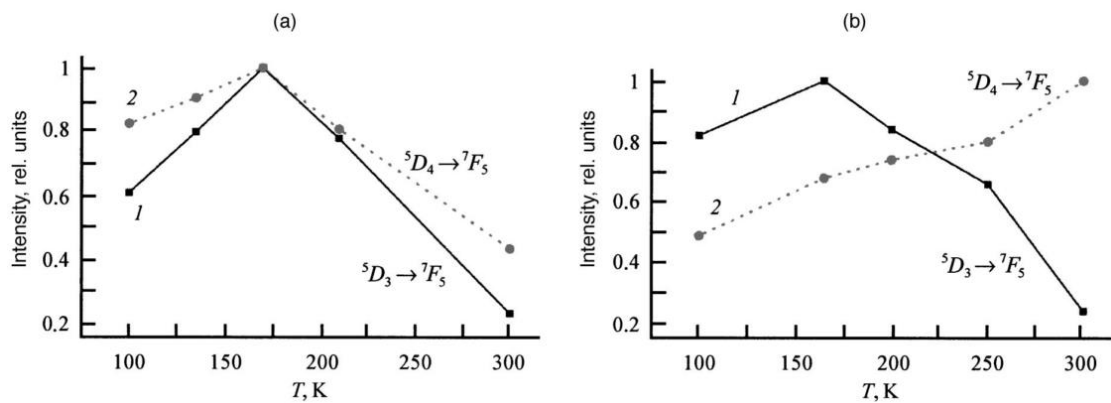
The temperature dependence of XRL performance of  $\text{Gd}_2\text{O}_2\text{S: Pr (Ce)}^*$  (provided by Saint-Gobain Crystals and Detectors) was studied and reported by Blahuta S et al [79]. The result shows that from 200 K to both low and high temperature, XRL intensity decreases by 60% as shown in Figure 2.7(a), which is closely related to the temperature dependence behaviour of the dominant emission peak at 514 nm ( ${}^3P_0 \rightarrow {}^3H_4$  transition of  $\text{Pr}^{3+}$ ). The further study of the luminescence decay time and thermoluminescence revealed the different cause of the temperature dependence of  $\text{Gd}_2\text{O}_2\text{S:Pr (Ce)}$  with respect to different temperatures. At low temperature, the low light yield is linked to the intense thermoluminescence around 120 K which ascribed to sulfur vacancies. These traps cause efficient electron trapping which competes with the prompt recombination mechanism. At higher energies, the excitation energy is lost due to the non-radiative energy loss caused by the high temperature quenching of  $\text{Pr}^{3+}$  and competitive electron capturing by defects (such as sulfur vacancies) other than  $\text{Pr}^{3+}$  activator.

Figure 2.8 The XRL temperature dependence of  $\text{Gd}_2\text{O}_2\text{S:Tb}$  is reported by Gorokhova E et al [80]. The intensities of individual XRL emission bands (peaks) of  $\text{Gd}_2\text{O}_2\text{S:Tb}$  ceramics before (Figure 2.8 (a)) and after (Figure 2.8 (b)) heat treatment were measured with respect to the increasing temperature. The result shows that the heat treatment has a significant effect on the XRL emission characteristic of  $\text{Gd}_2\text{O}_2\text{S:Tb}$  ceramics. The ceramic sample after the heat treatment shows stronger XRL intensity at

---

\*  $\text{Ce}^{3+}$  is added as a co-doping to reduce the afterglow and increase the radiation resistance. The PL and XRL spectra of  $\text{Gd}_2\text{O}_2\text{S: Pr (Ce)}$  is composed entirely of  $\text{Pr}^{3+} 4f^2 - 4f^2$  lines

higher temperatures. Moreover, the two most characteristic luminescence lines at 545 ( ${}^5D_4 \rightarrow {}^7F_5$ ) and 416 nm ( ${}^5D_3 \rightarrow {}^7F_5$ ) have different temperature dependences as it shown in Figure 2.8. For the  $Gd_2O_2S:Tb$  ceramic after heat treatment, the intensity change the two luminescence lines can be attributed to the temperature quenching of the short-wavelength series of lines or peaks, in which the excitation energy is transferred from the upper  ${}^5D_3$  multiplet to the lower  ${}^5D_4$  multiplet.



**Figure 2.8** The temperature dependence of the individual emission bands (peaks) of  $Gd_2O_2S:Tb$  ceramics before (a) and after heat treatment (b), reported by Gorokhova E et al [80]. 1—416 nm ( ${}^5D_3 \rightarrow {}^7F_5$ ) 545 nm ( ${}^5D_4 \rightarrow {}^7F_5$ ) luminescence lines.

Due to the lack of reported research, the temperature dependence of  $Gd_2O_2S:Eu$  has not been reviewed in this thesis. However, based on the research of other RE element doped  $Gd_2O_2S$ , it can be concluded that the XRL performance of  $Gd_2O_2S:RE$  is more or less affected by the temperature, and this temperature dependence is normally caused by thermal quenching of doped RE ions, or the competitive capturing of  $e^-—h^+$  pairs by the activator and defects in the scintillator, or sometimes both. As temperature dependence of the scintillator can be modified through improving synthesis

methods and heat treatment [72], [77], [78], [80], [81], it is possible to acquire  $\text{Gd}_2\text{O}_2\text{S}:\text{RE}$  with relatively satisfying XRL characteristics in the temperature range relative to medical radiation detection.

#### 2.4.5 X-ray energy dependence

The effect of the X-ray energy level on the XRL performance is an issue of interest, and also important for the practical application of  $\text{Gd}_2\text{O}_2\text{S}:\text{RE}$  scintillators. Though there is limited reported research comparing the XRL spectra under different incident X-ray energy levels or X-ray tube voltages, the X-ray absorption efficiency of  $\text{Gd}_2\text{O}_2\text{S}:\text{RE}$  have been studied and discussed by lots of researchers, which gives an indirect insight into the effect of incident X-ray energy level on the XRL spectra of  $\text{Gd}_2\text{O}_2\text{S}:\text{RE}$ .

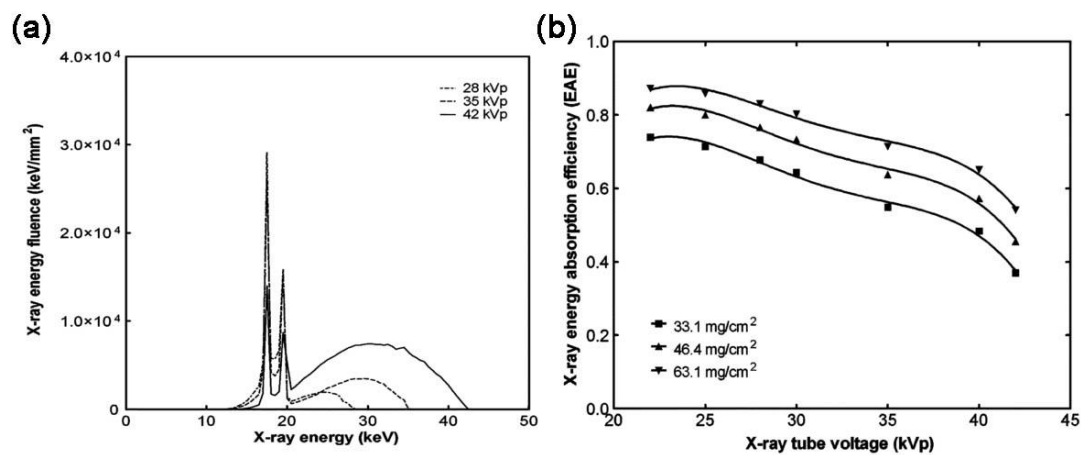


**Figure 2.9** X-ray energy fluence spectra of the X-ray tube at different voltages (a), and X-ray energy absorption efficiency for the  $\text{Gd}_2\text{O}_2\text{S}:\text{Eu}$  screens in the mammographic energy range.[82]

In 2008, Michail CM et al [82] examined  $\text{Gd}_2\text{O}_2\text{S}:\text{Eu}$  powder scintillator screens under X-ray mammography imaging conditions.  $\text{Gd}_2\text{O}_2\text{S}:\text{Eu}$  screens with different

thicknesses are tested. The X-ray spectra of the X-ray tubes (Figure 2.8 (a)) shows that the centre of wide emission bands moves towards larger X-ray energy levels and the intensity grows stronger as the X-ray tube voltage increases. The corresponding X-ray energy absorption efficiency decreases with respect to higher tube voltages. This negative effect of the X-ray tube voltage (in the range 20~50 KeV) on the X-ray absorption efficiency of Gd<sub>2</sub>O<sub>2</sub>S scintillators may be due to the change of photon attenuation coefficient ( $\mu \text{ cm}^{-1}$ ) of the Gd<sub>2</sub>O<sub>2</sub>S matrix ( $\mu_{\text{GOS}}$ ). In the energy range 20~50 KeV,  $\mu_{\text{GOS}}$  decreases with increasing X-ray energy and the probability of X-ray photons interacting with GOS is getting lower, thus X-ray photons are more penetrating, and the X-ray absorption efficiency is lower. Due to the negligible Eu<sup>3+</sup> dopant weight ratio in the compound, the photon attenuation coefficient ( $\mu$ ) of Gd<sub>2</sub>O<sub>2</sub>S:Eu is almost the same as that of Gd<sub>2</sub>O<sub>2</sub>S regardless of the doping ions, therefore the X-ray absorption efficiency of the Gd<sub>2</sub>O<sub>2</sub>S:Eu screen in Figure 2.9(b) decreases slightly as the X-ray tube voltage getting higher. Same behaviour is expected for low-dopant Gd<sub>2</sub>O<sub>2</sub>S:Tb and Gd<sub>2</sub>O<sub>2</sub>S:Pr.

Generally, Gd<sub>2</sub>O<sub>2</sub>S has a higher attenuation coefficient for incident photons in the diagnostic X-ray energy range (20 – 150 KeV) than those in the therapeutic energy range (1 – 25 MeV), which is partially due to the abrupt increase in the photoelectric absorption efficient at the K (50.24 KeV) and L<sub>1</sub> (8.38 KeV) edges of gadolinium (Z=64). This energy dependence on the part of the mass attenuation coefficients will be discussed in detail in chapter 3 from the point of view of basic photon interaction physics and further simulation in chapter 5.

On the other hand, with the same X-ray tube current, the XRL intensity of the  $\text{Gd}_2\text{O}_2\text{S}:\text{Eu}$  is getting higher with respect to rising X-ray tube voltage. This is because that the incident X-ray flux is higher, and more energy can be absorbed by the scintillator despite of slightly lower absorption efficiency. Considering the mechanism of XRL mechanism reviewed in above sections, the RE ions are excited indirectly by the X-ray photons and the emission process is independent of the X-ray energy, thus theoretically, changing the energy level of X-ray will not affect the characteristics of the XRL spectrum, but only change the intensity of the emission peaks. The research on  $\text{Gd}_2\text{O}_2\text{S}:\text{Tb}$  based optical fibre dosimeter reported by McCarthy et al [33] confirmed that the intensity of the maximum emission peak (at 544 nm) is proportional to the dose rate of the incident X-rays, and the width of the peak remains to be 16 nm.

Overall, this section (section 2.4) gives a detailed introduction to the inorganic scintillators  $\text{Gd}_2\text{O}_2\text{S}:\text{RE}$  from the aspects as scintillation mechanism, PL and XRL spectra, and the factors affecting the XRL performance. Scintillators  $\text{Gd}_2\text{O}_2\text{S}:\text{Tb}$  and  $\text{Gd}_2\text{O}_2\text{S}:\text{Pr}$  both show temperature dependence. The X-ray energy level affects the absorption efficiency, thus the intensity of the XRL is dependent of the X-ray energy, which is one of issue studied and discussed in the following chapters in this thesis.

## **2.5 Introduction to SFODs**

In this section, both plastic and inorganic SFODs are reviewed. Although plastic SFODs (PSOFDs) are not our research topic, considering the much longer history and research effort dedicated to PSOFDs, the valuable experience and phenomena explored and

reported by previous researchers will undoubtedly provide inspiration when developing our multi-point inorganic scintillator coupled optical fibre dosimeter (MPISOFD). Considering the large quantity of articles available in this research area, we will review some typical SOFDs.

### **2.5.1 Plastic scintillator coupled optical fibre dosimeters (PSOFDs)**

The plastic scintillators are aromatic hydrocarbon compounds which contain benzene ring structures interlinked in various ways[83]. The difference in the scintillation mechanism between the plastic scintillator and the inorganic scintillator is that the organic scintillator scintillates at a molecular level. The energy is transferred through the free valence electrons of the molecules ( $\pi$  electrons). As  $\pi$  electrons are associated with the whole molecule rather than any particular atom, each molecule of the plastic scintillator can act as a scintillation centre, which is different from the scintillation mechanism of the inorganic scintillator[83]. The plastic scintillators have similar effective atomic numbers and densities as that of water, thus they have similar photon absorption efficiency as that of water and human tissue. A plastic scintillator offers significant advantages in terms of the water-equivalent, good linearity to the radiation dose and energy independence in the megavoltage energy range.

The notion of PSOFDs emerged as early as 1969, when Byfield et al.[19] reported a fibre optics scintillation for intracavitary dosimetry. The scintillation part of the probe was encapsulated in a 17 cm long stainless probe. The light photons generated in the scintillator under radiation were conducted via a Lucite 'light pipe' and then converted into electric signals by means of a photomultiplier attached to the other end of the pipe.

The detector enabled the real-time dose registration of external radiotherapy beams from cobalt 60 and megavoltage X-rays in a phantom. Although this probe dosimeter might appear primitive, the scintillator-optical fibre coupling designs of various later SOFDs were more or less similar to this initial design.

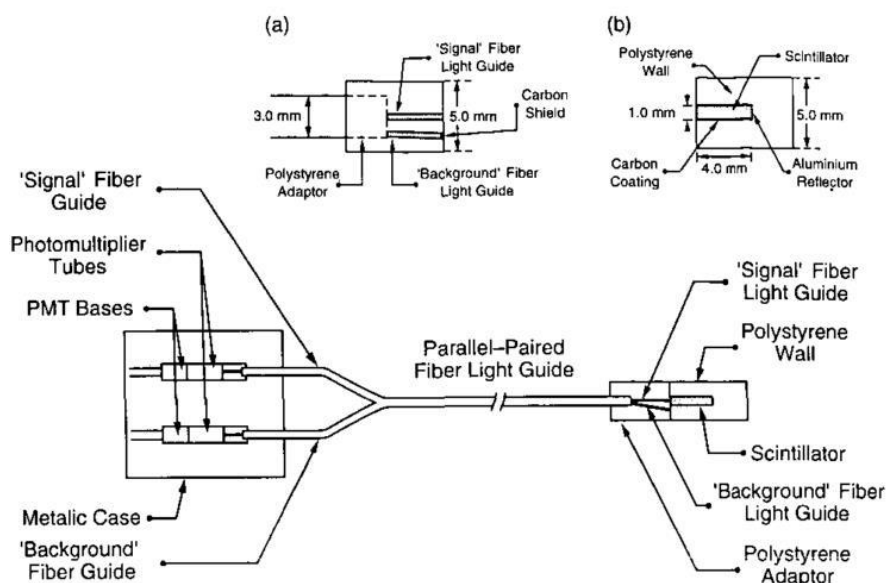


**Figure 2.10** A water-equivalent PSOFD developed by Beddar et al.[20]. The plastic scintillator is coupled to a bundle of plastic optical fibres, and a reference fibre is used to remove the Cherenkov effect.

In 1992, Beddar et al.[20] reported a water-equivalent plastic scintillation detector for high-energy beam dosimetry. The chosen scintillator was 'BC-400' (Bicron Corporation Premium Plastic and Liquid Scintillators, Newbury, OH, USA), which had a very short decay time (2 ns), a density of  $1.032 \text{ g}\cdot\text{cm}^{-3}$  and an electron density of  $10^{23} \text{ g}^{-1}$ . As shown in Figure 2.10, the radiation sensitive probe is comprised of cylinder-shaped polystyrene ( $\phi = 5.0 \text{ mm}$ ,  $l = 7.0 \text{ mm}$ ) with a plastic scintillator ( $\phi = 1.0 \text{ mm}$ ,  $l = 4.0 \text{ mm}$ ) embedded in its centre. The probe is connected to the photomultiplier (PMT) through an optical fibre. One important feature of this dosimeter

design is that it has applied a reference fibre to the measure the background signal generated in the optical fibre. Both the theoretical calculation and phantom experiment confirmed the probe to be almost water-equivalent, independent from the dose rate and energy, angular independent, and to exhibit high spatial resolution. This SOFD design using a reference fibre was also applied by Letourneau et al.[26] for small-field radiation therapy. Compared to the SOFD design reported in 1992, the optimisation was achieved by replacing the PMT with a photodiode in order to ensure a better stability response. The detector showed a spatial resolution comparable to a film-densitometer system under a 1 cm diameter and 6 MeV photon beam radiation.

Although negligible temperature dependence during the phantom experiment was reported by Beddar et al. in 1992[20], later clinical in vivo tests by their research group[84] found that the temperature dependence caused a systematic error. Buranurak et al.[46] presented a further investigation into the effect of temperature on a PSOFD that was designed for use in the dosimetry of brachytherapy sources and megavoltage photon beams used in external beam radiotherapy. Their study showed that the light yield in the peak regions of the scintillators decreases linearly with the increasing temperature. For plastic scintillators blue BCF-12 and green BCF-60 (Saint-Gobain, France), temperature coefficients of  $-0.15 \pm 0.01$  and  $-0.55 \pm 0.04\% \text{ K}^{-1}$ , respectively, were observed. As a result, the temperature dependence should be given careful consideration when measuring the radiation dose with a PSOFD.

Therriault-Proulx et al.[30] investigated the utilization of a PSOFD (the plastic scintillator is BCF-60) for the real-time detection of an iridium-192 high-dose-rate

treatment within a water phantom. The dose and dose rate values obtained from their PSOFD are compared to the TPS (treatment plan system). The mechanism and method of removing the interference from the stem effect are also discussed in this research. The research group also investigated the ability of the sensor to detect dwell position errors and its temporal resolution. According to the result, this kind of dosimeter shows good potential for various online verifications of treatment delivery quality.

In their further study, Therriault-Proulx et al.[85] investigated the feasibility of using a single-fibre multipoint plastic scintillation detector for  $^{192}\text{Ir}$  high-dose-rate brachytherapy dosimetry in a water phantom. This multi-point dosimeter contained a three-point detector system in which BCF-10, BCF-12 and BCF-60 scintillating elements are separated by two pieces of clear optical fibre (20—28 mm long) and then optically coupled to a single long plastic optical fibre. A hyperspectral approach was implemented to discriminate the different optical signals. They compared the accuracy of the measured dose at different source-to-detector distances and then investigated the strategies to improve the accuracy. The results indicated a high level of agreement with the expected dose for all scintillation elements.

### **2.5.2 Inorganic scintillator coupled optical fibre dosimeters**

The first ISOFD was reported by Swinth et al. in 1976[63]. The radiation sensitive probe, which employed a fibre-optic coupled NaI:Tl scintillator as a detector, was developed for in vivo counting of low energy radiation. As shown in Figure 2.11(a), a

large piece of NaI: Tl crystal, which is surrounded by an MgO reflector\*, is encased in a thin aluminium shell with the glass sealed in place by epoxy. The radiation sensitive part is connected to a bundle of glass optical fibres, and the diameter of a single fibre is 50  $\mu\text{m}$ , with a numerical aperture of 0.66. The probe shows a far better sensitivity response to low-energy  $^{239}\text{Pu}$  photons (17 KeV, 60 KeV) than the diode dosimeter developed for the same purpose. However, this improved sensitivity is largely due to the large size of the scintillator crystal, while the large volume of a single crystal would limit the application of this sensor for in vivo ionising photon counting.

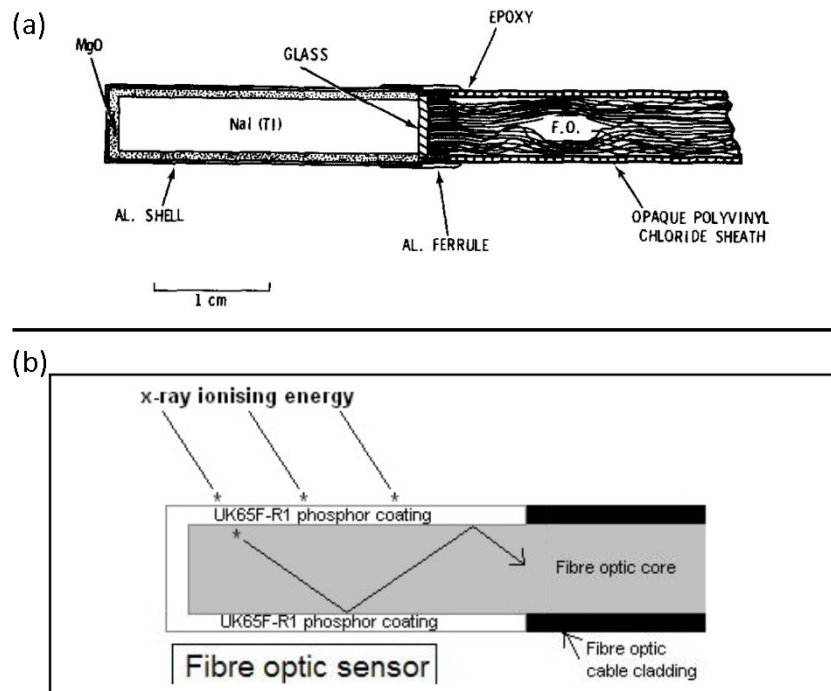


**Figure 2.11** Diagrams of the radiation sensitive probe of ISOFDs: (a) The single-crystal NaI: Tl based SOFD reported by Swinth et al.[63]. (b) The fibre optic radiation dosimeter sensor design reported by McCarthy et al.[86]

The ISOFD presented by McCarthy et al.[33], [86] used  $\text{Gd}_2\text{O}_2\text{S:Tb}$  powders as

\* ‘MgO’ is not radiation sensitive and only acts as reflector to reflect the optical light to the optical fibre and achieve a better scintillation light extraction efficiency.

the scintillator material. As shown in Figure 2.11(b), the probe was constructed by first removing the cladding layer of the PMMA (polymethyl methacrylate) optical fibre tip and then injecting an  $\text{Gd}_2\text{O}_2\text{S:Tb}$  powder-epoxy resin mixture into the mould surrounding the fibre tip. After the resin had hardened at room temperature, the  $\text{Gd}_2\text{O}_2\text{S:Tb}$  powders were uniformly distributed around the optical fibre core in the plastic mould. Under a calibrated X-ray source, the sensor was tested for low-dose, real-time X-ray dose monitoring. The results showed that this scintillator coupled optical fibre X-ray exhibited good response and repeatability of measurement for various levels of low energy ionizing X-ray energy (from 50 kVp\* to 140 kVp). The dosimeter also demonstrated excellent spectral response upon exposure to 6 MV and 15 MV ionizing  $\gamma$ -ray radiation energy. As for the stability of the dosimeter, it exhibited stable response to both low and high ionizing photon energy, showing a variation smaller than 2% of the full-scale value in each case. However, the result also indicates X-ray energy dependence for X-rays in low (0 – 150 kVp) and much higher (6 MeV and 15 MeV) energy levels. The energy dependence phenomenon maybe due to the dependence of the photon attenuation coefficient  $\mu$  on the X-ray energy level and the secondary electron absorption by the scintillator, which will be furtherly explored in following chapters.

---

\* kVp (Kilovoltage peak) is the peak voltage applied to the X-ray tube. It determines the highest energy of x-ray photon.

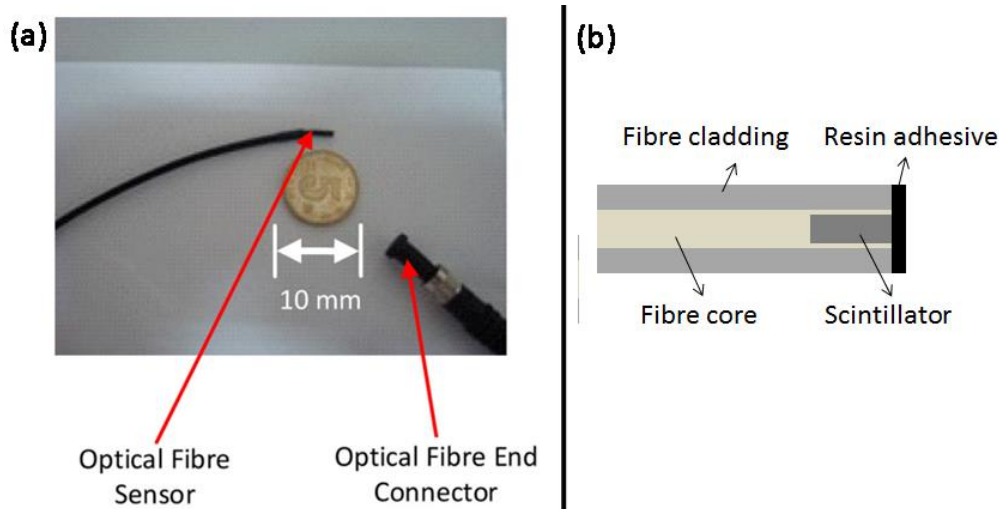


**Figure 2.12** Embedded structure of an SOFD. (a) The SOFD (photograph) presented by O’Keeffe et al.[36]. (b) The SOFD (schematic representation).

A novel sensor design for an embedded structure fibre-optic radiation dosimeter was presented by O’Keeffe et al.[36] and Zhuang et al.[37]. This design optimised the coupling efficiency between SD and the photon collective optical fibre by embedding the scintillator into the core of an optical fibre as it shown in Figure 2.12. When compared to the scintillator powder-resin mixture coating method, embedding the scintillator into the centre of the fibre core can serve to reduce the light transmission loss within the optical fibre. It can also help to isolate the scintillator material from the surrounding environment. Under 6 MeV monokinetic  $\gamma$ -ray, this novel ISOFD exhibited a strong signal response to the radiation and a high signal-to-noise ratio. The result also shows an excellent linearity and repeatability to the ionizing photon radiation. The radial and axial angular dependence have been tested. The sensor shows great isotropic response to the change of incident radiation beam angle along fibre radial, but anisotropic response to axial angular change of the incident radiation.

The ISOFD shared certain similarities with PSOFDs, including the basic idea of coupling the scintillator with the optical fibre as well as the setup of the PMT and photodetector. However, due to the considerably larger light yield of the inorganic scintillator when compared to that of an organic scintillator, the intensity of the scintillation light signal is much larger than the background noise produced in the optical fibre (Cherenkov effect\* and fluorescence). Hence, most of the introduced ISOFDs neglected the Cherenkov effect. Another important factor typically ignored in the detector characterisation of the reported ISOFDs is the temperature dependence, which might be partially due to the lack of information and data concerning the temperature dependence of inorganic scintillators. To ensure the accuracy of dosimetry, this factor should be considered in relation to detector calibration, and further studies are needed to illustrate the effect of temperature on the scintillation detector response to radiation.

### **2.5.3 Multi-point SOFDs (MPSOFDs)**

Multi-point SOFDs (MPSOFDs) are different from single-point SOFDs not only in terms of the number of radiation sensitive regions, but also in relation to the scintillator embedding and signal processing methods. Thus, despite the fact that current reports regarding MPSOFDs are limited and often discussed within the PSOFD category, this section will introduce MPSOFDs separately in order to provide more detailed insight into PSOFDs in relation to the scintillator-optical fibre decoupling and the overall

---

\* Cherenkov effect refers to the phenomenon that when a charged particle (such as an electron) passes through a dielectric medium at a speed greater than the phase velocity of light in that medium, the charged particle will emit radiation in or around visible light energy range.[120]

scintillation light signal processing method.

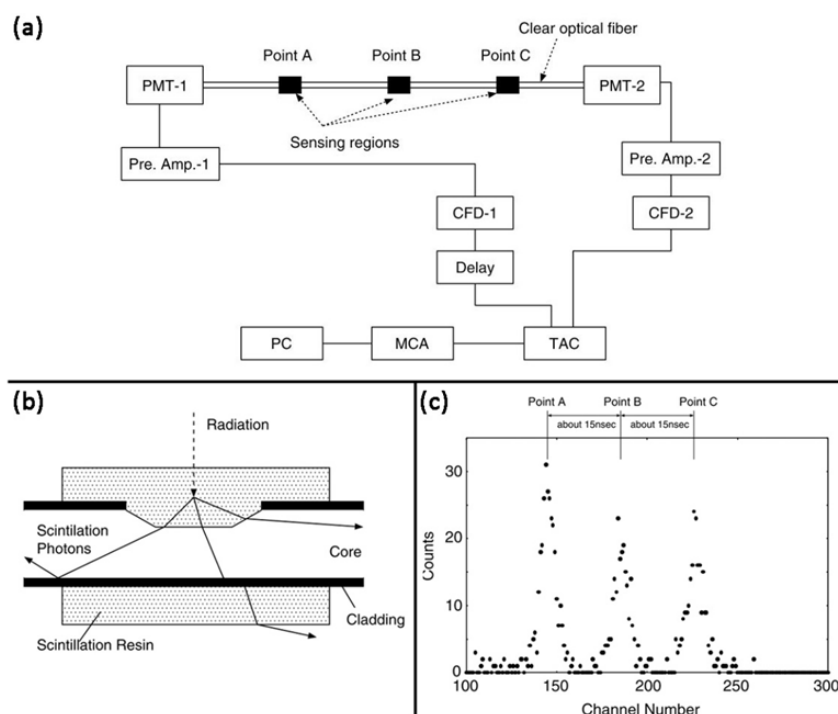


**Figure 2.13** The MPSOFD presented by Takada et al.[28]: (a) The system for the time-of-flight (TOF) measurement. (b) A schematic of a sensing region. (c) Result of the TOF measurements of radiation with a new optical fibre.

In 2004, Takada et al.[28] developed an MPSOFD with sensing regions in the cladding of the optical fibre. Three scintillation regions were distributed in three different locations, namely A, B and C, along the optical fibre. The scintillation light photons were collected by the fibre, and the radiation distribution was measured using the time-of-flight (TOF) technique. As shown in Figure 2.13(a), the light photons from the scintillators were converted into electric pulses by the PMTs before being amplified by the two fast preamplifiers (ORTEC and VT120) and then converted into timing signals by means of constant fraction discriminators (CFDs). The time difference between the two signals was measured using a time-to-amplitude converter (TAC). The

output from the TAC was then analysed using a multichannel analyser (MCA). The results were presented in the form of the photon count-channel number, as shown in Figure 2.13(c). The sensing region of the detector was fabricated by means of fibre modification. The cladding layer and the surface of the fibre core were first mechanically removed and then coated with plastic scintillator (PPO and POPOP)-added polystyrene using a mould. The scintillation region was partially embedded into the fibre core; thus, a small portion of scintillation light was trapped in the fibre core and transmitted to the PMTs. The as-prepared detector demonstrated good linearity in terms of the measured counts in a dose rate ranging between 4.2  $\mu\text{Sv}$  and 44  $\mu\text{Sv}$  with a closely placed  $^{60}\text{Co}$   $\gamma$ -ray source. One drawback of this system is the fact that due to the mechanical process involved in the fabrication of the sensing regions, the machining precision was relatively low in the micro scale, and it was very difficult to control the notches' depth and width. The low machining precision made it difficult to restrain the transmission loss of light and achieve a high and steady the measurement efficiency. A chemical modification method was hence suggested instead of the mechanical manufacturing method.

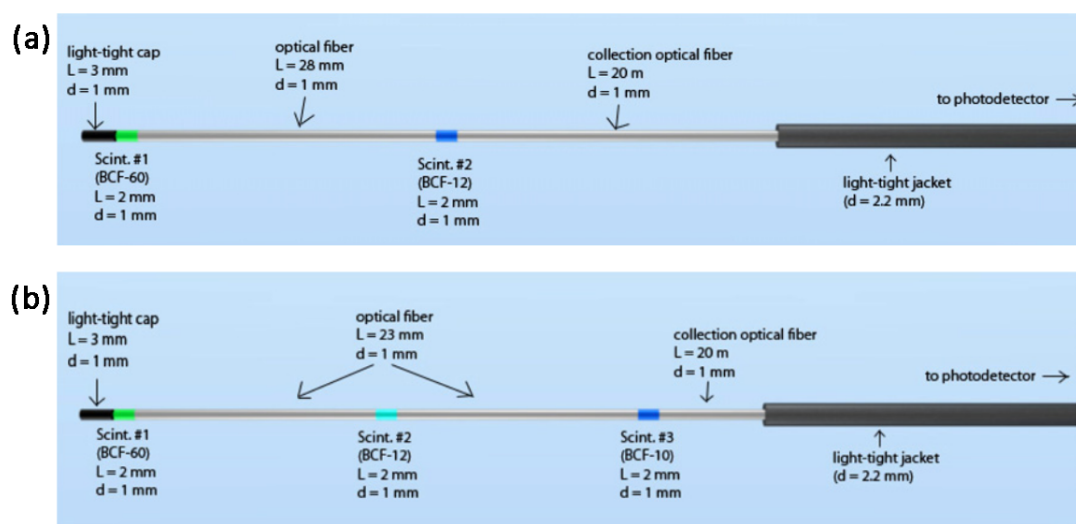


**Figure 2.14** Details of the two-points PSOFD and three-points PSOFD construction[31]

A novel type of multi-point PSOFD was reported by Therriault-Proulx and Beddar et al.[31]. Their research described a two-points PSOFD (Figure 2.14(a); plastic scintillators BCF-60 and BCF-12 were sourced from Saint-Gobain Crystals, Hiram, OH) and a three-point PSOFD (Figure 2.14(b); utilised plastic scintillators were BCF-60, BCF-12 and BCF-10), respectively. The radiation detection performance of both detectors was characterised with a 6 MeV photon beam at various depths and lateral positions in a water tank, and the results were compared with those of an ionising chamber. For the two-points PSFOD, the average relative differences between the MPSFOD and the ion chamber measurements for the depth-dose were  $2.4 \pm 1.6\%$  and  $1.3 \pm 0.8\%$  for scintillators BCF-60 and BCF-12, respectively. For the three-point MPSOFD, the average relative differences over all the conditions were  $2.3 \pm 1.1\%$ ,  $1.6 \pm 0.4\%$  and  $0.32 \pm 0.19\%$  for scintillators BCF-60, BCF-12 and BCF-10, respectively. These studies both demonstrate the practical feasibility of MPSOFDs as well as their potential application for real-time in vivo dosimetry.

It is worth noting that the three-point MPSOFD was based on a full-spectrum approach, which was presented by Archambault et al.[53] and developed from the spectral method proposed by Font et al.[27]. This method first assumed that the detected light is a linear superposition of the light coming from each light-emitting component. Therefore, the measured light spectrum ( $\mathbf{m}$ ) can be expressed as a linear superposition of each component's normalised emission spectrum ( $\mathbf{r}_i$ ) as follows:

$$\mathbf{m} = \mathbf{r}_{\text{BCF60}}x_{\text{BCF60}} + \mathbf{r}_{\text{BCF12}}x_{\text{BCF12}} + \mathbf{r}_{\text{BCF10}}x_{\text{BCF10}} + \mathbf{r}_{\text{stem}}x_{\text{stem}} \quad (2.6)$$

where  $x_i$  represents the intensity factor of each light-emitting component  $i$ . If the definition of the intensity of a specific wavelength in the measured spectrum is  $m_{\lambda i}$ , then the spectrum  $\mathbf{m}$  is replaced by a column vector  $\mathbf{m} = [m_{\lambda 1}; m_{\lambda 2}; \dots; m_{\lambda L}]$ . This can be represented by a highly over-determined set of linear equations when accounting for each individual wavelength  $m_{\lambda i}$ :

$$\mathbf{m} = \mathbf{R}\mathbf{x} \quad (2.7)$$

$$\begin{bmatrix} m_{\lambda 1} \\ m_{\lambda 2} \\ \vdots \\ m_{\lambda L} \end{bmatrix} = \begin{bmatrix} r_{\text{BCF60},\lambda 1} & r_{\text{BCF12},\lambda 1} & r_{\text{BCF10},\lambda 1} & r_{\text{stem},\lambda 1} \\ r_{\text{BCF60},\lambda 2} & r_{\text{BCF12},\lambda 2} & r_{\text{BCF10},\lambda 2} & r_{\text{stem},\lambda 2} \\ \vdots & \vdots & \vdots & \vdots \\ r_{\text{BCF60},\lambda L} & r_{\text{BCF12},\lambda L} & r_{\text{BCF10},\lambda L} & r_{\text{stem},\lambda L} \end{bmatrix} \begin{bmatrix} x_{\text{BCF60}} \\ x_{\text{BCF12}} \\ x_{\text{BCF10}} \\ x_{\text{stem}} \end{bmatrix} \quad (2.8)$$

The left pseudo-inverse technique (Archambault et al.[31]) is used to solve this system of equations for  $\mathbf{x}$ :

$$\mathbf{x} = (\mathbf{R}^T\mathbf{R})^{-1}\mathbf{R}^T\mathbf{m} \quad (2.9)$$

In order to calculate the dose to each scintillating element, one must perform at least one irradiation with a known dose ( $d_{i,\text{calib.}}$ ) to each scintillating element. The intensity value is calculated for that situation ( $x_{i,\text{calib.}}$ ), while the dose for any condition can therefore be calculated using a simple cross-product ratio

$$d_i = a_i x_i = (d_{i,calib}/x_{i,calib})x_i \quad (2.10)$$

This spectral method proves to be sound for both spectra decoupling and stem effect removal. Furthermore, Therriault-Proulx et al. tested this multi-point PSOFD detector for  $^{192}\text{Ir}$  high-dose-rate brachytherapy[31]. Their results showed that the three-point PSOFD achieved good agreement with the expected doses for all the scintillating elements, with average relative differences from the expected values of  $3.4\pm 2.1\%$ ,  $3.0\pm 0.7\%$  and  $4.5\pm 1.0\%$ , respectively, for the scintillating elements from the distal to the proximal. As for the MPSOFD we would like to develop with inorganic scintillators (different rare-earth doped  $\text{Gd}_2\text{O}_2\text{S}$ ), this spectra method will be adopted for the de-superposition of the overall spectra as measured by the photon detector.

#### **2.5.4 The Cherenkov effect**

The Cherenkov effect is the result of the fact that electrons can exceed the optical radiation phase velocity in materials with a refraction index greater than one (that is, almost all materials, except for transparent gases). It occurs in almost every clear material at electron energies above approximately 180 KeV[21]. The Cherenkov light signal (a continuum of spectrum optical radiation with a higher intensity at the UV wavelength end of the optical spectral range), which is emitted in a broad band spectrum ranging from ultraviolet to infrared, is highly dependent on the configuration of the optical fibre in the radiation beam, especially the angle between the electron path and the fibre. As a background signal in a SOFD, Cherenkov radiation from the optical fibre and scintillators is an interference to the scintillation signal analysis, thus normally the Cherenkov radiation need removed from the output signal. It is especially necessary for

PSOFD, as in the energy level as high as tens of MeV, the intensity of the Cherenkov radiation from the plastic optical fibre are strong enough that must not be ignored[21], [42], [87]. Investigations regarding the generation of Cherenkov radiation have been carried out for both silica and plastic optical fibres, including polymethylmethacrylate (PMMA)[21], [40], [88]–[90].

At least four different methods have been devised to correct the Cherenkov background. The first method, which was developed by Beddar et al.[20] and reviewed in section 2.4.1, removed the Cherenkov background signal by employing a second, parallel optical fibre located close to the signal fibre, but not coupled to a scintillator[21]. The light present in the second fibre is an approximation (or a reference) of the Cherenkov background in the signal fibre; however, any positional differences between the two fibres will introduce errors[90]. The second method, which was first proposed by de Boer et al.[42], exploits the spectral difference between the light generated in the scintillator and the Cherenkov light. Importantly, the intensity of the Cherenkov spectrum is proportional to  $\lambda^{-3}$  (where  $\lambda$  is the wavelength of the Cherenkov light). By using scintillation coupled with a longer wavelength emission and filtering out the light with a shorter wavelength, the Cherenkov emission was decreased from 6.5% to 2.8% of the scintillator's signal. Later, Fontbonne et al.[27] demonstrated that by using the equations related to the spectral method, the Cherenkov background signal can be, in principle, eliminated. Further research regarding the correction of the Cherenkov effect using this spectral discrimination method were reported by Frelin et al.[9], Guillot et al.[48] and Ishikawa et al.[35], [41], [91]. The third method, which was described by

Clift et al.[52], relies on the fact that the Cherenkov emission is a prompt process, whereas scintillation is a delayed process. Clift et al. showed that the Cherenkov signal could be reduced by reading the signal from the dosimeter between the linear accelerator pulses when the Cherenkov radiation was decayed to almost zero[52]. A scintillator with a long decay constant is used to maximise the amount of scintillation light emitted in between the linear accelerator pulses. Lambert et al.[42], on the other hand, used an air core light guide to transport the light from the scintillator to the light detector, thereby theoretically eliminating the generation of Cherenkov light at its source and thus providing a novel solution for addressing the Cherenkov effect.

## **2.6 Conclusion**

A review of scintillator materials based on an optical fibre dosimeter system has been provided in this chapter. First, some basic knowledge regarding scintillator material was introduced. Two major types of scintillators, namely plastic organic scintillators and inorganic scintillators, were reviewed in section 2.2 in terms of material density, scintillation efficiency, decay time, etc. Inorganic scintillator powder with a high density and scintillation efficient, such as  $Gd_2O_2S:RE$  ('RE' represents element Tb, Eu or Pr), was found to be an appropriate material for the construction of an MPSOFD. In section 2.3, the historic development of SOFDs was discussed. Water-equivalent PSOFDs usually display good linearity to the radiation dose and energy, while the response is also independent in the megavoltage energy range. However, the temperature-dependence remains a problem that needs to be addressed. The inorganic-material-based ISOFD showed great potential for in vivo low radiation dose monitoring.

The research concerning embedded-structure ISOFDs certifies that by optimising the scintillator coupling method, it is possible to improve the coupling efficiency between the scintillation region and the optical fibre. Yet, the energy dependence of ISOFDs, especially in the low energy range, requires further research effort. Two typical types of MPSOFDs were also reviewed in section 2.5. The spectral method proved to be an effective method for both spectra decoupling and stem effect removal. Cherenkov effect might introduce interference when the ISOFDs used for high energetic photon radiation, thus various methods intended to address background noise signals, especially the Cherenkov effect were discussed. In conclusion, by reviewing the research of SOFDS, the problems concerning ISOFDs' application for real-time in-vivo dosimetry have been examined. It further provides an insight into the aspects worthy of theoretical investigation for ISOFD optimization.

## **Chapter 3—Theory and Monte-Carlo simulation algorithms for photon interactions**

### **3.1 Introduction to photon interaction simulation**

The procedure of radiation dose detection associated scintillation optical fibre dosimetry is generally described as follows. First, the radiation beams (in the present case,  $\gamma$ -ray, X-ray, etc.) incident on the sensor. The scintillator materials then absorb the ionising photons and convert them into visible photons. Next, the generated visible photons are received by the photon detectors (photon diode, photon multiplier tube, etc.) and, subsequently, converted into electrical signals. This procedure has been illustrated in Figures 2.1 and 2.2 in chapter 2. Most prior reports concerning ISOFDs have focused on characterising the sensors' performance in relation to the response linearity to the dose rate, reproducibility and energy dependence through phantom or non-phantom experiments conducted with a medical radiation source. There are only a few cases in which the dominant physical processes of scintillation and photon transport are described to illustrate how the incident X-ray energy and SOFD configurations determine the sensing capability of the reported ISOFDs, especially by means of simulation. Until now, the reports involving SOFD simulation are limited to plastic SOFDs [92]–[95]. This gap in the research may be due to the relatively short history of ISOFDs' development as well as their apparent lack of clinical application when compared to plastic SOFDs. The existing reports concerning ISOFDs focus on purely experimental methods (such as changing the scintillator materials and sensor

configurations) in order to improve the radiation detection capability. However, studies regarding both radiation sensitivity and signal noise analysis from the perspective of photon interaction theory are currently lacking. Therefore, the simulation of ISOFDs will provide an insight into the factors that determine the radiation sensitivity and coupling efficiency of ISOFDs, and it will contribute to the optimisation of sensor design while also saving time and resources.

There has been a long tradition of employing simulation for X-ray photon interactions with media (e.g. phosphors and human tissues), which serves the purpose of optimising the imaging performance of medical X-ray phosphor screens[96]–[102]. Among the various available simulation methods, Monte Carlo (MC) simulation is perhaps the most commonly used due to its flexibility and ability to estimate quantities that are difficult to measure empirically. Based on the theoretical and experimental research concerning photons interacting with atoms and materials[103]–[109], models that can investigate these photon interactions using MC methods have been developed and proposed by different researchers[108], [110], [111]. These theories and methods laid the foundation for precise simulation intended to evaluate and optimise the performance of X-ray phosphor screens. For example, Chan et al.[112] applied MC methods for the simulation of X-ray diffusion in a phosphor layer in order to determine physical quantities such as the K reabsorption factor, quantum absorption efficiency and noise equivalent absorption. Later, in 1984, Jaffray et al.[100] conducted a MC simulation to study the basic X-ray absorption data concerning different phosphor materials used in phosphor screens. Their simulation took into account the emission

and reabsorption of characteristic X-rays ( $K_{\alpha}$  and  $K_{\beta}$  X-rays) by the high Z elements of the phosphor as well as the diffusion of X-ray photons. However, the existence of low Z materials, such as binder, and the reflective layer was neglected. The simulation also failed to account for the propagation of fluorescent light photons in the phosphor screens. Liaparinos et al.[101] reported a more specific MC method that simulated granular  $Gd_2O_2S:Tb$  screens. Their model investigated the processes of x-ray interaction with granular  $Gd_2O_2S:Tb$  particles as well as the propagation and attenuation of the emitted light photons by both phosphors and binding materials inside the phosphor screens. The simulation result showed a good level of agreement with the theoretical calculation.

As for ISOFD simulation, the description of the model differs from that of a medical phosphor screen in a number of ways. On the one hand, the simulation of an ISOFD differs from that of a medical X-ray screen in terms of the energy ranges of the photon radiation of interest. The simulation of an X-ray screen mainly focuses on a diagnostic X-ray with initial energy up to approximately 150 KeV. The application of an ISOFD, however, targets wider photon energy ranges, including both diagnostic X-ray and therapeutic  $\gamma$ -rays. Different from the relatively diagnostic X-ray photons, the interaction between  $\gamma$ -rays (with much higher energies) and media can generate fast secondary electrons and positrons with kinetic energy in the order of a few MeV. These secondary particles are usually considered to be locally absorbed if the kinetic energies are low (i.e. below a few KeV); however, for fast electrons and positrons, the attenuation length is much longer due to the high kinetic energies. In their paths

travelling in the material, these electrons and positrons keep on decelerating and losing energy to the medium through inelastic scattering events and bremsstrahlung effect, which will contribute to further energy absorption by the scintillation material. Generally, the interactions between the electrons/positrons and the material are ignored in prior works concerning X-ray phosphor screen modelling. In contrast to X-ray phosphor screens, in view of the small size of an ISOFD and the relatively high kinetic energy of the secondary electrons and positrons (resulting from primary photon interactions), the more detailed investigation of the energy absorption in the transport of these secondary electrons and positrons in the material is necessary. On the other hand, the geometry and packing density of an ISOFD are also different from those of phosphor X-ray screens. The most common model of an X-ray screen is a thin slab that is comprised of closely-packed phosphor grains glued together by a binding material. The packing density\* is around 50%, while the thickness varies from 80~200  $\mu\text{m}$  [101], [113], [114]. As for the ISOFDs reported by McCarthy et al. [33] and O’Keeffe et al. [34], the radiation sensitive part is a small fibre-like cylinder comprised of  $\text{Gd}_2\text{O}_2\text{S:Tb}$  grains glued together by epoxy resin, and it is attached to one tip of a plastic fibre. The length and diameter of the scintillation cylinder are 3 cm and 2.5 mm, respectively. The packing density is ~0.7%, which is much lower than that of phosphor screens. The differences in terms of the geometries and packing densities affect the response to the incident X-ray or  $\gamma$ -ray as well as the light propagation process. These factors will be

---

\* The packing density is the fraction of the space filled by scintillator particles in the scintillation domain.

considered in the following simulation of ISOFDs. Despite the many differences between ISOFDs and X-ray phosphor screens, previous works on the simulation of diagnostic radiology provide valuable inspiration for the modelling of ISOFDs. The simulation of ISOFDs presented in the following sections of this thesis will reference a lot of the work concerning the simulation of X-ray phosphor screens for relatively low photon energies (i.e. in the diagnostic energy range), including modelling the physical process of photon interactions with materials. The simulation methods, however, will be modified in order to adapt to our models and produce outcomes of interest.

In this study, the aim of the simulation is to optimise the design of ISOFDs through the theoretical calculation and Monte-Carlo (MC) simulation from the aspects of: a) the influence of different model configurations (single-point and double-point ISOFDs included) on the coupling efficiency between SD and the optical fibre; b) the absorption efficiency's dependence on the size and package density of the scintillator particles; and c) the response dependence of the incident ionising photon's energy. The MC simulation of the radiation detection is a stochastic process, including the radiation interaction inside the scintillator particles, fast electron interaction with the matter (which is only considered for high energy therapeutic  $\gamma$ -ray), the light reflection of refraction at the interface of different media, and the light photon extinction during transmission. We have chosen  $\text{Gd}_2\text{O}_2\text{S}$  as the scintillator subject for our modelling based on the overall compromise it offers in terms of various properties, such as the intrinsic efficiency, scintillation response-decay time and mean particle size of commercially available scintillators. Moreover, by choosing different  $\text{Gd}_2\text{O}_2\text{S}$ -doped

rare-earth elements, it is easy to simulate light propagation with spectra of multiple emission peaks. As for the radiation source, mono-energetic ionising photons in the energy ranges 20–80 KeV and 4–20 MeV are applied for each simulation program, which correspond to the diagnostic and therapeutic photon energy ranges, respectively.

This chapter focuses exclusively on the photon interaction, while the theory and simulation method concerning the electron/positron interaction with media will be introduced in the following chapter. First, the fundamental theory of photon interaction with material is briefly introduced in section 3.2. Second, the MC simulation method of each photon interaction is presented in section 3.3. After that, the modelling of ISOFDs incorporating MC simulation of the photon interactions and light photon tracing process is described in section 3.4. A summary of this chapter is given in the final section

### **3.2 X-ray photon interactions**

When a photon collides with an atom, four primary types of interaction may occur, namely photoelectric effect, coherent scattering (Rayleigh and Mie scattering), incoherent scattering (or Compton scattering) and  $e^- - e^+$  pair production (only possible for photon energy larger than 1.022 MeV). Photoelectric effect, incoherent scattering and pair production are the major interactions contributing to the partial or complete energy absorption of incident photons, while coherent scattering only changes the trace vector of the photon. In low X-ray energy range (a few to tens of KeV), photoelectric effect is the predominant photon interaction, while Compton scattering

and  $e^- - e^+$  pair production are dominant in much higher energy range (more than a few MeV). The mechanisms behind these different interactions have been well studied and thoroughly illustrated in numerous articles and books[47], [103]–[109], [115], [116], and we will hence only briefly introduce the fundamentals of these interactions and their influence on the responses of ISOFDs.

### 3.2.1 Photon cross-section and partial mass attenuation coefficient

In the case of a photon interaction with an atom, the type of interaction that takes place is determined by the probability of each interaction, which is often valued by the photon cross-section  $\sigma_i$  and the related function as the partial mass attenuation coefficient  $(\mu/\rho)_i$ . Here, we use  $\sigma_{\text{ph}}$  and  $(\mu/\rho)_{\text{ph}}$  to represent the cross-section and the partial mass attenuation coefficient of the atomic photoelectric effect, respectively, while  $\sigma_{\text{coh}}$  and  $(\mu/\rho)_{\text{coh}}$  are used for coherent scattering,  $\sigma_{\text{inco}}$  and  $(\mu/\rho)_{\text{inco}}$  for incoherent scattering, and  $\sigma_{\text{pp}}$  and  $(\mu/\rho)_{\text{pp}}$  for pair production. The partial mass attenuation coefficient  $(\mu/\rho)_i$  of the element has a linear relationship with the photon cross-section  $\sigma$ , which is given by[117]

$$\begin{aligned} (\mu/\rho)_i(\text{cm}^2 \cdot \text{g}^{-1}) &= \sigma_i(\text{cm}^2/\text{atom})/(u(\text{g}) \cdot A) \\ &= \sigma_i(\text{b}/\text{atom}) \cdot 10^{-24}/(u(\text{g}) \cdot A) \end{aligned} \quad (3.1)$$

where the contents of the brackets are the units of the parameters,  $u \equiv 1.6605402 \times 10^{-24} \text{ g}$  is the atomic mass unit and  $A$  is the relative atomic mass of the target element. The total cross-section  $\sigma_{\text{tot}}$  of the atom is the sum of all the photon interaction cross-sections, and the principle is the same for the calculation of the total

photon attenuation coefficient  $(\mu/\rho)_{\text{tot}}$  [47].  $\sigma_{\text{tot}}$  and  $(\mu/\rho)_{\text{tot}}$  of the photon attenuation are given by[117]:

$$\sigma_{\text{tot}} = \sigma_{\text{ph}} + \sigma_{\text{coh}} + \sigma_{\text{inco}} + \sigma_{\text{pp}} \quad (3.2)$$

and

$$\left(\frac{\mu}{\rho}\right)_{\text{tot}} = \left(\frac{\mu}{\rho}\right)_{\text{ph}} + \left(\frac{\mu}{\rho}\right)_{\text{coh}} + \left(\frac{\mu}{\rho}\right)_{\text{inco}} + \left(\frac{\mu}{\rho}\right)_{\text{pp}} \quad (3.3)$$

The magnitude of the photon cross-sections of the element depends on the photon energy and the target electron or atom. Systemic works intended to measure and calibrate the empirical data concerning the  $\sigma$  and  $(\mu/\rho)$  of photons in wide energy ranges for all elements have been reported by Hubbell et al.[47], [104], [106], [107], [117], while tabulated photon cross-section data regarding all elements can be acquired from the XCOM database[118]. The mass attenuation coefficients of the compound can be computed according to the additivity rule[119]

$$\left(\frac{\mu}{\rho}\right) = \sum_i w_i \left(\frac{\mu}{\rho}\right)_i \quad (3.4)$$

where  $w_i$  and  $(\mu/\rho)_i$  are the weight ratio and mass attenuation coefficient of the element with a  $Z_i$  atomic number, respectively.

As for the compound material  $\text{Gd}_2\text{O}_2\text{S}$ , the total attenuation coefficients and partial mass coefficients of  $\text{Gd}_2\text{O}_2\text{S}$  for photons in the diagnostic and therapeutic energy ranges (20~90 KeV and 4~24 MeV) are plotted in Figures 3.2 and 3.3 using data obtained from the tabulated XCOM database.

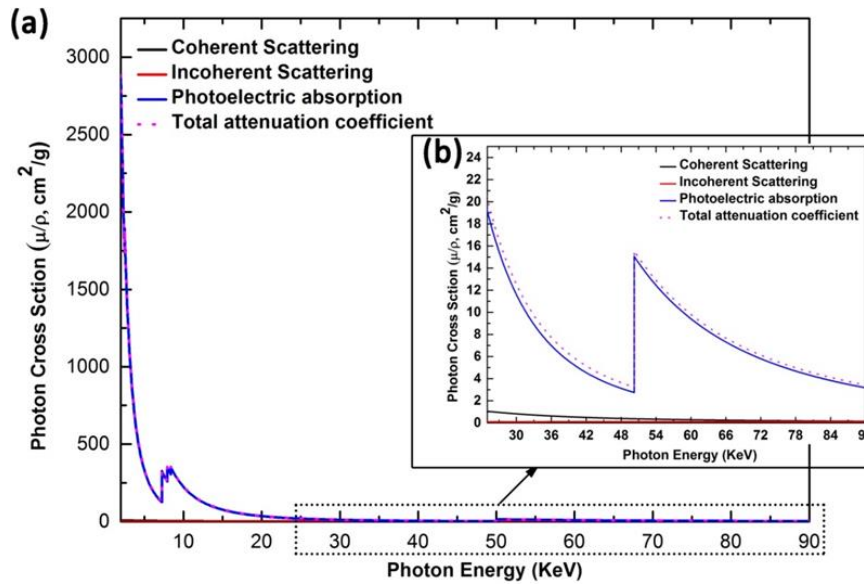


**Figure 3.1** The photon cross-sections (mass partial attenuation coefficients) of different photon interactions with the  $Gd_2O_2S$  compound in (a) the diagnostic X-ray energy range 2–90 KeV, and (b) a zoom in on the energy range 20–90 KeV

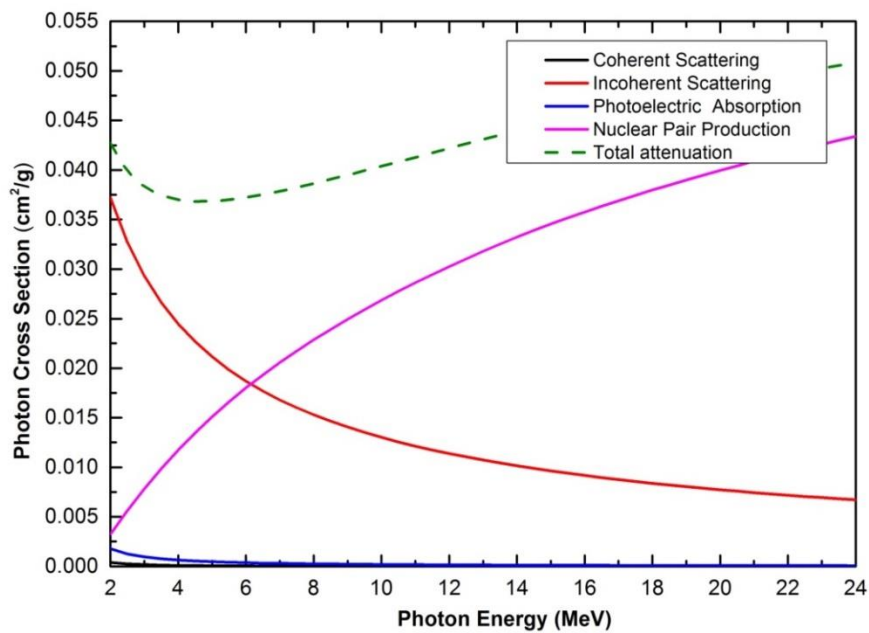


**Figure 3.2** The photon cross-sections of the  $Gd_2O_2S$  compound in the therapeutic energy range 2–24 MeV

As shown in Figure 3.1 and 3.2, the photoelectric effect is predominant in the lower photon energy range, while incoherent scattering and pair production are the main photon interaction types for higher therapeutic photons. The coherent scattering is

almost negligible in both energy ranges. Pair production is only possible when the photon energy is above 1.022 MeV and its importance grows as the energy increases, while the cross-section of the incoherent scattering decreases with the photon energy. This relationship between the photon cross-sections and photon energy needs to be considered in relation to the sensor simulation. The variation in the predominant photon interaction types seen in the diagnostic and therapeutic energy ranges must also be considered for the simulation of ISOFDs.

As the total mass attenuation coefficient measures the probability of an X-ray photon being attenuated along the photon trace, a simpler parameter for analytical calculation is the linear mass attenuation coefficient  $\mu$ , which represents the fraction of attenuated incident photons per unit thickness of a material. For a material with a mass density  $\rho$ , the linear attenuation coefficient  $\mu$  ( $\text{cm}^{-1}$ ) is the product of  $\left(\frac{\mu}{\rho}\right)_{tot}$  ( $\text{cm}^2 \cdot \text{g}$ ) and  $\rho$  ( $\text{g} \cdot \text{cm}^3$ ) as

$$\mu = \left(\frac{\mu}{\rho}\right)_{tot} \times \rho \quad (3.5)$$

The attenuation of a photon beam of initial flux energy  $I_0$  travelling along path length  $l$  in the medium is given by the Beer-Bouguer-Lambert exponential law of attenuation[120]

$$I(l) = I_0 \cdot \exp(-\mu \cdot l) \quad (3.6)$$

In the case of a single photon interaction, the probability of the photon travelling along the path length without being absorbed or attenuated can thus be derived from Equation (3.6) as

$$P_{tr} = \exp(-\mu \cdot l) \quad (3.7)$$

For the Monte Carlo simulation of generating the photon trace in the medium, Equation (3.7) is used to determine whether the photon interaction occurs or not after travelling a certain distance when the photon is treated as a particle rather than a wave. Given a transmission probability  $\xi^*$ , according to Equation (3.7), the corresponding transmission distance is derived as  $l_{\text{trans}} = -\ln \xi / \mu$ . If the travelling distance  $l$  is smaller than  $l_{\text{trans}}$ , the photon particle can travel without interacting with the matter, otherwise ( $l > l_{\text{trans}}$ ), the photon will interact with the matter through one (and one only) type of primary photon interactions (i.e., the photon is attenuated). Once it has been determined that the photon is attenuated, the interaction type can be determined according to probability derived from the photon interaction cross-sections  $\sigma_i$  or mass attenuation coefficient  $(\mu/\rho)_i$  [121], [122]. Before the detailed MC simulation methods are illustrated, we will first introduce some basic ideas and key parameters concerning the four primary types of photon interactions.

### 3.2.2 Photoelectric effect

During the photoelectric absorption process, as illustrated in Figure 3.3, the photon energy ( $E_0$ ) is absorbed by the target atom, which excites an electron (i.e. photoelectron) in the  $i^{\text{th}}$  shell with a kinetic energy  $E = E_0 - U_i$ , where  $U_i$  is the ionization energy of the shell. The vacancy left in the shell is quickly filled via the migration of an electron from the outer shell. The binding energy  $U_i$  is then liberated in the form of either characteristic X-ray fluorescence or Auger electron emission.

---

\*  $\xi$  is a pseudo-random value uniformly distributed in the interval (0,1)

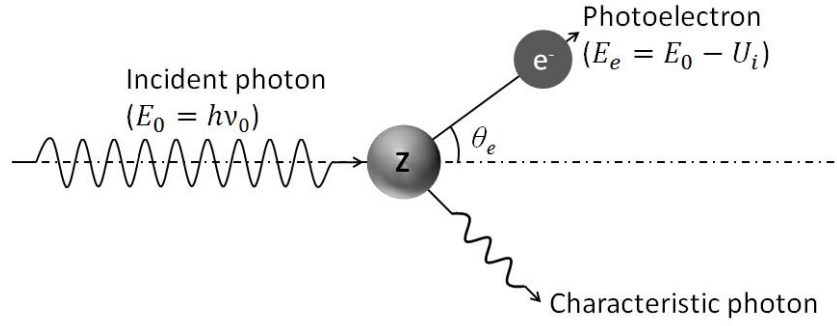


**Figure 3.3** A schematic of the photoelectric absorption

Hubbell et al. tabulated the experimental data concerning the photoelectric effect cross-section[47], while Sempau et al.[123] presented an accurate approximation of the atomic  $\sigma_{ph}$  in an analytical form

$$\sigma_{ph} = \begin{cases} G_k \sigma_{ph}^H(E, Z) & \text{if } E > E_c \equiv 5(Z + 15) \text{ KeV,} \\ \exp(A_s - B_s y + C_s y^{-1} + D_s y^{-2}) & \text{if } 1 \text{ KeV} < E < E_c \end{cases} \quad (3.8)$$

where  $G_k$  is a  $Z$ -dependent parameter,  $y \equiv \ln E_0$ , and  $A_s$ ,  $B_s$ ,  $C_s$  and  $D_s$  are the parameters characteristic of each element[108]. The function  $\sigma_{ph}^H(E, Z)$  is the empirical high energy formula suggested by Hubbell et al.[106]. The analytical form of  $\sigma_{ph}$  indicates that the probability of photoelectric effect increases rapidly with the atomic number  $Z$  ( $\propto Z^n$ , where  $n \in (4,5)$ ), while it decreases sharply with the incident photon energy  $E_0$  ( $\propto E_0^{-3.5}$  at low energies and  $\propto E_0^{-1}$  at high energies). It should be noted that  $\sigma_{ph}$  exhibits an abrupt increase at the K-edge. Photoelectric effect is the predominant interaction for low photon energies, and it is almost negligible for high energies (e.g. therapeutic  $\gamma$ -ray). Thus, the discussion of photoelectric interaction is vital for the simulation of the diagnostic X-ray detection of ISOFDs.

For a photon energy that is larger than the K-shell binding energy (i.e.  $U_K$ ), although it is possible for photoelectric effect to take place in any atomic shell, the K-

atomic shell interaction predominates due to the large K-shell cross-section. When  $E_0 > U_K$ , the analytical formula for the probability of K-shell ionisation, which is independent of the photon energy, is given by Sempau et al.[123]

$$P_K = \frac{1 + 8.76 \times 10^{-2}Z - 7.35 \times 10^{-4}Z^2}{0.965 + 0.107Z - 8.39 \times 10^{-4}Z^2} \quad (3.9)$$

The relaxation of the K-shell ionised atom occurs due to the way that an electron from the outer shell fills the vacancy in the K-shell, with the energy being released in the form of either K-characteristic X-ray radiation (K-X-ray) or Auger electron emission. The radiative emission processes considered in the simulation are K-L2, K-L3, K-M2, K-M3, K-N2, K-N3 and K-X (X denotes the outermost shell with negligible binding energy). The corresponding radiative transition probabilities  $p_{K-i}$  ( $i = L2, L3, M2, \dots$ ) have been taken from EPDL97 (the evaluated photo data library) [124]. Once this outer subshell is determined, the probability of either characteristic X-ray or Auger electron emission is determined by the K-fluorescent yield  $\omega_K$  of the atom, which can be acquired from the tabulation of the measured atomic shell X-ray fluorescence yields suggested by Hubbell et al.[109].

Characteristic X-rays or Auger electrons with low kinetic energies are usually absorbed locally near the interaction site due to their short attenuation lengths. However, for K-X-rays from high Z-atoms (e.g. rare-earth elements in inorganic phosphors and scintillators), the photon energy is a few tens of KeV, while the attenuation length is relatively longer. In the case of granular scintillators or phosphors, these K-characteristic X-ray photons may escape the grain where the initial photoelectric effect

takes place. For an X-ray phosphor screen, due to the high packing density, the escaping K-X-ray photons will be absorbed by closely packed phosphor grains, which is an undesirable outcome because it will introduce both error and noise to the imaging and decrease the resolution. Yet, the reabsorption of the K-X-rays will contribute to the energy absorption and the generation of a light signal, which improve the radiation sensitivity. Thus, the reabsorption of characteristic K-X-rays depends on the packing density of the scintillator/phosphor particles as well as the mass attenuation coefficient of the material. Considering the fact that the packing density of the ISOFD reported by McCarthy et al.[33] (~1% vol) is much lower than that of phosphor screens (>50% vol)[101], the probability of the reabsorption of characteristic X-rays will also be smaller than that of phosphor screens. Therefore, the influence of the packing density and scintillator particle size on the reabsorption of secondary radiation (i.e. characteristic X-rays) will be investigated during the simulation of ISOFDs.

### **3.2.3 Incoherent scattering (or Compton scattering)**

Incoherent scattering is usually referred to as Compton scattering, a process in which the photon interacts with a free or loosely bound electron. As shown in Figure 3.4, when the photon (energy equals  $h\nu$ ) collides with a bound electron, it loses part of its energy and momentum to that electron, and its propagation direction is deflected by the scattering event. The bound electron hit by the photon, which is known as a recoil electron, is knocked off its orbit.

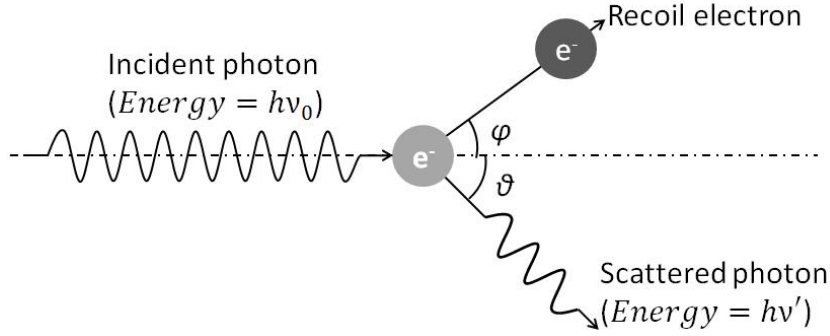


**Figure 3.4** Compton scattering of a photon with energy  $h\nu_0$  from a bound electron

Following the simple energy and linear momentum conservation law, the energy of a scattered photon is derived as[55]

$$E' = \frac{E_0}{1 + \kappa(1 - \cos \theta)} \quad (3.10)$$

where  $\theta$  is the polar deflection angle of the scattered photon from the incident photon trace and  $\kappa \equiv E_0/(m_e c^2)$  is the photon energy in the unit of  $m_e c^2$ . This relationship between  $\theta$  and the scattered photon energy shows that the larger the deflection angle is, the more energy will be transferred to the recoil electron. In an extreme situation wherein  $\theta = \pi$ , the minimum energy of the scattered photon is  $E'_{\min} \equiv E_0/(1 + 2\kappa)$ , while the maximum energy is  $E'_{\max} \equiv E_0$ , which indicates that there is always some energy retained by the photon after scattering. If the energy of the scattered photon is expressed as  $E' = \tau E_0$ , according to Equation (3.10), the fractional energy  $\tau$  (Non-dimensional quantity) is given by

$$\tau = \frac{1}{1 + \kappa(1 - \cos \theta)} \quad (3.11)$$

In extreme conditions, when  $\theta = \pi$ ,  $\tau_{\min} = \frac{1}{1+2\kappa}$ , while when  $\theta = 0$ ,  $\tau_{\max} = 1$ .

The atomic angular differential cross-section (DCS) per unit solid angle  $\Omega$  ( $\Omega = (\theta, \phi)$ ,  $\phi$  is the azimuth angle) of incoherent scattering for a free electron at rest is described by the Klein-Nishina formula[110]

$$\begin{aligned} \frac{d\sigma_{inco}^{KN}(\theta)}{d\Omega} &= \frac{r_e^2}{2} [1 + \kappa(1 - \cos \theta)]^{-2} \times [1 + \cos^2 \theta \\ &\quad + \frac{\kappa^2(1 - \cos \theta)^2}{1 + \kappa(1 - \cos \theta)}] \end{aligned} \quad (3.12)$$

where  $d\Omega \equiv 2\pi d(\cos \theta) = 2\pi \cdot \sin\theta d\theta$ . For simulation purposes, the Klein-Nishina DCS is expressed in terms of the fractional energy  $\tau$

$$\begin{aligned} \frac{d\sigma_{inco}^{KN}(\theta)}{d\tau} &= \frac{d\sigma_{inco}^{KN}(\theta)}{d\Omega} \frac{d\Omega}{d\tau} \\ &= \frac{d\sigma_{inco}^{KN}(\theta)}{d\Omega} \frac{2\pi d(\cos \theta)}{d\tau} \\ &= \frac{\pi r_e^2}{\kappa^3} \left( \frac{4}{\kappa^2} + \frac{\kappa^2 - 2\kappa - 2}{\tau} + (2\kappa + 1) + \kappa^2 \tau \right) \end{aligned} \quad (3.13)$$

Equations (3.12) and (3.13) provide a close approximation of the DCS of incoherent scattering for free electron collisions. However, for the incoherent interaction with the atomic shell electrons, the Klein-Nishina angular DCS given by Equation (3.13) cannot accurately describe the incoherent scattering model. Ribberfors et al.[125] used the relativistic impulse approximation (IA) to achieve a better description of the incoherent DCS for atomic electrons. The IA method accounts for the electron binding effect as well as the Doppler broadening effect of the Compton line (which is caused by the momentum distribution of the target electrons), and it yields a double differential cross-section (DDCS), which is differential in terms of the energy ( $E'$ ) and direction ( $\Omega$ ) of the scattered photon described by Equation (1) in [110] as

$$\frac{d^2\sigma_{in}}{dE'd\Omega} = \frac{r_e^2}{2} \left(\frac{E_C}{E_0}\right)^2 \left[1 + \left(\frac{p_z}{m_e c}\right)^2\right]^{-\frac{1}{2}} X J(p_z) \quad (3.14)$$

where  $E_C$  is the energy of the Compton line, that is, the energy of the photons scattered in direction  $\theta$  by free electrons at rest, which is given by

$$E_C \equiv \frac{m_e c^2 E_0}{m_e c^2 + E_0(1 - \cos \theta)} \quad (3.15)$$

$q$  is the modulus of the momentum transfer vector,  $\mathbf{q} \equiv \mathbf{k} - \mathbf{k}'$ , where  $\mathbf{k}$  and  $\mathbf{k}'$  are the momenta of the incident and the scattered photons, respectively, and  $q$  is given by

$$q = \frac{1}{c} \sqrt{E_0^2 + E'^2 - 2E_0E' \cos \theta} \quad (3.16)$$

$p_z$  in Equation (3.14) is the projection of the initial momentum  $\mathbf{p}$  of the electron in the direction of the scattering vector  $\mathbf{k}' - \mathbf{k} = -\mathbf{q}$ , which is given by

$$p_z = -\frac{\mathbf{p} \cdot \mathbf{q}}{q} \cong \frac{E_0 E' (1 - \cos \theta) - m_e c^2 (E_0 - E')}{c^2 q} \quad (3.17)$$

The parameter  $X$  in is defined by Equations (6~8) in [110], which is written as

$$X = \frac{R}{R'} + \frac{R'}{R} + 2 \left(\frac{1}{R} - \frac{1}{R'}\right) + \left(\frac{1}{R} - \frac{1}{R'}\right)^2 \quad (3.18)$$

with

$$R = \frac{E}{m_e c^2} \left\{ \left[1 + \left(\frac{p_z}{m_e c}\right)^2\right]^{1/2} + \frac{E - E' \cos \theta}{c q} \frac{p_z}{m_e c} \right\}, \quad (3.19)$$

and

$$R' = R - \frac{E'}{m_e c^2} \left(\frac{E}{E_C} - 1\right). \quad (3.20)$$

The function  $J(p_z)$  in Equation (3.14) is the Compton profile. For the  $i$ th atomic electron shell,  $J_i(p_z)$  gives the probability distribution of the component  $p_z$  of the electron momentum. As for the Compton profile  $J(p_z)$  of the atom, it is the sum of the

atomic Compton profiles  $J_i(p_z)$  of the electrons in all the atomic shells, which is given by

$$J(p_z) = \sum_i Z_i J_i(p_z) \quad (3.21)$$

where  $Z_i$  is the number of electrons in the  $i$ th shell. In the case of incoherent scattering in a compound material, the molecule's Compton profile can be calculated according to the additivity rule, that is, the sum of the atomic profiles of all the atoms in the molecule.

Through a series of reasonable simplifications and approximations, the incoherent DDCS given by Equation (3.14) is evolved as

$$\begin{aligned} \frac{d^2\sigma_{in}}{dE' d\Omega} &= \frac{r_e^2}{2} \left(\frac{E_c}{E}\right)^2 \left(\frac{E}{E_c} + \frac{E_c}{E} - \sin^2\theta\right) \\ &\times Q(p_z) \left(\sum_i Z_i \Theta(E - E' - U_i) J_i(p_z)\right) \frac{dp_z}{dE'} \end{aligned} \quad (3.22)$$

where  $\Theta(x)$  ( $=1$  if  $x>0$ ,  $=0$  otherwise) is the Heaviside step function, the factor

$$Q(p_z) \equiv \frac{E'}{E_c} \left(1 + \frac{E_c}{E_0} \frac{E \cos\theta - E'}{cq} \frac{p_z}{m_e c}\right) \left[1 + \left(\frac{p_z}{m_e c}\right)^2\right]^{-\frac{1}{2}},$$

and the analytical approximation

is given by

$$Q(p_z) = \begin{cases} 1 + \frac{cq_c}{E} \left(1 + \frac{E_c(E_c - E_0 \cos\theta)}{(cq_c)^2}\right) \frac{p_z}{m_e c}, & \text{if } |p_z| < 0.2m_e c \\ f(-0.2m_e c), & \text{if } p_z < -0.2m_e c \\ f(0.2m_e c), & \text{if } p_z > 0.2m_e c \\ 0, & \text{if } Q(p_z) < 0 \end{cases} \quad (3.23)$$

where  $q_c \equiv \frac{1}{c} \sqrt{E_0^2 + E_c^2 - 2E_0 E_c \cos\theta}$  is the momentum transfer associated with the energy  $E' \equiv E_c$  of the Compton line. The directional DCS is acquired by integrating the DDCS (in Equation (3.22)) over  $E'$  as

$$\begin{aligned}
 \frac{d\sigma_{in}}{d\Omega} &= \int \frac{d^2\sigma_{in}}{dE'd\Omega} dE' \\
 &= \frac{r_e^2}{2} \left(\frac{E_c}{E_0}\right)^2 \left(\frac{E_0}{E_c} + \frac{E_c}{E_0} - \sin^2\theta\right) \\
 &\quad \times \sum_i Z_i \theta(E_0 - E' - U_i) \int_{-\infty}^{p_{i,max}} Q(p_z) J_i(p_z) dp_z
 \end{aligned} \tag{3.24}$$

where  $p_{i,max}$  is the highest  $p_z$  value for which an electron in the  $i^{th}$  shell can be excited.

It is obtained from Equation (3.17) by setting  $E' = E_0 - U_i$ ,

$$p_{i,max}(E_0, \theta) = \frac{E_0(E_0 - U_i)(1 - \cos\theta) - m_e c^2 U_i}{c \sqrt{2E_0(E_0 - U_i)(1 - \cos\theta) + U_i^2}} \tag{3.25}$$

The function  $n_i(p_z)$  is introduced as

$$\int_{-\infty}^{p_{i,max}} Q(p_z) J_i(p_z) dp_z \cong n_i(p_{i,max}) \equiv \int_{-\infty}^{p_{i,max}} J_i(p_z) dp_z \tag{3.26}$$

$n_i(p_z)$  is a monotonously increasing function of  $p_z$ . The quantity  $Z_i n_i(p_{i,max})$  represents the number of electrons in the  $i^{th}$  shell that can be effectively excited in a

Compton interaction. The analytical form of  $n_i(p_{i,max})$  is given by

$$\begin{aligned}
 &n_i^A(p_{i,max}) \\
 &= \begin{cases} \frac{1}{2} \exp\left[d_1^2 - (d_1 - d_2 J_{i,0} p_{i,max})^2\right], & \text{if } p_{i,max} < 0, \\ 1 - \frac{1}{2} \exp\left[d_1^2 - (d_1 + d_2 J_{i,0} p_{i,max})^2\right], & \text{if } p_{i,max} \geq 0, \end{cases} \tag{3.27}
 \end{aligned}$$

where  $d_1 = \sqrt{\frac{1}{2}}$ ,  $d_2 = \sqrt{2}$ , and  $J_{i,0} \equiv J_i(p_z = 0)$  is the value of the Compton profile at  $p_z = 0$  obtained from the Hartree-Fock orbital[103]. The incoherent scattering function, which measures both the electron binding effect and the momentum distribution of bound electrons, is written as

$$S(E_0, \theta) = \sum_i Z_i \theta(E_0 - U_i) n_i^A(p_{i,max}) \tag{3.28}$$

After substituting  $S(E_0, \theta)$  into the formula of the angular DCS in Equation (3.24), the analytical form of the DCS is thus written as

$$\frac{d\sigma_{in}}{d\Omega} \cong \frac{r_e^2}{2} \left(\frac{E_c}{E_0}\right)^2 \left(\frac{E_0}{E_c} + \frac{E_c}{E_0} - \sin^2\theta\right) S(E_0, \theta) \quad (3.29)$$

Accordingly, the probability distribution function (PDF) of the polar deflection  $\cos \theta$  is given by

$$P_\theta(\cos \theta) = \left(\frac{E_c}{E_0}\right)^2 \left(\frac{E_c}{E_0} + \frac{E_0}{E_c} - \sin^2\theta\right) S(E_0, \theta) \quad (3.30)$$

After introducing  $\tau$  (Equation (3.11)) into the last equation, the PDF can be rewritten in the form of

$$P_\tau(\tau) = [u_1 P_1(\tau) + u_2 P_2(\tau)] T(\cos \theta) \quad (3.31)$$

where

$$u_1 = \ln(1 + 2\kappa), \quad u_2 = \frac{2\kappa(1+\kappa)}{(1+2\kappa)^2} \quad (3.32)$$

$$P_1(\tau) = \frac{1}{\ln(1+2\kappa)} \frac{1}{\tau}, \quad P_2(\tau) = \frac{(1+2\kappa)^2}{2\kappa(1+\kappa)} \tau \quad (3.33)$$

and

$$T(\cos \theta) = \left\{ 1 - \frac{(1 - \tau)[(2\kappa + 1)\tau - 1]}{\kappa^2 \tau (1 + \tau^2)} \right\} \times \frac{S(E_0, \theta)}{S(E_0, \theta = \pi)} \quad (3.34)$$

The functions and parameters expressed by the above-mentioned equations will be used in the rejection MC simulation method.

For the incident photon in the diagnostic energy range, the kinetic energy of the recoil electron is low and the attenuation length is short. Thus, it is reasonable to assume that the electron is locally absorbed. As for a gamma ray in the therapeutic energy interval 2~25 MeV, it is possible that the recoil electron carries a large part of the energy of the initial photon. Therefore, the probability of a fast electron escaping the scintillator

part increases sharply. In view of this increase in the attenuation path length with respect to the kinetic energy of the electron/positron, the simulation of therapeutic gamma ray detection should also consider the transport of fast electrons (and possibly positrons created by pair production, which will be discussed below).

### 3.2.4 Coherent scattering

Coherent scattering, as illustrated in Figure 3.5, refers to the elastic scattering process that affects the photon incident on the material. It can be divided into two types, namely Thomson scattering and Rayleigh scattering. The difference between these two types is that Thomson scattering concerns the interaction between a free electron and a photon of low energy, while Rayleigh scattering occurs between a photon and the internal structure of the target atom[120]. The cross-section of the coherent scattering of photons includes the effect of both elastic scattering types, and it is deduced from the correction of the cross-section of Thomson scattering.

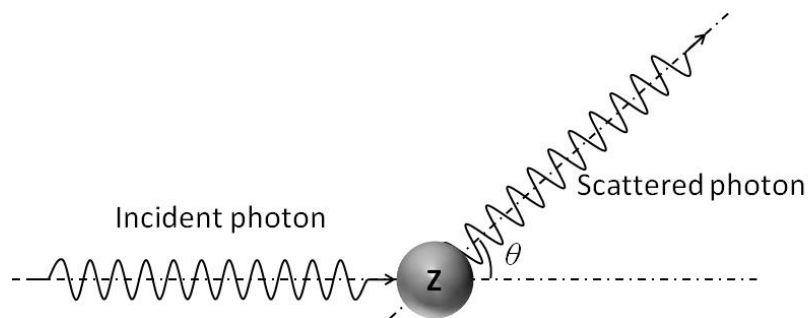


**Figure 3.5** A schematic of the coherent scattering of a photon by the target atom

The scattering angle  $\theta$  of the photon, which is defined as the deflection of the propagation direction of the scattered photon from the initial photon, is sampled from

the atomic DCS for coherent scattering (i.e.  $\frac{d\sigma_{\text{coh}}}{d\Omega}$ ). The approximation of the DCS of coherent scattering is given by [108]

$$\begin{aligned}\frac{d\sigma_{\text{coh}}}{d\Omega} &= \frac{d\sigma_{\text{Th}}}{d\Omega} \cdot [F(q, Z)]^2 \\ &= \frac{1}{2} r_e^2 (1 + \cos^2 \theta) \cdot [F(q, Z)]^2\end{aligned}\quad (3.35)$$

where  $\frac{d\sigma_{\text{coh}}}{d\Omega}$  is the Thomson DCS for scattering by a free electron at rest,  $d\Omega = 2\pi \sin\theta \, d\theta$  is the solid angle element,  $r_e \equiv 2.8179 \times 10^{-15}$  m is the classic electron radius,  $F(q, Z)$  is the atomic form factor, and  $q$  is the magnitude of the momentum transfer.  $q$  is given by

$$q = 2(E_0/c) \sin(\theta/2) = (E_0/c)[2(1 - \cos \theta)]^{1/2}\quad (3.36)$$

The square of the atomic form factor  $[F(q, Z)]^2$  is the probability that the  $Z$  electrons of the atom will take up a recoil momentum without absorbing energy. The numerical atomic form factors for all the elements and the photon energy from 100 eV to 100 MeV were tabulated by Hubbell et al.[104]. An analytical approximation was presented by Baró et al.[108]

$$F(q, Z) = \begin{cases} f(x, Z) \equiv Z \frac{1 + a_1 x^2 + a_2 x^3 + a_3 x^4}{(1 + a_4 x^2 + a_5 x^4)^2} \\ \max\{f(x, Z), F_K(q, Z)\} \text{ if } Z > 10 \text{ and } f(x, Z) < 2 \end{cases}\quad (3.37)$$

where the parameters  $a_1, a_2, a_3, a_4$  and  $a_5$  are listed in Table 1 in the article by Baró et al [108].  $x$  is introduced as a dimensionless variable instead of  $q$ , and it is defined as

$$x = \frac{q \cdot 10^{-8} \text{cm}}{4\pi\hbar} = 20.7074 q/mc\quad (3.38)$$

$F_K(q, Z)$  is the contribution of the two K-shell electrons to the form factor, which is given by

$$F_K(q, Z) = \frac{\sin(2\gamma \arctan Q)}{\gamma Q(1 + Q^2)^\gamma}\quad (3.39)$$

where  $\gamma \equiv (1 - \alpha^2)^{1/2}$  and  $a = \left(Z - \frac{5}{16}\right) \alpha$ , where  $\alpha \cong 1/137$  is the fine-structure constant and  $Q = q/(2m_e c a)$ .  $F(q, Z)$  is calculated by Equations (3.37) and (3.39), and it offers a close approximation of the atomic form factor of the atom. As for the coherent scattering DCS of the compound,  $[F(q, Z)]^2$  as used in Equation (3.35) is calculated according to the additive rule, assuming that the coherent cross-sections of the individual atoms combine independently[119]:

$$[F(q, Z)]^2 = \sum_{i=1}^N n_i [F_i(q, Z_i)]^2 \quad (3.40)$$

where  $N$  is the number of different kinds of atoms and  $n_i$  is the number of atoms of the same kind in the molecule.

Compared to the other three primary interaction types, the probability of coherent scattering is very small in the diagnostic X-ray energy range and it is almost negligible for photons in the high energy range. As a result, the coherent scattering process will be simulated for the diagnostic photon interaction, although it will be ignored for photons of megavoltage energies.

### 3.2.5 Electron-positron pair production

Pair production, as illustrated in Figure 3.6, is the process by which the incident photon is absorbed near a massive particle and an electron-positron ( $e^- - e^+$ ) pair is generated. This interaction can only occur when the energy of the incident photon exceeds a certain threshold. For pair production in the electric field of a nucleus, the threshold energy is  $2 m_e c^2$  (which equals 1.022 MeV), in which case the photon is totally absorbed and produces an electron-positron pair in the electric field of the nucleus. For this

interaction to occur in the field of an electron, the threshold energy is  $4 m_e c^2$  (which equals 2.044 MeV). This interaction not only creates an electron-positron pair, but also ionises or scatters the electron that the photon interacts with. Thus, three tracks can be seen in the imaging detector. Hence, in order to avoid confusion, this process is termed ‘triplet production’, since three particles (the electron-positron pair and a scattered electron) are detected after the interaction. In the therapeutic gamma ray energy interval, the probability of triplet production is much smaller than that near the nucleus[108], which is almost negligible.

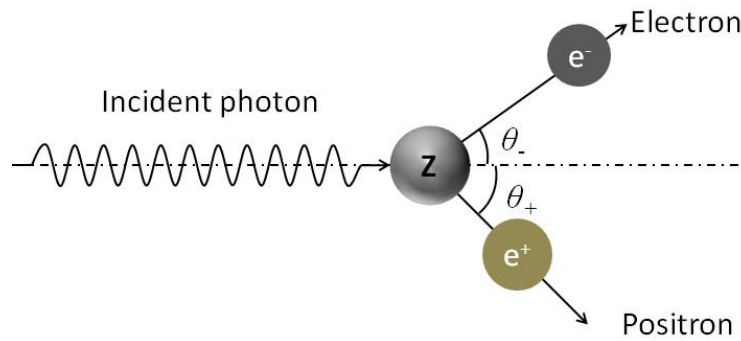


**Figure 3.6** A schematic of the pair production of a photon in the nucleus field

As a minimum energy of 1.022 MeV is required to create an  $e^- - e^+$  pair, pair production is only possible for high energy photon interactions (e.g. therapeutic  $\gamma$ -rays). The extra energy is shared by the electron and the positron, and the whole process can be expressed as[55]

$$E_+ + E_- = E_0 - 2m_e c^2 \quad (3.41)$$

where  $E_+$  and  $E_-$  are the kinetic energy of the electron and the positron, respectively. The DCS of the electron-positron pair production, in which the created electron has a kinetic energy  $E_- = \epsilon E_0 - m_e c^2$ , is given by[123]

$$\frac{d\sigma_{pp}}{d\epsilon} = \alpha r_e^2 Z[Z + \eta] \times \frac{2}{3} \left[ 2 \left( \frac{1}{2} - \epsilon \right)^2 \phi_1(\epsilon) + \phi_2(\epsilon) \right] \quad (3.42)$$

where  $\alpha$  is the fine-structure constant, which accounts for the creation of pairs in the field of electrons (i.e. triplet production).  $\phi_1(\epsilon)$  and  $\phi_2(\epsilon)$  are the analytical functions of the screening radius, which describes electronic screening, and they are given by Equations (50)–(53) in Ref [126]. The integration of the DCS over  $\epsilon$  gives the total atomic cross-section  $\sigma_{pp}$ , which rises sharply with the energy. Due to the positive contribution of the energy increase to the  $\sigma_{pp}$ , the pair/triplet production gradually becomes the predominant primary photon interaction for the incident photon of the therapeutic energy ranges.

The probability distribution function (PDF) of the directions of movement of the electron ( $\theta_-, \phi_-$ ) and the positron ( $\theta_+, \phi_+$ ), relative to the direction of the incident photon, are given by [127][123]

$$p(\cos \theta_{\pm}) = a_{pp}(1 - \beta_{\pm} \cos \theta_{\pm}) \quad (3.43)$$

where  $a_{pp}$  is a normalized constant and

$$\beta_{\pm} = \frac{\sqrt{E_{\pm}(E_{\pm} + 2m_e c^2)}}{E_{\pm} + 2m_e c^2} \quad (3.44)$$

The fast electron and positron created by the pair production interaction usually have kinetic energies in the order of a few MeV, and their propagations in the media introduce consecutive interactions (e.g. elastic and inelastic collision, bremsstrahlung radiative effect\*) with the media along their travel tracks. The theory and MC algorithm

---

\* Bremsstrahlung (a German word for braking radiation) refers to the radiation emitted by charged particles when they decelerate in a medium[120].

for modelling electron/positron interactions with mass will be discussed in the following chapter.

### 3.3 Detailed Monte-Carlo simulation of photon interactions with media

The single photon interaction model described in the previous section allows the detailed MC simulation of photon transport in a medium. Based on the DCS of the photoelectrons, the MC methods for randomly sampling energy loss, the angular deflection of the photon and the secondary particle generation caused by each photon interaction are described in this section. The simulation adopts the existing algorithms and MC methods for photon interactions [108], [110], [122], [123], although some changes are made so that these algorithms are adapted to our model.

#### 3.3.1 The attenuation of the X-/ $\gamma$ -ray photon

The intensity attenuation of a photon beam travelling in a medium can be described by exponential law (see Equation (3.6)). As for a single photon, the probability of it successfully transmitting through a medium with a distance of  $l$  is given by  $P = \exp(-\mu l)$ , where  $\mu$  is the linear attenuation coefficient. Accordingly, given the transmission probability  $\xi$  in the interval  $(0, 1)$ , the corresponding transmission path length is thus derived as

$$l_{\text{trans}} = -\frac{\ln \xi}{\mu} \quad (3.45)$$

If the photon travels a distance  $l > l_{tr}$ , it will be absorbed by the material. If the ionising photon is absorbed, only one type of primary interaction occurs, and the probability of each interaction type is determined by

$$p_i = \frac{(\mu/\rho)_i}{(\mu/\rho)_{tot}} \quad (3.46)$$

where  $i$  represents 'ph', 'coh', 'inco', 'pp', and  $(\mu/\rho)_{tot}$  is given by Equation (3.3). Once the type of the primary interaction is determined, the energy absorbed by the material, the deflection of the scattered photon with respect to the direction of movement of the initial photon, and the generation of the secondary particles (electrons, positrons and photons) will be simulated using the MC simulation methods described elsewhere in this chapter.

In the case of the X-ray photon attenuation simulation in Monte-Carlo simulation in this thesis, the linear attenuation coefficient  $\mu$  is derived as the product of the mass attenuation coefficient  $(\mu/\rho)_{tot}$  and the mass density  $\rho$ :

$$\mu = \left(\frac{\mu}{\rho}\right)_{tot} \cdot \rho \quad (3.47)$$

The total mass attenuation coefficient  $(\mu/\rho)_{tot}$  (unit  $\text{cm}^2/\text{g}$ ) and the partial mass attenuation coefficients  $(\mu/\rho)_i$  shown in Equation (3.3) are obtained from the XCOM database[118].

### 3.3.2 Photoelectric interaction

The simulation of the photoelectric effect follows the method described by Sempau et al.[123] and Liaparinos et al.[101]. In cases where the photon is absorbed by the compound material through photoelectric effect, the atomic number of the target atom is determined by the chemical formulae and the partial atomic attenuation coefficient of the compound. Let's consider the case of a compound  $X_a Y_b$ , whose molecules

consists of  $a$  atoms of the element  $X$  and  $b$  atoms of the element  $Y$ . The probability of the element  $X$  absorbing a photon is given by

$$p_{\text{ph},X} = w_X \cdot \frac{(\mu/\rho)_{\text{ph},X}}{(\mu/\rho)_{\text{ph}}} \quad (3.48)$$

where  $(\mu/\rho)_{\text{ph},X}$  is the atomic mass attenuation coefficient of the  $X$  element for photoelectric absorption and  $w_X$  is the corresponding weight ratio of element  $X$  in the compound  $(\mu/\rho)_{\text{ph}}$  is the partial mass attenuation coefficient, which is calculated according to the additivity rule (see Equation (3.4)), and the corresponding atomic cross-sections and partial mass attenuation coefficients are acquired from the EPDL-97 photon data library[124]. Once the target atom is determined, the probability of absorption in the  $i$ th subshell in order to ionise is expressed as

$$P_i(E) = \frac{\sigma_{\text{ph}}^i(E)}{\sigma_{\text{ph}}(E)} \quad (3.49)$$

where  $\sigma_{\text{ph}}(E)$  and  $\sigma_{\text{ph}}^i(E)$  are the total atomic photoelectric cross-section and the partial cross-section for  $i$ th shell ionisation, respectively.

For simplicity of simulation, only the relaxation process corresponding to K-shell ionisation is considered in detail. The energy is assumed to be totally deposited on the atom if the photoelectric interaction occurs in subshells other than the K-shell. For an incident photon with an energy larger than  $U_K$ , the probability of K-shell ionisation is given by  $P_K(E)$  (see Equation (3.9)), while the subshell electron required to fill the K-shell vacancy is randomly sampled according to the radiative transition probabilities of the subshells. The energy of the characteristic K-X-ray photon is given by

$$E_K = U_K - U_i \quad (3.50)$$

where  $U_i$  is the binding energy of the  $i$ th outer subshell. The polar and azimuth angles of the K-X-ray to the incident photon trace are uniformly distributed in the intervals  $(0, \pi)$  and  $(0, 2\pi)$ , respectively. The initial energy is assumed to be locally absorbed when (a) the photoelectric effect occurred in subshells other than the K-shell and (b) the X-ray was lower than 5 KeV (cut-off energy[101]). If a K-X-ray is emitted, the track of this new photon is simulated in the same way as that of the initial incident photon. Meanwhile, the Auger electron is assumed to be absorbed locally due to its low kinetic energy.

The transport of the characteristic X-ray photon follows the same simulation method as that of the initial photon. As for the transport of the photoelectron, an electron with low kinetic energy has a very short attenuation length. Thus, the photoelectron created by a diagnostic X-ray is assumed to be locally absorbed. However, for an incident photon with much higher energy (e.g. therapeutic  $\gamma$ -ray), the polar and azimuth angles of the photoelectron are sampled by adopting the MC method developed by Salvat et al.[122] and the propagation of the photoelectrons is simulated in detail, which will be discussed in chapter 4.

The random sampling procedure for photoelectric absorption and the corresponding atomic relaxation process is:

- i. If the initial photon energy  $E_0 < U_K$ , the photon energy is totally absorbed. In which case, go to step (vi); otherwise, generate a pseudo-random value  $\xi$ .

- ii. If  $\xi > P_K$ , the photon is totally absorbed and hence go to step vi; otherwise, the K-shell electron is ionized. The photoelectron is emitted with energy  $E_0 - U_K$ , so record the spatial information concerning the photoelectron.
- iii. Randomly sample the designator  $i$  of the outer subshells (L2, L3, M2, M3, N2, N3, etc.) according to the normalized transition probability.
- iv. Generate a new  $\xi$ .
- v. If  $\xi > \omega_K$ , an Auger electron is emitted and it is locally absorbed; hence, go to step (vi). Otherwise, a characteristic photon with the energy  $U_K - U_i$  is emitted, so record its spatial information.
- vi. The energy of the initial photon is totally absorbed. The sum of the absorbed energy is transferred into visible light based on the intrinsic x-ray to light conversion efficiency.

### 3.3.3 Incoherent scattering (Compton scattering)

The MC modelling of the incoherent scattering process is based on the algorithm proposed by Bursa et al.[110]. The polar angle of the scattered photon  $\theta$  is sampled according to the following steps:

- i. Sample a value of the integer  $i$  ( $= 1, \text{ or } 2$ ) according to the point probabilities

$$\pi(i) = \begin{cases} \frac{u_1}{u_1 + u_2}, & \text{if } i = 1 \\ \frac{u_2}{u_1 + u_2}, & \text{if } i = 2 \end{cases} \quad (3.51)$$

where  $u_1$  and  $u_2$  are determined by Equation (3.32).

- ii. Generate a random value of  $\xi$ , and then sample  $\tau$  from  $P_i(\tau)$  using the sampling formulae

$$\tau = \begin{cases} \tau_{min}^{\xi}, & \text{if } i = 1 \\ [\tau_{min}^2 + \xi(1 - \tau_{min}^2)]^{\frac{1}{2}}, & \text{if } i = 2 \end{cases} \quad (3.52)$$

where  $\xi$  is a random number in the range 0~1.

- iii. Determine  $\cos \theta$  using Equation (3.11)

$$\cos \theta = 1 - \frac{1 - \tau}{\kappa \tau} \quad (3.53)$$

- iv. Generate a new random number  $\xi$

$$T(\cos \theta) = \left\{ 1 - \frac{(1 - \tau)[(2\kappa + 1)\tau - 1]}{\kappa^2 \tau(1 + \tau^2)} \right\} \times \frac{S(E, \theta)}{S(E, \theta = \pi)} \quad (3.54)$$

If  $\xi > T(\cos \theta)$ , go to step (i). It should be noted that parameters such as  $p_{i,max}$  and  $n_i^A(p_{i,max})$  as well as the incoherent scattering function  $S(E, \theta)$  of the compound need to be calculated in advance using Equations (3.25), (3.27) and (3.28). In the case of a compound material, the incoherent scattering function  $S(E, \theta)$  is the superposition of the subshell electrons of all the atoms[96], and it is given by

$$S(E, \theta) = \sum_j N_j \sum_i Z_{j,i} \Theta(E - U_{j,i}) n_{j,i}^A(p_{j,i,max}) \quad (3.55)$$

where  $N_j$  is the number of atoms with the same atomic number.  $Z_{j,i}$ ,  $U_{j,i}$  and  $n_{j,i}^A(p_{j,i,max})$  are the number of subshell electrons, the subshell binding energy and the number coefficient of electrons corresponding to a particular  $i^{th}$  layer of the  $j^{th}$  element, respectively.

- v. Deliver  $\cos \theta$ . Once the polar angle  $\theta$  of the emerging photon is set, the energy of the photon after the interaction is sampled according to the following steps.
- vi. The active  $i^{th}$  electron shell is selected with a relative probability equal to  $N_j Z_{j,i} \Theta(E - U_i) n_i^A(p_{i,max})$  as given in Equation (3.27).

- vii. Generate a random value of  $p_z$  using the sampling formula

$$p_z = \begin{cases} \frac{1}{d_2 J_{i,0}} \left[ d_1 - (d_1^2 - \ln 2D)^{\frac{1}{2}} \right], & \text{if } D < \frac{1}{2} \\ \frac{1}{d_2 J_{i,0}} \left[ (d_1^2 - \ln 2(1-D))^{\frac{1}{2}} - d_1 \right], & \text{if } D > \frac{1}{2} \end{cases} \quad (3.56)$$

where  $D \equiv \xi n_i^A(p_{i,max})$ . If  $p_z < -mc$ , it is rejected and the program must return to step (vi), when a new layer number  $i$  and  $p_z$  value are sampled. Otherwise, the value  $Q(p_z)$  in Equation (3.23) is considered. Let  $Q_{max}$  denote the maximum value of  $Q(p_z)$ , which occurs at  $p_z = 0.2 mc$  or  $-0.2 mc$ . A random number  $\xi$  is generated and the value of  $p_z$  is accepted if  $\xi Q_{max} < Q(p_z)$ ; otherwise, return to step (vi) and the process of selecting a shell and a  $p_z$  value is re-initiated.

- viii. After  $\cos \theta$  and  $p_z$  are generated, the energy  $E'$  of the emerging photon is then calculated based on Equation (3.55)

$$E' = E \frac{\tau}{1 - t\tau^2} \left[ (1 - t\tau \cos \theta) + \text{sign}(p_z) \times \sqrt{(1 - t\tau \cos \theta)^2 - (1 - t\tau^2)(1 - t)} \right] \quad (3.57)$$

where  $t \equiv (p_z/mc)^2$  and  $\text{sign}(p_z) = \frac{p_z}{|p_z|}$ .  $E'$  will be rejected if  $E - E' < U_i$ , and you must go to step (vi).

- ix. The azimuthal scattering angle  $\phi$  of the photon is sampled uniformly in the interval  $(0, 2\pi)$ . The energy of the Compton electron is emitted with energy  $E_e = E - E' - U_i$ , with a polar angle  $\theta_e$  and an azimuthal angle  $\phi_e = \phi + \pi$  relative to the direction of the incident photon.  $\cos \theta_e$  is given by

$$\cos \theta_e = \frac{E - E' \cos \theta}{\sqrt{E^2 + E'^2 - 2EE' \cos \theta}} \quad (3.58)$$

The spatial information concerning the electron, including the coordinates and direction of movement, as well as the kinetic energy, is stored for the simulation of the fast electron transport problem, which will be discussed in chapters 6 and 7.

### 3.3.4 Coherent scattering

The simulation of the coherent scattering process intended to sample the deflection angle  $\theta$  follows the method described by Baró et al.[108]. By integrating the coherent scattering DCS expressed in Equation (3.35) over the solid angle  $\Omega (= 2\pi \cos \theta)$ , the probability distribution function (PDF) of the angular deflection  $\cos \theta$  is given by

$$p_{co}(\cos \theta) = \frac{1 + \cos^2 \theta}{2} [F(x, Z)]^2 \quad (3.59)$$

where  $x$  is given by Equation (3.38) and the  $[F(x, Z)]^2$  of the compound is calculated according to Equation (3.40). The parameters  $a_1, a_2, a_3, a_4$  and  $a_5$  for the elements of interest are shown in Table 3.1. The random sampling of the polar deflection proceeds as follows:

- i. Compute  $\Pi(x_{max}^2)$ , which is given by

$$\begin{aligned} \Pi(x_{max}^2) &= \int_0^{x_{max}^2} [F(x, Z)]^2 dx^2 \\ &= \int_0^{x_{max}^2} \sum_{i=1}^N n_i [F_i(x, Z)]^2 dx^2 \end{aligned} \quad (3.60)$$

- ii. Generate a pseudo-random number  $\xi$  and determine  $x^2$  using the equation

$$x^2 = \Pi^{-1}(\xi \Pi(x_{max}^2)) \quad (3.61)$$

Then,  $\cos \theta$  is determined as

$$\cos \theta = 1 - \frac{1}{2} \frac{x^2}{(20.6074)} \quad (3.62)$$

- iii. Generate a new pseudo-random number  $\zeta$ , if  $\xi > g(\cos \theta) \equiv \frac{1+\cos \theta}{2}$ , go to step (ii).
- iv. Deliver  $\cos \theta$ .

**Table 3.1** The parameters in Equation (3.40) for analytical approximation

$Z$	$a_1$	$a_2$	$a_3$	$a_4$	$a_5$
8 (O)	3.2455E+0	-3.6827E+0	1.2564E+1	6.5252E+0	1.2236E+0
16 (S)	1.9453E+1	-1.3639E+1	1.5521E+2	1.6170E+1	9.6229E+0
64 (Gd)	6.8486E+0	1.9174E+1	7.2468E-1	8.1677E+0	4.8462E-2

### 3.3.5 Electron-positron pair production

The distribution probability of the reduced electron energy derived from the pair production DCS is given by[108]:

$$\begin{aligned}
 p_{pp}(\epsilon) &= 2 \left( \frac{1}{2} - \epsilon \right)^2 \phi_1(\epsilon) + \phi_2(\epsilon) \\
 &= w_1 D_1(\epsilon) \varepsilon_1(\epsilon) + w_2 D_2(\epsilon) \varepsilon_2(\epsilon)
 \end{aligned} \tag{3.63}$$

with

$$w_1 = \frac{2}{3} \left( \frac{1}{2} - \frac{1}{\kappa} \right)^2 \phi_1 \left( \frac{1}{2} \right), \quad w_2 = \phi_2 \left( \frac{1}{2} \right) \tag{3.64}$$

$$\varepsilon_1(\epsilon) = \frac{3}{2} \left( \frac{1}{2} - \frac{1}{\kappa} \right)^{-3} \left( \frac{1}{2} - \epsilon \right)^2, \quad \varepsilon_2(\epsilon) = \frac{1}{2} \left( \frac{1}{2} - \frac{1}{\kappa} \right)^{-1} \tag{3.65}$$

and

$$D_1(\epsilon) = \frac{\phi_1(\epsilon)}{\phi_1(1/2)}, \quad D_2(\epsilon) = \frac{\phi_2(\epsilon)}{\phi_2(1/2)}, \tag{3.66}$$

The generation of a random  $\epsilon$  from the distribution Equation (3.63) is performed according to the following steps [108].

- i. Sample a value of the integer  $i$  ( $=1, 2$ ) according to the point possibilities

$$p(1) = \frac{w_1}{w_1+w_2} \text{ and } p(2) = \frac{w_2}{w_1+w_2};$$

- ii. Generate a pseudo-random number  $\xi$  ( $\in (0,1)$ ) and sample  $\epsilon$  from Equation

(3.58)

$$\epsilon = \begin{cases} \frac{1}{2} + \left(\frac{1}{2} - \frac{1}{\kappa}\right) (2\xi - 1)^{\frac{1}{3}}, & i = 1 \\ \frac{1}{\kappa} + \left(\frac{1}{2} - \frac{1}{\kappa}\right) 2\xi, & i = 2 \end{cases} \quad (3.67)$$

- iii. Generate a new pseudo-random number  $\xi$ .
- iv. If  $\xi > D_i(\epsilon)$ , go to step i.
- v. Deliver  $\epsilon$ .

The polar deflection of the movement of the electron ( $\theta_-$ ) and the positron ( $\theta_+$ ) with reference to the movement-direction of the initial incident photon are sampled according to the PDF of  $\theta_{\pm}$  as given by Equation (3.63).

- vi. The normalised constant  $a_{pp}$  corresponding to the kinetic energy  $\beta_{\pm}$  is calculated as

$$a_{pp}^{-1} = \int_{-1}^1 (1 - \beta_{\pm} \cos \vartheta_{\pm}) d \cos \vartheta_{\pm} \quad (3.68)$$

- vii. Generate a new random  $\xi$ , and then the polar angle  $\cos \theta_{\pm}$  is given by

$$\cos \theta_{\pm} = \left(1 - \frac{\xi}{a_{pp}}\right) / \beta_{\pm} \quad (3.69)$$

As the directions of the produced particles and the incident photon are not necessarily coplanar, the azimuthal angles  $\phi_-$  and  $\phi_+$  of the electron and the positron are sampled both independently and uniformly in the interval  $(0, 2\pi)$ [123]. The kinetic energies and the directions of movement of the electrons and positrons sampled according to the

above-mentioned MC method are stored for the further simulation of electron and positron transport in media.

### 3.4 Generation of random tracks of X-ray photons

The above sections provide a brief introduction to the theories of photon interaction with a single component material, as well as the MC method for simulating the energy absorption, the angle deflection of the initial photon and the generation of secondary particles (characteristic X-rays, electrons and positrons). The simulation of ISOFDs, however, is much more complicated, since the model is comprised of materials with different mass attenuation coefficients, mass densities, refractive indices and geometries. Therefore, in this section we introduce the method of sampling X-ray transport through different media and boundaries in a bi-materials model, which is based on the configuration of the ISOFD that will be introduced in the following chapter.

In this simple model, the media are classified into two types, namely those with low mass attenuation coefficients, which produce significantly less light photons via photon interactions, (e.g. water, binding material and silica) and those with much higher mass attenuation coefficients, which are capable of emitting light photons with a much higher intensity, (e.g. a scintillator). We use **A** to represent the former type of material and **B** to represent the latter type. Considering the small dimension of the scintillation-domain and following the assumption made early for the convenience of the simulation: (a) the incident X-ray photon is treated as a particle with energy  $E$ ; (b) the refractive

index of an X-ray in all media is approximated as 1\*, while the direction of the X-ray's trajectory is only changed when it is attenuated; (c) the step length that a photon travels in **A** is fixed to be  $l_{\text{mean}}$ , while the free path length in **B** is sampled randomly with Equation (3.45); (d) if the X-ray photon is attenuated by **A**, the photon dies; (e) if the photon is attenuated by medium **B**, the detailed photon interaction is simulated according the algorithms described in section 3.4; and (f) all the energy absorbed (minus the energy transferred to the secondary electron and positron emissions) is transferred into light photon emissions.

The parameters involved are the linear attenuation coefficients ( $\mu_A$  and  $\mu_B$ ), the mass total and partial attenuation coefficients  $(\mu/\rho)_i$  ( $i = \text{'tot'}$ , 'ph', 'inco', 'coh', and 'pp'), a fixed step length  $l_{\text{mean}}$  of transport in media **A**, the energy of the X-ray photon  $E$ , the position of the photon  $\vec{r}$ , and the direction of movement  $\vec{d}$ . In the description of the algorithm, we use the symbol  $\leftarrow$  in expression such as " $a \leftarrow b$ " to indicate that the value  $b$  replaces the value  $a$ , while  $\xi$  stands for a random number uniformly distributed in the interval  $(0, 1)$ . The practical generation of X-ray tracks in the bi-material consisting of **A** and **B** therefore proceeds as follows:

- i. Generate a new X-ray photon and then set the initial value  $E$ , position  $\vec{r}$  and direction of movement  $\vec{d}$  of this primary X-ray photon.
- ii. The photon travels a step length  $l_{\text{mean}}$  in medium **A** before colliding with the interface of medium **B**. According to Equation (3.7), the transmission

---

\* Due to the high energy of X-rays, the X-ray photon interacts weakly with the material, thus the actual refractive index of X-ray photons is extremely close to 1. For the convenience of calculation, the refractive index of X-ray can be approximated as 1.

probability of the travelling distance  $l_{\text{mean}}$  is given by  $P_{\text{trans},A} = \exp(-\mu_A \cdot l_{\text{mean}})$ .

- iii. Generate a random  $\xi$ . If  $\xi > P_{\text{trans},A}$ , the X-ray photon is absorbed by medium **A** and you should go to step (i); otherwise, the X-ray photon advances to the new location  $\vec{r} \leftarrow \vec{r} + l_{\text{mean}} \cdot \vec{d}$ .
- iv. Calculate the maximum path length  $l_{\text{max}}$  in medium **B**.
- v. Generate a new  $\xi$ ; the transmission distance  $l_{\text{trans},B}$  in medium B is given by
 
$$l_{\text{trans},B} = -\ln \xi / \mu_B \quad (3.70)$$
- vi. If  $l_{\text{max}} < l_{\text{trans},B}$ , the photon propagates through **B** without attenuation. Hence, advance to the next location  $\vec{r} \leftarrow \vec{r} + l_{\text{max}} \cdot \vec{d}$ ; otherwise, go to step (vii).
- vii. Simulate the detailed photon interaction with **B**:

The X-ray photon advances to the interaction site  $\vec{r} \leftarrow \vec{r} + l_{\text{trans},B} \cdot \vec{d}$ . Only one type of primary photon interaction occurs, and the type of that photon interaction is determined according to the interaction probabilities given by Equation (3.46) with a new random value of  $\xi$ . Sample the energy deposition  $\Delta E$  (transferred to light photons) on the scintillator, the angle deflection  $(\theta, \phi)$  of the X-ray photon with respect to the initial direction  $\vec{d}$ , as well as the energy  $E'$  and the direction  $(\theta', \phi')$  of movement of the secondary particles (electrons and positrons) created during the corresponding photon interaction according to the MC algorithms described in section 3.3. Perform a rotation of direction  $R(\theta, \phi)$  of the vector  $\vec{d}$  with the sampled  $(\theta, \phi)$ . First, store the spatial and energy information of the light photons and secondary particles (electrons and

positrons). Then, if the X-ray photon exists (including characteristic X-rays and X-rays scattered through coherent and incoherent scattering), update its spatial and energy information:  $\vec{d} \leftarrow R(\theta, \phi) \cdot \vec{d}$ , and  $E \leftarrow E - \Delta E - E'$  and then go to step (iv). If the X-ray dies ( $E = \Delta E + E'$ ), go to step (i).

- viii. Simulate the track of the light photons and secondary particles before starting a new primary track.

The interaction events of a high-energy ionising photon (X-/ $\gamma$ -ray) with the media of the ISOFD are simulated according to the method described in the above sections in chronological order. The tracks of the light photons generated in this process are modelled using another method, in which the light photons are treated as un-polarised particles and the Fresnel law of reflection and exponential attenuation law are adopted. This concept will be introduced in more detail in chapter 5.

### 3.5 Summary

In this chapter, the theory of X-ray photon interactions with media and the corresponding MC simulation algorithms are reviewed in sections 3.1 to 3.3. The simulation method described in section 3.4 considers the detailed simulation of four types of primary photon interaction events (photoelectric effect, coherent scattering, incoherent scattering and pair production) along the photon track history in chronological order. As secondary particles (characteristic X-ray photons, electrons and positrons) may be generated in the photon transport history, the simulation of the characteristic X-rays follows the same method as that of the primary photon, while the

modelling of electrons/positrons will be introduced in chapters 6 and 7. The above-mentioned simulation method is developed based on previously validated MC simulation algorithms; however, it requires further validation by means of comparing the simulation result with that obtained using other well-developed MC simulation codes such as EGSnr[121]. The simulation of light photon propagation is presented in chapter 4, within the detailed description of the ISOFD simulation process.

## **Chapter 4—The Monte-Carlo simulation method of diagnostic X-ray detection with ISOFDs**

### **4.1 Introduction to ISOFD modelling**

In the previous chapters, the theory and Monte-Carlo (MC) simulation algorithm of photon and electron interactions were introduced. As it highlighted in chapter 3, the application of MC simulation to ISOFD is appealing, not only because the MC simulation method has proven to be a flexible and powerful tool in medical radiotherapy, but also because of the opportunity it provides for a deeper insight into the key factors affecting the radiation sensitivity of the ISOFD; meanwhile saving time and resources. In this study, the ISOFD is simulated, for the first time, with the MC method to investigate the effect of configurations and properties of the materials on the radiation-detecting performance of the sensor under photon radiation of different energies, and optimize the sensor design further. The model of ISOFD is based on a multi-mode silica optical fibre coupled with a  $Gd_2O_2S$  (gadolinium oxysulfide, ‘GOS’ for short) scintillation-domain. The simulation method incorporates the MC simulation algorithm of ionizing particle (photon, electron and positrons) interaction and MC ray-tracing of light photons. The simulation results are validated with theoretical calculation regarding the energy transfer and deflection of the particle movement.

This chapter focuses on the simulation method of ISOFD for diagnostic X-ray in the energy interval (10~80 KeV). Firstly, the coordinate systems used in the simulation

are introduced in section 4.2. The model configurations such as geometries and materials are given in section 4.3, where the configurations of 3 models are described. The input parameters for diagnostic X-ray detection simulation are listed in the section 4.4. The detail of the simulation method is given in section 4.5, which includes a flow-chart assisted simulation process description, including the method of modelling of ionizing photon transport in the medium, and the ray tracing method of light photons. The section 4.6 gives the output parameters of interest for the analysis and valuation of photon radiation detection.

## 4.2 Coordinate system

Two major coordinate systems are involved in the modelling, i.e. Cartesian coordinate system and spherical coordinate systems, as shown in Figure 4.1. The dimensionless orthogonal unit vectors of the fixed Cartesian coordinate system are  $\mathbf{i}$ ,  $\mathbf{j}$  and  $\mathbf{k}$ , given by

$$\mathbf{i} = (1, 0, 0), \quad \mathbf{j} = (0, 1, 0), \quad \mathbf{k} = (0, 0, 1) \quad (4.1)$$

The spatial information of a particle is defined by its location

$$\mathbf{r} = (x, y, z) = x \cdot \mathbf{i} + y \cdot \mathbf{j} + z \cdot \mathbf{k} \quad (4.2)$$

and the direction of movement, given by a dimensionless unit vector

$$\vec{\mathbf{d}} = (d_1, d_2, d_3) = (\sin \theta \cos \varphi, \sin \theta \sin \varphi, \cos \theta) \quad (4.3)$$

where  $\theta$  and  $\varphi$  are the polar and azimuth angle respectively.

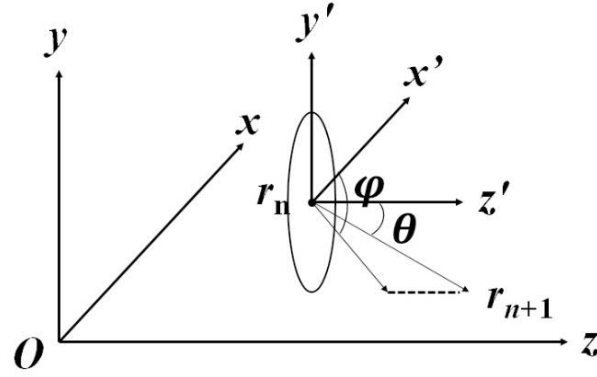


**Figure 4.1** The coordinate systems: a fixed Cartesian coordinate  $(x, y, z)$  system in origin point  $O$ ; a local coordinate system  $(x', y', z')$  and a spherical system  $(r, \theta, \varphi)$  which move with particle. The local Cartesian coordinate system is parallel to the fixed one.

When the particle moves a distance  $l$   $\mu\text{m}$  from the position  $\mathbf{r}_n$  to the next position  $\mathbf{r}_{n+1}$  along the direction  $\vec{\mathbf{d}}$ , the coordinate of  $\mathbf{r}_{n+1}$  is given by

$$\begin{aligned}\mathbf{r}_{n+1} &= \mathbf{r}_n + \vec{\mathbf{d}} \cdot l \\ &= (x_n, y_n, z_n) + (d_1, d_2, d_3) \cdot l\end{aligned}\quad (4.4)$$

If the direction of the movement is changed due to a photon scattering event, the vector  $\vec{\mathbf{d}}$  goes through a rotation, as shown in Figure 4.2. Here we define the local 3D orthogonal unit vectors  $\vec{\mathbf{e}}_1$ ,  $\vec{\mathbf{e}}_2$  and  $\vec{\mathbf{e}}_3$ , which are calculated with  $\vec{\mathbf{d}}$  and unit vectors  $(\mathbf{i}, \mathbf{j}, \mathbf{k})$ , given by

$$\vec{\mathbf{e}}_3 = \vec{\mathbf{d}} = (d_1, d_2, d_3) \cdot \begin{pmatrix} \mathbf{i} \\ \mathbf{j} \\ \mathbf{k} \end{pmatrix}, \quad (4.5)$$

$$\vec{\mathbf{e}}_1 = \frac{\mathbf{j} \times \vec{\mathbf{e}}_3}{|\mathbf{j} \times \vec{\mathbf{e}}_3|} = (d_4, d_5, d_6) \cdot \begin{pmatrix} \mathbf{i} \\ \mathbf{j} \\ \mathbf{k} \end{pmatrix}, \quad (4.6)$$

$$\vec{e}_2 = \frac{\vec{e}_3 \times \vec{e}_1}{|\vec{e}_3 \times \vec{e}_1|} = (d_7, d_8, d_9) \cdot \begin{pmatrix} i \\ j \\ k \end{pmatrix}, \quad (4.7)$$

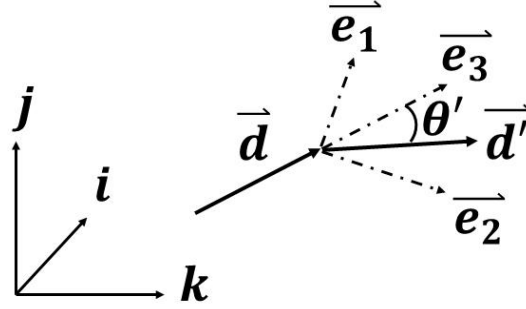


**Figure 4.2** The rotation of the motion vector from  $\vec{d}$  to  $\vec{d}'$ .

Accordingly, the transfer function from the matrix  $\begin{pmatrix} i \\ j \\ k \end{pmatrix}$  to  $\begin{pmatrix} \vec{e}_1 \\ \vec{e}_2 \\ \vec{e}_3 \end{pmatrix}$  is  $TR1_{3 \times 3}$ , expressed

as

$$TR1 = \begin{pmatrix} d_1, d_2, d_3 \\ d_4, d_5, d_6 \\ d_7, d_8, d_9 \end{pmatrix} \quad (4.8)$$

and

$$\begin{pmatrix} \vec{e}_1 \\ \vec{e}_2 \\ \vec{e}_3 \end{pmatrix} = TR1 \cdot \begin{pmatrix} i \\ j \\ k \end{pmatrix} \quad (4.9)$$

For the scattered particle,  $\theta'$  represents the polar angle deflection of the direction of movement  $\vec{d}'$  with reference to the initial vector  $\vec{d}$ , and  $\varphi'$  represents the azimuth angle of  $\vec{d}'$  in the new orthogonal coordinate system defined by  $\vec{e}_1$ ,  $\vec{e}_2$  and  $\vec{e}_3$ , the scattered motion vector  $\vec{d}'$  is thus given by

$$\vec{d}' = (\sin \theta' \cos \varphi', \sin \theta' \sin \varphi', \cos \theta') \cdot \begin{pmatrix} \vec{e}_1 \\ \vec{e}_2 \\ \vec{e}_3 \end{pmatrix} \quad (4.10)$$

substitute Equation (4.9) into Equation (4.10),  $\vec{d}'$  is derived as

$$\begin{aligned}\vec{d}' &= (\sin \theta' \cos \varphi', \sin \theta' \sin \varphi', \cos \theta') \cdot TR1 \cdot \begin{pmatrix} i \\ j \\ k \end{pmatrix} \\ &= \mathbf{R}(\theta', \varphi') \cdot \vec{d}\end{aligned}\tag{4.11}$$

Above equations are important for modelling the movement vector of scattered particles and will also be applied to calculate the direction of secondary particles (electrons or positrons) as the result of photon interactions.

### 4.3 Geometry of the ISOFD model and material properties

In this section, the geometry of an ISOFD model based on a modified multi-mode optical fibre is presented in section 4.3.1. After that, the properties of materials comprising the ISOFD are introduced in section 4.3.2, and the attenuation performance of the photon in these media is discussed in detail. At last, the configurations of three different ISOFD adopted in simulation are given in section 4.3.3.

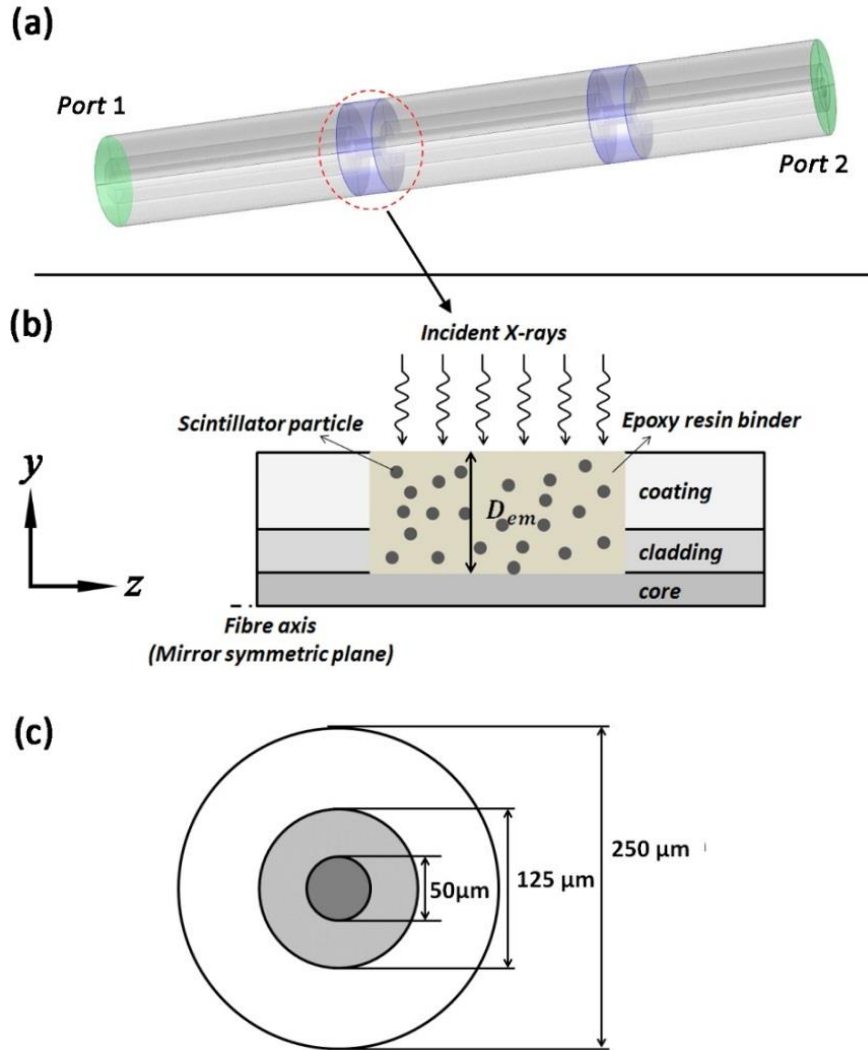


**Figure 4.3** (a) 3D image of MPISOFD, (b) The 2D diagram of the scintillation-domain, (c) the cross section of optical fibre

#### 4.3.1 Basic geometry of a single scintillation-domain

The models of the ISOFD to be simulated in this thesis contain one single or multiple units of the basic scintillation-domains shown in Figure 5.3 (b). One piece of the fibre cladding layer is removed, and the groove is embedded with  $\text{Gd}_2\text{O}_2\text{S:RE}$  ('RE' = Tb, Eu, and Pr) and curable epoxy resin mixture, following the scintillator coating procedure described by McCarthy et al.[33] A multi-mode step-

index silica fibre was applied, as shown in Figure 4.3(c), the core material is germanium doped silica with a diameter  $D_{core}$  of 50  $\mu\text{m}$  and the refractive index (RI) of 1.455. The cladding material is pure silica with RI of 1.45 and the out diameter of cladding is  $D_{core} = 125 \mu\text{m}$ . The fibre is coated with polymer material, with RI of 1.3 and outer diameter of  $D_{coating} = 250 \mu\text{m}$ , and the polymer is assumed to be water equivalent. The substrate is vacuum, where the photon travels without energy loss.

### 4.3.2 Properties of materials

The basic properties of the materials used are listed in Table. 4.1. The binding material for gluing the scintillator particles is the mixture of epoxy resin (*ER*) and hardener, which is comprised of several materials[128]. For the simplicity of calculation, here we use a single formula  $\text{C}_{59}\text{H}_{91}\text{O}_8\text{N}_5$  to represent the binding material, and this formula approximation is based on the actual fractional weight of all components in binding material. Considering the low doping of germanium in core, except from the difference of RI, both core and cladding share the same physical properties with those of pure  $\text{SiO}_2$ . Polymer coating is water-equivalent, thus here we use water to replace the polymer material. Table 4.1 lists the physical properties of common materials constituting the optical fibre.

**Table 4.1** Materials used in ISOFD models

	Material	Formula	Density (g/cm <sup>3</sup> )	Refractive index
Core & cladding	Silica	SiO <sub>2</sub>	2.65	1.455, 1.45
Polymer Coating	water-equivalent	H <sub>2</sub> O	1	1.33
Binding material	<i>ER</i>	C <sub>59</sub> H <sub>91</sub> O <sub>8</sub> N <sub>5</sub>	1.22	1.58
Scintillator	Gd <sub>2</sub> O <sub>2</sub> S	Gd <sub>2</sub> O <sub>2</sub> S	7.5	2.3+0.626i

### The photon attenuation in media

The total mass attenuation coefficients of the materials (shown in Table. 4.1) are required from ‘XCOM: Photon Cross Sections Database’[118], and plotted in Figure 4.4(a). If we consider the exponential law of attenuation (see Equation (3.7)), the mean free path length of the photon, in some cases also known as ‘attenuation length’, is given by

$$\lambda = \frac{1}{\mu} \quad (4.12)$$

where  $\mu$  is the linear attenuation coefficient, which can be obtained by the product of the density  $\rho$  and mass attenuation coefficient  $\mu/\rho$ . This parameter represents the average distance travelled by a photon between successive collisions with the molecule or atoms in an isotropic homogeneous medium. As for the discussion about the photon attenuation ability of different materials in the following content, the linear attenuation coefficient is calculated with total mass attenuation length  $\mu_{\text{tot}}$ , which considers the photon attenuation caused by all types of photon interactions for photons in the range 20 – 80 KeV.

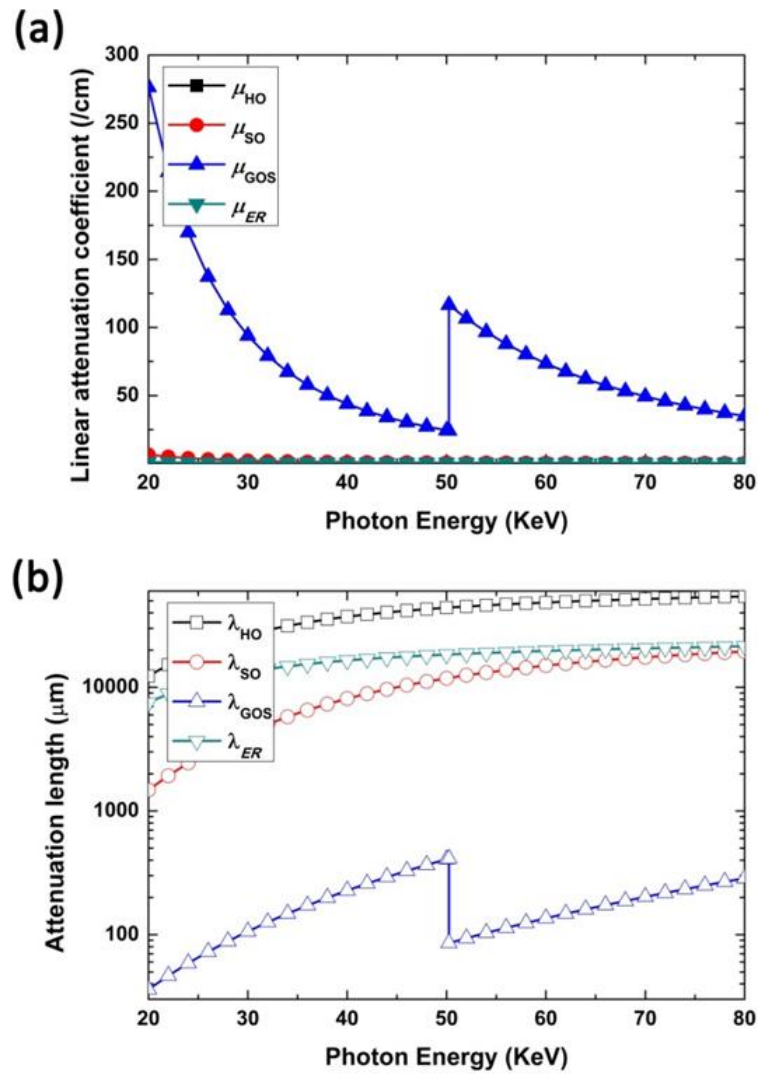


**Figure 4.4** (a) The linear attenuation coefficients  $\mu$ , and (b) the mean free path lengths  $\lambda$  of the material  $\text{H}_2\text{O}$ ,  $\text{SiO}_2$ ,  $\text{ER}$  and  $\text{Gd}_2\text{O}_2\text{S}$  for X-ray photons.

The mean free path lengths of a photon in the media  $\text{H}_2\text{O}$ ,  $\text{SiO}_2$ ,  $\text{ER}$  and  $\text{Gd}_2\text{O}_2\text{S}$  are expressed as  $\lambda_{\text{HO}}$ ,  $\lambda_{\text{SO}}$ ,  $\lambda_{\text{ER}}$  and  $\lambda_{\text{GOS}}$  respectively, and  $\lambda_i$  (where ‘i’ represents ‘HO’, ‘SO’, ‘ER’, or ‘GOS’) for initial photons in the diagnostic X-ray range are plotted in Figure 4.4. From the figure, we can see that the scintillator  $\text{Gd}_2\text{O}_2\text{S}$  has the highest coefficient  $\mu_{\text{GOS}}$  with respect to photon energy range 20 – 80 KeV, while the attenuation coefficients of  $\text{H}_2\text{O}$ , epoxy resin and  $\text{SiO}_2$  ( $\mu_{\text{HO}}$ ,  $\mu_{\text{ER}}$  and  $\mu_{\text{SO}}$ ) are much

lower. Accordingly, the mean free path lengths of the X-ray photon transport in H<sub>2</sub>O, ER and SiO<sub>2</sub> are normally more than a few millimetres, much longer than that in Gd<sub>2</sub>O<sub>2</sub>S. More importantly, for X-ray photon transport in the scintillator binding material  $\lambda_{ER}$  is much larger than the geometric dimension of the ISOFD model, and the photon will either transport out of the scintillation-domain or collide with a scintillator particle rather before interacting with epoxy resin. The difference of the attenuation length indicates that the possibility of photon attenuated by the material of low density and effective atomic number\* (H<sub>2</sub>O, ER and SiO<sub>2</sub>) is quite low. The sudden rise of the attenuation coefficient  $\mu_{GOS}$  near 50 KeV shown in Figure 4.4(a) is due to the K-absorption of Gd element in Gd<sub>2</sub>O<sub>2</sub>S. When the photon energy larger than the K-shell binding energy of Gd, the K-shell can be excited through photoelectric effect, thus there is a sudden increase of the total photon interaction cross section and mass attenuation coefficient. Accordingly, the sudden fall of the mean free path length  $\lambda_{GOS} = 1/\mu_{GOS}$  is witnessed in Figure 4.4(b).

It should be noted that, there are many research examples reported which utilising MC simulation for photon transport investigation (e.g. X-ray absorption and scattering inside X-ray phosphor screen), the mean free path length  $\lambda$  is used as the step length. However, for the simulation of an ISOFD model, if the mean free path length  $\lambda_{ER} \equiv$

---

\* For a compound material  $A_xB_yC_z$ ,  $Z_{eff}$  can be calculated according to the equation[58]:  $Z_{eff} = \sqrt[4]{\frac{xM_aZ_a^4+yM_bZ_b^4+zM_cZ_c^4}{xM_a+yM_b+zM_c}}$ , where  $M_a$ ,  $M_b$  and  $M_c$  are atomic masses of element  $A$ ,  $B$  and  $C$ , respectively.  $Z_a$ ,  $Z_b$  and  $Z_c$  are the atomic number of  $A$ ,  $B$  and  $C$ , respectively.

$1/\mu_{ER}$  is applied as the step length for modelling photon transport in the binding material, it will introduce systemic errors as  $\lambda_{ER}$  is much larger than the size of the scintillation-domain. Therefore, a new expression of mean free path length —  $l_{\text{mean},ER}$  is defined, which represents the average distance travelled by a photon (both X-ray and light) between successive collisions with scintillator particles in the binding material ( $ER$ ) of SD. This parameter is determined by the packing density ( $\eta_{\text{pk}}$  vol%) of the scintillator particles in SD, the density ( $\rho_{GOS}$ ) of the scintillator  $\text{Gd}_2\text{O}_2\text{S}$ , and the average size of the scintillator particles, and is given by [129]

$$l_{\text{mean},ER} = \frac{V_{\text{tot}}}{N_{\text{sp}}\sigma_{\text{sp}}} \quad (4.13)$$

where  $V_{\text{tot}}$  is the volume of phosphor bulk,  $N_{\text{sp}}$  is the number of scintillator particles and  $\sigma_{\text{sp}}$  is the cross section of the particle. As all particles are approximated as sphere and share same diameter, the particle number  $N_{\text{sp}}$  is expressed as

$$N_{\text{sp}} = m_{\text{sp}} / \left( \frac{4}{3} \pi r_{\text{p}}^3 \cdot \rho_{\text{sp}} \right) \quad (4.14)$$

where  $m_{\text{sp}}$  is the overall mass of the scintillator particles,  $\sigma_{\text{sp}}$  is the cross section of the particle with radius of  $r_{\text{p}}$ , which given by

$$\sigma_{\text{sp}} = \pi r_{\text{p}}^2 \quad (4.15)$$

Substituting Equation (4.14) and (4.15) into Equation (4.13), the mean free path is derived as:

$$l_{\text{mean},ER} = \frac{4}{3} \cdot \frac{V_{\text{tot}} \cdot r_{\text{p}} \cdot \rho_{\text{p}}}{m_{\text{p}}} = \frac{4}{3} r_{\text{p}} \cdot \left( \frac{V_{\text{tot}}}{V_{\text{sp}}} \right) = \frac{4}{3} r_{\text{p}} / \eta_{\text{pk}} \quad (4.16)$$

In the simulation, the packing density and particles size are variable so that these parameters can be optimised for better incident radiation absorption and light photon transportation.

### 4.3.3 Models with different configurations

IOSFDs based on single scintillation-domain coupling and that has double-scintillation-domains are used for modelling. The double-domain model is a simplification of multi-point ISOFD, aiming to investigate the attenuation of light photon by the adjacent SD. The distance between two SDs is 1000  $\mu\text{m}$ . For the radiation source, the primary X-ray photon is generated on the plane on top of SD and parallel to the  $xy$  plane (the fibre axis is parallel to  $z$ -axis). To collect the scintillation-light photons transmitted along the fibre, two ports are put in the optical fibre with a distance of 1000  $\mu\text{m}$  from the terminal of SDs, as shown in Figure 4.3(a). Each single radiation sensitive SD distributed along the fibre is comprised of a SD embedded in the groove of the optical fibre (cladding layer of the fibre is pre-removed), just as shown in the Figure 4.3(b). The length of SD ( $l_{\text{SD}}$ ) along the fibre axis is set as 100  $\mu\text{m}$ .  $D_{\text{em}}$  is used to represent the embedding depth along the fibre radius into the fibre, which is variable.

The scintillator particles are uniformly distributed in the domain and glued together using adhesive *ER*. As the distribution of these particles is isotropic, they are assumed to be a perfect sphere with same radius equal to the mean particle size  $r_p$  of the scintillator powder. The mean particle size of commercially available scintillator powders  $\text{Gd}_2\text{O}_2\text{S:RE}$  ranges from 2.5  $\mu\text{m}$  to 25  $\mu\text{m}$  [64], therefore, single-domain ISOFD models with different particle sizes are simulated so that an optimal particle size can be determined.

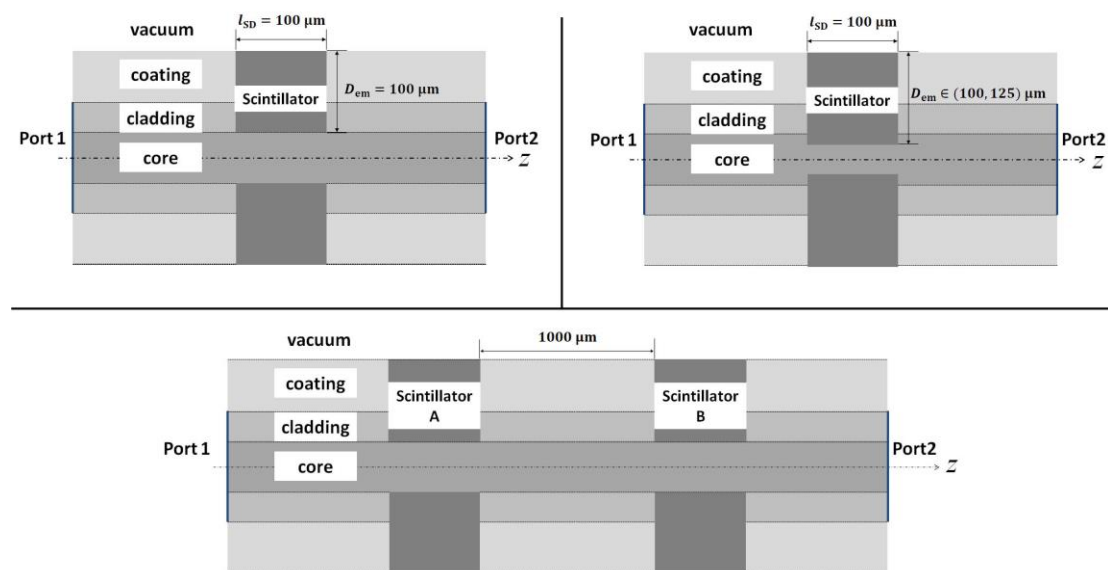


**Figure 4.5** the models of ISOFD to be simulated, 3 models are simulated: Model 1 in which the cladding layer is removed while the fibre core is intact; Model 2 in which the fibre cladding and outer layer of fibre core is removed; Model 3 with two SDs ‘A’ and ‘B’ embedded into fibre cladding layer

As is introduced at the beginning of this section, different configurations are modelled. The variable parameters include the number of scintillation-domains and the embedding depth  $D_{em}$ . As shown in Figure 4.5, three basic models are simulated. In Model 1, the cladding layer has been completely removed and the fibre core is coated by scintillator-resin mixture. The embedding depth of Model 2 is larger than that of Model 1, and a part of the fibre core in Model 2 is also removed. The Model 1 and Model 2 are single scintillation-domain ISOFD, while Model 3 is a double scintillation-domain ISOFD, in which each domain resembles that of Model 1.

#### 4.4 Required input data for Monte-Carlo simulation

The input physical data required for the Monte Carlo simulation program include: the energy of incident photon ( $E_0$ ), the mean radius of scintillator particle ( $r_p$ ), packing density of the scintillator ( $\eta_{pk}$ ), the mean path length of X-rays in the  $ER$  binding material, chemical compositions of all material in ISOFD, density of the material, the numerical values of physical parameters and coefficients relevant to ionizing photon interaction and light photon transport. All the data relating to photon interaction are sourced from validated databases, libraries and articles. In particular, the parameters and coefficients applied are the following: the total mass attenuation coefficients of all materials[118], the mass partial interaction coefficients of the scintillator[118], the mass partial interaction coefficients of each element of scintillator and their fractional weight[118], probability of the K-shell ionization[123], radiative transition probabilities  $p_{K-i}$  ( $i = L2, L3, M2, \dots$ )[124], the K-fluorescent yield  $\omega_K$  for characteristic K-X-ray emission[109], the incoherent scattering function calculated with the Compton profile[103], the coherent scattering function[104], [108], the screening radius[126], the scintillator's intrinsic conversion efficiency[130], the refractive indices of the material, and the linear attenuation coefficients of the material for light photon.

#### 4.5 Simulation of diagnostic X-ray photon absorption

The MC simulation of X-ray photon transport and attenuation in the ISFOD model introduced in this section focuses on the diagnostic X-ray attenuation. The method

considers the attenuation of the X-ray photon particle along the trajectory, specific photon interaction such as the generation of characteristic X-ray through photoelectric absorption, the track deflection by scattering events, and the reabsorption of secondary X-ray photons. All energy absorbed by scintillator particle is transferred to visible photon, and the simulation method of light photon transport in the ISOFD is introduced in the next section.

In chapter 3, we introduced the MC simulation method of the X-ray history generation in a bi-material model. This model contains a material **A** with low mass attenuation coefficient and a material **B** with a much higher attenuation-coefficient. For the ISOFD models shown in Figure 4.3 and 4.5, all types of material are categorised into '**A**' or '**B**' according to their linear attenuation coefficients and attenuation length. As it revealed in section 4.3.2, the linear attenuation coefficients of H<sub>2</sub>O, epoxy resin and SiO<sub>2</sub> are small and corresponding attenuation lengths are much larger than dimension of the ISOFD model, it is reasonable to classify H<sub>2</sub>O, ER (C<sub>59</sub>H<sub>91</sub>O<sub>8</sub>N<sub>5</sub>) and SiO<sub>2</sub> as '**A**' type material. In the simulation program, **A1**, **A2**, and **A3** are used to represent H<sub>2</sub>O, ER (C<sub>59</sub>H<sub>91</sub>O<sub>8</sub>N<sub>5</sub>) and SiO<sub>2</sub> respectively. The photon interaction is ignored when the X-ray photon transport is in the '**A**' type materials, and conversely the X-ray photon is assumed to be totally attenuated if the randomly sampled transmission length (see Equation (3.42) in chapter 3) is smaller than the path length in **A** material, such that no light signal is generated during this process. Gd<sub>2</sub>O<sub>2</sub>S is classified as '**B**' type material, and the X-ray is attenuated followed by the detailed simulation of photon interactions. In this simulation, except for K-X-ray emission, all energy lost during the

photon interaction is assumed to be absorbed by the scintillator  $Gd_2O_2S$  and transferred to light photons.

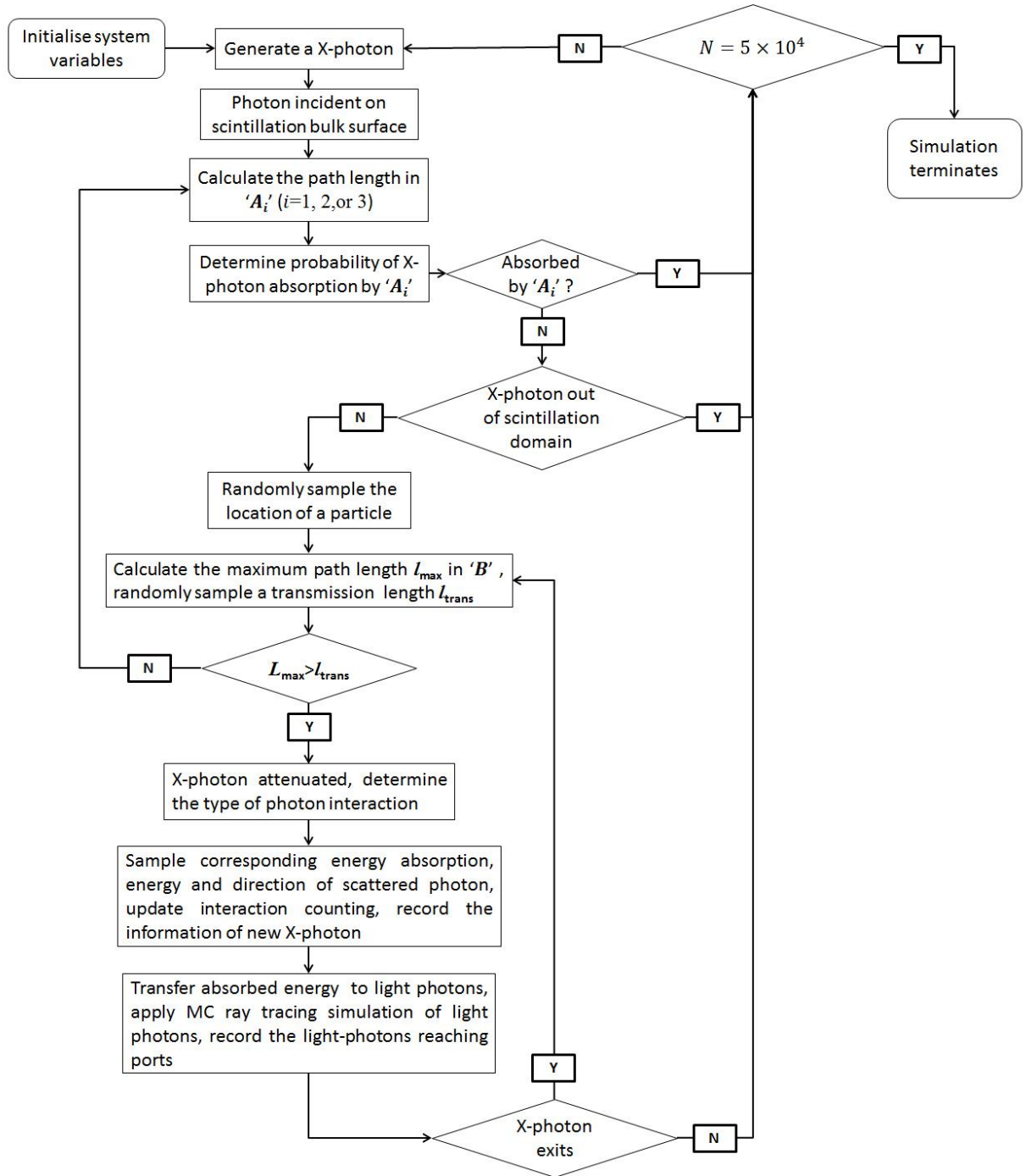


**Figure 4.6** The flow-chart of Monte-Carlo simulation of diagnostic X-ray photon transport in a single-domain ISOFD

The simulation code based on the process described by the flow chart shown in Figure 4.6 is written by the myself with Matlab 2014a. The transport history of each X-ray photon with initial energy  $E_0$  is simulated and the total number of X-ray photons emitted is set as  $5 \times 10^4$ . The transport history of each X-ray photon is terminated if the photon is totally absorbed by the media or transports out of SD. Combining the coordinate systems described in section 4.2, the MC simulation of a bio-material system in chapter 3, and the configuration of IOSFD, the X-ray photon transport history in ISOFD is simulated in following steps:

- i. Generate an X-ray photon from the plane parallel to  $xy$  plane on top of the cylinder SD, with an initial energy  $E$  and direction of movement  $\vec{d} = (0, 1, 0)$ . The photon incident on the surface of SD without energy loss. The initial incident location at the vacuum— $ER$  interface is  $\mathbf{r}$ .
- ii. X-photon travels a step length of  $l_{\text{mean},ER}$  in  $ER$  (**A2**), update the location  $\mathbf{r} \leftarrow \mathbf{r} + \vec{d} \cdot l_{\text{mean},ER}$ . If  $\mathbf{r}$  is out of the scintillation- domain, go to step viii.
- iii. Generate a random value  $\xi$ , calculate the transmission length  $l_{\text{trans}} = -\ln \xi / \mu_{A2}$ . If  $l_{\text{trans}} < l_{\text{mean},ER}$ , photon absorbed by **A2**, go to step viii.
- iv. The X-photon collides with scintillator particle (**B2**), the orientation of the particle is randomly sampled as follow:

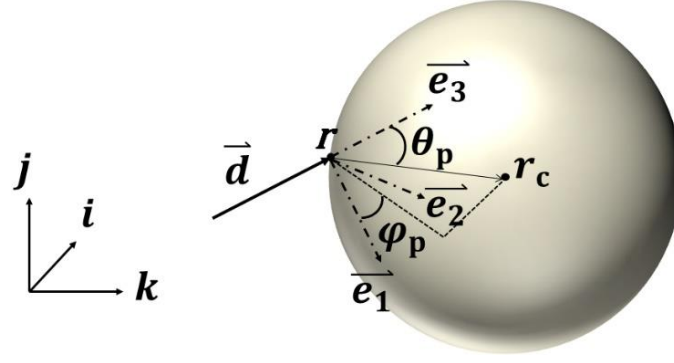


**Figure 4.7** Schematic of the orientation of the scintillator particle upon collision by the X-ray photon

A local coordinate system is established following the procedure given in section 4.2. As shown in Figure 4.6, the random polar angle  $\theta_p$  is uniformly distributed in the interval  $(0, \pi/2)$ , and the azimuth angle  $\varphi_p$  is uniformly distributed in the interval  $(0, 2\pi)$ . The location of the scintillator sphere centre is thus given by

$$\mathbf{r}_c = \mathbf{r} + r_p(\overline{\mathbf{e}}_1 \sin \theta_p \cos \varphi_p + \overline{\mathbf{e}}_2 \sin \theta_p \sin \varphi_p + \overline{\mathbf{e}}_3 \cos \theta_p) \quad (4.17)$$

The maximum possible path length of X-ray transport in the scintillator particle is  $l_{\text{trav},B} = 2r_p \cdot \cos \theta_p$ .

- v. Generate a new random value of  $\xi$ , the transmission length in scintillator is  $l_{\text{trans},B} = -\ln \xi / \mu_B$ . If  $l_{\text{trans},B} < l_{\text{trav},B}$ , the X-ray photon is attenuated. The photon first advances to the new location  $\vec{\mathbf{r}} \leftarrow \vec{\mathbf{r}} + \vec{\mathbf{d}} \cdot l_{\text{trans},B}$ , then interacts  $\mathbf{B}$  (scintillator) molecule. Otherwise, go to step ii.
- vi. According to the mass partial interaction coefficients of  $\mathbf{B}$ , the type of interaction is determined. The MC simulation method of photon interaction has been given in chapter 3. The energy absorption  $\Delta E$ , the direction of movement and energy of X-rays after collision with the molecule are sampled. If the photon

energy is not totally absorbed and the X-ray photon still exists after interaction, obtain the new photon energy  $E \leftarrow E - \Delta E$  and movement-direction  $\vec{d}$ . The energy absorbed is transferred to a light ray. The MC simulation method of light photon ray tracing is introduced elsewhere in this chapter (section 4.5).

- vii. If X-ray photon exists, calculate the new maximum path length in  $\mathbf{B}$ , go to step v otherwise, proceed.
- viii. If the whole looping time reaches 50000, terminate simulation program, otherwise go to step (i).

The above simulation procedure is applied for modelling diagnostic X-ray interactions. For therapeutic photons of much higher initial energies, the transport of fast secondary electrons and positrons are simulated with the method proposed in later chapters. The simulation method of light photon generation and transport in IOSFOD is given in the next section.

#### **4.6 Simulation of Light-ray production and transport**

The energy absorption by the scintillator through X-ray photon interaction contributes to the production of visible light. The total energy  $E_{\text{vis}}$  of the visible photon created is given as follows:

$$E_{\text{vis}} = \eta_c \Delta E \quad (4.18)$$

where  $\eta_c$  is the intrinsic X-ray to light conversion efficiency ( $\eta_c = 0.15$  for  $\text{Gd}_2\text{O}_2\text{S}$  [131] ) of the phosphor,  $\Delta E$  is the X-ray energy absorbed by the scintillator.

In this simulation, the visible photons are treated as a ray containing photons that move in the same direction. This photon ray is emitted in a random direction from the scintillation site. The polar and azimuth angle of photon direction is distributed uniformly in the interval  $(0, \pi)$  and  $(0, 2\pi)$  respectively. The materials *ER* and silica are clear materials with good light transmission properties. Considering the small dimension of the model, the attenuation of the light photon ray in these materials is neglected. The attenuation of the light in the medium  $\text{Gd}_2\text{O}_2\text{S}$  utilises the same rule as that adopted in the simulation of a single X-ray photon transport in '*A*' type material. The probability of the light-ray travelling a distance  $l$  is given by  $P_{\text{trans}} \equiv \exp(-\mu l)$ . By comparing  $P_{\text{trans}}$  with a random number  $\xi$ , the ray either transmits without attenuation or is totally absorbed. The linear attenuation coefficient of  $\text{Gd}_2\text{O}_2\text{S}$  for light photons is derived from the complex refractive index given in Table 4.1.

The reflection and transmission probabilities of the light photon at the interfaces or boundaries adopt the Fresnel law. When a light photon hits the interface  $S_{n_1-n_2}$  from the material with refractive index  $n_1$ , the local coordinate system is first established on the incident interface, based on the direction of photon movement, and the unit vector normal to this  $S_{n_1-n_2}$  surface. Assuming the unit vector normal to  $S_{n_1-n_2}$  plane is  $\vec{e}_\perp$ , and the unit direction vector is  $\vec{d}$ , this local coordinate system is given by

$$\mathbf{k}' = \vec{e}_\perp, \quad (4.19)$$

$$\mathbf{j}' = \frac{\mathbf{k}' \times \vec{d}}{|\mathbf{k}' \times \vec{d}|}, \quad (4.20)$$

$$\mathbf{i}' = \frac{\mathbf{j}' \times \mathbf{k}'}{|\mathbf{j}' \times \mathbf{k}'|}, \quad (4.21)$$

The incident angle is  $\theta_{in}$ , and the transmission angle (or refractive angle)  $\theta_{tr}$  is calculated according to Snell's law. The probability of reflection is given by

$$p_{\text{refl}} = \frac{1}{2} \left[ \left( \frac{n_1 \cos \theta_{in} - n_2 \cos \theta_{tr}}{n_1 \cos \theta_{in} + n_2 \cos \theta_{tr}} \right)^2 + \left( \frac{n_2 \cos \theta_{in} - n_1 \cos \theta_{tr}}{n_1 \cos \theta_{tr} + n_2 \cos \theta_{in}} \right)^2 \right] \quad (4.22)$$

In the simulation, a random value  $\xi \in (0,1)$  is generated. The light ray is reflected if  $\xi < p_{\text{refl}}$  or the incident angle is larger than the critical angle at the interface. If the photon is reflected, then and direction of the reflected photon is

$$\overrightarrow{\mathbf{d}}_{\text{refl}} = -\mathbf{k}' \cos \theta_{in} + \mathbf{i}' \sin \theta_{in} \quad (4.23)$$

If the photon transmits through the interface, the refractive angle is

$$\overrightarrow{\mathbf{d}}_{\text{refr}} = \mathbf{k}' \cos \theta_{tr} + \mathbf{i}' \sin \theta_{tr} \quad (4.24)$$

The MC tracing method of light-rays considers the reflection and transmission at the following boundaries as: *ER*-scintillator particle, *ER*-vacuum, *ER*-coating, *ER*-cladding, *ER*-core, coating-vacuum, coating-cladding, and cladding-core. The critical angle at these interfaces are listed in the table 5.2. When the incident angle is larger than the critical angle, the light-ray is reflected. The multiple reflection and transmission at these boundaries are simulated until the light-ray is absorbed by terminal boundaries or transmits out of the model's outmost boundaries. The simulation of the light-ray trace in ISOFD is terminated in following cases: a) the light is absorbed by the scintillator, b) the light-ray transmits out of IOSFOFD boundary into vacuum, and c) the photon reaches the ports. The simulation output will return results of energy

loss during propagation so that the effect of ISOFD configuration on the light transport can be studied.

The whole X-ray absorption and light-ray tracing program is written in a sequential order. After the X-ray energy absorption, the light-ray tracing program is run to simulate the propagation of the light-ray inside the ISOFD model. After the light-ray tracing program is terminated, the simulation will return to the X-ray transport simulation program looping.

#### 4.7 Output parameters

##### Mean free path length $l_{\text{mean},ER}$

The mean free path length  $l_{\text{mean},ER}$ , given by the Equation (4.16), is an important parameter as it affects the probability of photon colliding with the scintillator particle when travelling in the binding material of SD. The  $l_{\text{mean},ER}$  variance is calculated against the change of packing density  $\eta_{\text{pk}}$  and mean particle size  $r_p$  of the scintillator.

##### Photon interaction probabilities $p_{\text{ph},1}$ , $p_{\text{incoh},1}$ , and $p_{\text{int}}$

$p_{\text{ph},1}$  and  $p_{\text{incoh},1}$  represent the probability of initial incident X-ray photon undergoing photoelectric absorption, and incoherent scattering respectively.  $p_{i,1}$  ( $i = \text{'ph'}$  or  $\text{'incoh'}$ ) which is the ratio of the number of first-order interactions ( $N_{i,1}$ , the photon interaction for primary incident photons) and total number of initial X-ray photons ( $N_{\text{tot}}$ ) emitted, given by

$$p_{i,1} = \frac{N_{i,1}}{N_{\text{tot}}} \quad (4.25)$$

$p_{int}$  is the times of all interactions experienced by every single X-/ $\gamma$ - photon during its propagation, given by

$$p_{int} = \frac{N_{int}}{N_{tot}} \quad (4.26)$$

### **Characteristic K-X-ray emission $p_{KX}$ and reabsorption probability $p_{KX-ab}$**

The probability of K-X-ray emission for each photon incident on SD is given by

$$p_{KX} = \frac{N_{KX}}{N_{tot}} \quad (4.27)$$

where  $N_{KX}$  is the number of K-X-ray emission events. The parameter  $p_{KX-ab}$  represents the probability of characteristic K-X-rays being reabsorbed by photoelectric effect, which is the ratio of the number of K-X-ray photoelectric reabsorption events ( $N_{KX-ab}$ ) and total number of K-X-ray emission events ( $N_{KX}$ ), and is given by

$$p_{KX-ab} = \frac{N_{KX-ab}}{N_{KX}} \quad (4.28)$$

This parameter is simulated with respect to variable incident photon energy  $E_0$  which is larger than the K-shell binding energy ( $U_K = 50.03$  KeV) of the element gadolinium.

### **The location distribution probability of X-ray termination events**

Among all incident photons, only a small proportion of X-ray photons can interact and be absorbed by scintillator particles. By recording the location where the energy of incident history is totally absorbed, the penetration depth of the X-ray into the fibre core can be studied.

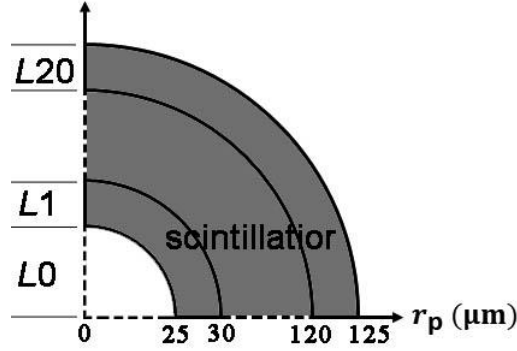


**Figure 4.8** The cross section of SD (Model 1) is divided into 21 layers:  $L0$ — $L20$ . The grey area (layer  $L1$ — $L20$ ) is the scintillator, while  $L0$  is the fibre core.

As shown in Figure 4.8, the cross section of SD is divided into 21 layers along the radial direction of the fibre. The inner layer  $L0$  represents the fibre core without scintillator embedding, and layers  $L1$ — $L20$  are SD. The outer radii of all layers are listed in table 4.2. The thickness of each layer from  $L1$  to  $L2$  is  $5 \mu\text{m}$ .

**Table 4.2** The radii of all layers along the fibre radius

Layer	$L0$	$L1$	$L2$	$L3$	$L4$	$L5$
Radius ( $\mu\text{m}$ )	0-25	25-30	30-35	35-40	40-45	45-50
Layer	$L6$	$L7$	$L8$	$L9$	$L10$	$L11$
Radius ( $\mu\text{m}$ )	50-55	55-60	60-65	65-70	70-75	75-80
Layer	$L12$	$L13$	$L14$	$L15$	$L16$	$L17$
Radius ( $\mu\text{m}$ )	80-85	85-90	90-95	95-100	100-105	105-110
Layer	$L18$	$L19$	$L20$			
Radius ( $\mu\text{m}$ )	110-115	115-120	120-125			

For each X-ray termination event (through photon interaction exclusively), the location of the event is recorded as  $\mathbf{r}_t = (x_t, y_t, z_t)$ . By calculating the radius of the  $\mathbf{r}_t$  ( $\mathbf{r} = \sqrt{x_t^2 + y_t^2}$ ), the number of X-ray termination events in each layer is counted. If the number of the event in the  $i$ th layer is  $N_{t,i}$ , the location distribution probability of X-ray termination event in the  $i$ th layer is then given by

$$p_{t,i} = \frac{N_{t,i}}{\sum_{j=1}^{20} N_{t,j}} \quad (4.29)$$

### The energy distribution coefficient of the scintillation light generation

The energy distribution coefficient of the scintillation light generation resembles the calculation of the location distribution of X-ray terminations, but this parameter records the energy of scintillation light with respect to the location. If the total energy of the scintillation light generated in the  $i$ th layer is  $E_{SC,i}$ , the energy distribution coefficient  $q_{SC,i}$  is then given by

$$q_{SC,i} = \frac{E_{SC,i}}{\sum_{j=1}^{20} E_{SC,j}} = \frac{E_{SC,i}}{E_{SC,tot}} \quad (4.30)$$

where  $E_{SC,tot}$  is the total energy of scintillation light generated in SD. Along with the parameter  $p_{t,i}$ , the effect of the X-ray penetration on the transmission efficiency of the scintillation light can be investigated, with respect to different incident photon energies.

### Scintillation efficiency $\eta_{sc}$

$\eta_{sc}$  is the ratio of the total energy of all scintillation light-rays ( $E_{SC,tot}$ ) and total energy of incident X-ray photons. If the energy of initial X-ray photon is  $E_0$ ,  $\eta_{sc}$  is then given by

$$\eta_{sc} = \frac{E_{SC,tot}}{E_{tot}} = \frac{E_{SC,tot}}{E_0 \cdot N_{tot}} \quad (4.31)$$

### Transmission efficiency $\eta_{trans}$

$\eta_{trans}$  is the ratio of the energy of the visible photons reaching the port and the energy of all scintillation light, and is given by

$$\eta_{\text{trans}} = \frac{E_{\text{SC,port}}}{E_{\text{SC,tot}}} \quad (4.32)$$

This parameter reveals the efficiency of the specific ISOFD model configuration for light transport, and also investigates the influence of light attenuation by adjacent SD in double SD system.

### **Detection efficiency $\eta_{\text{de}}$**

$\eta_{\text{de}}$  represents the detection efficiency of the ISOFD model, which is given by

$$\eta_{\text{de}} = \frac{E_{\text{SC,port}}}{E_{\text{tot}}} = \eta_{\text{sc}} \cdot \eta_{\text{trans}} \quad (4.33)$$

The expression of the detection efficiency shows that  $\eta_{\text{de}}$  depends on the scintillation efficiency  $\eta_{\text{sc}}$  and transmission efficiency  $\eta_{\text{trans}}$ , both of which change with respect to the incident photon energy and the configuration of the ISOFD model.  $\eta_{\text{de}}$  gives a general idea of how much energy of incident X-ray radiation can be detected by the ports and helps to determine the necessity of application of the photon multiplier to boost the light signal.

## **4.8 Summary**

In this chapter, the Monte-Carlo simulation method of the diagnostic X-ray energy detection with ISOFD models is proposed. This method is based on the integration of the MC simulation algorithms of photon interactions (given in chapter 3) and the light-ray tracing method. Firstly, the coordinate systems and vector rotation used for particle track simulation are presented. Afterwards, the properties of the materials and the configuration of the ISOFD model are described. The simulation codes are written in

Matlab. The simulation of diagnostic X-ray detection is comprised of two parts: the MC simulation of the X-ray photon propagation and interaction in the scintillation-domain, and MC ray-tracing simulation of light in ISOFDs. The details of the simulation process have been introduced from sections 4.4 to 4.6. The output parameters evaluate the energy absorption efficiency of X-rays and light transmission efficiency in ISOFDs. The results of the simulation of the ISOFD for X-ray will be given and discussed in the next chapter.

## **Chapter 5—Simulation of ISOFDs for diagnostic X-ray detection: results and analysis**

### **5.1 Introduction**

The simulations described in this chapter aim to optimise the design of the ISOFD and investigate the response of the scintillator to the X-ray radiation from aspects of the detailed photon interactions as well as the light ray transmission efficiency. The simulations were run under the condition that a single initial parameter was variable, while the other parameters remained constant. The simulations that investigate the effect of the mean particle size ( $r_p$ ), packing density ( $\eta_{pk}$ ) and incident photon energy ( $E_0$ ) are based on the model with a single SD (Model 1, see Figure 4.5 (a)), and the corresponding results are provided in sections 5.2 to 5.4. The response dependence on the embedding depth  $D_{em}$  was simulated using Model 1 and Model 2, and the related results and analysis are given in section 5.5. The dependence of the transmission efficiency  $\eta_{trans}$  on the position of the ports is discussed in section 5.6. The result of the simulation using Model 3 (a double scintillator domain ISOFD) is provided in section 5.7. The factors that can introduce simulation errors are discussed in section 5.8. The chapter is concluded in section 5.9.

### **5.2 The influence of the mean radius of the scintillator particles**

In the simulation of models featuring different sizes of scintillator ( $Gd_2O_2S$ ) particles, the mean particle size  $r_p$  varies from 1.5  $\mu m$  to 4  $\mu m$  with the step length of 0.5  $\mu m$ , while the other parameters remain constant. The parameters of the model configuration

has been described in Figure 4.5: the length of SD ( $l_{SD}$ ) is 100  $\mu\text{m}$ , the embedding size is  $D_{em} = 100 \mu\text{m}$ , the packing density is  $\eta_{pk} = 18.18\%$  and the initial energy of the incident X-ray photon is  $E_0 = 60 \text{ KeV}$ . In order to collect the light photons, two ports are set at a distance of 1000  $\mu\text{m}$  from the terminals of the scintillator domain along the fibre axis. The mean free path length of X-ray and light photon transport in the binding material of SD ( $l_{mean,ER}$ ), the primary interaction probability  $p_{int}$ , the scintillation efficiency  $\eta_{sc}$ , the transmission efficiency  $\eta_{trans}$  and the overall detection efficiency  $\eta_{de}$  were all established for use in the analysis of the results.

### 5.2.1 Result of the simulation with respect to different $r_p$

SD is comprised of two materials, namely, the scintillator particles ( $\text{Gd}_2\text{O}_2\text{S:RE}$ ) and the epoxy resin ( $ER$ ) which binding the particles. This sub-section discusses the influence of the mean particle size of the scintillator particle, so it is necessary to keep other parameter constant, especially the packing density  $\eta_{pk}$ . If the total volume of SD  $V_{SD}$ , the total weight of all scintillator particle  $M_0$ , and the density of the scintillator  $\rho$  are known, then the packing density  $\eta_{pk}$  can be expressed as  $(\frac{M_0}{\rho})/V_{SD}$ , which is totally independent of the mean particle size. As long as the total weight of all the scintillator particles in SD remain unchanged, the packing density of the scintillator in SD will also remain constant. Since the packing density remains constant, the mean free path  $l_{mean,ER}$  in the epoxy resin ( $ER$ ) is proportional to the mean radius of the scintillator particle as determined by Equation (4.16). As shown in Figure 5.1(a), when the particle radius  $r_p$  increases from 1.5  $\mu\text{m}$  to 4  $\mu\text{m}$ , the  $l_{mean,ER}$  grows from 11  $\mu\text{m}$  to 29.33  $\mu\text{m}$ . Hence, the proportional coefficient is  $l_{mean,ER}/r_p = 7.33$ .

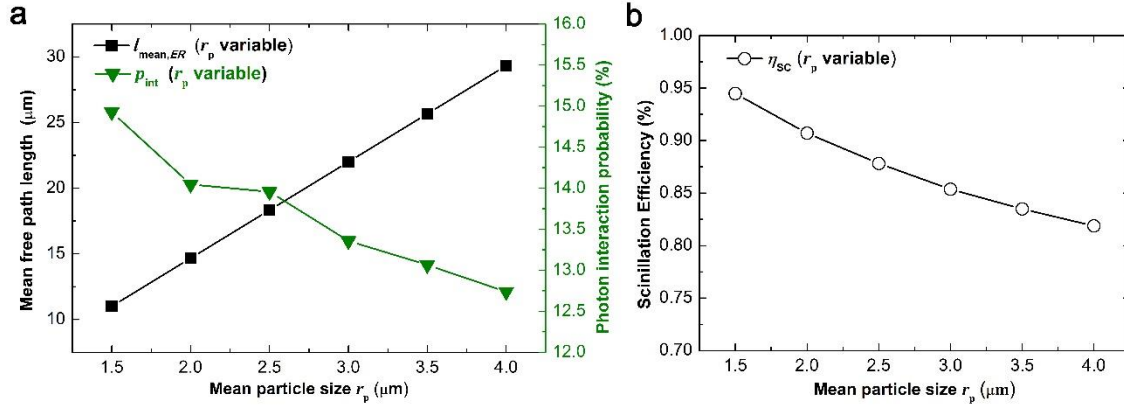


**Figure 5.1** The mean free path length  $l_{\text{mean,ER}}$  and the overall photon interaction probability  $p_{\text{int}}$  (a), and the overall scintillation efficiency  $\eta_{\text{sc}}$  (b) as simulated corresponding to different particle sizes from 1.5—4.0  $\mu\text{m}$ .

For a photon travelling in a limited space, the larger the mean free path length  $l_{\text{mean,ER}}$  is, the lower the probability of the X-ray photon colliding with the scintillator particles becomes. Thus, the overall photon interaction probability  $p_{\text{int}}$  exhibits a negative relationship with the  $r_p$ , and it decreases from 14.9% to 12.7%. The overall scintillation efficiency  $\eta_{\text{sc}}$  (the ratio of the energy of the scintillation light to all the incident energy), as shown in Figure 5.1(b), follows the same trend as that of the interaction probability  $p_{\text{int}}$ , and it decreases from 0.94% to 0.81%.

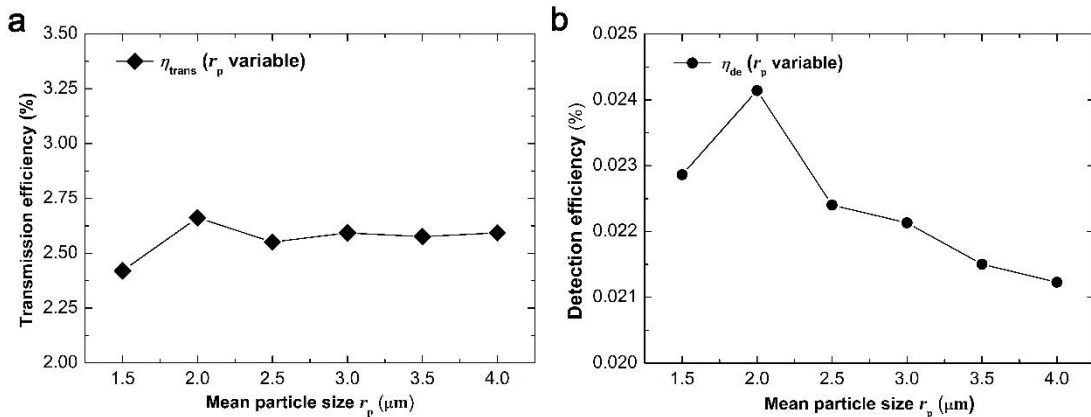


**Figure 5.2** The transmission efficiency  $\eta_{\text{trans}}$  (a), and the overall X-ray detection efficiency  $\eta_{\text{de}}$  as simulated with respect to different particle sizes (b)

After a light-ray has been generated inside a scintillator particle, the light-ray first transport out of the particle. Then, through a series of reflection and transmission at different interfaces (colliding with other particles or interfaces between SD and the optical fibre), the light-ray may either escape SD and enter the optical fibre or be lost (transmit through the outmost surface of SD) during the propagation. After multiple reflections or transmissions in the optical fibre, the light-ray may either transport out of the fibre or be collected by the ports some distance away. The transmission efficiency  $\eta_{\text{trans}}$  shown in Figure 5.2(a) measures the average percentage of the light-ray energy collected by the two ports (see Equation (4.31)). The result shows for various mean particle sizes, the transmission efficiency fluctuates around 2.6%. The maximum  $\eta_{\text{trans,max}} = 2.66\%$  is reached when the  $r_p = 2 \mu\text{m}$ , while the minimum  $\eta_{\text{trans,min}} = 2.47\%$  corresponds to  $r_p = 1.5 \mu\text{m}$ . The low transmission efficiency indicates that most of the light-rays have been lost during the transport process. More specifically, the simulation of the energy loss at the interfaces between different materials show that about 46% of all light-rays transmit out of SD through the outer surface.

Figure 5.2(b) shows that the maximum overall value of the X-ray detection efficiency is  $\eta_{\text{de}} = 0.0241\%$  when  $r_p = 2 \mu\text{m}$ , while the minimum value of  $\eta_{\text{de}}$  is  $0.0211\%$  ( $r_p = 3 \mu\text{m}$ ). Based on the relationship between the particle size and the overall efficiency,  $r_p = 2 \mu\text{m}$  is applied for the following discussion of the simulation.

### 5.2.2 Discussion regarding the effect of particle size on radiation sensitivity

Under the condition that all the models shared the same packing density ( $\eta_{\text{pk}} = 18.18\%$ ), by decreasing the mean particle size ( $r_p$ ), the mean free path  $l_{\text{mean,ER}}$

(between successive collisions with the scintillator particles) of a photon travelling in an *ER* binding material is reduced. The length  $l_{\text{mean},ER}$  as calculated with different values of  $r_p$  is in the interval 11~30  $\mu\text{m}$ . Due to the smaller  $l_{\text{mean},ER}$ , the probability of the X-ray photon interacting with the scintillator particles is enhanced, which contributes to the improved photon absorption and scintillation efficiency. However, the small particle size does not correspond to the high detection efficiency  $\eta_{de}$ , since the transmission efficiency of the smallest  $r_p$  is lower. Therefore, for the given packing density  $\eta_{pk} = 18.18\%$ , the value of  $r_p = 2 \mu\text{m}$  results in the highest detection efficiency, while the particle size in the simulation is afterwards set to  $2 \mu\text{m}$ . However, the highest transmission efficiency corresponding to  $r_p = 2 \mu\text{m}$  is still quite low. One possible reason may be due to relatively energy loss in SD. The simulation of the visible energy loss of all light-rays shows that about 46% of all light-ray energy are lost in SD, most of which through the transmission at the outmost surface of SD (cylinder).

### 5.3 Packing density $\eta_{pk}$ of SD

In addition to the particle size  $r_p$ , the packing density  $\eta_{pk}$  represents another factor that determines the mean free path length  $l_{\text{mean},ER}$ . While the other configuration sizes of the model remain unchanged, the variance of the  $l_{\text{mean},ER}$  affects the interaction probability between the incident photons and the scintillator, as described in the previous section. For the simulation discussed in this section, the packing density  $\eta_{pk}$  of SD varies as either 0.72%, 1%, 2%, 5.26%, 10%, 18.18% or 30.77%, while the other parameters remain constant so that the length of SD is 100  $\mu\text{m}$ , the embedding size is  $D_{em} = 100 \mu\text{m}$ , the particle size is  $r_p = 2 \mu\text{m}$  and the initial energy is  $E_0 = 60 \text{ KeV}$ .

The packing density  $\eta_{pk} = 0.72\%$  is as same as that of the ISOFD reported by Mccarthy et al[33], so that we can assess the radiation sensitivity of this reported ISOFD.

### 5.3.1 Result of the simulation with respect to different $\eta_{pk}$

Figure 5.3(a) shows the dependence of mean free path length  $l_{mean,ER}$  and photon interaction probability  $p_{int}$  on the packing density  $\eta_{pk}$ . Different from the mean particle size  $r_p$ , the  $l_{mean,ER}$  is inversely proportion to the packing density  $\eta_{pk}$ . The value of the  $l_{mean,ER}$  decreased from 371.90  $\mu\text{m}$  to 8.67  $\mu\text{m}$  while the  $\eta_{pk}$  increased from 0.72% to 30.77%. Considering the limited volume of SD, for the lowest packing density of  $\eta_{pk} = 0.72\%$ , there are only a few particles distributed in SD, thus the corresponding photon interaction probability is minimal ( $p_{int} = 5.16\%$ ). The maximum  $\eta_{pk,max} = 30.77\%$  corresponds to the minimum  $l_{mean,ER}$  and the maximum photon interaction probability  $p_{int,max} = 0.95\%$ . The identified relationship between the  $\eta_{pk}$  and the interaction probability indicates that a high packing density is desirable.

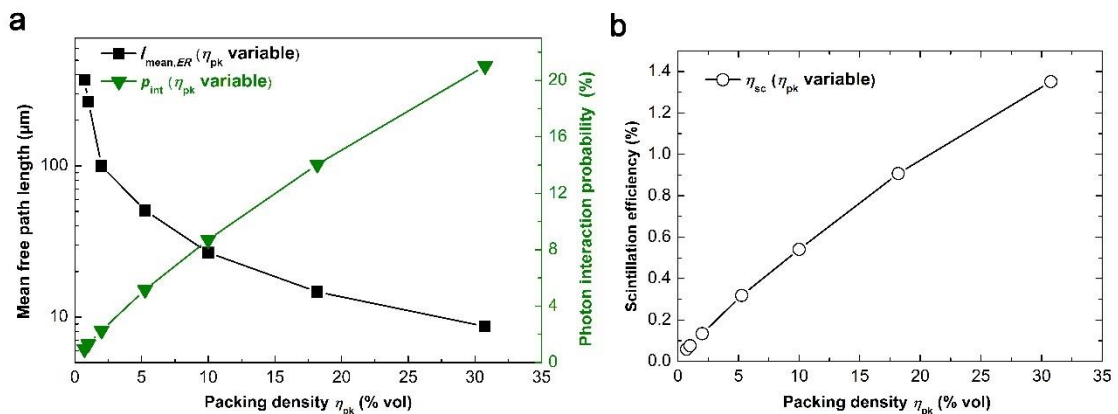


**Figure 5.3** The mean free path length  $l_{mean,ER}$  and the overall photon interaction probability  $p_{int}$  (a), and the scintillation efficiency  $\eta_{sc}$  (b) as simulated

corresponding to different packing density from 0.7%—30% vol.

The packing density  $\eta_{pk}$  clearly contributes to the probability of photon interaction  $p_{int}$ . While the intrinsic energy conversion efficiency of the scintillator ( $\eta_C$ )\* remains constant during the simulation, the scintillation efficiency  $\eta_{sc}$  increases in accordance with the energy absorbed via the photon interactions. As shown in Figure 5.3 (b), the lowest  $\eta_{sc}$  (when  $\eta_{pk} = 0.72\%$ ) is 0.059%, while the highest  $\eta_{sc}$  (when  $\eta_{pk} = 30.77\%$ ) is 1.351%.

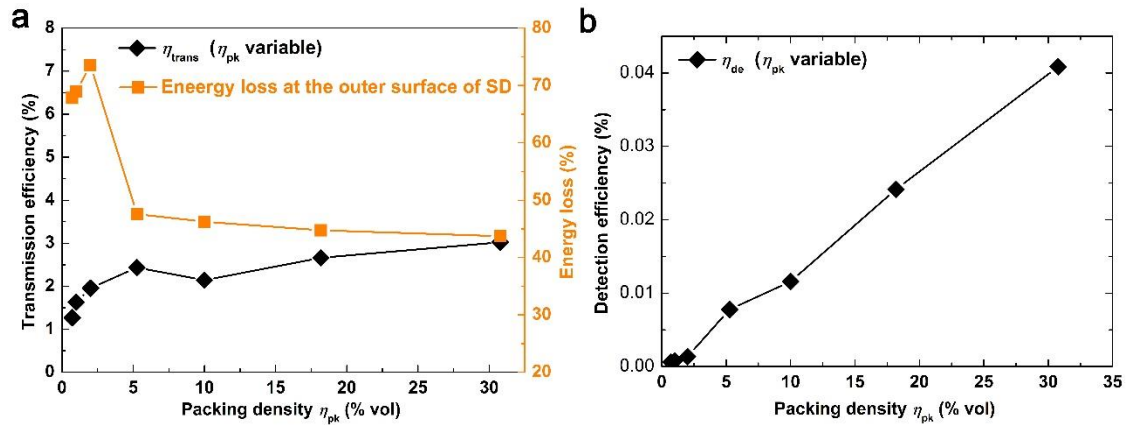


**Figure 5.4** The transmission efficiency  $\eta_{trans}$  and the energy loss at the outer surface of SD (a), and the overall X-ray detection efficiency  $\eta_{de}$  (b) as simulated using models (based on Model 1) of different SD packing densities.

As shown in Figure 5.4(a), the transmission efficiency gradually is increased from 1.27% to 3.022%. The highest packing density of 30.77% produced the highest transmission efficiency. The simulation of energy loss shows that, the energy lost at the outer surface of SD is as high as  $\sim 70\%$  for  $\eta_{pk} = 0.72\%$ , 1% and 2% vol, but decrease

\* The intrinsic energy conversion efficiency measures the ratio of the integrated luminescent energy and the total absorbed energy.

to  $\sim 45\%$  when  $\eta_{pk}$  is higher than 5% vol. This may be due to the increased probability of the multiple reflection by the scintillator particles near the outer surface of SD, less light rays can transmit out of SD through the outer surface. Figure 5.4(b) shows that the detection efficiency  $\eta_{de}$  rises as the  $\eta_{pk}$  increases. The lowest  $\eta_{de}$  corresponding to the smallest  $\eta_{pk} = 0.72\%$  is  $5.90E-4$ , while the highest  $\eta_{de} = 0.04\%$  corresponds to a very high packing density of 30.77%.

### 5.3.2 Discussion regarding the effect of the packing density $\eta_{pk}$

The effect of the packing density on the overall X-ray detection capability of the ISOFD is clear. According to Equation (4.16), the  $l_{mean,ER}$  is inversely proportional to the  $\eta_{pk}$ . Thus, the higher the density, the smaller the mean free path  $l_{mean,ER}$  becomes, which further contributes to the higher interaction probability. The interaction probability  $p_{int}$  and the scintillation efficiency  $\eta_{sc}$  of the maximum packing density of  $\eta_{pk,max} = 30.77\%$  are, respectively, approximately 21.1 and 21.9 times higher than those simulated with the minimum packing density of  $\eta_{pk,min} = 5.263\%$ .

The transmission efficiency, is relatively low for  $\eta_{pk} = 0.72\%$ , 1% and 2% vol, and is enlarged by the larger packing density. One possible reason, as it been analysed in previous section, is the enhanced multiple reflection by scintillator particles near the outer surface of SD corresponding to higher packing density  $\eta_{pk}$ .

All experiment results indicate that the high value of  $\eta_{pk}$  favours the X-ray detection. In terms of the practical ISOFD sensor fabrication, however, achieving a packing density that is as high as that of an X-ray phosphor screen is still questionable due to the limits of the fabrication techniques currently available for ISOFDs. The X-

ray phosphor screens or films fabricated with sintering, sedimentation, or so-gel methods[132]–[136] have high packing density, usually more than 50%. The fabrication of ISOFD, on the other hand, uses epoxy resin as the binder and adhesive to glue scintillator powders together on a specific surface of a modified optical fibre. The packing density is determined by the size of scintillator particles, the density and the viscosity of the resin, the compatibility between the scintillator and the resin, etc., which need more research effort. The high packing density is currently unlikely to require. Therefore, in the simulations discussed in other sections in this chapter, the packing density is set as 18.18% for the theoretical calculation of the  $l_{\text{mean,ER}}$ .

#### **5.4 Response to incident photons of different initial energies 10~80 KeV**

The response of an inorganic scintillator-based dosimeter to X-ray radiation is theoretically energy dependent due to the cross-sections of the dominant photon interactions for different energies. In order to study the energy dependent correspondence of the ISOFD, the model is simulated under different energies in the interval 10~80 KeV. The step length is 10 KeV, while a particular value ( $E_0 = 51$  KeV) near the K-edge (50.24 KeV) of the Gd element is also added. The other parameters remain constant so that the length of SD is 100  $\mu\text{m}$ , the embedding size is  $D_{\text{em}} = 100$   $\mu\text{m}$ , the mean particle size is  $r_p = 2$   $\mu\text{m}$ , the packing density is  $\eta_{\text{pk}} = 18.18\%$  and the distance from the port to the terminal of SD is 1000  $\mu\text{m}$ .

### 5.4.1 Simulation result with respect to different initial photon energies

The interaction probability and the scintillation efficiency of the X-ray photons in the energy interval 10~80 KeV are shown in Figure 5.5. The average probability of the primary interaction for each photon decreases as the initial photon energy increases. The largest interaction probability  $p_{\text{int,max}}$  and scintillation efficiency  $\eta_{\text{sc,max}}$  are 85.21% and 11.87%, respectively, which corresponds to the smallest initial incident energy of 10 KeV. The lowest  $p_{\text{int,min}}$  and  $\eta_{\text{sc,min}}$  are 7.10% and 0.58%, respectively, which corresponds to the largest initial energy of  $E_0 = 80$  KeV. Sudden increases in the  $p_{\text{int}}$  and  $\eta_{\text{sc}}$  can be observed near the K-edge, where the  $p_{\text{int}}$  ( $E_0 = 51$  KeV) rose to 20.76% and the  $\eta_{\text{sc}}$  ( $E_0 = 51$  KeV) rose to 1.05%. The  $p_{\text{int}}$  ( $E_0 = 51$  KeV) is 322.4% higher than that seen at  $E_0 = 50$  KeV, although the  $\eta_{\text{sc}}$  at  $E_0 = 51$  KeV is only 69.4% higher than that seen at  $E_0 = 50$  KeV. This inconstant change in the overall scintillation efficiency will be discussed later.

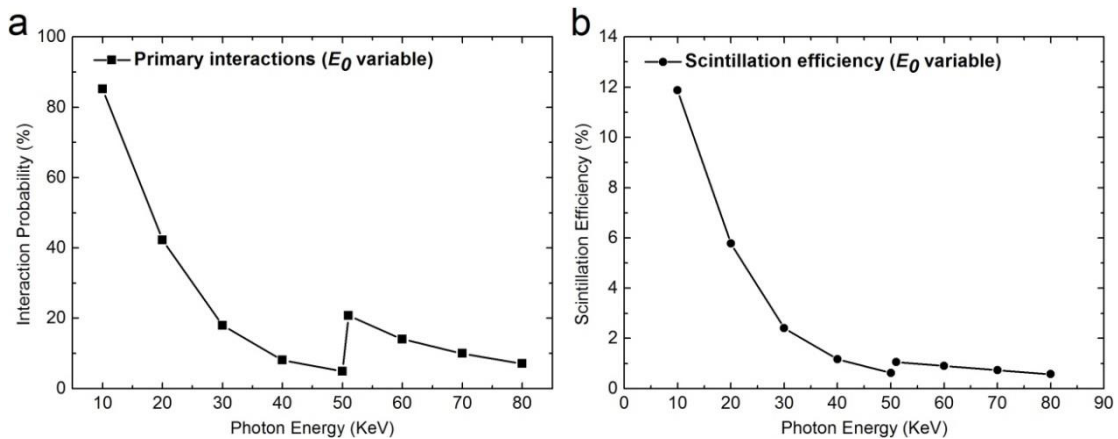


**Figure 5.5** (a) The primary interaction probability  $p_{\text{int}}$  and (b) the overall scintillation efficiency  $\eta_{\text{sc}}$  under incident X-ray radiation of initial energies in the interval 10~80 KeV

The probabilities of first-order photoelectric absorption ( $p_{\text{ph},1}$ ) and first-order incoherent scattering ( $p_{\text{incoh},1}$ ) as well as the K-X-ray emission probability ( $p_{\text{KX}}$ ) and the K-X-ray reabsorption probability ( $p_{\text{KX-ab}}$ ) are presented in Table 5.1 for some of the photon energies. The corresponding total photon attenuation coefficients  $(\mu/\rho)_{\text{tot}}$  of  $\text{Gd}_2\text{O}_2\text{S}$  required from XCOM database[118] have also been listed in Table 5.1. These statistical data show that the probabilities of the first-order photon interactions are consistent with the photon partial mass interaction coefficients of the  $\text{Gd}_2\text{O}_2\text{S}$ . Photoelectric absorption is the dominant photon interaction type for the diagnostic X-rays attenuated by the scintillator particles. The photons with an initial energy lower than the K-shell binding energy of Gd, that is,  $E_0 < U_{\text{K}} \equiv 50.24 \text{ KeV}$ , cannot generate the characteristic K-X-rays. The probability of K-X-ray emission for each X-ray photon incident on SD  $p_{\text{KX}}$  is determined by the first-order interaction probability  $p_{\text{ph},1}$  and the K-fluorescent yield  $\omega_{\text{K}}$ . In this study, the  $\omega_{\text{K}}$  is assumed to be constant; thus, the  $p_{\text{KX}}$  changes in accordance with the  $p_{\text{ph},1}$ . The reabsorption probability of K-X-ray emission  $p_{\text{KX-ab}}$ , as shown in Table 5.1, is as low as 2.64~3.22%. Two factors limit the reabsorption of K-X-rays. The first is the fact that the photon energy of the K-X-ray is in the energy interval 42.29~50.21 KeV (below the K-edge of Gd element), while the corresponding mass partial attenuation coefficient of photoelectric absorption for the  $\text{Gd}_2\text{O}_2\text{S}$  is small. The other key factor is the low probability of the K-X-ray colliding with the scintillator particles. As the scintillation site is located deep towards the fibre axis inside SD, the average number of scintillator particles distributed in the straight path of the K-X-ray is smaller than that of the initial incident photons. Thus, the  $p_{\text{KX-ab}}$

is lower than the  $p_{\text{ph},1}$  for an initial photon energy of 60 KeV. The relatively high K-X-ray emission probability and the low K-X-ray reabsorption probability lead to considerable energy loss, which is why the probability contrast between  $\eta_{\text{sc}}(E_0 = 50 \text{ KeV})$  and  $\eta_{\text{sc}}(E_0 = 51 \text{ KeV})$  is smaller than the probability contrast between  $p_{\text{int}}(E_0 = 50 \text{ KeV})$  and  $p_{\text{int}}(E_0 = 51 \text{ KeV})$ , as shown in Figure 5.5.

**Table 5.1** The photon attenuation coefficient  $\left(\frac{\mu}{\rho}\right)_{\text{tot}}$  and interaction probabilities ( $p_{\text{ph},1}$ ,  $p_{\text{incoh},1}$ ,  $p_{\text{KX}}$ , and  $p_{\text{ph,KX}}$ ) with respect to various incident photon energies.

	10 KeV	20 KeV	50 KeV	51 KeV	60 KeV	70 KeV	80 KeV
$\left(\frac{\mu}{\rho}\right)_{\text{tot}} \text{ cm}^2 \cdot \text{g}$	228.5	36.87	3.274	14.95	9.814	6.591	4.666
$p_{\text{ph},1}$	84.03%	40.81%	4.91%	20.26%	14.03%	9.60%	6.23%
$p_{\text{incoh},1}$	1.18%	1.554%	~0	0.50%	0.35%	0.32%	0.01%
$p_{\text{KX}}$				15.56%	10.80%	7.36%	5.30%
$p_{\text{ph,KX}}$				3.22%	3.21%	2.93%	2.64%

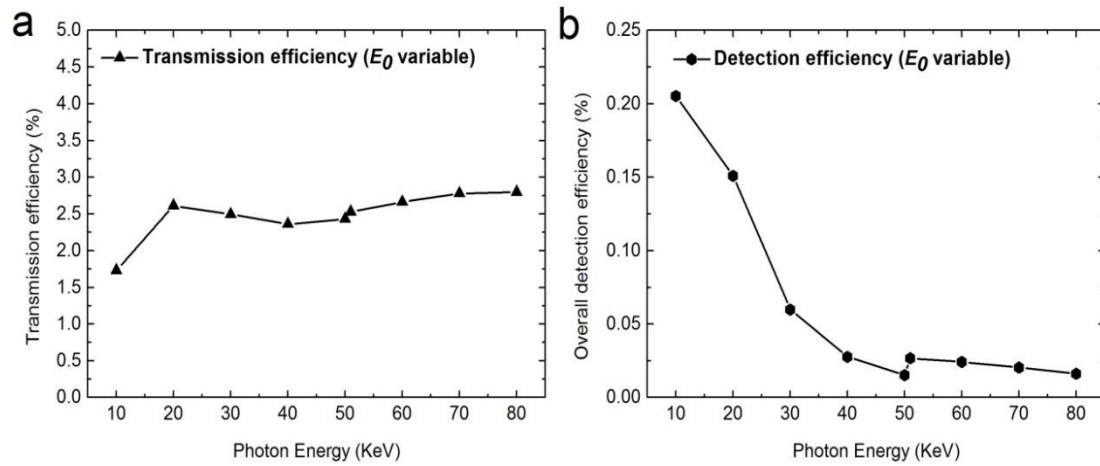


**Figure 5.6** (a) The transmission efficiency  $\eta_{\text{trans}}$  and (b) the overall X-ray detection efficiency as simulated under radiation in the energy interval 10—80 KeV

For the different initial incident photon energies, the transmission efficiency  $\eta_{\text{trans}}$  shown in Figure 5.6(a) fluctuates around 2.58% (average value of  $\eta_{\text{trans}}$  for the energy

interval 20–80 KeV). However, the  $\eta_{\text{trans}} = 1.763\%$  for the incident photon energy  $E_0 = 10$  KeV deviates from this average value. In terms of the overall detection efficiency in the energy range of interest (Figure 5.6(b)), the model is most sensitive to the lowest energy at 10 KeV with the highest  $\eta_{\text{de,max}} = 0.2053\%$ , while the lowest  $\eta_{\text{de,min}} = 0.0162\%$  corresponds to the largest initial energy of 80 KeV. Although the  $\eta_{\text{de}}$  is affected by both the scintillation and transmission efficiencies, the scintillation efficiency dominates in this case and an incident photon with a higher scintillation efficiency  $\eta_{\text{sc}}$  normally exhibits a higher overall detection efficiency  $\eta_{\text{de}}$ .

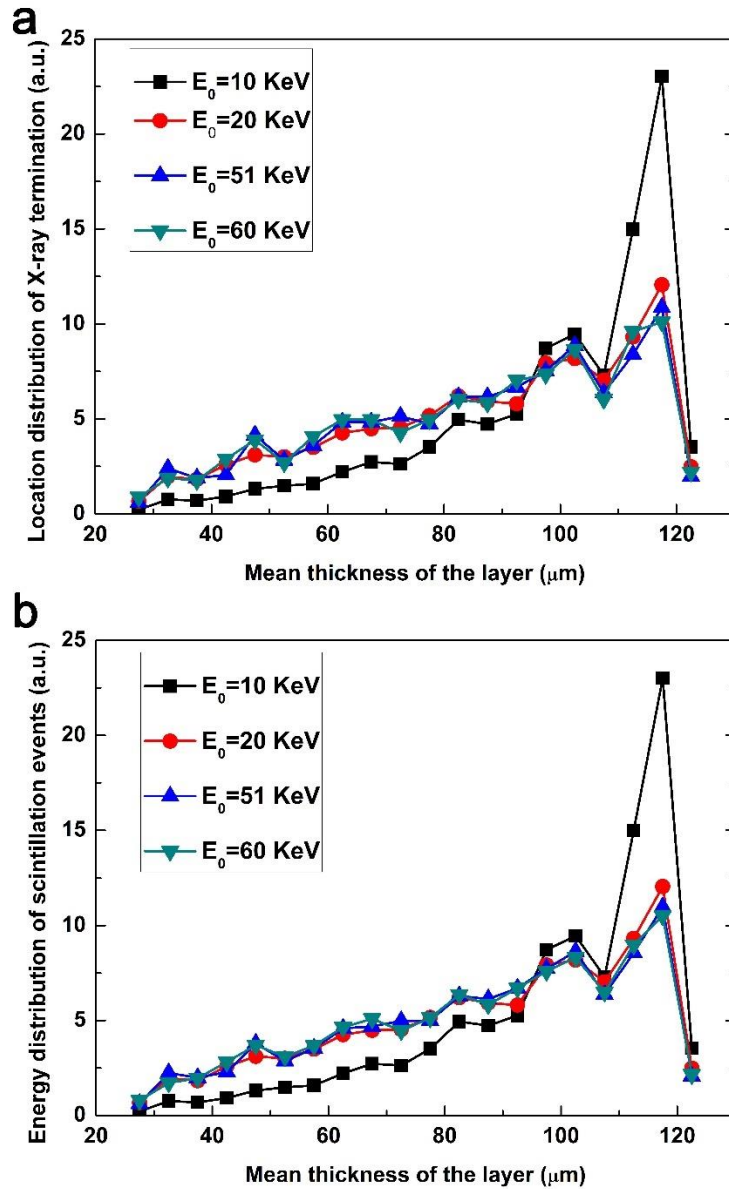


**Figure 5.7** (a) The normalised distribution probability of X-ray track termination locations under X-ray radiation of 10 KeV, 20 KeV, 51 KeV and 60 KeV, and (b) the normalised distribution probability of light generation locations along the radial direction of SD.

In terms of the smaller transmission efficiency seen under the initial photon radiation of  $E_0 = 10$  KeV, a simple simulation was run to investigate the location distribution of the X-ray track termination and the light photon generation in SD. These

distribution probabilities help to reveal the penetration of the X-rays into the fibre core as well as the effect of light generation on the light transmission efficiency.

The probability distribution of the X-ray termination events and the energy distribution of light generation were investigated under four different incident photon energies, namely 10 KeV , 20 KeV, 51 KeV and 60 KeV. The simulation of the probability distribution of the X-ray track termination locations (Figure 5.7(a)) shows that under X-ray, the main peak is in layer *L19* (mean thickness is 117.5  $\mu\text{m}$ ), while there is a side peak in layer *L18* (mean thickness of 112.5  $\mu\text{m}$ ), which indicates that a considerable number of X-rays were absorbed by the scintillator particles distributed in the radius 110~120  $\mu\text{m}$ . However, approximately 38.0% of the X-ray photons were totally absorbed in layers *L19* and *L20* (thickness between 115 and 125  $\mu\text{m}$ ) for the incident photon energy  $E_0 = 10$  KeV, with this value being much higher than that seen for the other photon energies. Yet, for the lower energy of  $E_0 = 10$  KeV , the probability of the initial X-ray energy being totally absorbed by the scintillator in the inner layers *L1~L8* (thickness 30—65  $\mu\text{m}$ ) is 9.18%, which is smaller than the probability seen under radiation with higher energies (for example, the value corresponding to  $E_0 = 60$  KeV is 22.51%). The energy distribution of the scintillation light generation is consistent with the location distribution of the X-ray termination events, as shown in Figure 5.7(b). The proportion of the scintillation light generated in the layers with a radius smaller than the outer cladding surface (i.e. smaller than 62  $\mu\text{m}$ ) with respect to the initial photon energy of  $E_0 = 10$  KeV is also smaller than that related to the initial energy of 60 KeV.

### 5.4.2 Discussion regarding the simulation results for variable initial energies

The simulation of Model 1 under different initial X-ray energies proves the radiation sensitivity's dependence on the incident photon energy. Generally, the overall scintillation efficiency  $\eta_{sc}$  of a photon with relatively low energy is higher, owing to the relationship between the mass attenuation coefficient of the scintillator and the photon energy. The abrupt increase in the photon interaction probability seen at 51 KeV is caused by the sudden increase in the photoelectric absorption coefficient at the K-edge of the gadolinium element.

On the other hand, for the incident photons with initial energies in the range where  $(\mu/\rho)_{tot}$  of the scintillator are higher, the energy is deposited at a site closer to the incident interface of SD. In terms of the transmission efficiency, the light photons generated in the inner layers close to the fibre axis have a greater probability of reaching the ports via travelling through the optical fibre. For incident X-ray photon corresponding to higher  $(\mu/\rho)_{tot}$ , the light photons resulting from radioluminescence may generated in the location near the outer surface of SD and have a greater chance of escaping SD and the optical fibre, which is a possible reason for the low  $\eta_{trans}$  of the initial photon energy  $E_0=10$  KeV. Although the overall detection efficiency  $\eta_{de}$  is the product of the scintillation efficiency and the transmission efficiency, the scintillation efficiency remains the dominant factor, and the  $\eta_{de}$  changes in accordance with the total attenuation coefficient of the incident X-rays.

### 5.5 The simulation of models of different scintillator embedding depths $D_{em}$

The embedding depth  $D_{em}$ , as shown in Figure 5.9, measures the thickness of SD that is embedded within the optical fibre. In order to study the influence of the  $D_{em}$ , the other parameters remain constant so that the length of SD is 100  $\mu\text{m}$ , the mean particle size is  $r_p = 2 \mu\text{m}$ , the packing density is  $\eta_{pk} = 18.18\%$  and the distance from the port to the terminal of SD is 1000  $\mu\text{m}$ . The depth  $D_{em}$  values under discussion are 100  $\mu\text{m}$ , 110  $\mu\text{m}$ , 120  $\mu\text{m}$  and 125  $\mu\text{m}$ . The depth of  $D_{em} = 100 \mu\text{m}$  corresponds to Model 1 (see Figure 4.5), while the other values of the  $D_{em}$  correspond to Model 2.

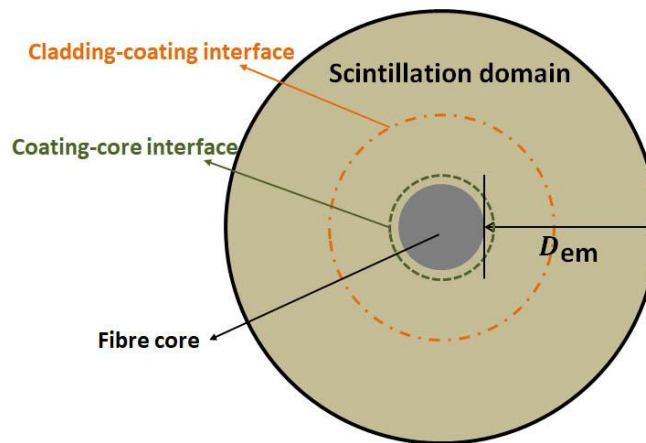


**Figure 5. 8** The schematic showing the cross section of the scintillation domain, and a relative size of  $D_{em}$  with reference to the position of interfaces between different parts of the optical fibre.

#### 5.5.1 Simulation result of models with different scintillator embedding depths

As it shown in Figure 5.9, it can be predicted that increasing the embedding depth  $D_{em}$  can contribute to the detection of X-ray from two aspects as it shown. The first one is that due to the larger  $D_{em}$ , the area of the cross section of SD is also enhanced. The the average path length of the X-ray photon travelling inside SD is getting longer and the

probability of the photon absorption by colliding with scintillator particles is enhanced, therefore contributing to the energy absorption of X-rays. The second one is that as the inner surface of SD is getting closer to the fibre axis by increasing  $D_{em}$ , as a result, the area of the interface (cross section only) between SD and fibre core also grows. The probability of the scintillation light transport in the fibre core after escaping SD may also be increased, and furtherly enhance the transmission efficiency.

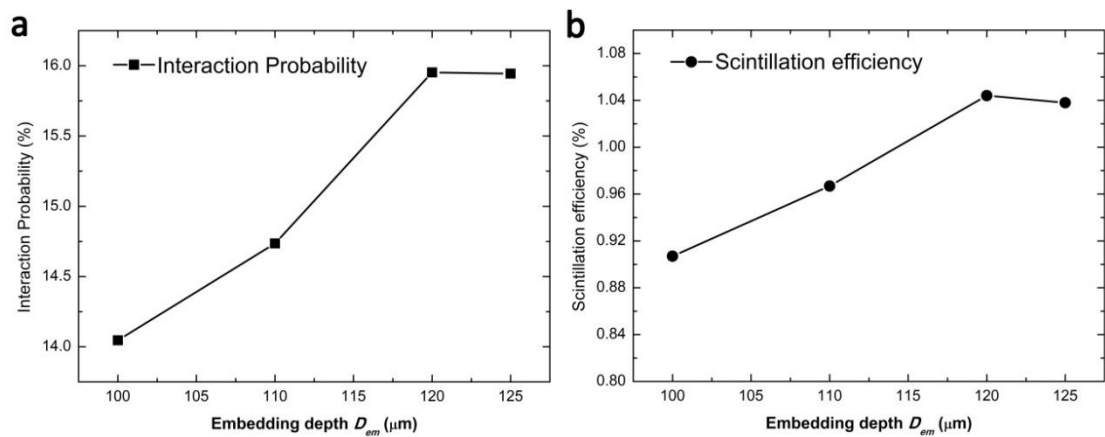


**Figure 5.9** (a) The interaction probability and (b) the scintillation efficiency of an ISOFD with different embedding depths: 100  $\mu\text{m}$ , 110  $\mu\text{m}$ , 120  $\mu\text{m}$ , and 125  $\mu\text{m}$

The interaction probability and the scintillation efficiency of the X-ray incident on an ISOFD with different embedding depths are shown in Figure 5.9. As the  $D_{em}$  increases from 100  $\mu\text{m}$  to 125  $\mu\text{m}$ , the interaction probability first rises from 14.05% ( $D_{em} \geq 120 \mu\text{m}$ ) to 15.95%, and it then remains constant for  $D_{em} \geq 120 \mu\text{m}$ . The scintillation efficiency also increases to the maximum ( $p_{int,max} = 1.044\%$ ,  $D_{em} = 120 \mu\text{m}$ ) as the inner surface of SD is embedded deeper towards the fibre axis within the fibre core (i.e. the thickness of SD is increased), before it decreases slightly

to 1.038%. In short, increasing the embedding depth contributes to the X-ray absorption of SD, just as it predicted in the last paragraph.

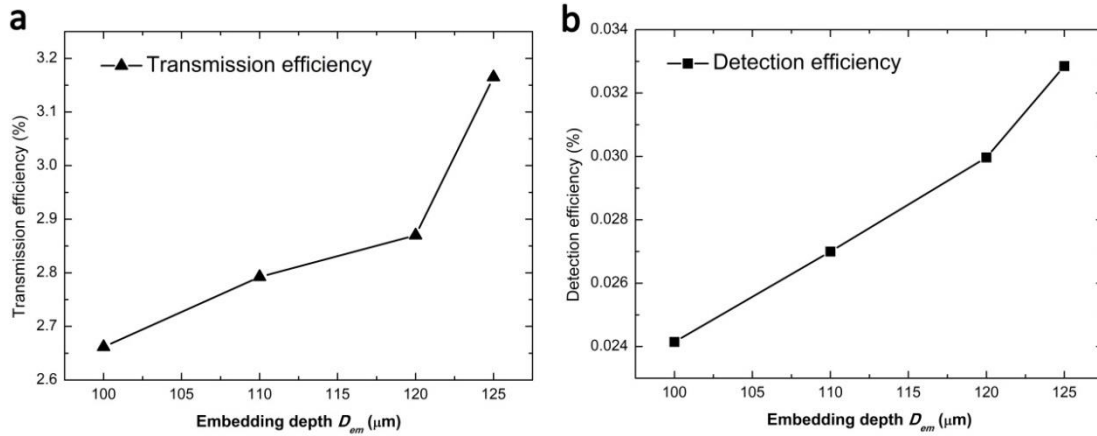


**Figure 5.10** The transmission efficiency (a) and the detection efficiency of an ISOFD with different SD embedding depths (b)

The transmission efficiency  $\eta_{\text{trans}}$  of the ISOFD is enhanced by the increasing depth  $D_{\text{em}}$ . As shown in Figure 5.9(a), for the ISOFD model of the minimum  $D_{\text{em}}$  (Model 1), the transmission efficiency  $\eta_{\text{trans}}$  is 2.6617%. When SD is embedded more deeply (Model 2), the  $\eta_{\text{trans}}$  is increased with respect to the  $D_{\text{em}}$ , and the maximum value is  $\eta_{\text{trans,max}} = 3.165\%$  when the depth is  $D_{\text{em,max}} = 125 \mu\text{m}$ . It should be noted that the maximum embedding depth corresponds to the model wherein the fibre core is completely removed, and that small piece of fibre is replaced by SD. The overall detection efficiency  $\eta_{\text{de}}$ , as shown in Figure 5.9(b), also exhibits a positive relationship with the  $D_{\text{em}}$ , which is consistent with the relationships  $\eta_{\text{sc}} - D_{\text{em}}$  and  $\eta_{\text{trans}} - D_{\text{em}}$ . The minimum detection efficiency  $\eta_{\text{de,min}}$  equals 0.0241% when the  $D_{\text{em}} = 100 \mu\text{m}$ , while the  $\eta_{\text{de,max}}$  equals 0.0329% when the  $D_{\text{em}} = 125 \mu\text{m}$ . After increasing the

embedding depth by 25  $\mu\text{m}$ , the  $\eta_{\text{de}}(E_0 = 125 \mu\text{m})$  can be seen to be approximately 35.5% times higher than the  $\eta_{\text{de}}(E_0 = 100 \mu\text{m})$ .

### 5.5.2 Discussion of models with different embedding depth

By increasing the embedding depth  $D_{\text{em}}$  of SD within the optical fibre, the overall detection performance of the sensor is enhanced. This positive effect on the photon interaction probability is the result of the larger cross-section areas of SD. The initial energy of the incident X-ray photons is set as 60 KeV (larger than K-edge of the Gd); thus, the larger cross-section area not only contributes to the photoelectric absorption of the primary photons, but also enhances the re-absorption of the K-X-rays. For example, when the depth  $D_{\text{em}}$  is increased from 100  $\mu\text{m}$  to 110  $\mu\text{m}$ , the cross-section area of SD ( $S_{\text{SD}}$ ) is increased by 540  $\mu\text{m}^2$ , which is approximately 2.67% times the  $S_{\text{SD}} = 15000 \mu\text{m}^2$  for 100  $\mu\text{m}$   $D_{\text{em}}$ . The probability of first-order photoelectric absorption is increased from 14.0% to 15.0%, while the probability of K-X-ray absorption is increased from 2.68% to 3.12%. As for the transmission efficiency, more scintillation light rays are generated in locations near the fibre axis as the  $D_{\text{em}}$  increases; hence, it contributes to the effective transmission of the light ray in the optical fibre. In addition to a high scintillator packing density, increasing the embedding depth  $D_{\text{em}}$  is seen to be another effective means of enhancing the overall X-ray detection efficiency  $\eta_{\text{de}}$ , owing to the positive influence it exerts on the scintillation efficiency and the transmission efficiency.

## 5.6 The effect of the location of the port

The energy loss that occurs during the process of the scintillation light reaching the ports can be classified into two types. One is the energy lost during the process whereby the light travels out of SD (which resembles the 'extraction efficiency' of LED devices), while the other is the energy lost when the light propagates in the optical fibre. In the simulation, two ports for light photon collection are set at a certain distance from the terminals of SD (TSDs, i.e. the terminals of the scintillation domain). The distance between the port and SD terminal ( $l_{\text{port-TSD}}$ ) affects the second type of energy loss. The light rays that travel out of SD and propagate into the optical fibre may exhibit a transmission direction beyond the numerical value of the optical fibre, while a portion of light rays entering the fibre cladding layer or fibre coating will suffer energy loss due to the transmission at the core-cladding interface and cladding-coating interface. In view of this type of transmission energy loss, the port is set at different distances ( $l_{\text{port-TSD}}$ ) from the TSD in order to study the effect of the position of the port on the transmission efficiency. Five values of  $l_{\text{port-TSD}}$  are (500  $\mu\text{m}$ , 1000  $\mu\text{m}$ , 2000  $\mu\text{m}$ , 4000  $\mu\text{m}$ , 6000  $\mu\text{m}$  and 10000  $\mu\text{m}$ ) selected, while the other parameters remain constant so that the length of SD is 100  $\mu\text{m}$ , the mean particles size is  $r_p = 2 \mu\text{m}$ , the scintillator packing density is  $\eta_{\text{pk}} = 18.18\%$  and the embedding depth  $D_{\text{em}} = 100 \mu\text{m}$ .

### 5.6.1 Simulation result of models with different locations of the port

The simulation of models (Model 1based) with different  $l_{\text{port-TSD}}$  values first compares the photon interaction probability  $p_{\text{int}}$  and scintillation efficiency  $\eta_{\text{sc}}$  to

confirm that the light generation in of all these models are almost the same, so that the effect of the scintillation process can be removed from the result analysis.

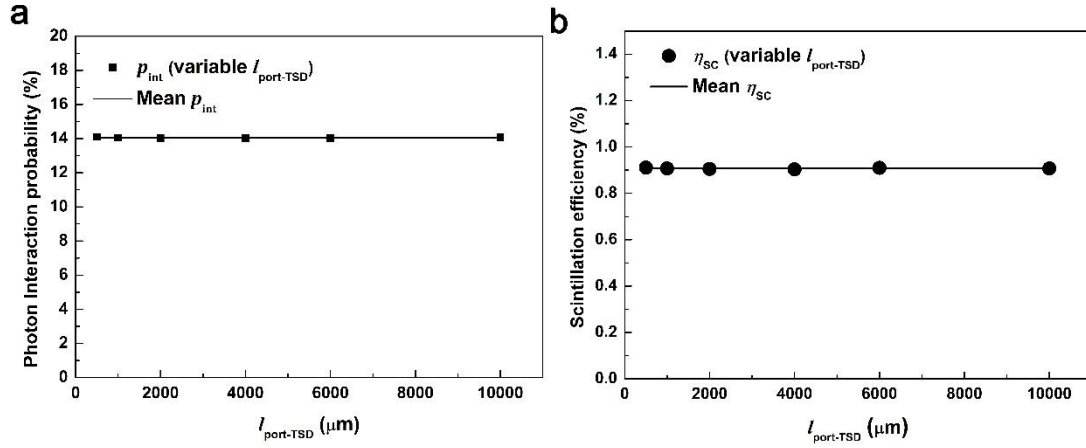


**Figure 5.11** The photon interaction probability  $p_{\text{int}}$  (a), and the overall scintillation efficiency  $\eta_{\text{sc}}$  of Model 1 (b) for different values of port-TSD distance  $l_{\text{port-TSD}}$ .

For models with different  $l_{\text{port-TSD}}$ , the interaction probability and the scintillation efficiency are simulated in order to ensure that both parameters are the same for all the simulations. As shown in Figure 5.11(a), the average value of the  $p_{\text{int}}$  simulated is 14.04%, while the standard error of the  $p_{\text{int}}$  is  $1.35\text{E-}4$ . The average value of the  $\eta_{\text{sc}}$  (as shown in Figure 5.11(b)) is 0.907%, while the corresponding standard error is  $1.15\text{E-}5$ . The small standard errors of the  $p_{\text{int}}$  and  $\eta_{\text{sc}}$  indicate that changing the value of the  $l_{\text{port-TSD}}$  will not affect the interaction probability or the scintillation efficiency.

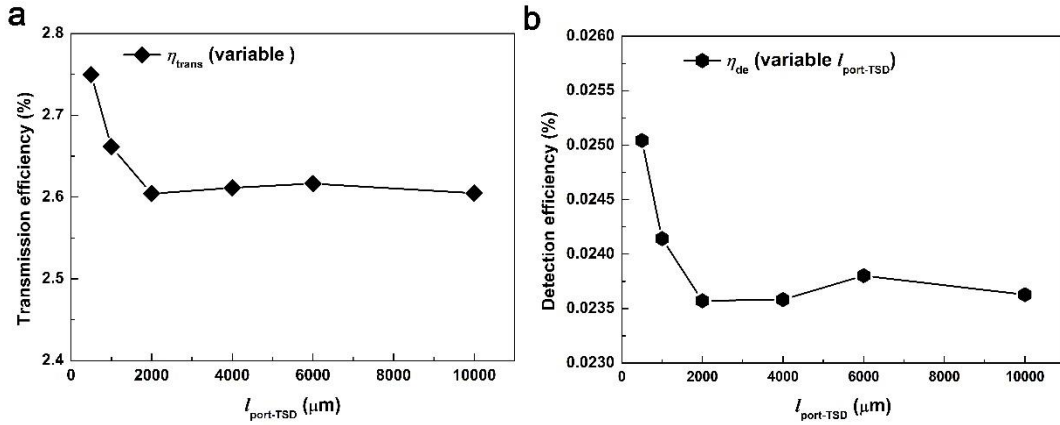


**Figure 5.12** (a) The transmission efficiency  $\eta_{\text{trans}}$  and (b) the overall detection efficiency  $\eta_{\text{de}}$  of Model 1 for different port-TSD distances  $l_{\text{port-TSD}}$

The transmission efficiency  $\eta_{\text{trans}}$  simulated with an  $l_{\text{port-TSD}}$  ranging from 500  $\mu\text{m}$  to 10000  $\mu\text{m}$  (Figure 5.12(a)) shows that the model of the shortest  $l_{\text{port-TSD},\text{min}}$  possesses the highest transmission efficiency  $\eta_{\text{trans},\text{max}} = 2.75\%$ . For an  $l_{\text{port-TSD}}$  larger than 2000  $\mu\text{m}$ , the  $\eta_{\text{trans}}$  fluctuates around the average value  $\overline{\eta_{\text{trans}}} = 2.61\%$  (the standard error is  $2.92 \text{ E-}5$ ). However, the  $\eta_{\text{trans},\text{max}}$  is only approximately 0.14% higher than the  $\overline{\eta_{\text{trans}}}$  (for  $l_{\text{port-TSD}} > 2000 \mu\text{m}$ ), which indicates that the energy loss is almost negligible if the  $l_{\text{port-TSD}}$  is further increased when the  $l_{\text{port-TSD}} > 2000 \mu\text{m}$ . As the scintillation efficiency remains unchanged, the detection efficiency  $\eta_{\text{de}}$  changes in accordance with the  $\eta_{\text{trans}}$ . The maximum value  $\eta_{\text{de},\text{max}}$  is 0.0250% for a  $l_{\text{port-TSD}} = 500 \mu\text{m}$ , while the average value of the  $\overline{\eta_{\text{de}}} = 0.0236\%$ . The difference between the  $\eta_{\text{de},\text{max}}$  and the  $\overline{\eta_{\text{de}}}$  is  $1.4\text{E} - 4$ .

### 5.6.2 Discussion regarding the effect of the port location

The results show that when the port is placed near SD, more light rays can be detected, but when the port is set far enough away, the transmission efficiency remains stable.

As the light ray tracing in the model utilised Fresnel's equation, the reason for this behaviour in terms of the  $\eta_{\text{trans}}$  change is explored by studying the reflection and refraction at the interfaces.

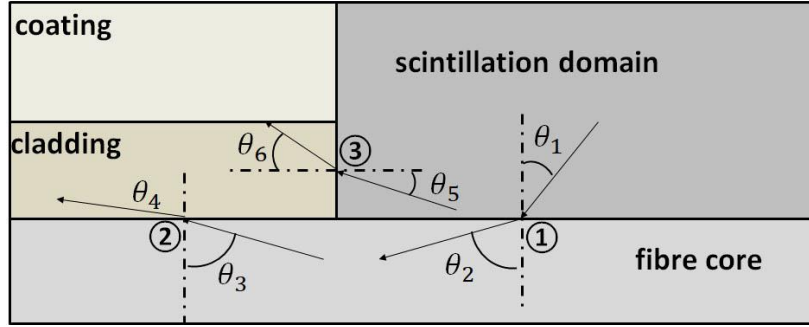


**Figure 5.13** The reflection and transmission of light-rays incident at the inner interfaces of ISOFD. The inner interfaces including: ① *ER*—core, ② core—cladding and ③ *ER*-cladding.

The parameters  $\theta_{\text{cr,core-clad}}$  ( $85.25^\circ$ ),  $\theta_{\text{cr,ER-core}}$  ( $67.06^\circ$ ),  $\theta_{\text{cr,ER-clad}}$  ( $65.6^\circ$ ) and  $\theta_{\text{cr,clad-coat}}$  ( $63.71^\circ$ ) represent the critical angles at the core—cladding, *ER*—core, *ER*—cladding and cladding—coating interfaces, respectively, and their values are listed in Table 5.2. Now we consider case ① in Figure 5.13 where the light rays incident on the *ER*—core interface from SD. The incident angle is  $\theta_1$ , while the refractive angle is  $\theta_2$ . As the refractive index of the fibre core (1.455) is smaller than that of *ER*, thus only light rays with  $\theta_1$  smaller than the critical angle  $\theta_{\text{cr,ER-core}}$  (i.e.  $\theta_1 < 67.06^\circ$ ) can transmit into the fibre core from *ER*. After the light-ray transmits into the fibre core, the incident angle  $\theta_3$  at the core-cladding boundary equals  $\theta_2$  according to the symmetry of the optical fibre. In terms of transmission in the fibre core with total reflection at the core-cladding boundary as case ② shows in Figure 5.13, the incident angle  $\theta_3$  should be larger than  $\theta_{\text{cr,core-clad}}$  (i.e.  $\theta_2 = \theta_3 > 85.25^\circ$ ). Correspondingly, the incident angle  $\theta_1$  on the SD side should be larger than  $65.59^\circ$ . According to above

analysis, light-rays at the *ER*–core interface with an incident angle  $\theta_1 \in (65.59^\circ, 67.06^\circ)$  can transmit into the fibre core and propagate in the core without energy loss.

If the light ray transmits into the cladding layer from the core, and if the refractive angle  $\theta_4 > \theta_{\text{cr,clad-coat}} = 63.71^\circ$ , the ray will be totally reflected at the cladding–coating interface, which means that the incident angle  $\theta_3$  in this case is larger than  $63.31^\circ$ . As  $\theta_2 = \theta_3$ , and the angle  $\theta_1$  corresponding to the  $\theta_2 < 63.31^\circ$  is  $\theta_1 > 55.37^\circ$ . Therefore, to transmit through the *ER*–core interface and reaching the ports without energy loss, the angle interval can be expanded as  $(55.37^\circ, 67.06^\circ)$ . On the other hand, all light rays with incident angle  $\theta_1 < 67.06^\circ$  can transmit into the fibre core from *ER*. Therefore, the probability of the light rays escaping SD from the *ER*–core interface and transmit inside the fibre without any energy loss is relatively low.

As for the light-rays incident on the *ER*–cladding interface like case ③ in Figure 5.13, in order to transmit out of SD, the incident angle  $\theta_5$  must be smaller than  $\theta_{\text{cr,ER-clad}} = 65.60^\circ$ . To achieve total reflection at the cladding–coating interface requires that the refractive angle  $\theta_6 < 63.71^\circ$ , which corresponds to  $\theta_5 < 55.37^\circ$ . Therefore, if a light ray incident on the *ER*-cladding interface with a  $\theta_5 < 55.37^\circ$  transmits into the cladding, it will propagate in the optical fibre without any energy loss.

The discussion concerning the relationship between the incident angle and the critical angle at the different interfaces shows that only a small part of the scintillation light emitted from SD can transmit without energy loss. Placing the port near to the terminals of SD helps to collect the light energy that might otherwise be lost during long-distance propagation. When the port is placed far enough away, the collected light

energy would consist of the light rays transmitting out of SD that have an incident angle  $\theta_1 \in (55.37^\circ, 67.06^\circ)$  at the *ER*—core interface or  $\theta_5 \in (0^\circ, 55.37^\circ)$  at the cladding—coating interface. This may explain why the transmission efficiency first decreases and then remains stable as the distance  $l_{\text{port-SBT}}$  increases.

It should be noted that these conditions are limited by the refractive indices of the materials constituting both the optical fibre and SD. If we choose an optical fibre with a core material featuring a higher refractive index, the transmission efficiency of the optical fibre will be optimised due to the larger critical angle  $\theta_{\text{cr,ER-core}}$  and the expanded energy intervals of the incident angle, as it discussed in the preceding paragraphs.

**Table 5.2** The critical angles at the different interfaces

Interface	Core-cladding	Cladding-coating	<i>ER</i> -core
Critical angle	85.25 °	63.71 °	67.06 °
Interface	<i>ER</i> -cladding	<i>ER</i> -coating	Scintillator- <i>ER</i>
Critical angle	65.60 °	55.36 °	43.39 °

### 5.7 The effect of the adjacent SD

One objective of this research is to investigate the practicability of distributed dose monitoring with ISOFD with multiple SDs. It is initially done by the simulation of the X-ray absorption and light transport in a double SD-ISOFD (ISOFD of double scintillation domains) model. Two SDs, namely ‘A’ and ‘B’, are embedded into one single optical fibre as shown in Figure 5.14. When utilized in medical X-ray detection,

the signal from one SD (SD 'A' in this case) will inevitably suffer the interference from the adjacent SD (e.g. SD 'B' in this case). The interference may be partly owing to three aspects. The first one is the spectra overlap; the second one is radioluminescence from adjacent SD under the radiation leaked from the SD through photon scattering, K-X-ray emission, or secondary electron interaction; the third one is the interference from the adjacent SD on the light transmission efficiency.

As it shown in Figure 2.6 (section 2.4.3), though the XRL spectra of three types of  $Gd_2O_2S:RE$  peaks differ from one another and dominant emission peaks do not overlap, the weaker emission peaks may more or less overlap with the dominant peak of another scintillator. The differential spectral method proposed by Font et al. [27] which reviewed in section 2.5.3 provide one solution to solve this problem, thus will not be discussed here. The interference from the adjacent SD in terms of K-X-ray reabsorption and transmission efficiency depend on the configuration of the double SD-ISOFD, and these later two kinds of interference will be considered in the simulation.

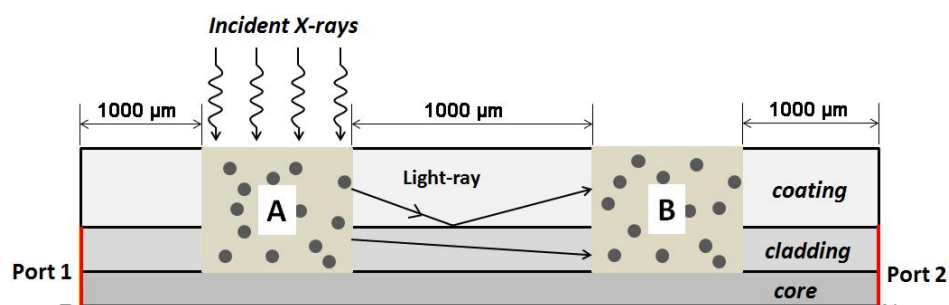


**Figure 5.14** Diagram of the double SD-ISOFD model. It is noted that the ratio of different parts in this figure does not coincide with the real size of the model.

In this section, Model 3 (see Page) will be used for simulation, the general configuration has been introduced, more detailed parameters of the configuration will

be introduced as follow. Save for the difference in the locations of the two SDs, 'A' and 'B' are comprised of same material ( $\text{Gd}_2\text{O}_2\text{S}$ ) share exactly the same configuration, namely, the length of each SD is  $100\ \mu\text{m}$ , the mean size of the scintillator particles is  $r_p = 2\ \mu\text{m}$ , the scintillator packing density is  $\eta_{pk} = 18.18\%$  and the embedding depth is  $D_{em} = 100\ \mu\text{m}$ . The distance between 'A' and 'B' is  $1000\ \mu\text{m}$ . Two ports are set  $1000\ \mu\text{m}$  away from the terminals of two SDs respectively. By comparing the energy of the scintillation light received by port 2 with that received by port 1, the influence of adjacent SD 'B' on the transport of the light generated from SD 'A' can be revealed (as shown in Figure 5.14). Moreover, the energy reabsorption of the scattered X-ray and K-X-ray photons (escaping domain 'A') by domain 'B' can also be counted.

**Table 5.3** The simulation result of the double SD-ISOFD\*

X-ray photon absorption by 'B'	Light collected by port 1	Light collected by port 2	Light escaping from outer surface of 'B'
0	2.671%	0.249%	1.501%

For the incident energy of  $60\ \text{KeV}$  (above the K-edge of the Gd element), the result is presented in Table 5.3. The reabsorption probability of the X-ray escaping SD 'A' is 0. Thus, there is no interference from the X-ray energy reabsorption by the adjacent scintillator 'B', and all the light photons detected by port 1 and port 2 are generated from the X-ray radiated domain 'A'.

\* It should be noted that the result in the second row of Table 5.1 is the ratio between the energy  $E$  passing through or collected at the boundary and the total energy of all scintillation light-rays, i.e.,  $E/E_{SC,tot}$ .

The scintillation light energy reaching port 1 accounts for 2.671% of all the scintillation light generated, while port 2 detected only 0.249% of all the light energy. The previously calculated transmission efficiency without adjacent bulk is 2.662%. Hence, the adjacent domain 'B' has a negative effect on the light transport, which lowers the transmission efficiency of the scintillation light. The simulation also shows that the scintillation light energy escaping the domain 'B' from the outer surface of 'B' accounts for 1.501% of all scintillation energy. Considering that only 2.671% of all scintillation energy can be detected by each port without adjacent SD with  $l_{\text{port-STD}} = 1000 \mu\text{m}$ , thus a considerable portion of the scintillation light loss is through the light transmission at the outer surface of 'B', which may be caused by the multiple reflection by the scintillator particles and interfaces in domain 'B'. To improve the transmission efficiency of double SD-ISOFD, reflective coating provides one possible solution, and it will arise more challenge to the development of the fabrication techniques.

### 5.8 Error analysis

A systemic error might be introduced into the simulation of diagnostic X-ray detection due to the approximations and assumptions made in order to ensure the simplicity of calculation. The first such assumption is that only photoelectric absorption by the gadolinium atoms is considered, while the absorption by the sulphur and oxygen atoms is neglected. The error caused by this assumption is valued with the cross-sections of the elements in the  $\text{Gd}_2\text{O}_2\text{S}$  molecule. The modified elemental cross-sections of photoelectric absorption are given by  $\sigma'_{\text{ph},i} = (\mu/\rho)'_{\text{ph},i} \cdot w_i$  ( $i = \text{'Gd'}$ ,  $\text{'O'}$  or  $\text{'S'}$ , and  $w_i$  is the weight ratio of the element). Table 5.4 gives the  $\sigma'_{\text{ph,Gd}}$  and  $(\sigma'_{\text{ph,O}} + \sigma'_{\text{ph,S}})$  of

the  $Gd_2O_2S$  for X-rays in the energy interval 10~80 KeV. According to these modified photon cross-sections, the probability of photoelectric absorption occurring in the Gd atoms is around 0.979~0.998, and this probability grows larger with respect to higher photon energies. Therefore, the error introduced by replacing  $Gd_2O_2S$  with Gd element when it comes to the simulation of photoelectric absorption would decrease with respect to the growing X-ray energy level.

**Table 5.4** The photoelectric cross-sections of the elements Gd, O, and S, which are modified by the elemental weight ratio in the compound  $Gd_2O_2S$

Photo energy KeV	$\sigma'_{ph,Gd}$ $cm^2/g$	$\sigma'_{ph,O} + \sigma'_{ph,S}$ $cm^2/g$	Photo energy KeV	$\sigma'_{ph,Gd}$ $cm^2/g$	$\sigma'_{ph,O} + \sigma'_{ph,S}$ $cm^2/g$
10	220.735	4.646	50	2.752	0.034
15	75.592	1.397	52.5	13.375	0.029
17.5	49.888	0.877	55	11.830	0.025
20	34.809	0.585	57.5	10.518	0.022
22.5	25.197	0.408	60	9.396	0.019
25	18.875	0.295	62.5	8.432	0.017
27.5	14.538	0.219	65	7.604	0.015
30	11.448	0.168	67.5	6.880	0.013
32.5	9.163	0.131	70	6.245	0.012
35	7.458	0.104	72.5	5.687	0.010
37.5	6.156	0.083	75	5.195	0.009
40	5.145	0.068	77.5	4.758	0.008
45	3.697	0.047	80	4.368	0.008
47.5	3.177	0.040			

The second type of error is introduced by the assumption that all the secondary electrons, including the photoelectrons, Auger electrons and incoherent scattering

excited electrons, are absorbed locally near the photon interaction site. As we have established, the kinetic energy of a free photon is gradually attenuated during its path. Thus, there is a chance that the secondary electrons with high kinetic energies might travel far away from the scintillation site and hence escape the scintillator particles rather than being absorbed locally. Therefore, the energy absorbed by the scintillator is likely smaller than the simulated energy.

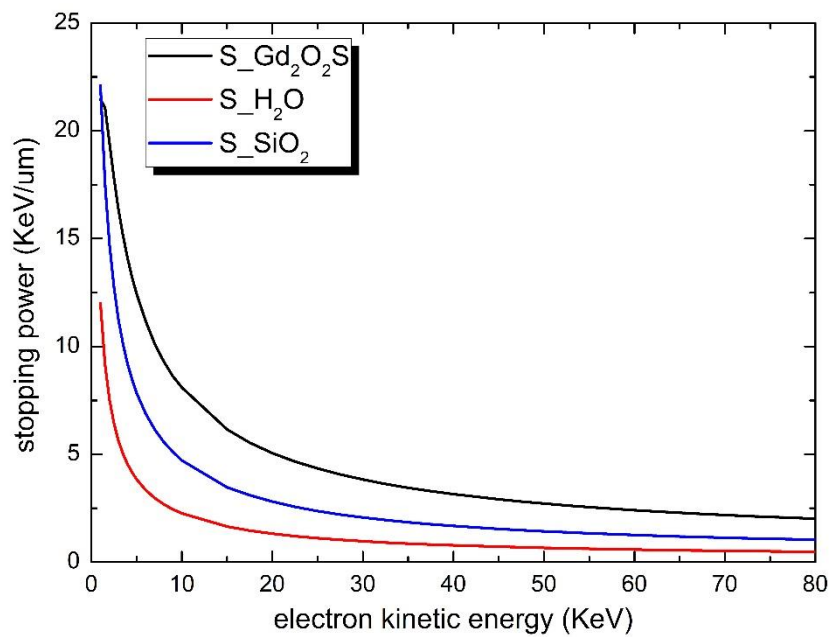


**Figure 5.15** The stopping power  $S(E)$  of the electron in different media

As the photoelectric effect in the Gd atom is the dominant photon interaction seen for diagnostic X-rays, we will focus on the energy attenuation of photoelectrons. For a photon energy higher than the K-edge of the Gd element, photoelectric absorption occurs in either K-shell or L-shell, while the probability of K-shell excitation is 0.8216. If the photoelectric effect occurs in the K-shell, the kinetic energy of the photoelectron is  $(E_0 - U_K)$ ; otherwise, the L-shell is ionised, and the kinetic energy of the photoelectron is  $(E_0 - U_L)$ . For an incident photon of 60 KeV, the possible kinetic

energies of the photoelectron are 9.76 KeV and 51.62 KeV, which correspond to K-shell excitation and L-shell excitation, respectively. In terms of the electron transport in a homogeneous medium, the energy attenuation is measured by the 'stopping power'  $S(E) = -dE/dx$ . For an electron with kinetic energy in the range 1~80 KeV, the  $S(E)$  is shown in Figure 5.15. The stopping power is higher in the case of lower electron energy and materials with a higher density. For the  $Gd_2O_2S$ , the stopping power of an electron with the kinetic energy  $E_e = 9.76$  KeV and  $E_e = 51.62$  KeV is  $S(E = 9.76 \text{ KeV}) = 8.21 \text{ KeV}/\mu\text{m}$  and  $S(E = 51.62 \text{ KeV}) = 2.66 \text{ KeV}/\mu\text{m}$ , respectively. The relatively high  $S(E)$  seen for the K-shell photoelectron indicates that it is reasonable to assume that the photoelectron generated by K-shell ionisation is absorbed locally. However, the photoelectron emitted from the L-shell has higher kinetic energy and lower stopping power. In the case of a small scintillator particle size, the probability of the L-shell photoelectron escaping the scintillator particle is much higher than that associated with the K-shell photoelectron. This will create an error when calculating the energy deposition inside the scintillator particle.

The third type of error concerns the energy conversion process inside the scintillator. In this simulation, the intrinsic X-ray to light efficiency  $\eta_c$  is assumed to be constant, but in practical process, the conversion efficiency  $\eta_c$  shows a statistic fluctuation due to the electron transition probabilities seen in the low energy atomic levels[123]. Moreover, during the sensor fabrication that will be discussed later in this thesis,  $Gd_2O_2S$  doped with different rare-earth elements is used as the scintillator rather than pure  $Gd_2O_2S$ . Using the doped element as an activator affects the energy

conversion efficiency[137]. The dependence of the  $\eta_c$  on the mean particle size of the scintillator has also been reported[131]. Therefore, the fluctuation seen in the  $\eta_c$  inevitably introduces uncertainty into the simulation result.

As for the simulation of the light transport process, the error lies in the assumption that the refractive indices of all the materials for light remains constant, while the scintillation light spectrum is neglected in the simulation. However, in reality, the refractive index of a light photon is wavelength dependent. This error could be reduced by adding the scintillation spectrum into the simulation process.

### **5.9 Conclusion of simulation with respect to X-rays**

Based on the simulation of an ISOFD under X-ray radiation in the diagnostic energy range 20~80 KeV, the following conclusions can be drawn:

- i. Under X-ray radiation, the smaller average size of the scintillator particles contributes to the X-ray absorption by the scintillator, while the ISOFD model with a scintillator—particle size of 2  $\mu\text{m}$  shows the best performance with regard to X-ray detection.
- ii. A high packing density  $\eta_{pk}$  of SD is desirable due to the high photon absorption probability and detection efficiency of X-rays; thus, using up-to-date fabrication techniques, acquiring high  $\eta_{pk}$  has a high priority.
- iii. Increasing the embedding depth  $D_{em}$  of SD within the optical fibre can improve the detection efficiency in relation to both the X-ray interaction probability and light transmission efficiency. Although the current simulation

shows that increasing the  $D_{em}$  has a positive effect on the detection efficiency, in a real sensor fabrication situation, the mechanical properties and fabrication precision will limit the available value of the  $D_{em}$ .

- iv. The response of the ISOFD to the incident X-rays is energy dependent due to the relationships between the photon interaction cross-sections (or mass attenuation coefficients) of the scintillator  $Gd_2O_2S$ . The model simulated is most sensitive to the lowest initial energy of  $E_0 = 10$  KeV, while an abrupt increase in the overall detection efficiency can be seen at 50.24 KeV, that is, the K-edge of the gadolinium element. The high probability of characteristic K-X-ray emission and the low probability of K-X-ray reabsorption attenuate the scintillation efficiency. The value of the initial photon energy also affects the energy distribution of the scintillation generation, such that the transmission efficiency of the scintillation light, as generated under the incident photon with a high attenuation coefficient, is relatively low. Nevertheless, the mass attenuation coefficient remains the dominant factor determining the overall X-ray detection efficiency.
- v. The simulation regarding the position of the port indicates that there is energy loss during the light propagation that occurs inside the ISOFD. In the simulation, the scintillation light ray is emitted randomly in an isotropic direction. The reflection and refraction at the interfaces of different materials in the ISOFD cause transmission energy loss. When the port is set as far away

as 2000  $\mu\text{m}$ , the transmission efficiency reaches a stable value of approximately 2.61%.

- vi. The simulation of the double scintillation-domain ISOFD verifies that the adjacent SD greatly weakens the transmission efficiency. Yet, when the distance between the two ports is set as 1000  $\mu\text{m}$ , the adjacent SD does not generate any scintillation light; thus, there is no interference from the adjacent SD.

## **Chapter 6—Review: theory and MC simulation algorithms of electron interactions**

### **6.1 Introduction**

The free electrons or positrons generated by photon interactions include photoelectron (by photoelectric effect), Auger electron (by photoelectric effect), recoil electron (by incoherent scattering) and electron-positron (by pair production). Different from photons, an electron gradually loses energy when traveling in the medium. In this process, a cascade of interactions between the electrons/positrons and the medium will happen. The energy deposited in the material during these interactions contributes to lattice vibration (heat), atom ionization, and secondary radiation emission. The attenuation length of the electron/positron depends on the density of the material and the kinetic energy of the particle. The electrons/positrons created by photon interactions in the diagnostic X-ray energy range have relatively low kinetic energies and are usually assumed to be absorbed locally near the interaction sites. However, for therapeutic  $\gamma$ -ray interaction, the secondary electrons and positrons may have kinetic energies in the order of a few MeV or even higher. Due to the high kinetic energy, these free electrons/positrons might propagate a relatively long distance before being captured or annihilated (for positrons). For detectors of small sizes (dimensions not exceed 1~2 cm [55]), the fast electrons have great probability of escaping the detector before detected, causing considerable energy loss. For secondary electrons/positrons (created by  $\gamma$ -ray interactions) transport in ISOFDs, considering the small dimensions of ISOFDs and the low packing density of the scintillation-domain, the interactions of fast electrons and positrons should be taken into account regarding their energy absorption and loss. For therapeutic  $\gamma$ -rays detection using

ISOFDs, the MC simulation should focus not only on the ionizing photon interactions, but also on the energy absorption efficiency through attenuation of secondary electrons and positrons.

The transport problem of the electron in the matter has attracted great attention since last century; part of the reason is that the electron beam probing is an effective way to study the material. This issue is also of great interest for radiation dosimetry and radiotherapy. The physic mechanism and related experimental data of the electron/positron interaction with matter have been well explored and reported by lots of researchers[138]–[141]. The basic modes of the electron interaction with matter include ionization or excitation of atoms, Møller scattering, Bhabha scattering, electron-positron annihilation and Bremsstrahlung emission[120]. For the simplification of the simulation, it is more convenient to classify these modes into four basic types according to energy loss and angular deflection. These four interactions are elastic scattering, inelastic collision, bremsstrahlung emission and positron annihilation[142]. Resembling the coherent photon scattering, the elastic scattering (i.e. Møller scattering) only changes the direction of the electron and there is no energy transfer, thus this type of interaction is determined exclusively by the scattering angle  $\theta$ . As for inelastic collisions, the electron loses part of its energy and momentum to the targeted atoms. The targeted atom is excited or ionized, and the return from higher electronic or nuclear state to the ground is through the emission of one or more particles. This interaction is determined by the energy loss  $W$  and angular deflection  $\theta$ . Bremsstrahlung emission (also referred to as radiative energy loss), is the process in which the electron decelerates when deflected by charged particles (nucleus or shell electrons), and the deceleration will contribute to the emission of electromagnetic radiation. For positron annihilation, the positron is annihilated when colliding the atomic electron and the energy released is assumed to be in the form of two photons emission[143].

Like photon interactions, cross sections are also used to describe the electron/positron interactions with matter. Another important parameter analogue to the photon attenuation coefficient is the energy stopping power  $S(E)$ , which measures the energy loss per unit length and is given by

$$S(E) = -\frac{dE}{dx} \quad (6.1)$$

The mean free path of each interaction is determined as [144]

$$\lambda = \frac{1}{N\sigma} \quad (6.2)$$

where  $N$  is the number of atoms per unit volume, and  $\sigma$  is the total cross section of electron interaction. The cross section, energy stopping power and mean free path of the elastic collision, inelastic collision, radiative energy loss and positron annihilation are expressed as  $(\sigma_{el}, \lambda_{el})$ ,  $(\sigma_{col}, S_{col}(E), \lambda_{col})$ ,  $(\sigma_{rad}, S_{rad}(E), \lambda_{rad})$  and  $(\sigma_{an}, S_{an}(E), \lambda_{an})$  respectively.

MC simulation algorithms for electron transport simulation are all based on the evaluation of proper cross section, DCS, energy stopping power and mean free path of corresponding electron interactions. Commonly used MC simulation methods include ‘detailed’ MC simulation method, ‘condensed’ MC method, and ‘mixed’ MC method [138], [142], [144]–[146]. The ‘detailed’ MC method simulates all interactions the electron/positron experienced in a chronological succession, and it is feasible for low energy or small medium dimension. If the incident electron energy is high while the medium is thick, the total number of interaction events per track is so large that the detailed simulation of all scattering events becomes too complicated and time consuming, thus ‘condensed’ MC method was developed which allows the simulation of the global effect of a large number of scattering events per step length of the track. The drawback of this method is that the spatial distribution information of the electron travelling a certain path length in the medium is lost, and inevitable systematic error is introduced. The magnitude of the systematic error increases with the step length applied in the

simulation. The third method, ‘mixed’ MC algorithm, takes the advantages of the ‘detailed’ and ‘condensed’ MC methods, and combines these two by cautiously selecting cutoff polar scattering angle  $\theta_S$  and cutoff energy loss  $W_C$ . Based on pre-defined  $\theta_S$  and  $W_C$ , the elastic scattering with scattering angle  $\theta < \theta_S$ , inelastic collision with energy loss  $W < W_{CC}$ , and bremsstrahlung emission with radiative energy loss  $W < W_{Cr}$  are defined as soft events, and their global effect is simulated via ‘condensed’ MC method. Those interaction events with scattering angle or energy loss larger than cutoff values are defined as ‘hard’ events, and each hard event is simulated with ‘detailed’ MC method. This algorithm achieved good balance between the simulation accuracy and efficiency, thus widely adopted by various MC simulation codes for electron transport simulation.

The selection of MC method applied for the simulation of secondary electron transport in ISOFDs depends on the dimension of the material and the kinetic energy of the electron/positron. As the photon interactions between therapeutic  $\gamma$ -rays and matter can create electrons with kinetic energy as high as a few MeV, according to the standard proposed by Baro et al[142], we should choose the ‘mixed’ MC method. However, the selection of ‘mixed’ MC method over ‘detailed’ MC method may be inappropriate considering the small dimension of SD. To choose the right MC simulation method for electron transport in this thesis, parameters like the partial DCS and mean free path length will be calculated using both ‘detailed’ and ‘mixed’ MC method, and compared to the size of SD of ISOFDs. The average number of electron scattering events when the secondary electrons/positrons travelling inside a scintillator particle is first evaluated. If the total number of the electron interactions along the track of electrons in the scintillator is small, then ‘detailed’ simulation method will be used, otherwise, ‘mixed’ simulation method will be adopted.

As both algorithms are involved, thus in the next sections, we will first introduce the single scattering DCS and mean free path for elastic scattering described by Fernández-Varea et

al[144] and Baró et al[145] in section 6.2.1, then the semiempirical cross sections for collision energy loss, bremsstrahlung emission and positron annihilation is described according to theory given by Salvat et al[126]. After introducing the basic knowledge of single scattering event, the ‘mixed’ MC method is reviewed according to the description of Baró et al. [142] in section 6.3. The feasibility of using either ‘detailed’ or ‘mixed’ method for the simulation of electron transport in ISOFD models will be discussed in next chapter.

## 6.2 Theory of electron and positron interactions

### 6.2.1 Elastic scattering

The simulation of single elastic scattering adopts the W2D model\* based approximate method introduced by Baró et al[145]. For the convenience of calculation, instead of the scattering angle  $\theta$ , the angular deflection produced by single scattering event is given in terms of the variable

$$\mu \equiv \frac{1 - \cos \theta}{2} \quad (6.3)$$

The W2D single scattering DCS is given by

$$\frac{d\sigma_{el}^{(W)}}{d\mu} = \sigma_{el}^{(W)} p_{ap}^{(W)}(\theta) \quad (6.4)$$

$\sigma_{el}^{(W)}$  in the right-hand side of Equation (6.4) is the total cross section for elastic scattering, expressed as (cf. Equation (25) in Ref [144])

$$\sigma_{el}^{(W)} = \frac{(ZZ'e^2)^2}{(p\beta c)^2} \frac{\pi}{A(1+A)} \quad (6.5)$$

where  $Z$  is the atomic number,  $Z'$  ( $= -1$  for electron,  $= 1$  for positron) is the charge of scattered particle,  $p$  is the momentum of the particle, and  $\beta$  is the speed of the particle in the units of the speed of the light  $c$ . The screening parameter  $A$  is given by

---

\* The W2D model refers to a model describing the elastic scattering of electrons, which is based on the Wentzel DCS model proposed by Fernández-Varea et al[144], and furtherly modified by Baró et al[145].

$$A = \frac{1}{4} \left( \frac{\hbar}{p} \right)^2 (0.885Z^{-1/3}a_0)^{-2} [1.13 + 3.76(\alpha Z/\beta)^2] \quad (6.6)$$

where  $a_0 (\equiv 5.292 \times 10^{-11} \text{m})$  is the Bohr radius,  $\alpha \cong 1/137$  is the fine-structure constant.

The probability distribution function of  $\mu$ , i.e.,  $p_{ap}^{(W)}(\theta)$  in Equation (6.4) is given by

$$p_{ap}^{(W)}(\theta) = \frac{A(1+A)}{(A+\mu)^2} \quad (6.7)$$

The mean free path  $\lambda^{(W)}$  based on the Wentzel DCS is thus given by

$$\lambda^{(W)} = 1/(N\sigma^{(W)}) \quad (6.8)$$

and the first and second mean free path is expressed as

$$\lambda_1^{(W)} = (N\sigma_{el}^{(W)}G_1^{(W)})^{-1}, \quad \lambda_2^{(W)} = (N\sigma_{el}^{(W)}G_2^{(W)})^{-1} \quad (6.9)$$

where  $G_1^{(W)}$  and  $G_2^{(W)}$  are the corresponding first and second transport coefficients, given by

$$G_1^{(W)} = 2A[(1+A)\ln\left(\frac{1+A}{A}\right) - 1] \quad (6.10)$$

$$G_2^{(W)} = 6A(1+A)[(1+2A)\ln\left(\frac{1+A}{A}\right) - 2] \quad (6.11)$$

The first and second mean free paths ( $\lambda_1^{(W)}$  and  $\lambda_2^{(W)}$ ) are important parameters for the determination of the mean free paths of soft and hard elastic events in the ‘mixed’ MC method.

### 6.2.2 Inelastic collisions

The simulation of inelastic collisions of electrons and positrons in dense media adopts the analytic DCSs and MC method described by Salvat and Fernández-Varea[126]. The basis of this algorithm is a generalized oscillator strength model. In this model, each electron shell is replaced by a single oscillator with strength  $f_i$  equal to the number of electrons in the shell and resonance energy  $W_i = aU_i$ , where  $U_i$  is the ionization energy of the shell[142]. For the electrons with binding energies less than a few tens of eV (e.g. valance band and conduction band electrons), the excitation energy is  $W_{vb} = b\Omega_p(f_{vb}/Z)^{1/2}$ , where  $f_{vb}$  is total number of these loosely bound electrons,  $b$  is in a parameter in the order of unity and  $\Omega_p =$

$(4\pi\hbar^2 NZe^2)^{1/2}$  is the plasma energy corresponding to the total electron density in the material.

The numerical value of the semi-empirical adjustment factor  $a$  is given by

$$\ln a = (Z - f_{vb})^{-1} [Z \ln I - f_{vb} \ln W_{vb} - \sum f_i \ln U_i] \quad (6.12)$$

where  $I$  is the mean excitation energy, and the values of  $I$  for all elemental substances were tabulated in Berger's report[141]. As for compound material  $A_x B_y$ , the mean excitation energy

$I$  is approximated with the additivity-rule:

$$\ln I = Z_M^{-1} [xZ(A) \ln I_A + yZ(B) \ln I_B] \quad (6.13)$$

where  $Z_M = xZ(A) + yZ(B)$  is the number of electrons per molecule, and  $I_A$  stands for the mean excitation energy of element  $A$ .

The DCS for inelastic collision is a function of the energy loss  $W$  and the polar scattering angle  $\theta$ . Instead of the scattering angle  $\theta$ , it is customary to use the recoil energy  $Q$  defined by

$$Q(1 + 2m_e c^2) = c^2(p^2 + p'^2 - 2pp' \cos \theta) \quad (6.14)$$

where  $p$  and  $p'$  are the magnitude of the momentum of the projectile ( $e^-$  or  $e^+$ ) before and after collision, which given by

$$(cp)^2 = E(E + 2m_e c^2) \quad (6.15)$$

and

$$(cp')^2 = (E - W)(E - W + 2m_e c^2) \quad (6.16)$$

For  $i$ th oscillator, the excitation spectrum  $F(W_i; Q, W)$ , which measures the contribution to the generalized oscillator strength of a unit strength oscillator with resonance energy  $W_i$ , is written in term

$$F(W_i; Q, W) = \delta(W - W_i)\theta(W_i - Q) + \delta(W - Q)\theta(Q - W_i) \quad (6.17)$$

where  $\delta(x)$  is the Dirac delta function and  $\theta(x)$  is the Heaviside step function. According to the description in Ref [142], the first term in this expression corresponds to distant collisions, in which a shell-electron is excited with small momentum transfer. The allowed recoil energies

in distant collision lies in the interval from  $Q_- = Q(\theta = 0)$  to  $W_i$ . The second term corresponds close collisions, which are described as binary collisions with a free electron at rest ( $Q = W$ ), by means of the Møller and Bhabha DCSs.

The energy loss DCS per atom is expressed in the form of the summation of DCSs of close collisions and distant collisions over the different oscillators:

$$\frac{d\sigma_{\text{col}}}{dW} = \sum_i^M f_i \left( \frac{d\sigma_{ci}}{dW} + \frac{d\sigma_{di}}{dW} \right) \quad (6.18)$$

The partial DCS per unit oscillator strength of the close collision for  $i$ th oscillator, which is based on the Rutherford DCS, is given by

$$\frac{d\sigma_{ci}}{dW} = \frac{2\pi e^4}{m_e v^2} \frac{1}{W^2} F^{(\pm)}(E, W) \times \theta(W - W_i) \theta(W_{\text{max}} - W) \quad (6.19)$$

where  $v$  is the velocity of the particle, and the values  $W_{\text{max}}$  of the maximum energy loss  $W_{\text{max}}$  for electron and positron are different, given by

$$W_{\text{max}} = \begin{cases} E, & \text{positron} \\ E/2, & \text{electron} \end{cases} \quad (6.20)$$

The function  $F^{(\pm)}(E, W)$  are the ratios of the Møller and Bhabha DCSs to the Rutherford DCS and are given by

$$F^{(-)}(E, W) \equiv 1 + \left( \frac{\kappa}{1 - \kappa} \right)^2 - \frac{\kappa}{1 - \kappa} + \left( \frac{\gamma - 1}{\gamma} \right)^2 \left( \kappa^2 + \frac{\kappa}{1 - \kappa} \right) \quad (6.21)$$

for electron and

$$F^{+}(E, W) \equiv 1 - \left( \frac{\gamma - 1}{\gamma} \right)^2 \left\{ \frac{2(\gamma + 1)^2 - 1}{\gamma^2 - 1} \kappa - \frac{\kappa^2}{(\gamma + 1)^2} \times [3(\gamma + 1)^2 + 1 - 2\gamma(\gamma - 1)\kappa + (\gamma - 1)^2 \kappa^2] \right\} \quad (6.22)$$

for positrons.  $\kappa \equiv W/E$  is the energy loss, and  $\gamma \equiv 1 + E/m_e c^2$ .

The corresponding DCS for distant interactions in Equation (6.18) is

$$\frac{d\sigma_{di}}{dW} = \frac{2\pi e^4}{m_e v^2} \frac{1}{W_i} \left[ \ln \left( \frac{W_i Q_- + 2m_e c^2}{Q_- W_i + 2m_e c^2} \right) + \ln \left( \frac{1}{1 - \beta^2} \right) - \beta^2 \right. \\ \left. - \delta \right] \delta(W - W_i) \quad (6.23)$$

where  $\delta$  is the density effect correction and is negligible for high-energy (cf. Equation (26) in Ref [126]).

The (unnormalized) distribution function of  $Q$  is approximately given by

$$P_d(Q) = \frac{1}{Q \left( 1 + \frac{Q}{2m_e c^2} \right)} \quad \text{if } Q_- < Q < W, \quad (6.24)$$

The mean free path between inelastic collisions  $\lambda_{\text{col}}(E)$  and the collision stopping power  $S_{\text{col}}(E)$  are given by

$$\lambda_{\text{col}}^{-1}(E) = N\sigma_{\text{col}} = N \int_0^E \frac{d\sigma_{\text{col}}}{dW} dW \quad (6.25)$$

$$S_{\text{col}}(E) = N \int_0^E W \frac{d\sigma_{\text{col}}}{dW} dW \quad (6.26)$$

The purely analytical expressions of  $\frac{d\sigma_{\text{col}}}{dW}$  and  $P_d(C)$  allow the random sampling of the energy loss  $W$ , recoil energy  $Q$  and corresponding polar scattering angle  $\theta$  by using purely analytical methods which described in Ref [126].

### 6.2.3 Radiative losses (Bremsstrahlung emission)

The simulation of the bremsstrahlung emission utilizes the theory and MC method proposed by Salvat et al[126]. In his article, a semiempirical DCS of the energy loss for bremsstrahlung emission is derived in the form as a corrected Bethe-Heitler-Wentzel (BHW) DCS formula with exponential screening:

$$\frac{d\sigma_{\text{rad}}^{(-)}}{dW} = (E + m_e c^2)^{-1} \frac{d\sigma_{\text{BHW}}^{(-)}}{d\epsilon} \quad (6.27)$$

where  $d\sigma_{\text{BHW}}/d\epsilon$  is the DCS in terms of the reduced energy loss  $\epsilon \equiv W/(E + m_e c^2)$ , and is given by

$$\frac{d\sigma_{\text{BHW}}^{(-)}}{d\epsilon} = a_0^2 \alpha^5 Z[Z + \eta] \times \frac{2}{3} \left[ 2 \left( \frac{1}{2} - \epsilon \right)^2 \phi_1(\epsilon) + \phi_2(\epsilon) \right] \quad (6.28)$$

where  $\phi_1(\epsilon)$  and  $\phi_2(\epsilon)$  are analytical functions of the screening radius. As the bremsstrahlung emission is closely related to the electron-positron pair creation,  $\phi_1(\epsilon)$  and  $\phi_2(\epsilon)$  share the same analytical expression with those in the corrected Bethe-Heitler DCS of the pair production (cf. Equation (3.39)). As for positrons, a factor  $F_p(Z, E)$  is introduced into the correct the BHW DCS:

$$\frac{d\sigma_{\text{BHW}}^{(+)}}{d\epsilon} = F_p(Z, E) \frac{d\sigma_{\text{BHW}}^{(-)}}{d\epsilon} \quad (6.29)$$

where the detailed expression of  $F_p(Z, E)$  is given by Equations (59) and (60) in Ref [126]. The value of  $F_p(Z, E)$  is generally smaller than one, and approaches one as the electron kinetic energy grows. Therefore, the radiative DCS for positrons will closely approach the radiative DCS for electrons at high energies.

The analytical expression of cross section  $\sigma_{\text{rad}}$  can be calculated by integrating  $\frac{d\sigma_{\text{rad}}}{dW}$  over the energy loss  $W$ , and the mean free path is given by

$$\lambda_{\text{rad}}^{-1}(E) = N\sigma_{\text{rad}} = N \int_0^E \frac{d\sigma_{\text{rad}}}{dW} dW \quad (6.30)$$

the radiative stopping power of the radiative energy loss is given by

$$S_{\text{rad}}(E) = N \int_0^E W \frac{d\sigma_{\text{rad}}}{dW} dW \quad (6.31)$$

The random sampling algorithm of the energy loss based on the DCS, mean free path can be found in section 6.3 in Ref [126]. In addition, the angular deflections of the electron trajectory due to bremsstrahlung effect are small and can be neglected. As for the photon emitted, let  $(\theta',$

$\varphi'$ ) denote the polar and azimuthal angles of the direction of the emitted photon with reference to the electron trajectory, the normalized distribution function of the polar angle  $\theta$  is given by (Equation 16 in ref [123])

$$p(\cos \theta) = \frac{3}{16\pi} \left[ 1 + \left( \frac{\cos \theta - \beta}{1 - \beta \cos \theta} \right) \right] \times \frac{1}{\gamma^2 (1 - \beta \cos \theta)^2} \quad (6.32)$$

with  $\gamma^2 = 1/(1 - \beta^2) = 1 + E/(m_e c^2)$

### 6.2.4 Positron annihilation

The positron annihilation refers to the process in which the positron annihilates in collision with electrons, and the energy is released through the emission of two photons. The simulation utilizes the algorithm described in Ref. [142] and [143], in which the mean free path of the positron annihilation is given by (cf. Equation (2.12.14) in Ref [143])

$$\lambda_{\text{an}}^{-1} = NZ \frac{\pi r_e^2}{(\gamma + 1)(\gamma^2 - 1)} \times \left\{ (\gamma^2 + 4\gamma + 1) \ln \left[ \gamma + (\gamma^2 - 1)^{\frac{1}{2}} \right] - (3 + \gamma)(\gamma^2 - 1)^{\frac{1}{2}} \right\} \quad (6.33)$$

The algorithm sampling energies and trace vectors of the two photons emitted is illustrated in the report of Nelson et al[143]. For positron with high kinetic energy  $E_0$ , the target electron in the atom or molecule can be approximated to be free and at rest. As two photons created may have different energies, say  $E_1$  and  $E_2$  ( $E_1 + E_2 = E_0 + 2m_e c^2$ ), here we first define that  $E_1 \leq E_2$ , and  $E_1, E_2$  are expressed as

$$E_1 = \zeta(E_0 + 2m_e c^2) \quad (6.34)$$

and

$$E_2 = (1 - \zeta)(E_0 + 2m_e c^2) \quad (6.35)$$

where the maximum value of  $\zeta$  is  $1/2$ , and minimum value is given by

$$\zeta_{\text{min}} = \frac{1}{\gamma + 1 + (\gamma^2 - 1)^{1/2}} \quad (6.36)$$

According to the conservation of energy and momentum, the directions of the photons is given by

$$\cos \theta_1 = (\gamma^2 - 1)^{-1/2}(\gamma + 1 - 1/\zeta) \quad (6.37)$$

and

$$\cos \theta_2 = (\gamma^2 - 1)^{-1/2}[\gamma + 1 - 1/(1 - \zeta)] \quad (6.38)$$

The DCS for two-photon annihilation can be written as[122]

$$\frac{d\sigma_{an}}{d\zeta} = \frac{\pi r_e^2}{(\gamma + 1)(\gamma^2 - 1)} [S(\zeta) + S(1 - \zeta)] \quad (6.39)$$

where

$$S(\zeta) = -(\gamma + 1)^2 + (\gamma^2 + 4\gamma + 1) \frac{1}{\zeta} - \frac{1}{\zeta^2} \quad (6.40)$$

### 6.3 The mixed MC method of electron/positron interaction

The ‘mixed’ MC method, proposed by Fernández-Varea et al[144], takes the advantage of the fact that most of the collisions between the electron and the media atoms along the electron’s track are ‘soft’\*. The combined effect of these soft events between two consecutive hard collision events can be described by an artificial elastic event with the polar angular deflection  $\theta$  and energy loss  $\omega$ . Meanwhile, the hard events are simulated using ‘detailed’ MC method. The accuracy of this algorithm can be improved by choosing small cutoff values ( $\theta_s, W_{cc}$ , and  $W_{cr}$ ), and further decreasing the step length of the soft events between consecutive hard events.

The application of the ‘mixed’ MC for the simulation of the electron/positron interaction has certain restrictions. It is only applicable to amorphous material[126]. The energy of the electron/positron must be high, more than  $\sim 500$  KeV, and the geometry of the media should

---

\* ‘Soft’ means that the energy loss and the scattering angle of the electron caused by collisions are very small, more specifically, smaller than the pre-defined values  $\theta_s$  (scattering angle) and  $W_c$  (energy loss). It has been introduced in Page 169, section 6.1.

also be thick so that the quantity of the collision (elastic, inelastic, radiative and annihilation) events in the trajectory of the charged particles is more than a few thousand. Under these circumstances, the ‘detailed’ MC method is too complicated and time consuming, and the more efficient ‘mixed’ MC method is applied.

This section reviews the ‘mixed’ MC simulation algorithm described by Baró et al [142]. The parameters and functions defining the soft and hard events will be introduced. Furthermore, the method of generating random tracks in an infinite single-element medium is proposed according to ‘PENELOPE’ algorithm.

### 6.3.1 Step lengths of hard events

The quantities and functions defining the step length and interaction probabilities of hard event and positron annihilation are the mean free path lengths ( $\lambda_{\text{el}}^{(h)}$ ,  $\lambda_{\text{col}}^{(h)}$ ,  $\lambda_{\text{rad}}^{(h)}$ , and  $\lambda_{\text{an}}$ ). As for artificial soft event, important parameters and functions include the stopping power  $S_s$ , energy straggling  $\Omega$  and the probability distribution function of deflection angle (namely  $F_a(\theta, t)$ ).

The mean free path of the hard-elastic event is given by

$$\lambda_{\text{el}}^{(h)}(E) = \max \left\{ \lambda_{\text{el}}(E), \min \left[ C_1 \lambda_1(E), C_2 \frac{E}{S(E)} \right] \right\} \quad (6.41)$$

where the mean free path  $\lambda_{\text{el}}(E)$  is given by Equation (6.8),  $\lambda_1(E)$  given by Equation (6.9), and  $S(E)$  is total stopping power, which is given by

$$S(E) = S_{\text{col}}(E) + S_{\text{rad}}(E) \quad (6.42)$$

The parameter  $C_1$  and  $C_2$ , which are custom, serve to control the computer time, while controlling the accuracy. The empirical values of  $C_1$  and  $C_2$  to require stable simulation results are within the interval  $(0, 0.1)$ , and in this study, both  $C_1$  and  $C_2$  are set to be 0.05. When  $\lambda_{\text{el}}^{(h)}(E) < 2\lambda_{\text{el}}(E)$ , detail simulation is used instead, as it’s faster to simulate the real elastic scattering using W2D model than simulate an artificial elastic event.

For hard events involving energy loss, according to Equation (6.25) and (6.30), the mean free paths for hard collision event and radiative event are given by

$$\lambda_{\text{col}}^{(\text{h})}(E) = \left( N \int_{W_{\text{cc}}}^E \frac{d\sigma_{\text{col}}}{dW} dW \right) \quad (6.43)$$

$$\lambda_{\text{rad}}^{(\text{h})}(E) = \left( N \int_{W_{\text{cr}}}^E \frac{d\sigma_{\text{rad}}}{dW} dW \right) \quad (6.44)$$

and the free path for positron annihilation  $\lambda_{\text{an}}$  is given by Equation (6.33). The mean free path between any consecutive hard events is given by

$$\frac{1}{\lambda^{(\text{h})}} = \frac{1}{\lambda_{\text{el}}^{(\text{h})}(E)} + \frac{1}{\lambda_{\text{col}}^{(\text{h})}(E)} + \frac{1}{\lambda_{\text{rad}}^{(\text{h})}(E)} + \frac{1}{\lambda_{\text{an}}} \quad (6.45)$$

According to the exponential attenuation law, the PDF of the step length  $t$  between hard events is expressed as

$$P(t) = \frac{1}{\lambda^{(\text{h})}} \exp\left(-\frac{t}{\lambda^{(\text{h})}}\right) \quad (6.46)$$

The type of hard event taking place each time is determined by the probability

$$p_i = \lambda^{(\text{h})} / \lambda_i^{(\text{h})} \quad (6.47)$$

where  $i = \text{'el'}$ ,  $\text{'col'}$ ,  $\text{'rad'}$ , or  $\text{'an'}$ .

### 6.3.2 Energy loss and angular deflection of soft event

The energy loss of soft event is caused by the soft stopping interactions (soft inelastic collision and soft radiative energy loss). The stopping power  $S_s(E)$  and the energy straggling  $\Omega_s^2(E)$  is given by

$$S_s(E) = N \int_0^{W_{\text{cc}}} W \frac{d\sigma_{\text{col}}}{dW} dW + N \int_0^{W_{\text{cr}}} W \frac{d\sigma_{\text{rad}}}{dW} dW \quad (6.48)$$

and

$$\Omega_s^2(E) = N \int_0^{W_{cc}} W^2 \frac{d\sigma_{col}}{dW} dW + N \int_0^{W_{cr}} W^2 \frac{d\sigma_{rad}}{dW} dW \quad (6.49)$$

The first moments of the energy loss distribution after the path length  $t$  is

$$\langle \omega \rangle = S_s(E)t \quad (6.50)$$

and the variance of the energy loss distribution is

$$\text{var}(\omega) = \Omega_s^2(E)t \quad (6.51)$$

If the number of soft interactions along the path length  $t$  is statistically sufficient ( $>20$ ), the approximation to probability distribution function  $G(\omega; t)$  of energy loss  $\omega$  and step length  $t$  is by

$$G_a(\omega; t) = b\delta(\omega) + (1 - b) \frac{1}{\omega_2 - \omega_1} \theta(\omega - \omega_1)\theta(\omega_2 - \omega) \quad (6.52)$$

with

$$\begin{aligned} b &= 0, \quad \omega_1 = \langle \omega \rangle - [3\text{var}(\omega)]^{1/2}, \\ \omega_2 &= \langle \omega \rangle + [3\text{var}(\omega)]^{1/2}, \quad \text{if } \langle \omega \rangle^2 > 3\text{var}(\omega) \end{aligned} \quad (6.53)$$

and

$$\begin{aligned} b &= \frac{3\text{var}(\omega) - \langle \omega \rangle^2}{3\text{var}(\omega) + 3\langle \omega \rangle^2}, \quad \omega_1 = 0, \\ \omega_2 &= \frac{3\text{var}(\omega) + 3\langle \omega \rangle^2}{2\langle \omega \rangle}, \quad \text{if } \langle \omega \rangle^2 < 3\text{var}(\omega) \end{aligned} \quad (6.54)$$

The artificial elastic event, which simulate the global angular deflection  $\mu = (1 - \cos \theta)/2$ , caused by the multiple soft event in the step length  $t$ , is determined by the probability distribution function  $F_a(\mu; t)$  of  $\mu$  and  $t$  [145]

$$F_a(\mu; t) = (1 - \langle \mu \rangle^{(s)})\delta(\mu - \mu_1) + \langle \mu \rangle^{(s)}(\mu - \mu_2) \quad (6.55)$$

where the value of parameters  $\langle \mu \rangle^{(s)}$ ,  $\mu_1$  and  $\mu_2$  are calculated according the expression given in Equation (45)~(55) in the Ref [145].

### 6.3.3 Generation of random tracks

Here is an example of the simulation of the free electron transportation, in which case a free electron travels in the arbitrary material of the single-component with infinite dimension. It is a simplification of the arbitrary material structures consisting of different materials and boundaries described in the article of Baró et al[142], and the simulation proceeds as follows:

- i. Set the initial kinetic energy  $E$ , positron  $\mathbf{r}$  and direction of movement  $\vec{\mathbf{d}}$  of the primary particle.
- ii. Sample the distance  $t$  to be travelled up to the following hard event, and the expression of  $t$  is derived according to Equation (6.46):

$$t = -\lambda^{(h)} \ln \xi \quad (6.56)$$

- iii. Generate a length  $\tau = t\xi$  of the step to the next artificial elastic event. Let the particle moves in the direction  $\vec{\mathbf{d}}$ :  $\mathbf{r} \leftarrow \mathbf{r} + \tau\vec{\mathbf{d}}$ .
- iv. Sample the energy loss  $\omega$  due to the soft stopping interactions along the step  $\tau$  from the distribution  $G_a(\omega; \tau)$ , and reduce the kinetic energy:  $E \leftarrow E - \omega$ . If  $E < E_{\text{abs}}$ , go to last step x.
- v. Simulate artificial elastic event:  
 Sample the polar angular deflection  $\theta$  from the distribution  $F_a(\theta; t)$ ; Sample the azimuth scattering angle as  $\varphi = 2\pi\xi$ . Perform the rotation  $R(\theta; \varphi)$  according to sampled  $\theta$  and  $\varphi$ :  $\vec{\mathbf{d}} \leftarrow R(\theta; \varphi)\vec{\mathbf{d}}$ .
- vi. Recalculate the path length:  $\tau \leftarrow t - \tau$ .
- vii. Let the particle advances distance  $\tau$  in the direction  $\mathbf{r} \leftarrow \mathbf{r} + \vec{\mathbf{d}}\tau$ .
- viii. Do as step (iv).
- ix. Simulate the hard event:  
 Sample the type of interaction according to the point probabilities given by Equation (6.47). Sample the polar deflection  $\theta$  and the energy loss  $W$  from the corresponding

DCS. Generate the azimuthal scattering angle as  $\varphi = 2\pi\xi$ . Perform a rotation  $\mathbf{R}(\theta; \phi)$  of the vector  $\vec{\mathbf{d}}$  to obtain the new direction:  $\vec{\mathbf{d}} \leftarrow \mathbf{R}(\theta; \varphi)\vec{\mathbf{d}}$ . If a secondary electron (delta ray generated due to primary electron interaction) is emitted in a direction  $\vec{\mathbf{d}}_s$  with energy  $E_s > E_{\text{abs}}$ , store its initial state  $(E_s, \mathbf{r}, \vec{\mathbf{d}}_s)$ . Reduce the kinetic energy of the electron (or positron):  $E \leftarrow E - W$ . Go to step (ii) if  $E > E_{\text{abs}}$ .

- x. Simulate the tracks of the secondary electrons produced by the primary particle (or by other secondary particles previously followed) before starting a new primary track.

For electron transport simulation in ISOFD comprised of different materials, the boundary effect is considered, and the step length between successive hard event is recalculated when the electron hit on the boundary of different materials. The spatial and energy information of the secondary particles generated by electrons will be stored for further simulation. The energy loss (minus secondary X-ray and electron emission) by multiple soft events, hard inelastic collision and positron annihilation when the electron travelling in the scintillator is assumed to be locally absorbed and contributes to visible light emission. The track of the scintillation light-ray is simulated individually using MC method given in chapter 5 before the program moving to next electron track simulation.

## 6.4 Summary

In this chapter, the theory and MC simulation algorithms of electron interactions have been reviewed. The expressions of DCS and PDF with respect to the energy loss and angular deflection caused by electron scattering events are considered for electron and positron transport simulations. Two types of simulation methods of electron transport in the medium have been reviewed: the 'detailed' MC method for electrons with low kinetic energies transport in a relatively small-size medium, while 'mixed' simulation method for electrons with high

kinetic energies transport in a relatively large size medium. For the simulation of secondary electrons generated by  $\gamma$ -ray interactions with the scintillator of ISOFD, the choice of which simulation method to be used is somewhat difficult to make, as the kinetic energy of the secondary electron or positron is high, but the dimensions of the scintillation-domain, especially the that of scintillator, is small. In the next chapter, the specific simulation method of the secondary particles transport in the scintillation-domain is determined considering the model dimensions, the particle's kinetic energy and corresponding mean free path lengths of electron interactions.

## Chapter 7—The Monte-Carlo simulation of ISOFD for therapeutic $\gamma$ -ray detection

### 7.1 Introduction

The simulation method of ISOFD modeling with therapeutic  $\gamma$ -rays is distinctively different from that using a diagnostic X-ray source. The dominant interaction mechanism varies since the incident photon energy of therapeutic  $\gamma$ -rays is much larger than diagnostic X-rays. For therapeutic  $\gamma$ -rays, incoherent scattering is predominant at lower photon energies while pair-production is the dominant interaction mechanism at higher energies. Moreover, the secondary electrons and positrons, generated as a result of photon interactions, have considerably high kinetic energy, will interact with not only scintillators, but also low mass materials like the binding material (*ER*), and the optical fibre. It will affect the efficiency of energy transfer from ionizing photon to scintillation light photon. More importantly, interference may be introduced in the form of bremsstrahlung emission.

In this chapter, the photon interaction is simulated for  $\gamma$ -rays in the energy range (2~24 MeV). First, the attenuation length of the photon and the kinetic energy distribution of secondary electrons/positrons created by photon interactions in different media are investigated. Secondly, as for the transport of fast secondary electrons/positrons, the Monte-Carlo simulation method described previously in chapter 6 is used to calculate the mean free path lengths and the energy stopping power of the corresponding electron interaction in the medium ( $\text{Gd}_2\text{O}_2\text{S}$  and *ER*) of scintillator domain. The feasibility of the simulation methods for electron transport is investigated.

After that, the electron transport in a single scintillator particle is simulated. The final section concludes the whole chapter.

## **7.2 The simulation of $\gamma$ -ray absorption and the electron/positron generation**

The overall absorption efficiency of the incident  $\gamma$ -ray photon beam not only depends on the photon attenuation coefficients in the medium, but also is influenced by the sensitivity of the scintillator material to the secondary electrons and positrons. As for the simulation of the ISOFD model under  $\gamma$ -ray radiation, the basic idea of MC simulation methods utilized for ionizing photon interaction and light transportation resembles that of simulating the diagnostic X-ray detection introduced in chapter 4. However, pair-production is included in the primary photon interaction simulation when a  $\gamma$ -ray photon is attenuated by the scintillator. Moreover, rather than simply assumed to be locally absorbed by the GOS, the energy and spatial information (location and direction of movement) of the secondary electron/positron is stored, and the electron transport will be simulated with a sub-MC simulation program adopting the method and algorithm introduced previously in chapter 6.

In this section, the theoretical free path lengths and energy stopping power of the  $\gamma$ -ray photons in different materials are calculated. To better understand the  $\gamma$ -ray interaction with the scintillator material, the  $\gamma$ -ray transport in the GOS of infinite dimension is first simulated. The transmission path length of the  $\gamma$ -ray and the kinetic energy distribution of the electron/positron generated during the photon interaction process are randomly sampled with MC simulation.

### 7.2.1 The mean free path length of $\gamma$ -ray photons

The track of  $\gamma$ -ray travelling in the ISOFD is determined by the transmission path of the photon in different media, and the interaction when the photon collides with target atoms or molecules, which alters the energy and direction of the original photon. The transmission length of the incident photon changes accordingly with the incident photon energy and the density of the medium. As discussed in chapters 3 and 4, for diagnostic X-ray photon energies between 10-80 KeV, the total mass attenuation coefficient ( $\mu/\rho$ ) has a negative relationship with the photon energy (except for the sudden rise at K-edge), however, for the therapeutic  $\gamma$ -rays of much higher energy, the variation of  $\mu/\rho$  with respect to photon energy is different from that in lower photon energy range.

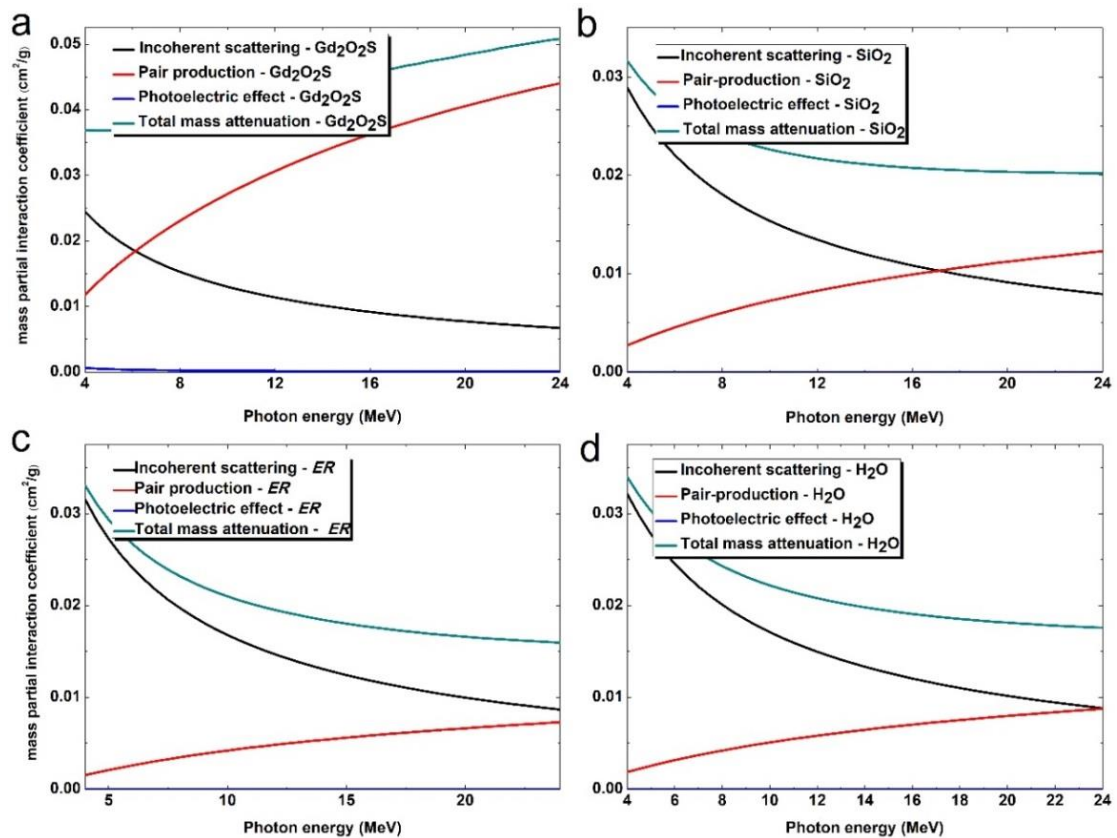


**Figure 7.1** The mass partial interaction coefficients and total mass attenuation coefficients of (a)  $\text{Gd}_2\text{O}_2\text{S}$ , (b)  $\text{SiO}_2$ , (c) epoxy resin (*ER*) and (d) water ( $\text{H}_2\text{O}$ ).

The partial mass interaction coefficients and total mass attenuation coefficients of the materials used in ISOFD for incident photons in the energy range 4~24 MeV are acquired from XCOM database. As shown in Figure 7.1, the incoherent scattering and pair-production are the dominant interactions, and other interaction modes are negligible. The partial interaction coefficient of incoherent scattering  $(\mu/\rho)_{\text{incoh}}$  decreases while pair-production  $(\mu/\rho)_{\text{pp}}$  increases with respect to the rising photon energy for all materials. However, for the total mass attenuation coefficient  $(\mu/\rho)_{\text{tot}}$  at higher photon energies,  $(\mu/\rho)_{\text{tot,GOS}}$  of  $\text{Gd}_2\text{O}_2\text{S}$  (with high effective atomic number) increases, while the coefficient  $(\mu/\rho)_{\text{tot}}$  of materials with lower effective atomic numbers ( $\text{SiO}_2$ ,  $ER$ , and  $\text{H}_2\text{O}$ ) decreases.

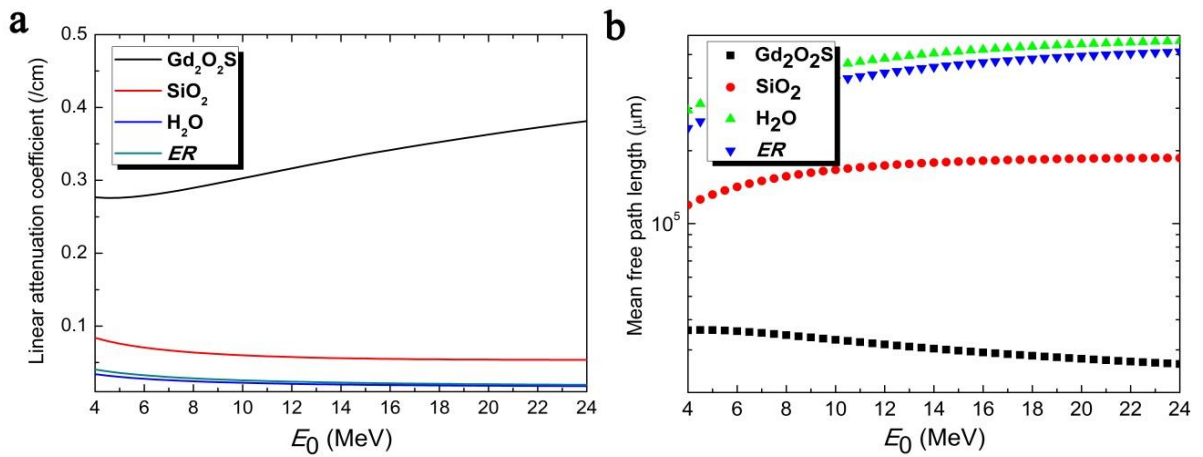


**Figure 7.2** The linear attenuation coefficient (a), and (b) mean free path of  $\text{Gd}_2\text{O}_2\text{S}$ ,  $\text{SiO}_2$ ,  $ER$  and  $\text{H}_2\text{O}$  calculated with corresponding total mass attenuation coefficient.

According to Equation (3.5), by multiplying  $(\mu/\rho)_{\text{tot}}$  with the density ( $\rho$ ) of the material, the linear attenuation coefficients ( $\mu$ ) of  $\text{Gd}_2\text{O}_2\text{S}$ ,  $\text{SiO}_2$ ,  $ER$  and  $\text{H}_2\text{O}$  are presented in Figure 7.2(a). The minimum linear attenuation coefficient of  $\text{Gd}_2\text{O}_2\text{S}$  ( $\mu_{\text{GOS}}$ ) is  $0.27668 \text{ cm}^{-1}$ , at least, 3.30 times that of  $\mu_{\text{SiO}_2}$ , 6.85 times that of  $\mu_{ER}$ , and

8.13 times that of  $\mu_{\text{H}_2\text{O}}$ ; this gap gets larger as the energy rises. Correspondingly, the mean free paths  $\lambda_{\text{mean}} (= 1/\mu)$  of  $\text{SiO}_2$ ,  $ER$  and  $\text{H}_2\text{O}$  are 3.30~21.7 times that of  $\text{Gd}_2\text{O}_2\text{S}$ , as shown in Figure 7.2 (b). For photon energy of 4 MeV, the mean path length  $\lambda_{\text{mean,GOS}}$ ,  $\lambda_{\text{mean,SiO}_2}$ ,  $\lambda_{\text{mean,ER}}$ , and  $\lambda_{\text{mean,H}_2\text{O}}$  are 3.61 cm, 11.9 cm, 24.8 cm and 29.4 cm respectively. Though the mean free path of  $\text{Gd}_2\text{O}_2\text{S}$  is shorter than those of other materials, it is still way much larger than the dimension of the scintillator-bulk in the ISOFD model. Therefore, it can be predicted that, the probability of the  $\gamma$ -ray interaction with the scintillator each time when the photon colliding with the scintillator particle is quite low.

In this section, the mean free paths  $\lambda_{\text{mean}}$  of  $\gamma$ -ray photon transport in different media are calculated. The absorption of  $\gamma$ -rays by materials other than  $\text{Gd}_2\text{O}_2\text{S}$  does not contribute to the characteristic scintillation process, moreover, when considering the mean free path lengths of the  $\gamma$ -ray photon in different media and the size of the ISOFD model, the Monte-Carlo simulation of the  $\gamma$ -ray photon transport in the scintillation-domain only considers the specific photon interaction with  $\text{Gd}_2\text{O}_2\text{S}$ . The photon energy absorbed by the materials  $ER$  and  $\text{SiO}_2$  is assumed be lost. Regarding the explicit photon interaction, the probability distribution of the energy loss and polar deflection of the photon, kinetic energy of secondary electrons or positrons are calculated via the theoretical model given in chapter 3 and presented in the following sections.

### 7.2.2 Compton scattering (incoherent scattering) in $\text{Gd}_2\text{O}_2\text{S}$

As it has been reviewed in chapter 3, the double differential cross section (DDCS) of Compton scattering —  $d^2\sigma_{\text{icnoh}}/(d\Omega dE')$  gives the probability of the secondary photon (scattered) with energy  $E'$  in the deflection angle  $\Omega(\theta, \phi)$  relative to the propagation direction of the incident photon. The simplest case of Compton scattering

is that a photon is scattered by a free electron at rest. The relationship between the scattered photon energy  $E_C$  and polar deflection angle  $\theta$  is given by Equation (3.15), in which case, a simplified DCS  $d\sigma_{\text{incoh}}^{KN}/d\Omega$  (the Klein – Nishina (KN) differential cross section formula shown in Equation (3.12) is used instead of DDCS. As for the Compton scattering which occurs in collision with bound electrons in a molecule, the DDCS is expressed with the relativistic impulse approximation (IA) theory[110], and related formula is shown in Equation (3.19) and Equation (3.55). For an incident photon with energy much higher than the binding energy of target bound-electron, the value of DCS and energy loss relate to the polar angular deflection can be approximated with KN scattering theory.

To study the energy transfer and angular deflection of particles involved in the Compton scattering of  $\gamma$ -rays interacting with  $\text{Gd}_2\text{O}_2\text{S}$ , the Monte-Carlo simulation method (cf. section 3.43) developed by Brusa et al[110] is applied. 400 Compton scattering events are simulated with same initial parameters for each specific initial photon energy in the interval (4, 8, 12, 16, 20, 24) MeV. The energy of the scattered photon ( $E'$ ), and the kinetic energy of the recoil electron ( $E_e$ ) are plotted against the polar angular deflection  $\theta$  of the scattered photon. The result is compared with the theoretical calculation with the model where the scattering event occurs between the incident photon and a free electron at rest. The probability distribution function (PDF) of the polar deflection ( $\cos \theta$ ) is calculated against incident photon energy  $E_0$  according to the IA theory.

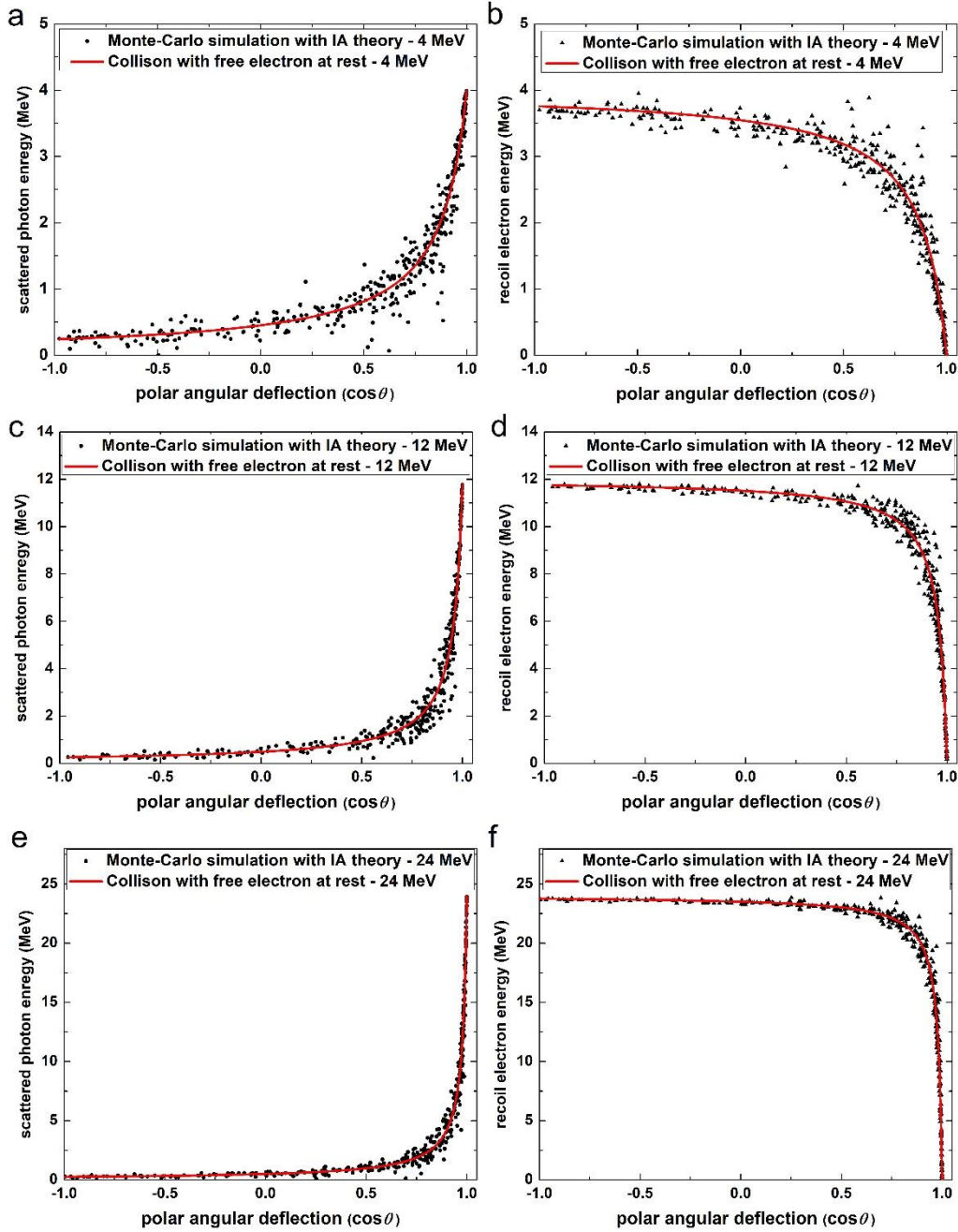


**Figure 7.3** The photon energy and the kinetic energy of recoil electron (created by Compton scattering by GOS molecule) with respect to the polar angular deflection of the scattered photon relative to the direction of the initial photon movement, for the initial photon energies of (a, b) 4 MeV, (c, d) 12 MeV and (e, f) 24 MeV.

In the Compton scattering process, the incident photon is deflected by a target electron, and loses part of its energy to the electron. As it shown in Figure 7.3 (a, c, e, g, j, and i), the more the photon is deflected from its original path (i.e.  $\cos\theta \rightarrow -1$ ),

the larger is the energy loss ( $E_0 - E'$ ). Both the Monte-Carlo simulation with the IA approximation method and the theoretical calculation using free electron collision model proves this trend. However, the deviation of the  $E' - \cos \theta$  simulated by IA based simulation method (the black dots) from the Compton line (the red line) is observed. This is caused by the correction of binding energy and Doppler broadening effects, and these two effects are suppressed as the incident photon energy increases. As it shows in the Figure 7.3, the deviation of MC simulated ( $E', \cos \theta$ ) discrete dots from the Compton line is smaller with respect to higher initial energies. The kinetic energies of the recoil electron, on the other hand, increase accordingly with the polar deflection angle.

Considering the Compton line and the binding energy of the target electron, the minimum and the maximum values of the scattered photon energy  $E'$  and the kinetic energy  $E_-$  can be approximately valued as

$$E'_{\min}(\cos \theta = -1) = \frac{1}{1 + 2\kappa} E_0, \quad E'_{\max}(\cos \theta = 1) = E_0 \quad (7.1)$$

$$E_{-, \min}(\cos \theta = 1) = 0, \quad E_{-, \max}(\cos \theta = -1) = \frac{2\kappa}{1 + 2\kappa} E_0 - U_i \quad (7.2)$$

where  $\kappa \equiv \frac{E_0}{m_e c^2} = \frac{E_0}{0.511 \text{ MeV}}$ , and  $U_i$  is the binding energy of the target electron. Here we assume that the Compton scattering event occurs when a  $\gamma$ -ray photon is scattered by a gadolinium atom. The minimum energy of scattered photon —  $E'_{\min}$ , and the maximum kinetic energy of the recoil electron for different initial photon energies are sampled with the Equation (7.1) and (7.2), and the corresponding result is listed in Table 7.1. From these values, we can see that there is always some energy left (theoretically around 0.5 MeV) for scattered photons. For the kinetic energy of recoil electron, the minimum value of  $E_{e, \max}$  corresponds to the inner K-shell electron excitation, and the

maximum value of  $E_{e,\max}$  corresponds to the photon scattered by an electron in its outmost orbit whose binding energy is almost negligible compared to the initial photon energy in the interval 4~24 MeV.

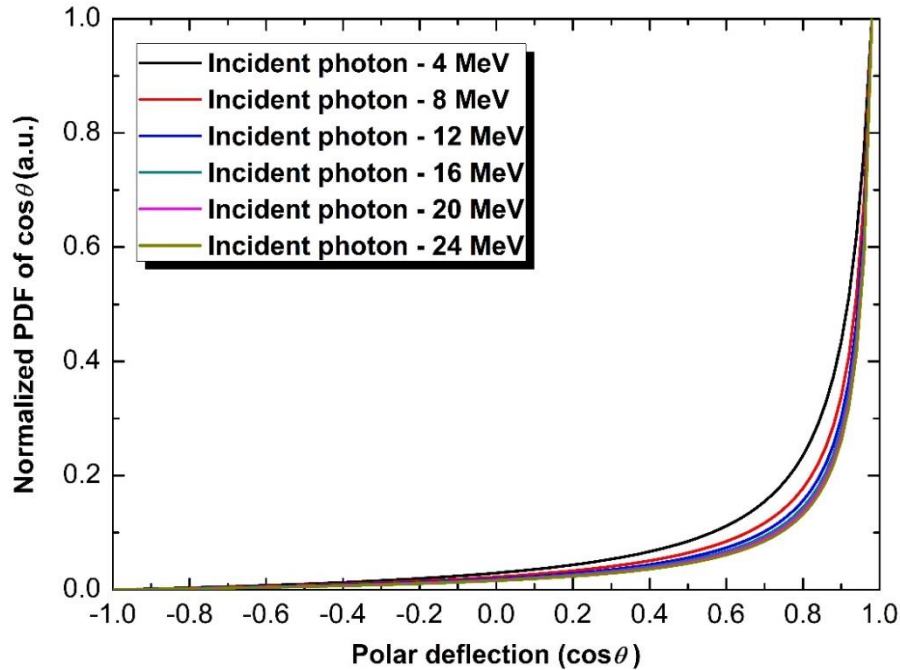


**Figure 7.4** The normalized PDF of polar deflection  $\cos\theta$  for the photon incoherently scattered by  $\text{Gd}_2\text{O}_2\text{S}$  molecules

Figure 7.3 not only gives a general idea of the relationships between the polar deflection and the energy transfer in Compton scattering, it also shows the probability distribution of  $\cos\theta$  according to the density distribution of  $(\cos\theta, E_e)$  dots against certain initial photon energies. From Fig 7.3 we can see that, the values of  $\cos\theta$  are distributed in the interval 0.5~1 and account for the major part of the sampled polar deflection  $\cos\theta$ . Furthermore, a clearer idea can be obtained by studying the probability distribution function (PDF) of polar deflection  $\cos\theta$ . The theoretical values of PDF with respect to different incident photon energies are calculated according to the expression given in Equation (3.27) (Ref [110]). As shown in Figure 7.4, the PDF for smaller polar deflection angles is larger than that for larger angles. Obviously, the

increase in PDF is witnessed for  $\cos \theta > 0.5$  indicating that the polar deflection of the photon caused by the Compton scattering is heavily forward oriented for high energy photons. The comparison of PDF for different initial photon energies, such as 4 MeV and 24 MeV, shows that photons with high initial energies are less likely to be scattered by a large polar deflection angle, which is in accordance with the dots distribution density of Monte-Carlo simulated  $(\cos \theta, E_e)$  shown in Figure 7.3.

**Table 7.1** The minimum energy of scattered photon and the maximum kinetic energy of the recoil electron after Compton scattering event in a gadolinium atom.

Photon energy MeV	$E'_{\min}$ MeV	$E_{e,\max}$ MeV
4	0.453	3.496~3.547
8	0.480	7.469~7.520
12	0.490	11.460~11.510
16	0.495	15.455~15.505
20	0.498	19.451~19.502
24	0.500	23.449~23.500

### 7.2.3 Electron-positron pair production in $\text{Gd}_2\text{O}_3$

The pair-production is only possible for the photon with energy higher than 1.02 MeV. In pair-production, the photon is totally absorbed, and an electron-positron pair is generated. The Monte-Carlo simulation of pair-production here adopts the algorithms in ref [108][123]. The kinetic energy of the electron is  $E_- = \epsilon E_0 - m_e c^2$  ( $\epsilon$  represents the electron reduced energy), and the corresponding kinetic energy of the positron generated is  $E_+ = (1 - \epsilon)E_0 - m_e c^2$ . The maximum and minimum value of  $E_-$  are

$$E_{-,max} = E_0 - 2m_e c^2, \quad E_{-,min} = 0 \quad (7.3)$$

Accordingly, the maximum and minimum value of  $\epsilon = (E_- + m_e c^2)/E_0$  are

$$\epsilon_{max} = 1 - \frac{1}{k}, \quad \epsilon_{min} = \frac{1}{\kappa} \quad (7.4)$$

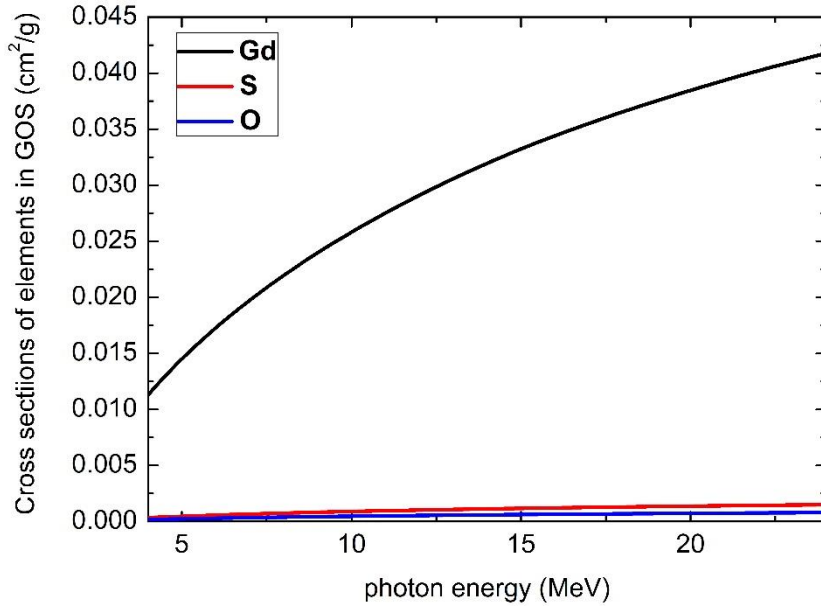


**Figure 7.5** The modified photon cross section of pair-production for the elements Gd, S and O in the scintillator  $\text{Gd}_2\text{O}_2\text{S}$ .

In the case of pair-production in the scintillator, the atoms which the photon interacts with is determined by the weight ratio and the partial mass interaction cross sections (i.e. attenuation coefficient) of the element, which is given by

$$P_i = \frac{\left(\frac{\mu_{pp}}{\rho}\right)_i \cdot w_i}{\sum_j \left(\frac{\mu_{pp}}{\rho}\right)_j \cdot w_j} \quad (7.5)$$

where  $\left(\frac{\mu_{pp}}{\rho}\right)_i$  ( $i=\text{Gd, O, or S}$ ) is the photon cross section of the pair production for an element, and  $w_i$  is weight ratio of the element in the molecule. The modified photon cross section  $\left(\frac{\mu_{pp}}{\rho}\right)_i \cdot w_i$  of the element against the photon energy in the range 4~24 MeV is plotted in Figure 7.5. The figure shows that the value of  $\left(\frac{\mu_{pp}}{\rho}\right)_i$  increases with respect to the growing photon energy. The modified photon cross section of Gd is in the interval  $1.13 \times 10^{-2} \sim 4.1810^{-2} \text{ cm}^2 \cdot \text{g}^{-1}$ , which is much larger than those of the

elements S and O (S:  $3.40 \times 10^{-4} \sim 1.50 \times 10^{-3} \text{ cm}^2 \cdot \text{g}^{-1}$ , O:  $(1.71 \times 10^{-4} \sim 7.93 \times 10^{-4} \text{ cm}^2 \cdot \text{g}^{-1})$ ). Therefore, here we only discuss the pair-production by the element Gd for simplicity. For initial photon energies in the interval 4~24 MeV, the ranges of  $E_-$  calculated with the atomic parameters of Gd are listed in Table 7.2.

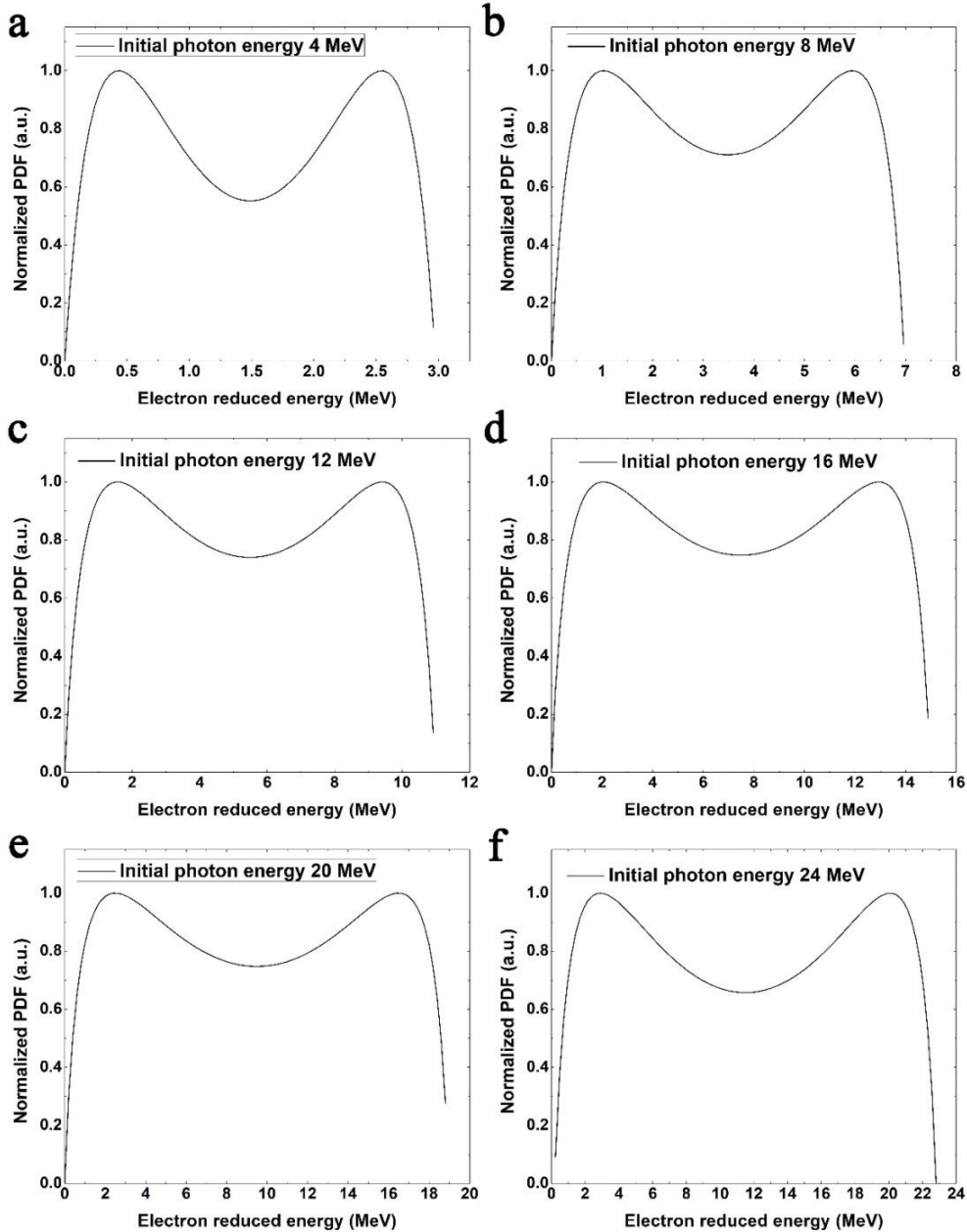


**Figure 7.6** The normalized PDF of the electron reduced energy produced by pair-production of the initial photon energy 4~24 MeV by the Gd element

The probability distribution function (PDF) of  $\epsilon$  given in Ref [108] has been introduced in Equation (3.62) (section 3.3.5, chapter 3). By calculating the PDF with

respect to the electron reduced energy  $\epsilon$ , the probability distribution of the kinetic energy  $E_-$  of the electron generated through pair-production is acquired. As is presented in Figure 7.6, the PDF of the recoil electron energy  $E_-$  shows symmetry against the value  $E_- = \frac{1}{2}E_0 - m_e c^2$  (i.e.  $\epsilon = 1/2$ ). The value PDF declines sharply near the maximum and minimum limits. Due to the symmetry of PDF, two peaks of PDF are witnessed at the electron reduced energy  $\epsilon$  of 0.768 (0.238), 0.804 (0.194), 0.823 (0.173), 0.842 (0.162), 0.846 (0.146), and 0.861 (0.141) corresponding the initial photon energy 4, 8, 12, 16, 20 and 24 MeV respectively. Compared to the recoil electron in Compton scattering, the kinetic energy of electron created by pair production is more evenly distributed in a wide energy range.

**Table 7.2** The energy limit of the secondary photon generated by pair-production

Photon Energy MeV	$E_{-,max}$ MeV	$\epsilon_{max}$	$\epsilon_{min}$
4	2.978	0.12775	0.87225
8	6.978	0.06388	0.93613
12	10.978	0.04258	0.95742
16	14.978	0.03194	0.96806
20	18.978	0.02555	0.97445
24	22.978	0.02129	0.97871

#### 7.2.4 Conclusion of the simulation of the $\gamma$ -ray photon interactions

In this section, two major photon interactions, i.e. Compton scattering and pair-production, for  $\gamma$ -ray in the energy interval 4~24 MeV were investigated via Monte-Carlo simulation and theoretical calculation. The simulation focused on the aspects of attenuation length in different media, the energy loss due to secondary electron, and

probability distribution of polar deflection and electron energy loss. The result of simulation and theoretical analysis shows that:

- i. The  $\gamma$ -ray photons travelling in  $\text{Gd}_2\text{O}_2\text{S}$  have higher attenuation coefficient and shorter mean free path length than those travelling in other materials, due to the higher density and effective atomic number of  $\text{Gd}_2\text{O}_2\text{S}$ . However, the probability of a single  $\gamma$ -ray photon absorbed by the scintillator particles in the ISOFD is quite small.
- ii. The kinetic energy recoil electron generated by Compton scattering has a positive relationship with the polar deflection angle  $\theta$  of the scattered photon, and study of the PDF of  $\cos \theta$  shows that the direction of the scattered photon is heavily forward oriented.
- iii. The kinetic energy of secondary electrons generated by pair-production is distributed in the interval  $(0, E_0 - 2m_e c^2)$ . There are two small PDF peaks in the PDF –  $\cos \theta$  figure, but in a wide energy range, the peaks are not sharp, indicating that the kinetic energy of the electron is more evenly distributed in the corresponding energy interval compared to that of recoil electrons in Compton scattering.

### **7.3 Mean free path length for electron/positron interactions**

In the previous section, the kinetic energy distribution of the electrons/positrons generated as the result of the photon interaction events (Compton scattering and electron-positron pair production) were discussed. The secondary particles (electrons and positrons) generated by the  $\gamma$ -ray interaction with  $\text{Gd}_2\text{O}_2\text{S}$  have possible kinetic energy in the order of a few MeV or tens of MeV, and carries a part or even most of the primary photon energy. These particles will generally lose energy along their transport

paths in SD or the optical fibre. Figure 7.7 shows the track of an electron (generated through photon interaction) travelling in SD and optical fibre. The propagation of the particle is terminated if the kinetic energy of the particle is totally absorbed by the medium (annihilation for positron), or the particle travels out the ISOFD model. To study the energy loss of these particles, more specifically, the energy absorbed by different media, the electron/positron transport in ISOFD is simulated with respect to the energy loss, angular deflection of the particle, the step path length between two consecutive electron interactions, and secondary radiation emission as a result of the electron/positron interaction with the media.

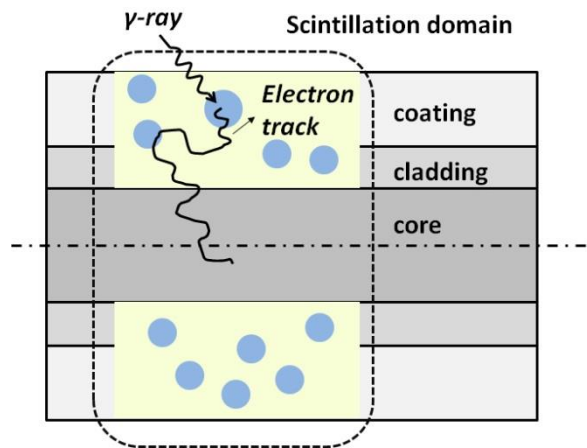


**Figure 7.7** The 2D illustration of an electron/positron travelling in SD and the optical fibre

The Monte-Carlo simulation method of the electron transport was reviewed in chapter 6. This method, is based on the ‘mixed’ algorithm proposed by Fernández-Varea et al[144] and Baró et al[142]. Combining ‘detailed’ MC method and ‘condensed’ MC method, the ‘mixed’ method models the global effect of the ‘soft’ events (i.e. the ‘condensed’ simulation) and detailed interaction process of the ‘hard’ events (i.e., the detailed simulation). The utilization of either detailed simulation method or condensed method in ISOFD modelling is determined by the kinetic energy of the electron (or

positron), the mean free path lengths of the electron interaction, and the size of the model structure. Under the condition that the kinetic energy is high,  $\lambda_{\text{el}}^{(\text{h})}(E) > 2\lambda_{\text{el}}(E)$  and the quantity of the scattering events in the media is sufficiently large, the ‘condensed’ method is applied. Otherwise, all the electron interactions (elastic scattering, inelastic collision, radiative collision, and positron annihilation for positron) should be simulated in detail in chronological order.

In the following sub-sections, the mean free path lengths of the electron interactions (elastic collision, inelastic collision, radiative collision, and positron annihilation) in different media  $\text{Gd}_2\text{O}_3$  and  $ER$  were calculated, and the applicability of the ‘detailed’ simulation method and ‘mixed’ simulation method was determined.

### 7.3.1 The elastic scattering of electrons

The elastic scattering only changes the direction of the electron. The simulation of a single elastic scattering event adopts the simulation method proposed by Fernández-Varea et al[144] (cf. chapter 6), which is based on the modified Wentzel model (‘W2D’ model). One important factor determining the utilization of ‘detailed’ or ‘condensed’ MC method is the comparison between the mean free path lengths  $\lambda_{\text{el}}(E)$  and  $\lambda_{\text{el}}^{(\text{h})}(E)$  (cf. Equation (6.8) & (6.39)). When  $\lambda_{\text{el}}^{(\text{h})}(E) < 2\lambda_{\text{el}}(E)$ , the kinetic energy of the electron is damped such that ‘condensed’ method is no longer appropriate, and the simulation becomes purely ‘detailed’. The mean free paths  $\lambda_{\text{el}}(E)$  and  $\lambda_{\text{el}}^{(\text{h})}(E)$  of the electron transport different media were calculated with respect to the kinetic energies of interest.

Section 6.1 introduced the theory of elastic scattering proposed by Baró et al[145], including analytical expressions of the total cross section  $\sigma_{\text{el}}^{(\text{W})}$ , DCS, and mean free

paths ( $\lambda_{el}$ ,  $\lambda_1$ , and  $\lambda_2$ ) for electrons and positrons scattered by atoms in a single element material with atomic number  $Z$ . The mean free path length for hard elastic event is given by (cf. Equation (6.39))

$$\lambda_{el}^{(h)}(E) = \max \left\{ \lambda_{el}(E), \min \left[ C_1 \lambda_1(E), C_2 \frac{E}{S(E)} \right] \right\} \quad (7.6)$$

Therefore, to calculate  $\lambda_{el}^{(h)}(E)$ , the mean free path lengths  $\lambda_{el}(E)$ ,  $\lambda_1(E)$  and total stopping power  $S(E)$  need to be pre-calculated.

For the compound materials  $Gd_2O_2S$ , and  $ER$ , the additivity rule was applied to calculate corresponding parameters. Taking  $Gd_2O_2S$  (GOS) for example, the mean free path length  $\lambda_{el,GOS}$  is

$$\lambda_{el,GOS} = 1 / \sum_i \sigma_{el,i}^{(W)} N_i \quad (7.7)$$

where  $\sigma_{el,i}^{(W)}$  (cf. Equation (6.5)) is the total elastic cross section of  $i$ th element ( $'i'$  represents Gd, O, or S) respectively.  $N_i$  is the number of the atoms with the same atomic number  $Z_i$  per unit volume, and is given by

$$N_i = \frac{N_A \rho_{GOS}}{A_{GOS}} n_i \quad (7.8)$$

in which  $\rho_{GOS}$  and  $A_{GOS}$  are the density and the molecular weight of  $Gd_2O_2S$ , and  $n_i$  is the number of  $i$ th element atoms per molecule. The first and second mean free paths are also calculated with the additivity rule as

$$\lambda_{1,GOS} = \left( \sum_i \sigma_{el,i}^{(W)} N_i G_{1,i}^{(W)} \right), \quad \lambda_{2,GOS} = \left( \sum_i \sigma_{el,i}^{(W)} N_i G_{2,i}^{(W)} \right) \quad (7.9)$$

where  $G_{1,i}^{(W)}$  and  $G_{2,i}^{(W)}$  are the first and second transport coefficient for  $i$ th element (cf. Equation (6.9)). The analytical expression of stopping power  $S(E) = S_{col}(E) + S_{rad}(E)$  is given in chapter 6, however, for the simplicity of calculation, a numerical value of  $S_{GOS}(E)$  were required from the 'ESTAR' physical measurement

Laboratory[147]. It should be noted that, the positron shares exactly the same values of elastic scattering related parameters with those of an electron with the same kinetic energy, thus here we only consider the elastic scattering event of electrons.

Abovementioned paragraphs give a brief insight into computing the mean free path lengths  $\lambda_{el}$ ,  $\lambda_1$  and  $\lambda_2$  of electron travelling in compound materials. To calculate the mean free path of 'hard' elastic events ( $\lambda_{el}^{(h)}$ ), the custom parameters  $C_1$  and  $C_2$  were set to be 0.05, so as to require stable simulation results while saving time. The related parameters of fast electron transport in *ER* were also calculated with the same method, and corresponding values are listed in Table 7.3. The result shows that in the energy interval 4~24 MeV,  $\lambda_{el,GOS}$ —the mean free path length of the practical elastic scattering event in  $Gd_2O_2S$  is in the interval 0.173~0.176  $\mu m$ , while in *ER*,  $\lambda_{el,ER}$  increases from 1.109  $\mu m$  to 1.123  $\mu m$  as energy grows. The value of  $\lambda_{el}$  seems quite insensitive to the kinetic energy change for high energetic electrons. This short distance indicates that the electron might go through a considerable number of elastic collisions before totally being absorbed or travelling out of the scintillator particle.  $\lambda_{el}^{(h)}(E)$  of the 'hard' elastic scattering event is much larger than that of practical elastic event in both media, i.e.  $\lambda_{el}^{(h)}(E) \gg 2 \lambda_{el}(E)$ , therefore, from the aspect of the free path length, the 'condensed' method is appropriate for simulating electron transport in media with large over dimensions. However, the simulation of electron transport in an ISOFD of limited size is a more much complicated situation, as it considers not only the theoretical mean free path lengths of related electron scattering event, but also the collision at the boundaries of different materials. In some extreme cases, where the size of the medium is so small that the actual number of scattering events in each track step segment is not large enough to use 'condensed' method. Therefore, in the following sections, the mean

free path lengths of the ‘hard’ events for electron scattering are calculated, and then a simplified simulation of the electron transport is run with a single scintillator-particle model.

**Table 7.3** the mean free paths of elastic scattering

Energy MeV	Gd <sub>2</sub> O <sub>2</sub> S		ER	
	$\lambda_{el,GOS}$ $\mu\text{m}$	$\lambda_{el,GOS}^{(h)}$ $\mu\text{m}$	$\lambda_{el,ER}$ $\mu\text{m}$	$\lambda_{el,ER}^{(h)}$ $\mu\text{m}$
4	0.173	67.895	1.109	2674.026
6	0.174	134.256	1.117	5342.055
8	0.174	220.426	1.120	8829.173
10	0.174	325.752	1.121	13111.2
12	0.174	449.750	1.122	18170.04
14	0.174	592.037	1.122	23991.34
16	0.174	752.297	1.123	30563.29
18	0.174	930.265	1.123	37875.86
20	0.175	1125.711	1.123	45920.42
24	0.175	1568.259	1.123	64175.94

### 7.3.2 The inelastic collisions between electrons and Gd<sub>2</sub>O<sub>2</sub>S

In chapter 6, the simulation method of inelastic collision between electrons and media based on a generalized oscillator strength model, which is described by Liljequist et al[148] and Salvat et al[126], is reviewed. In this method, each subshell of an atom is treated as an oscillator with a single oscillator with strength  $f_i$  equal to the number of electrons in the shell and resonance energy  $W_i = aU_i$ , where  $U_i$  is the shell binding energy. The coefficient  $a$  is valued with the atomic shell data (e.g. electron binding energies and the number of electrons in each shell) and the mean excitation energy  $I$  of the atom (cf. Equation (6.12) and Equation (6.13)). The mean free path length  $\lambda_{col}(E)$  and stopping power  $S_{col}(E)$  were calculated with the semi-empirical expressions (cf.

Equation (6.25) and Equation (6.26)) with respect to electron kinetic energy in the interval 4~8 MeV.

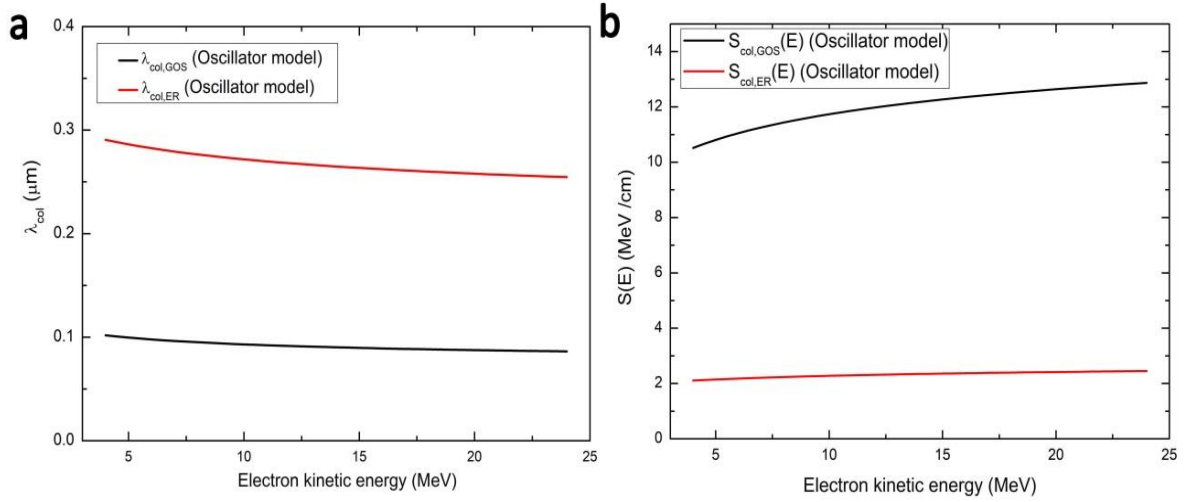


**Figure 7.8** (a) The mean free path length  $\lambda_{col}$ , and (b) energy stopping power  $S(E)$  of the electron inelastic collision in the media  $\text{Gd}_2\text{O}_2\text{S}$  and  $ER$  for electron kinetic energy in the interval 4~24 MeV.

The mean free path lengths of inelastic collision in  $\text{Gd}_2\text{O}_2\text{S}$  and  $ER$  calculated with the oscillator model are shown in Figure 7.8(a). For the electron energy of interest,  $\lambda_{col}$  of the electron in both media gradually decreases as the electron kinetic energy grows. The mean free path length  $\lambda_{col,GOS}$  is close to 0.1  $\mu\text{m}$ , which is shorter than than  $\lambda_{col,ER}$  (near 0.3  $\mu\text{m}$ ) due to the higher electron density of  $\text{Gd}_2\text{O}_2\text{S}$ . The stopping power  $S(E)$  of the scintillator shown in Figure 7.8(b) is in the interval 10.51~12.87  $\text{MeV} \cdot \text{cm}^{-1}$ , while  $S_{col,ER}(E)$  is in the interval 2.11~2.45  $\text{MeV} \cdot \text{cm}^{-1}$ , which is in accordance with the electron density and collision stopping power of the correspond material.

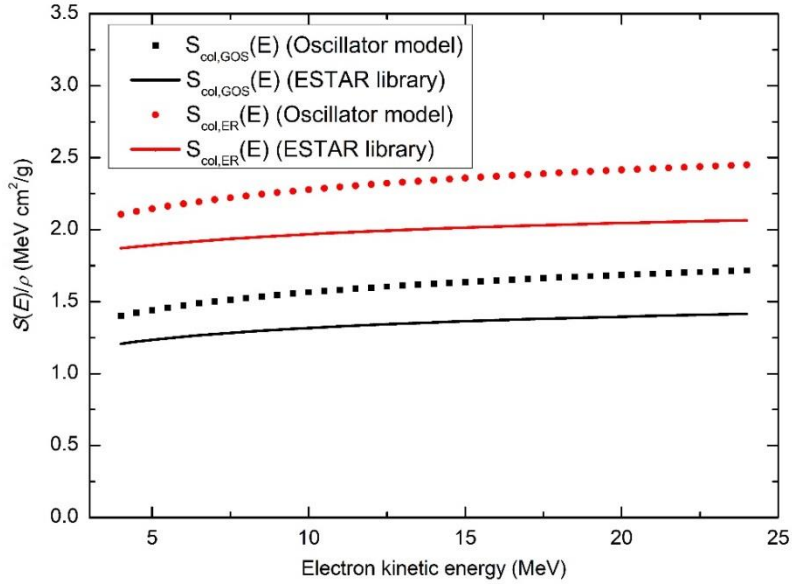


**Figure 7.9** The ratio  $S(E)/\rho$  (MeV·cm<sup>2</sup>/g) calculated with the oscillator model (dot) and those acquired from the ESTAR library (line) for electrons transport in the media Gd<sub>2</sub>O<sub>2</sub>S and ER.

The  $S_{\text{col}}(E)/\rho$  results calculated is compared those acquired from the ESTAR library in Figure 7.9. The stopping power  $S(E)/\rho$  sampled with ‘oscillator’ model is a little bit higher than those tabulated in ESTAR database. This is because that although the electron interaction data in Ref[126] is obtained by the method similar to the data calculation method adopted by ESTAR database, the ‘oscillator’ approximation model in Ref[126] uses slightly different oscillator strengths  $f_i$  and excitation energies  $I$ , which leads to the deviation from the ESTAR data.

Now we consider the ‘hard’ inelastic collision ( $\lambda_{\text{col,GOS}}^{(h)}$ ) in the medium Gd<sub>2</sub>O<sub>2</sub>S. Setting the critical energy loss  $W_{\text{cc}}$  as 5 KeV, the mean free path length  $\lambda_{\text{col,GOS}}^{(h)}$  and the energy stopping power in the form of  $S(E)/\rho$  with respect to different electron energies are listed in Table 7.4. Similar to elastic scattering discussed in last section,  $\lambda_{\text{col,GOS}}^{(h)}$  of the electron’s hard inelastic collision event is much larger than the path

length  $\lambda_{\text{col,GOS}}$  of practical collision event (nearly 800 times). As for the inelastic collision of positrons, the mean free path length  $\lambda_{\text{p,col}}$  is longer than that of electrons, owing to the smaller energy stopping power  $S_{\text{p,col}}(E)$  of the positron.

**Table 7.4** The mean free path length of inelastic collision ( $\lambda_{\text{col,GOS}}$ ,  $\lambda_{\text{col,GOS}}^{(\text{h})}$ ) for electrons and positrons transport in the medium  $\text{Gd}_2\text{O}_2\text{S}$ .

Energy MeV	Electron			Positron		
	$\lambda_{\text{e,col}}$ $\mu\text{m}$	$\lambda_{\text{e,col}}^{(\text{h})}$ $\mu\text{m}$	$S_{\text{e,col}}(E)/\rho$ $\text{MeV} \cdot \text{cm}^2/\text{g}$	$\lambda_{\text{p,col}}$ $\mu\text{m}$	$\lambda_{\text{p,col}}^{(\text{h})}$ $\mu\text{m}$	$S_{\text{p,col}}(E)/\rho$ $\text{MeV} \cdot \text{cm}^2/\text{g}$
4	0.102	80.964	1.402	0.514	94.478	1.139
6	0.098	79.574	1.473	0.486	91.263	1.2303
8	0.095	78.521	1.525	0.469	89.057	1.295
10	0.093	77.705	1.565	0.458	87.429	1.345
12	0.092	77.048	1.597	0.446	86.157	1.386
14	0.090	76.505	1.624	0.438	85.125	1.420
16	0.089	76.046	1.647	0.431	84.263	1.450
18	0.088	75.650	1.667	0.426	83.526	1.478
20	0.088	75.304	1.685	0.421	82.886	1.499
22	0.087	74.997	1.701	0.417	82.322	1.519
24	0.086	74.723	1.716	0.413	81.821	1.538

### 7.3.3 Bremsstrahlung emission in $\text{Gd}_2\text{O}_2\text{S}$

In last chapter, Bremsstrahlung emission, the radiative energy loss process, was described with the algorithm given in Ref [126]. This algorithm utilizes corrected Bethe-Heitler DCS for electrons (cf. Equation (6.27) and (6.28)), which is quite similar to the DCS of the pair-production of the photon interaction. In the expression of  $d\sigma_{\text{BHW}}/dW$ , the energy loss  $W$  is replaced by the variable  $\epsilon \equiv W/(E_0 + m_e c^2)$  for convenience of calculation. As the total cross section for Bremsstrahlung emission is infinite when integrating DCS over  $W$  in the interval  $0 \sim E_0$ , thus the cutoff energy  $W_{\text{cr}}$  is chosen as the lower energy loss limit, in this study, the value of  $W_{\text{cr}}$  is set as 5 KeV.

The mean free path length of the radiative energy loss  $\lambda_{\text{rad}}$  and the energy stopping power  $S(E)/\rho$  corresponding to the electron and positron travelling in  $\text{Gd}_2\text{O}_2\text{S}$  are calculated.

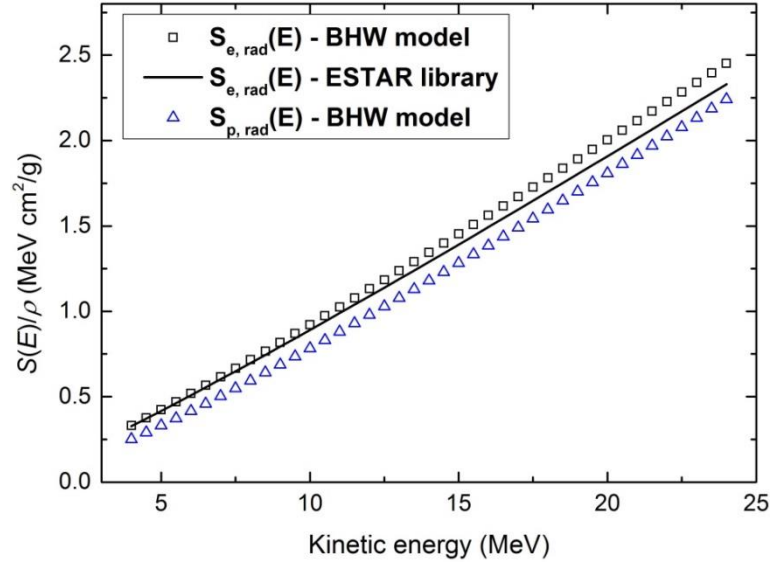


**Figure 7.10** The energy stopping power  $S(E)/\rho$  of radiative energy loss (i.e., the Bremsstrahlung emission) for electrons and positrons in  $\text{Gd}_2\text{O}_2\text{S}$ .

The energy stopping power calculated with  $d\sigma_{\text{BHW}}/dW$  for the electrons' Bremsstrahlung effect is compared with that tabulated in the ESTAR library. The  $S_{e,\text{rad}}(E)/\rho$  calculated with BHW DCS coincides well with the ESTAR data at relatively low kinetic energies, but the deviation grows at higher energies. This is caused by the approximation applied. For the simulation of radiative energy loss in the compound, 'equivalent' single-element material is used to replace the molecule with the method in Ref [142]. The equivalent atomic number, atomic weight and atomic density of the equivalent single element to approximate  $\text{Gd}_2\text{O}_2\text{S}$  are 55.2,  $140.57 \text{ g} \cdot \text{mol}^{-1}$ , and  $3.46 \times 10^{28} \text{ m}^{-3}$  respectively. The screening factor,  $R$ , of cesium ( $Z=55$ ) is used. The error caused by this approximation is enhanced at higher electron kinetic energies. The ESTAR library only lists the energy stopping power for electrons, thus here only the

values of  $S_{p,\text{rad}}(E)/\rho$  (BHW model) are plotted in Figure 7.10. The result shows that, for the radiative energy loss,  $S_{p,\text{rad}}(E)/\rho$  for positrons is slightly lower than  $S_{e,\text{rad}}(E)/\rho$  for electrons, which is in accordance with the correction factor  $F_P(Z, E) < 1$  introduced into the radiative DCS  $d\sigma_{\text{BHW}}^{(-)}/d\epsilon$  for electrons in order to produce the correct DCS  $d\sigma_{\text{BHW}}^{(+)}/d\epsilon$  of radiative energy loss for positrons.

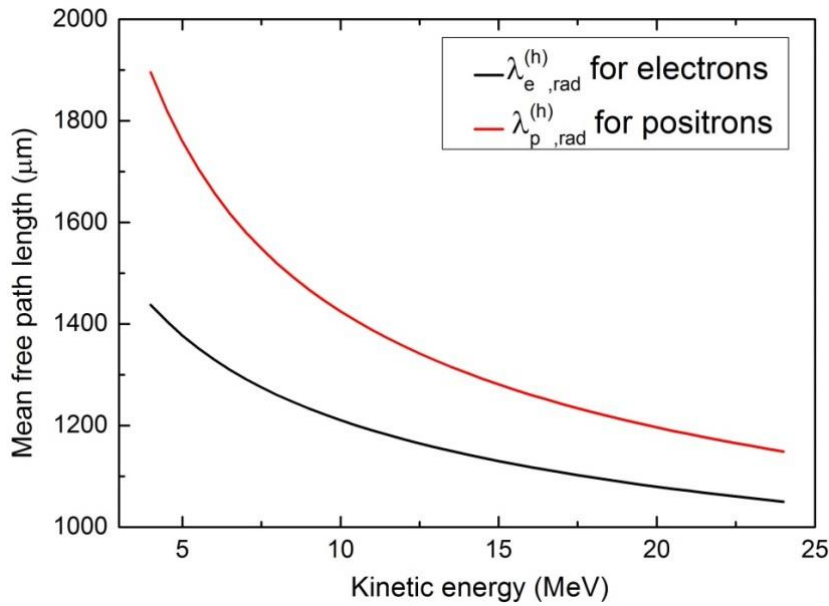


**Figure 7.11** The mean free path lengths of ‘hard’ radiative event for electrons ( $\lambda_{e,\text{rad}}^{(h)}$ ) and positrons ( $\lambda_{p,\text{rad}}^{(h)}$ ) travelling in  $\text{Gd}_2\text{O}_2\text{S}$

The mean free path lengths of a ‘hard’ radiative energy loss event for electrons and positrons in  $\text{Gd}_2\text{O}_2\text{S}$  are shown in Figure 7.11. The mean free path length of the radiative event for the positron is higher than that of the electron, owing to the smaller DCS of the radiative energy loss (i.e. bremsstrahlung emission) for the positron compared to that of the electron (see Equation (6.29) at Page 175 for more detail). The length  $\lambda_{\text{rad}}^{(h)}$  for electrons and positrons both decrease with respect to the growing kinetic energies, and  $\lambda_{e,\text{rad}}^{(h)}$  is clearly larger than  $\lambda_{p,\text{rad}}^{(h)}$ . Under the condition that the cutoff

energy is  $W_{cr} = 5$  KeV,  $\lambda_{e,rad}^{(h)}$  of an electron with the kinetic energy 4 MeV is about 1438  $\mu\text{m}$ , and this value drops to 1050  $\mu\text{m}$  for the kinetic energy of 24 MeV. As for positrons,  $\lambda_{p,rad}^{(h)}$  falls from 1895  $\mu\text{m}$  to 1149  $\mu\text{m}$ . Though  $\lambda_{rad}^{(h)}$  is reduced by growing electron/positron energy,  $\lambda_{rad}^{(h)}$  is still much higher than the mean size of the scintillation-domain of the ISOFD, indicating the small probability of Bremsstrahlung emission during the particle transport process.

### 7.3.4 Positron annihilation

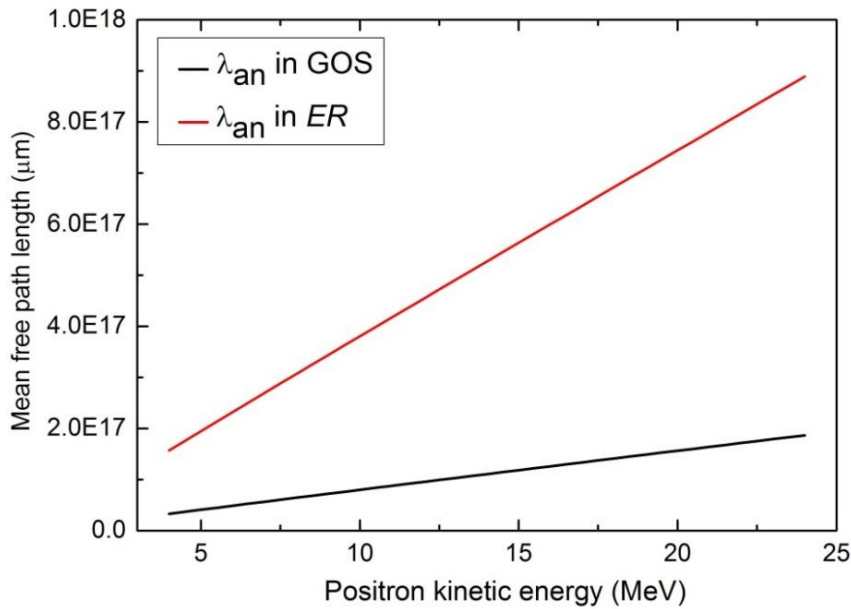


**Figure 7.12** The mean free path length  $\lambda_{an}$  for positron annihilation in media  $\text{Gd}_2\text{O}_2\text{S}$  and  $ER$ .

The simulation of positron annihilation is considered for a positron travelling in the medium. Though multiple photons may be generated during this interaction, here we only consider the two-photon emission process. With the expression of mean free path length for positron annihilation  $\lambda_{an}^{-1}$  given in Equation (6.33),  $\lambda_{an}$  for positron transport in the media  $\text{Gd}_2\text{O}_2\text{S}$  and  $ER$  are calculated and presented in Figure 7.12. The mean free path length  $\lambda_{an}$  increases accordingly with the positron energy.  $\lambda_{an}$  in  $\text{Gd}_2\text{O}_2\text{S}$  is

shorter than that in *ER*, indicating the larger cross section of positron annihilation in  $\text{Gd}_2\text{O}_3$ . The reason seems obvious, the electron density of  $\text{Gd}_2\text{O}_3$  and *ER* are  $4.006 \times 10^{29} / \text{m}^3$  and  $1.908 \times 10^{30} / \text{m}^3$  respectively. As the positron is annihilated by colliding with an electron, the probability is determined by the electron density of the material (also shown in Equation (6.33)), thus the probability of positron annihilation in  $\text{Gd}_2\text{O}_3$  clearly higher than that in *ER* of lower electron density. On the other hand, the value of  $\lambda_{an}$  is much smaller than the mean free path length of other positron interactions, therefore the probability of positron annihilation is the minimum among all electron interactions.

### 7.3.5 The mean free path length for general electron interactions

In the previous 5 sub-sections, the mean free path lengths of three major types of electron interactions with  $\text{Gd}_2\text{O}_3$ , both practical (for ‘detailed’ simulation method) and hard (for ‘condensed’ simulation method), were calculated and investigated. With these tabulated values, the mean free path length of an electron/positron transport in the medium is

$$\frac{1}{\lambda_{\text{mean}}} = \frac{1}{\lambda_{\text{el}}} + \frac{1}{\lambda_{\text{col}}} + \frac{1}{\lambda_{\text{rad}}} + \frac{1}{\lambda_{\text{an}}} \quad (7.10)$$

This value represents the average path length an electron travelled between the successive practical electron interaction events. As for the mean free path length of combined ‘hard’ electron interactions, the mean free path length  $\lambda_{\text{mean}}^{(h)}$  is given by

$$\frac{1}{\lambda_{\text{mean}}^{(h)}} = \frac{1}{\lambda_{\text{el}}^{(h)}} + \frac{1}{\lambda_{\text{el}}^{(h)}} + \frac{1}{\lambda_{\text{el}}^{(h)}} + \frac{1}{\lambda_{\text{an}}} \quad (7.11)$$

The existence of  $\lambda_{an}$  is taken into account only for positron interactions.

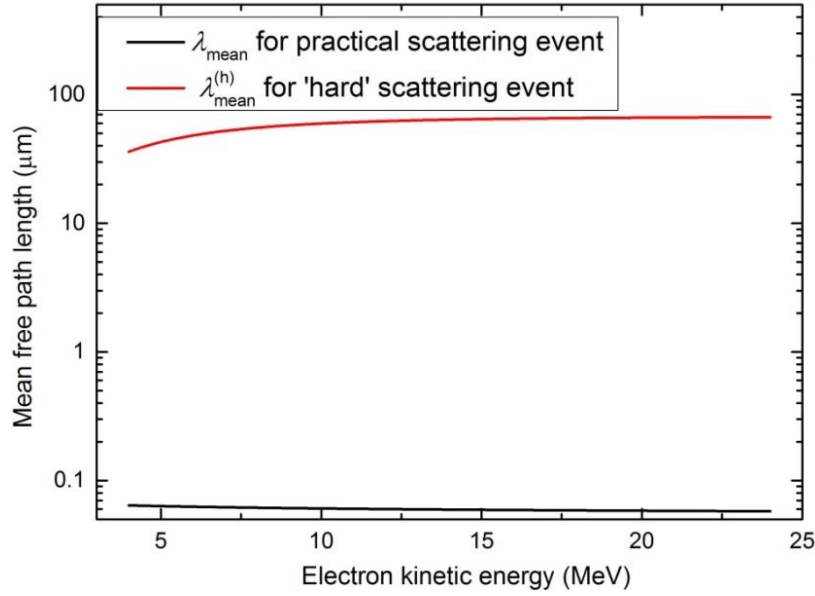


**Figure 7.13** The mean path length for general practical and ‘hard’ electron scattering event for electrons with kinetic energy of 5~24 MeV in  $\text{Gd}_2\text{O}_2\text{S}$  material.

The mean free path length of general electron scattering events calculated with Equation (7.10) and (7.11) are shown in Figure 7.13. The path length  $\lambda_{\text{mean}}$  of practical scattering event is in the range 0.057~0.064  $\mu\text{m}$ , while  $\lambda_{\text{mean}}^{(h)}$  of ‘hard’ scattering event is between 36.003~66.788  $\mu\text{m}$ . The mean free path length  $\lambda_{\text{el}}^{(h)} \gg \lambda_{\text{el}}$  calculated in section 7.2.1 indicates that the ‘mixed’ MC simulation method seems favorable for the electron kinetic energy of interest, and the ratio of  $\lambda_{\text{mean}}^{(h)}$  to  $\lambda_{\text{mean}}$  shown in Figure 7.12 also supports this point. However, the mean free path length  $\lambda_{\text{el}}^{(h)}$  of the hard event is also much larger compared to the mean size of  $\text{Gd}_2\text{O}_2\text{S}$  particle (e.g.,  $r_p$  simulated in last chapter is 2  $\mu\text{m}$ ). If the ‘mixed’ simulation method applied, the randomly sampled electron transport step length  $t (= -\lambda_{\text{mean}}^{(h)} \ln \xi)$  has a great probability of exceeding  $2r_p$ , introducing more uncertainties into the simulation. Though minimizing the cutoff parameters  $C_1$ ,  $C_2$ ,  $W_{\text{cc}}$  and  $W_{\text{cr}}$  can shorten  $\lambda_{\text{mean}}^{(h)}$  and the difference between  $\lambda_{\text{mean}}^{(h)}$  and  $r_p$ , it will also make the simulation process inefficient and closer

to the detailed simulation. Therefore, the ‘detailed’ simulation method is more appropriate for modeling of electron transport in a  $\text{Gd}_2\text{O}_2\text{S}$  particle with the kinetic energy as high as a few tens of MeV.

### **7.3.6 Conclusion of the electron/positron interactions theoretical calculation**

In the above sections, regarding the secondary electron/positron transport in the medium of ISOFD, the mean free path lengths  $\lambda$  and energy stopping power  $S(E)$  of electron/positron scattering events for secondary particles (electron and positron) with the kinetic energy in the interval 4~24 MeV were investigated. The comparison of the mean free paths in different materials shows that an electron is more easily absorbed in the materials with higher atomic numbers and electron densities. On the other hand, for different electron scattering events, the elastic scattering and inelastic collisions exhibit much shorter mean free path lengths compared to Bremsstrahlung emission, indicating a much greater interaction probability for the electron energy of interest.

The feasibility of different electron transport simulation methods was also discussed from the aspects of the mean free path lengths of practical and ‘hard’ electron interactions, and also the size of a scintillator particle. Thoroughly considering the magnitude of the mean free path length  $\lambda$ ,  $\lambda^{(h)}$  and the scintillator-particle size  $r_p$ , the ‘detailed’ simulation method of explicit electron interactions was chosen over the ‘mixed’ simulation method for the study of electron transport in a single scintillator particle in the next section.

## **7.4 The simulation of the electron transport in a single scintillator particle**

The previous section focused on the important parameters relating to the electron/positron energy attenuation, including the energy stopping power and the mean free path length of practical and ‘hard’ electron interaction in the materials constituting

SD of ISOFD. In this section, the process of electron transport in a single scintillator-particle is simulated using ‘detailed’ simulation method with the tabulated mean free path length and energy stopping power for electron interactions calculated in previous sections. The simulation samples the energy loss and deposition as well as the angular deflection caused by the electron scattering events for the secondary electrons transport in  $\text{Gd}_2\text{O}_2\text{S}$  material.

#### 7.4.1 The simulation method

The MC simulation of the electron attenuation in the scintillator part of ISOFD utilizes a single  $\text{Gd}_2\text{O}_2\text{S}$  scintillator particle model. The simulation models the energy loss caused by the inelastic scattering collision and the Bremsstrahlung emission and the angular deflection caused by the elastic scattering and the inelastic collision. The energy loss of inelastic collisions is assumed to be locally absorbed by the scintillator, and transferred to the scintillation light. The radiative energy loss of electrons is in the form of Bremsstrahlung emission and does not contribute to the scintillation process. The reason for this treatment is that the probability of radiative energy loss is much smaller compared to other electron interactions, and neglecting it does not affect the outcome of the energy absorption for scintillation. Moreover, the spectrum of Bremsstrahlung is quite complicated to simulate, and also time consuming.

The input parameters to initialize the simulation include: the physical properties of the scintillator (material density and molecule formula), the average size of the scintillator particle, the atomic data of elements like the number of subshell electrons [124], the mean excitation energies of elements[141], the screening radius  $r_s$  (for radiative event)[108], the mean free path lengths calculated in section 7.3, the energy stopping power from ESTAR database[147] and the cutoff energy for electron total absorption  $E_{\text{abs}}$  (= 50 KeV).

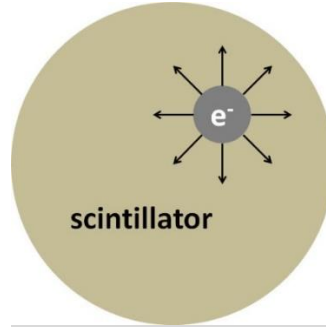


**Figure 7.14** A schematic of an electron moving in the arbitrary direction inside a scintillator particle.

As shown in Figure 7.14, assume the particle center is in the original point  $(0, 0, 0)$ , and the simulation of the electron transport follows the process as:

- i. A new electron with an initial kinetic energy  $E$  is generated in an arbitrary location  $\mathbf{r}_0$  inside the particle. The electron moves in a random isotropic direction  $\vec{\mathbf{d}}$ . The total looping time  $n_{\text{looping}}$  is increased by 1  $n_{\text{looping}} \leftarrow n_{\text{looping}} + 1$ .
- ii. Acquire the mean free path length  $\lambda_{\text{mean}}$  of electron interactions with respect to the energy  $E$  from the tabulated data of  $\lambda_{\text{mean}}$ . Generate a random number  $\xi$ , the step length is randomly sampled as  $l = -\lambda_{\text{mean}} \ln \xi$ , where  $\xi$  is a pseudo-random number between 0~1.
- iii. The electron moves a distance  $l$  towards the direction  $\vec{\mathbf{d}}$  to the next electron interaction site  $\mathbf{r}_0 \leftarrow \mathbf{r}_0 + \vec{\mathbf{d}} \cdot l$ .
- iv. If the electron travels out of the particle, go to step (vi).
- v. The type of the electron interaction is determined by the probabilities of the electron interactions (cf. Equation (6.47)), then the energy loss  $W$  and angular deflection  $\theta$  are sampled according to the corresponding DCS. The azimuth deflection angle  $\varphi$  is randomly sampled as  $2\pi\xi$ . Perform the rotation of the

movement direction  $\vec{d} \leftarrow \mathbf{R}(\theta, \varphi)\vec{d}$  (the transferring method cf. section 4.2 in chapter 4). The kinetic energy of the electron is reduced as  $E \leftarrow E - W$ . If  $E < E_{abs}$ , the electron is captured by the material and its kinetic energy is totally absorbed, otherwise go to step (ii).

- vi. The simulation of the track of this electron inside the scintillator particle is terminated. If  $n_{looping} < 10^4$ , go to step (i), otherwise, the whole simulation process is terminated.

The output parameters include the average interaction numbers of each electron interaction event ( $\bar{n}_i$  where 'i' stands for 'el', 'col' or 'rad') per electron experienced, the average energy absorbed by the scintillator via inelastic collisions ( $\overline{W_{col}}$ ), and the average energy of the Bremsstrahlung emission for an electron ( $\overline{W_{rad}}$ ).

#### 7.4.2 The simulation result and discussion

The average energy loss and electron scattering number for electron transport in the scintillator particle is listed in Table 7.5. For certain initial electron energies, the energy loss caused by the inelastic collision is much higher than the radiative energy loss due to Bremsstrahlung emission. For example, when the initial electron energy is 4 MeV, the collision energy loss is  $\overline{W_{col}} = 6.38 \times 10^{-2}$  MeV, which is about 380 times that of  $\overline{W_{rad}}$ . This confirms that the energy deposition of secondary electrons inside the scintillator particle is via inelastic collisions with  $Gd_2O_2S$  molecule. From the aspects of efficiency of the scintillator for electron energy absorption, the energy attenuation by a single  $Gd_2O_2S$  particle is quite low ( $\sim 0.057\%$ ). However, compared to the  $\gamma$ -ray photon interactions, the mean free path length between successive electron interactions is shorter, indicating a high probability energy absorption event, just as  $\bar{n}_{col}$  shown in Table 7.5. Since the Compton scattering and pair-production interactions are dominant for  $\gamma$ -ray absorption,

and secondary electron emission is inevitable, this high probability of inelastic collision guarantees a stable contribution to the generation of the scintillation light for every  $\gamma$ -ray photon interaction with a scintillator particle.

On the other hand, the change of initial electron energy has little effect on the average energy loss  $\overline{W_{\text{col}}}$ . The energy attenuation  $\overline{W_{\text{col}}}$  of electrons is in the range 5.55E-2~6.38E-2 MeV (i.e. 55.2~63.8 KeV). This range is very narrow considering the initial electron changes from 0.5 MeV to 24 MeV. This insensitivity of  $\overline{W_{\text{col}}}$  to the electron kinetic energy in the energy interval 0.5~24 MeV can be explained by the energy stopping power shown in Figure 7.7.  $S(E)$  only changes slightly with respect to the kinetic energy increase. Considering the limited angular deflection caused by the scattering event, statistically, the average distance of the electron transport inside the scintillator particle is only dependent of the particle radius. Therefore, under the condition that the average path length inside the particle and energy stopping power remains almost stable, the value of  $\overline{W_{\text{col}}}$  will be stable for the kinetic energy of interest. The deviation of the value of  $\overline{W_{\text{col}}}$  from energy stopping power might be caused by the limited number of electrons sampled and therefore, needs further investigation.

**Table 7.5** The average energy loss, and average numbers of electron scattering events

Energy MeV	$\overline{W_{\text{col}}}$ MeV	$\overline{W_{\text{rad}}}$ MeV	$\overline{n_{\text{el}}}$	$\overline{n_{\text{col}}}$	$\overline{n_{\text{rad}}}$
0.5	6.12E-2	1.40E-05	9.5	14.1	7.50E-04
4	6.38E-2	1.68E-04	7.4	12.5	1.10E-03
6	5.55E-2	1.24E-04	6.3	11.1	1.60E-03
10	5.72E-2	1.88E-06	6.3	11.8	6.31E-04
20	6.36E-2	5.06E-06	7.1	13.9	1.28E-04
24	6.38E-2	5.68E-04	7.0	14.0	1.24E-03

### 7.4.3 Conclusion of the electron transport

In this section, the electron transport in a single scintillator particle model is simulated with respect to the electron energy in the range 0.5~24 MeV. The result of the sampled energy loss verifies that the inelastic collision is the dominant energy attenuation and absorption mechanism of the electron transport in  $\text{Gd}_2\text{O}_2\text{S}$ , while the radiative energy loss caused by the Bremsstrahlung emission is almost negligible. The energy deposited in a single  $\text{Gd}_2\text{O}_2\text{S}$  particle accounts for a very small portion of the total electron energy. The comparison of the average collision energy loss with respect to different electron energy confirms that for initial electron energy in the interval 0.5~24 MeV, the collision energy loss  $\overline{W}_{\text{col}}$  experienced by each electron is independent of the electron energy, and would only be affected by the size of the scintillator particle.

### 7.5 Conclusions

This chapter focused on the  $\gamma$ -ray detection of ISOFD via the simulation of  $\gamma$ -ray photon interactions, secondary particle (electrons and positrons) generation, and the electron interaction within the scintillator particles. Firstly the  $\gamma$ -ray interactions with media constituting ISOFD were investigated. The comparison of the attenuation lengths of  $\gamma$ -ray photons in different materials has confirmed that the absorption of the  $\gamma$ -ray energy inside the scintillation-domain mainly depends on the photon interactions with  $\text{Gd}_2\text{O}_2\text{S}$  scintillator particles. The incoherent scattering and electron-positron pair production have been proved to be the dominant photon interactions. The energy and angular distribution of the secondary electrons and positrons which were generated during photon interactions have been studied with the MC simulation method and the result demonstrated a narrow kinetic energy distribution of recoil electrons (for Compton scattering) and a wider energy distribution of electrons produced via pair-production.

Regarding the energy deposition of the secondary electrons and positrons in SD, the theoretical calculation of the energy attenuation of electrons via electron interactions was carried out. For electrons and positrons travelling in  $\text{Gd}_2\text{O}_2\text{S}$  with kinetic energies in the energy range 4~24 MeV, the mean free path lengths and energy stopping powers of different electron interaction types were calculated. Corresponding parameters calculated are consistent with the existing electron interaction library. The inelastic collision and elastic scattering have a small mean free path length and demonstrated a large interaction probability inside the scintillator particle. The detailed MC simulation method has been identified as a feasible method to simulate the electron transport in the scintillation-domain. Furthermore, a single sphere model was used to study the electron attenuation in the  $\text{Gd}_2\text{O}_2\text{S}$ . The inelastic scattering proves to be the major energy absorption mode for electrons, which contribute to the scintillation process and the detection of  $\gamma$ -rays. However, the energy absorbed by the scintillator particle accounts for a very small portion of the electron energy. Furthermore, the comparison of the simulation result with different electron energies demonstrated that, for electrons with kinetic energy in megavolts energy range, the energy attenuation and absorption by the scintillator particle has little energy dependence, which is in accordance with the relative energy stopping power for electrons. However, this energy-independent behavior needs more investigation for wider initial energy range. Furthermore, the integration of the  $\gamma$ -ray interaction and the secondary electrons and positron transport simulations is necessary to study the overall  $\gamma$ -ray detection efficiency of the ISOFD.

## Chapter 8 — Conclusion and future work

### Conclusion

This thesis has focused on the theoretical investigation of ISOFD for use in real-time in-vivo radiotherapy dosimetry. The problems encountered by current ISOFDs reported have been examined. Firstly, the coupling efficiency between the scintillation-domain and the optical fibre needs improving for the efficient transmission of scintillation light. Secondly, ISOFDs exhibit a non-linear energy-dependence to the incident X-ray radiation over different energy ranges. Thirdly, the distributed radiation dose monitoring with MPSOFD is attractive, but challenging to achieve with inorganic scintillators. However, most of the reported research has tried to solve these problems with purely empirical methods. The investigation of the incident radiation absorption mechanisms, and the relationship between the scintillation light extraction efficiency and the sensor configuration are inadequate.

Regarding the above problems, in this thesis, the Monte-Carlo simulation method has been utilized, for the first time, to assist in the development of an ISOFD. Aspects of scintillation taken into account are: material selection, scintillator-optical fibre configuration optimization, and radiation detection mechanism investigation. To establish the proper ISOFD model for the simulation, the background of SOFD development was first reviewed in chapter 2. In particular, the research of inorganic scintillators and ISOFD has been discussed in detail.  $\text{Gd}_2\text{O}_2\text{S}$  doped with rare earth elements (Tb, Eu or Pr) in the form of powders, have been found to be the appropriate scintillation material for ISOFD fabrication, considering their high scintillation efficiencies and commercial availability. The variable emission spectra of  $\text{Gd}_2\text{O}_2\text{S}$

acquired by doping different rare earth elements make them favourable for MPSOFD fabrication. However, the temperature dependence of scintillators, either organic or inorganic, remains a problem. Incorporating a temperature sensor in the IOSOFD can enable a correction with an empirical temperature correction coefficient. As for the coupling efficiency between the scintillator and the optical fibre, it has been proved by other researchers that it can be improved through the reflective layer coating or core-embedding method. Regarding the spectra superposition problem of MPSOFD and interference introduced by the stem effect, a spectrum-decoupling method should be applied into the signal processing part of the IOSOFD detection.

The ionizing photons like X-rays and  $\gamma$ -rays are absorbed by the scintillator through photon interactions, including photoelectric absorption, coherent scattering, incoherent scattering (or Compton scattering), and electron-positron pair production. The MC simulation of the IOSOFD leads to a determination of the value of radiation energy absorption based on simulation of these detailed photon interactions. Therefore, chapter 3 reviewed the theory and MC simulation methods related to photon interactions. The study of the photon interaction cross sections of different photon interactions has verified that the energy absorption mechanisms for X-ray photons and  $\gamma$ -ray photons are different. Photoelectric absorption is the dominant photon interaction for diagnostic X-ray absorption while Compton scattering and pair-production are dominant for the therapeutic  $\gamma$ -ray absorption. Therefore, different methods were applied for the simulation of the energy absorption process of X-rays and  $\gamma$ -rays in the scintillator material within the IOSOFD model.

The simulation method of X-ray detection with IOSOFDs has been given in chapter 4. The method has integrated the MC simulation of X-ray interaction and the light ray

tracing. In this model, a scintillation-domain is embedded into an optical fibre. The simulation with different ISOFD configurations shows that the X-ray absorption efficiency can be enhanced by choosing small particle sizes, high scintillator packing densities, and deeper scintillation-domain embedding depth. Among them, the efficiency enhancement that is achieved by the high packing density is most prominent; therefore, the practical ISOFD should pursue packing density as priority. The simulation of the ISOFD with respect to different X-ray energies has confirmed that the energy dependence of the X-ray absorption efficiency is caused by the cross section of corresponding photon interactions as well as the K-X-ray emission and reabsorption for higher photon energies. In the case of practical applications of ISOFDs, this energy-dependent response to X-rays can be corrected if the energy distribution profile is provided. On the other hand, the simulation of the double SDs has verified a strong light attenuation by the adjacent scintillation-domain, which needs further research for the fabrication of MPSOFD for real time, in-vivo dosimetry.

The ISOFD designed is intended for not only diagnostic X-ray radiation dosimetry, but also the detection of therapeutic  $\gamma$ -rays. The scintillator interacts with  $\gamma$ -rays in a way more complicated than the X-ray of lower energy. Instead of the photoelectric effect, the  $\gamma$ -rays interact with the matter through Compton scattering and the pair-production. More importantly, the energy deposition of the secondary electrons and positrons created via photon interactions can't be neglected, thus in chapter 6, the theory and MC simulation methods of electrons and positrons interacting with matter have been reviewed. With the aforementioned MC simulation method of photon interactions and electron interactions, the  $\gamma$ -rays and secondary electrons interacting with the materials constituting the ISOFD have been simulated in chapter 7. The linear attenuation coefficient of  $\text{Gd}_2\text{O}_2\text{S}$  shows that the energy absorption efficiency of  $\gamma$ -rays

is much smaller than that of X-rays, and the photon energy is absorbed in the scintillation-domain via the interactions with scintillator materials. The theoretical energy distributions of the secondary electrons and positrons have been calculated and the result demonstrates that the kinetic energies of the secondary electrons and positrons are in a wide energy range with up limit in the order a few MeV. As for the electron transport in the scintillator, the simulation results of the mean free path length and the energy stopping power of the electron interactions were in agreement with those acquired from ESTAR library. Concerning the attenuation of secondary electrons inside scintillator particles in the scintillation-domain, a single  $Gd_2O_2S$  scintillator particle model is utilized for the MC simulation of the electron interactions. The result has confirmed that the energy of electrons is attenuated via inelastic collisions. For electrons with kinetic energy in the range 0.5~24 MeV, the average energy deposited per electron is determined by the size of the scintillator particle. However, this energy absorption in the particle counts for a very small portion of the electron energy, indicating considerable energy loss out of the scintillator particle. The simulation of the  $\gamma$ -ray and electron/positron interactions illustrated some features of the energy absorption process of ISOFD under  $\gamma$ -ray radiation. However, this aspect is far from adequate, as the simulation of  $\gamma$ -ray interactions and electron interactions were carried out separately. Future work integrating the simulation of these two interaction processes in the scintillation-domain of ISOFD is necessary.

## **Future Work**

The future work covers two aspects, the further simulation of ISOFDs and the experiments involving sensor fabrication and characterization. The simulation finished with respect to sensor configuration optimization has discussed the influence of the scintillator particle size, the packing density of the scintillation-domain, and the embedding depth. However, the optical fibre used in the ISOFD models was restricted to a step-index multi-mode silica fibre with constant specifications. The numerical aperture is small, so is the diameter of the fibre core (50  $\mu\text{m}$ ). This limited the effective transmission of the scintillation light. Therefore, the models with different optical fibres, both step-index and graded-index fibres, need to be incorporated in the simulation.

The radiation source used in this simulation was set as monoenergetic photon beams incident on the scintillation-domain in a direction normal to the fibre axis. However, the practical radiation incident on the sensor has more complicated energy distribution profile, thus the future simulation will consider the variable conditions of the radiation source.

The simulation of the  $\gamma$ -ray absorption with the scintillation-domain also needs further work, just as it discussed and concluded in the final section of chapter 7. In the future, the simulation will be refined by accounting for the integration of the  $\gamma$ -ray interactions, secondary electron and light ray tracing simulation into the ISOFD model. The overall energy absorption with respect to different photon energies will be investigated.

The future work of the fabrication of a ISOFD will focus on the optical fibre modification and scintillator embedding methods. As the simulation of ISOFDs has verified the factors affecting the scintillator and optical fibre coupling efficiency, it requires micro-/nano- modification of the optical fibre to achieve the efficient

scintillation light extraction out of the scintillation-domain. The feasibility of different micro-machining techniques like acid etching, focused ion beam (FIB) etching and plasma etching shall be explored for fibre coating and cladding removing procedure. Once the ISOFDs are fabricated, the characterization of these sensors will be carried out in air and water-phantom environment to test their sensitivity, durability and response linearity to the medical radiation in both diagnostic and therapeutic energy ranges. The result acquired will provide important information guiding the simulation in return.

## Reference

- [1] S. C. Lillicrap, B. Owen, J. R. Williams, and P. C. Williams, “Code of Practice for high-energy photon therapy dosimetry based on the NPL absorbed dose calibration service,” *Phys. Med. Biol.*, vol. 35, no. 10, pp. 1355–1360, 1990.
- [2] D. I. Thwaites, D. T. Burns, S. C. Klevenhagen, A. E. Nahum, and W. G. Pitchford, “The IPEMB code of practice for electron dosimetry for radiotherapy beams of initial energy from 2 to 50 MeV based on an air kerma calibration,” *Phys. Med. Biol.*, vol. 41, no. 12, pp. 2557–2603, 1996.
- [3] R. P. Symonds, C. Deehan, C. Meredith, and J. A. Mills, *Walter and Miller’s Textbook of Radiotherapy: Radiation Physics, Therapy and Oncology*, Seventh. Elsevier Health Sciences, 2012.
- [4] R. Lake, A. Mckenzie, E. M. Macaulay, H. M. Morgan, T. J. Jordan, and S. K. Powley, “IPEM Report 81 - Physics Aspects of Quality Control in Radiotherapy,” 1999.
- [5] W. Bogdanich, “Radiation Offers New Cures , and Ways to Do Harm Radiation,” pp. 1–16, 2010.
- [6] W. Bogdanich, “As Technology Surges, Radiation Safeguards Lag,” *New York Times*, vol. 15, pp. 1–13, 2010.
- [7] R. Garcia, H. Nyström, C. Fiorino, and D. Thwaites, “Does a too risk-averse approach to the implementation of new radiotherapy technologies delay their clinical use?,” *Br. J. Radiol.*, vol. 88, no. 1051, 2015.
- [8] K. Tanderup, S. Beddar, C. E. Andersen, G. Kertzscher, and J. E. Cygler, “In vivo dosimetry in brachytherapy.,” *Med. Phys.*, vol. 40, no. 7, p. 70902, 2013.
- [9] S. O’Keeffe, D. McCarthy, P. Woulfe, M. W. D. Grattan, a R. Hounsell, D. Sporea, L. Mihai, I. Vata, G. Leen, and E. Lewis, “A review of recent advances in optical fibre sensors for *in vivo* dosimetry during radiotherapy,” *Br. J. Radiol.*, vol. 88, no. 1050, p. 20140702, 2015.
- [10] J. F. Lester, L. M. Evans, Z. Yousef, a Penney, P. N. Brown, and R. Perks, “A

- National Audit of Current Cardiac Device Policies from Radiotherapy Centres across the UK,” *Clin. Oncol.*, vol. 26, no. 1, pp. 45–50, 2014.
- [11] A. Last, “Radiotherapy in patients with cardiac pacemakers.,” *The British Journal of Radiology*. American Public Health Association, 28-Jan-1998.
- [12] P. Y. Borius, B. Debono, I. Latorzeff, J. A. Lotterie, J. Y. Plas, E. Cassol, P. Bousquet, F. Loubes, P. Duthil, and A. Durand, “Dosimetric stereotactic radiosurgical accident: Study of 33 patients treated for brain metastases.,” *Neurochirurgie.*, vol. 56, no. 5, pp. 368–373, 2010.
- [13] M. V Williams, “Radiotherapy near misses, incidents and errors: radiotherapy incident at Glasgow,” *Clin. Oncol.*, vol. 19, no. 1, pp. 1–3, 2007.
- [14] C. W. Hurkmans, E. Scheepers, B. G. F. Springorum, and H. Uiterwaal, “Influence of radiotherapy on the latest generation of implantable cardioverter-defibrillators,” *Int. J. Radiat. Oncol. Biol. Phys.*, vol. 63, no. 1, pp. 282–289, 2005.
- [15] S. Hoecht, P. Rosenthal, D. Sancar, S. Behrens, W. Hinkelbein, and U. Hoeller, “Implantable cardiac defibrillators may be damaged by radiation therapy,” *J. Clin. Oncol.*, vol. 20, no. 8, pp. 2212–2213, 2002.
- [16] A. Makkar, J. Prisciandaro, S. Agarwal, M. Lusk, L. Horwood, J. Moran, C. Fox, J. A. Hayman, H. Ghanbari, B. Roberts, D. Belardi, R. Latchamsetty, T. Crawford, E. Good, K. Jongnarangsin, F. Bogun, A. Chugh, H. Oral, F. Morady, and F. Pelosi, “Effect of radiation therapy on permanent pacemaker and implantable cardioverter-defibrillator function,” *Hear. Rhythm*, vol. 9, no. 12, pp. 1964–1968, 2012.
- [17] B. Mijnheer, S. Beddar, J. Izewska, and C. Reft, “In vivo dosimetry in external beam radiotherapy.,” *Med. Phys.*, vol. 40, no. 7, p. 70903, 2013.
- [18] Standard Imaging Inc., “Exradin W1 Scintillator,” *Standard Imaging Inc*, 2017. [Online]. Available: <http://www.standardimaging.com/exradin/exradin-scintillator/>.
- [19] J. Byfield, P. Chan, and J. E. M. P. D, “A Flexible Fiber Optics Scintillation Probe for Intracavitary Dosimetry 1,” *Radiology*, vol. 92, no. 5, pp. 1120–1123, 1969.

- [20] A. S. Beddar, T. R. Mackie, and F. H. Attix, "Water-equivalent plastic scintillation detectors for high-energy beam dosimetry: I . Physical characteristics and theoretical considerations," *Phys. Med. Biol.*, vol. 37, no. 10, pp. 1883–1900, 1992.
- [21] A. S. Beddar, T. R. Mackie, and F. H. Attix, "Cerenkov light generated in optical fibres and other light pipes irradiated by electron beams," *Phys. Med. Biol.*, vol. 37, no. 4, pp. 925–935, 1992.
- [22] A. S. Beddar, T. R. Mackie, and F. H. Attix, "Water-equivalent plastic scintillation detectors for high- energy beam dosimetry: II. Properties and measurements A," *Phys. Med. Biol.*, vol. 37, no. 10, pp. 1883–1900, 1992.
- [23] S. F. De Boer, a S. Beddar, and J. a Rawlinson, "Optical filtering and spectral measurements of radiation-induced light in plastic scintillation dosimetry," *Phys. Med. Biol.*, vol. 38, no. 7, pp. 945–958, 1993.
- [24] T. Maekawa, M. Yoda, K. Tanaka, T. Masumaru, and S. Morimoto, "Fiber-optic Multipoint Radiation Sensing System using Waveguide Scintillators," *J. Nucl. Sci. Technol.*, vol. 33, no. 5, pp. 381–389, 1996.
- [25] M. R. Arnfield, H. E. Gaballa, R. D. Zwicker, Q. Islam, and R. Schmidt-Ullrich, "Radiation-induced light in optical fibers and plastic scintillators: Application to brachytherapy dosimetry," *Nucl. Sci. IEEE Trans.*, vol. 43, no. 3, pp. 2077–2084, 1996.
- [26] D. Létourneau, J. Pouliot, and R. Roy, "Miniature scintillating detector for small field radiation therapy," *Med. Phys.*, vol. 26, no. 12, pp. 2555–2561, 1999.
- [27] J. M. Fontbonne, G. Iltis, G. Ban, A. Battala, J. C. Vernhes, J. Tillier, N. Bellaize, C. Le Brun, B. Tamain, K. Mercier, and J. C. Motin, "Scintillating fiber dosimeter for radiation therapy accelerator," *IEEE Trans. Nucl. Sci.*, vol. 49 I, no. 5, pp. 2223–2227, 2002.
- [28] E. Takada, D. Yamada, and H. Kuroda, "A new optical fibre sensor for multipoint radiation measurement with sensing regions in its cladding," *Meas. Sci. Technol.*, vol. 15, no. 8, pp. 1479–1483, 2004.
- [29] J. Lambert, Y. Yin, D. R. McKenzie, S. H. Law, A. Ralston, and N. Suchowerska, "A prototype scintillation dosimeter customized for small and dynamic

- megavoltage radiation fields.,” *Phys. Med. Biol.*, vol. 55, no. 4, pp. 1115–26, 2010.
- [30] F. Therriault-Proulx, T. M. Briere, F. Mourtada, S. Aubin, S. Beddar, and L. Beaulieu, “A phantom study of an in vivo dosimetry system using plastic scintillation detectors for real-time verification of  $^{192}\text{Ir}$  HDR brachytherapy.,” *Med. Phys.*, vol. 38, no. 5, pp. 2542–2551, 2011.
- [31] F. Therriault-Proulx, L. Archambault, L. Beaulieu, and S. Beddar, “Development of a novel multi-point plastic scintillation detector with a single optical transmission line for radiation dose measurement.,” *Phys. Med. Biol.*, vol. 57, no. 21, pp. 7147–59, 2012.
- [32] S. F. Jackson, S. D. Monk, and K. Lennox, “Testing of a scintillator and fibre optic based radiation sensor,” *Radiat. Meas.*, vol. 59, pp. 50–58, 2013.
- [33] D. McCarthy, S. O’Keeffe, E. Lewis, D. G. Sporea, A. Sporea, I. Tiseanu, P. Woulfe, and J. Cronin, “Radiation dosimeter using an extrinsic fiber optic sensor,” *IEEE Sens. J.*, vol. 14, no. 3, pp. 673–685, 2014.
- [34] S. O’Keeffe, M. Grattan, A. Hounsell, D. McCarthy, P. Woulfe, J. Cronin, E. Lewis, and S. O’Keeffe, “Radiotherapy dosimetry based on plastic optical fibre sensors,” *Proc. SPIE*, vol. 8794, p. 879418, 2013.
- [35] M. Ishikawa, N. Nagase, T. Matsuura, J. Hiratsuka, R. Suzuki, N. Miyamoto, K. L. Sutherland, K. Fujita, and H. Shirato, “Development of a wavelength-separated type scintillator with optical fiber (SOF) dosimeter to compensate for the Cerenkov radiation effect,” *J. Radiat. Res.*, vol. 56, no. 2, pp. 372–381, 2015.
- [36] S. O’Keeffe, W. Zhao, W. Sun, D. Zhang, Z. Qin, Z. Chen, Y. Ma, and E. Lewis, “An Optical Fibre Based Sensor for Real-Time Monitoring of Clinical Linear Accelerator (Linac) Radiotherapy Delivery,” *IEEE J. Sel. Top. Quantum Electron.*, vol. 22, no. 3, pp. 35–42, 2015.
- [37] Q. Zhuang, H. Yaosheng, M. Yu, Z. Wenhui, S. Weimin, Z. Daxin, C. Ziyin, and L. Elfed, “Embedded structure fiber-optic radiation dosimeter for radiotherapy applications,” *Opt. Express*, vol. 24, no. 5, p. 5172, 2016.
- [38] N. Suchowerska, M. Jackson, J. Lambert, Y. B. Yin, G. Hruby, and D. R. McKenzie, “Clinical trials of a urethral dose measurement system in

- brachytherapy using scintillation detectors,” *Int. J. Radiat. Oncol. Biol. Phys.*, vol. 79, no. 2, pp. 609–615, 2011.
- [39] J.-C. Gagnon, D. Thériault, M. Guillot, L. Archambault, S. Beddar, L. Gingras, and L. Beaulieu, “Dosimetric performance and array assessment of plastic scintillation detectors for stereotactic radiosurgery quality assurance.,” *Med. Phys.*, vol. 39, no. 1, pp. 429–36, 2012.
- [40] J. Lambert, Y. Yin, D. R. McKenzie, S. Law, and N. Suchowerska, “Cerenkov light spectrum in an optical fiber exposed to a photon or electron radiation therapy beam.,” *Appl. Opt.*, vol. 48, no. 18, pp. 3362–3367, 2009.
- [41] A. M. Frelin, J. M. Fontbonne, G. Ban, J. Colin, M. Labalme, A. Batalla, A. Isambert, A. Vela, and T. Leroux, “Spectral discrimination of Čerenkov radiation in scintillating dosimeters,” *Med. Phys.*, vol. 32, no. 9, pp. 3000–3006, 2005.
- [42] J. Lambert, Y. Yin, D. R. McKenzie, S. Law, and N. Suchowerska, “Cerenkov-free scintillation dosimetry in external beam radiotherapy with an air core light guide.,” *Phys. Med. Biol.*, vol. 53, no. 11, pp. 3071–3080, 2008.
- [43] D. McCarthy, S. O’Keeffe, G. Leen, and E. Lewis, “Optical fibre radiation dosimetry for low dose applications,” *2010 IEEE Sensors*, no. October 2015, pp. 1663–1666, 2010.
- [44] R. Nowotny and a Taubeck, “A method for the production of composite scintillators for dosimetry in diagnostic radiology.,” *Phys. Med. Biol.*, vol. 54, no. 6, pp. 1457–68, 2009.
- [45] L. Wootton and S. Beddar, “Temperature dependence of BCF plastic scintillation detectors.,” *Phys. Med. Biol.*, vol. 58, no. 9, pp. 2955–67, 2013.
- [46] S. Buranurak, C. E. Andersen, A. R. Beierholm, and L. R. Lindvold, “Temperature variations as a source of uncertainty in medical fiber-coupled organic plastic scintillator dosimetry,” *Radiat. Meas.*, vol. 56, pp. 307–311, 2013.
- [47] J. H. Hubbell, “Photon mass attenuation and energy-absorption coefficients,” *Int. J. Appl. Radiat. Isot.*, vol. 33, no. 11, pp. 1269–1290, 1982.
- [48] P. Woulfe, S. O’Keeffe, D. McCarthy, M. Grattan, A. Hounsell, J. Cronin, and

- E. Lewis, *Characterisation of radioluminescence based optical fibre dosimeter in radiotherapy beam applications*. IEEE, 2013.
- [49] D. A. Jackson, “Novel fibre-optic-based ionization radiation probes,” *Proc. SPIE*, vol. 5502, pp. 234–238, 2004.
- [50] K. W. Jang, D. H. Cho, S. H. Shin, W. J. Yoo, J. K. Seo, B. Lee, S. Kim, J. H. Moon, Y. H. Cho, and B. G. Park, “Characterization of a scintillating fiber-optic dosimeter for photon beam therapy,” *Opt. Rev.*, vol. 16, no. 3, pp. 383–386, 2009.
- [51] S. O’Keefe, C. Fitzpatrick, E. Lewis, and a. I. Al-Shamma’a, “A review of optical fibre radiation dosimeters,” *Sens. Rev.*, vol. 28, no. 2, pp. 136–142, 2008.
- [52] M. a Clift, P. N. Johnston, and D. V Webb, “A temporal method of avoiding the Cerenkov radiation generated in organic scintillator dosimeters by pulsed megavoltage electron and photon beams,” *Phys. Med. Biol.*, vol. 47, no. 8, pp. 1421–1433, 2002.
- [53] L. Archambault, F. Therriault-Proulx, S. Beddar, and L. Beaulieu, “A mathematical formalism for hyperspectral, multipoint plastic scintillation detectors,” *Phys. Med. Biol.*, vol. 57, no. 21, pp. 7133–45, 2012.
- [54] M. Nikl, “Scintillation detectors for x-rays,” *Meas. Sci. Technol.*, vol. 17, no. 4, pp. R37–R54, 2006.
- [55] G. E. Knoll and J. Wiley, *Radiation Detection and Measurement*, 3rd ed. John Wiley & Sons, Ltd., 2000.
- [56] C. W. E. Van Eijk, “Inorganic scintillators in medical imaging,” *Phys. Med. Biol.*, vol. 47, no. 8, pp. 85–106, 2002.
- [57] M. Moszyński, “Inorganic scintillation detectors in  $\gamma$ -ray spectrometry,” *Nucl. Instruments Methods Phys. Res. Sect. A Accel. Spectrometers, Detect. Assoc. Equip.*, vol. 505, no. 1–2, pp. 101–110, 2003.
- [58] M. Ishii and M. Kobayashi, “Single crystals for radiation detectors,” *Prog. Cryst. Growth Charact.*, vol. 23, pp. 245–311, 1991.
- [59] M. J. Weber, “Inorganic scintillators: Today and tomorrow,” *J. Lumin.*, vol. 100, no. 1–4, pp. 35–45, 2002.
- [60] C. Greskovich and S. Duclos, “Ceramic Scintillators,” *Annu. Rev. Mater. Sci.*,

- vol. 27, no. 1, pp. 69–88, 1997.
- [61] L. Beaulieu and S. Beddar, “Review of plastic and liquid scintillation dosimetry for photon, electron, and proton therapy.,” *Phys. Med. Biol.*, vol. 61, no. 20, pp. R305–R343, 2016.
- [62] P. a. Rodnyi, P. Dorenbos, and C. W. E. van Eijk, “Energy Loss in Inorganic Scintillators,” *Phys. Status Solidi*, vol. 187, no. 1, pp. 15–29, 1995.
- [63] K. L. Swinth and J. H. Ewins, “Biomedical probe using a fiber-optic coupled scintillator,” *Med. Phys.*, vol. 3, no. 2, p. 109, 1976.
- [64] “Phosphor Technology IR/UV Phosphors.” [Online]. Available: <http://www.phosphor-technology.com/products/iruv.htm>.
- [65] E. I. Gorokhova, V. a Demidenko, S. B. Mikhrin, P. a Rodnyi, and C. W. E. van Eijk, “Luminescence and scintillation properties of  $Gd_2O_2S : Tb, Ce$  ceramics,” *Ieee*, vol. 0, no. C, pp. 813–816, 2004.
- [66] I. D. Jung, M. K. Cho, S. M. Lee, K. M. Bae, P. G. Jung, C. H. Lee, J. M. Lee, S. Yun, H. K. Kim, S. S. Kim, and J. S. Ko, “Flexible  $Gd_2O_2S:Tb$  scintillators pixelated with polyethylene microstructures for digital x-ray image sensors,” *J. Micromechanics Microengineering*, vol. 19, no. 1, p. 15014, Jan. 2009.
- [67] C. M. Michail, G. P. Fountos, I. G. Valais, N. I. Kalyvas, P. F. Liaparinos, I. S. Kandarakis, and G. S. Panayiotakis, “Evaluation of the Red Emitting  $Gd_2O_2S:Eu$  Powder Scintillator for Use in Indirect X-Ray Digital Mammography Detectors,” *IEEE Trans. Nucl. Sci.*, vol. 58, no. 5, pp. 2503–2511, 2011.
- [68] G. Fern, T. Ireland, J. Silver, R. Withnall, A. Michette, C. McFaul, and S. Pfauntsch, “Characterisation of  $Gd_2O_2S:Pr$  phosphor screens for water window X-ray detection,” *Nucl. Instruments Methods Phys. Res. Sect. A Accel. Spectrometers, Detect. Assoc. Equip.*, vol. 600, no. 2, pp. 434–439, 2009.
- [69] J.-C. G. Bünzli, “Benefiting from the Unique Properties of Lanthanide Ions,” *Acc. Chem. Res.*, vol. 39, no. 1, pp. 53–61, 2006.
- [70] P. A. Rodnyi, “Energy Levels of Rare-Earth Ions in  $Gd_2O_2S$ ,” *Opt. Spectrosc.*, vol. 107, no. 2, pp. 270–274, 2009.
- [71] T. Hang, Q. Liu, D. Mao, and C. Chang, “Long lasting behavior of  $Gd_2 O_2S:Eu^{3+}$

- phosphor synthesized by hydrothermal routine,” vol. 107, no. 7, pp. 142–147, 2008.
- [72] A. A. da Silva, M. A. Cebim, and M. R. Davolos, “Excitation mechanisms and effects of dopant concentration in  $\text{Gd}_2\text{O}_2\text{S}:\text{Tb}^{3+}$  phosphor,” *J. Lumin.*, vol. 128, no. 7, pp. 1165–1168, 2008.
- [73] J. Lian, X. Sun, T. Gao, Q. Li, X. Li, and Z. Liu, “Preparation of  $\text{Gd}_2\text{O}_2\text{S}:\text{Pr}$  Scintillation Ceramics by Pressureless Reaction Sintering Method,” *J. Mater. Sci. Technol., Vol.25*, vol. 25, no. 2, pp. 254–258, 2009.
- [74] J. Lian, H. Qin, P. Liang, B. Wang, and F. Liu, “Controllable synthesis and photoluminescence properties of  $\text{Gd}_2\text{O}_2\text{S}:\text{x}\%\text{Pr}^{3+}$  microspheres using an urea-ammonium sulfate (UAS) system,” *Ceram. Int.*, vol. 41, no. 2, pp. 2990–2998, 2015.
- [75] H. Huang and B. Yan, “In situ sol-gel composition of multicomponent hybrid precursors to luminescent novel unexpected microrod of  $\text{Y}_2\text{SiO}_5:\text{Eu}^{3+}$  employing different silicate sources,” *Solid State Commun.*, vol. 132, no. 11, pp. 773–777, 2004.
- [76] W. Wang, Y. Li, H. Kou, S. Liu, H. Liu, Y. Shi, J. Li, X. Feng, Y. Pan, and J. Guo, “ $\text{Gd}_2\text{O}_2\text{S}:\text{Pr}$  Scintillation Ceramics from Powder Synthesized by a Novel Carbothermal Reduction Method,” *J. Am. Ceram. Soc.*, vol. 98, no. 7, pp. 2159–2164, 2015.
- [77] S. A. Osseni, S. Lechevallier, M. Verelst, C. Dujardin, J. Dexpert-Ghys, D. Neumeyer, M. Leclercq, H. Baaziz, D. Cussac, V. Santran, and R. Mauricot, “New nanoplatform based on  $\text{Gd}_2\text{O}_2\text{S}:\text{Eu}^{3+}$  core: Synthesis, characterization and use for in vitro bio-labelling,” *J. Mater. Chem.*, vol. 21, no. 45, pp. 18365–18372, 2011.
- [78] Y. Tian, W. H. Cao, X. X. Luo, and Y. Fu, “Preparation and luminescence property of  $\text{Gd}_2\text{O}_2\text{S}:\text{Tb}$  X-ray nano-phosphors using the complex precipitation method,” *J. Alloys Compd.*, vol. 433, no. 1–2, pp. 313–317, 2007.
- [79] S. Blahuta, B. Viana, A. Bessière, E. Mattmann, and B. Lacourse, “Luminescence quenching processes in  $\text{Gd}_2\text{O}_2\text{S}:\text{Pr}^{3+},\text{Ce}^{3+}$  scintillating ceramics,” *Opt. Mater. (Amst.)*, vol. 33, no. 10, pp. 1514–1518, 2011.

- [80] E. I. Gorokhova, V. a. Demidenko, O. a. Khristich, S. B. Mikhrin, and P. a. Rodnyi, "Luminescence properties of ceramics based on terbium-doped gadolinium oxysulfide," *J. Opt. Technol.*, vol. 70, no. 10, p. 693, 2003.
- [81] C. He, Z. Xia, and Q. Liu, "Microwave solid state synthesis and luminescence properties of green-emitting  $\text{Gd}_2\text{O}_2\text{S}:\text{Tb}^{3+}$  phosphor," *Opt. Mater. (Amst.)*, vol. 42, pp. 11–16, 2015.
- [82] C. M. Michail, I. G. Valais, A. E. Toutountzis, N. E. Kalyvas, G. P. Fountos, S. L. David, I. S. Kandarakis, and G. S. Panayiotakis, "Light Emission Efficiency of  $\text{Gd}_2\text{O}_2\text{S}:\text{Eu}$  (GOS:Eu) Powder Screens Under X-Ray Mammography Conditions," *IEEE Trans. Nucl. Sci.*, vol. 55, no. 6, pp. 3703–3709, 2008.
- [83] W. R. Leo, *Techniques for Nuclear and Particle Physics Experiments*. 1994.
- [84] S. Beddar, "On possible temperature dependence of plastic scintillator response," *Med. Phys.*, vol. 39, p. 6522, 2012.
- [85] F. Therriault-Proulx, S. Beddar, and L. Beaulieu, "On the use of a single-fiber multipoint plastic scintillation detector for  $^{192}\text{Ir}$  high-dose-rate brachytherapy.," *Med. Phys.*, vol. 40, no. 6, pp. 1–10, 2013.
- [86] D. McCarthy, S. O'Keeffe, E. Lewis, D. Sporea, A. Sporea, and I. Tiseanu, "Optical fibre X-ray radiation dosimeter sensor for low dose applications," *Proc. IEEE Sensors*, pp. 121–124, 2011.
- [87] L. Archambault, A. S. Beddar, L. Gingras, R. Roy, and L. Beaulieu, "Measurement accuracy and cerenkov removal for high performance, high spatial resolution scintillation dosimetry," *Med. Phys.*, vol. 33, no. 1, pp. 128–135, 2006.
- [88] a. Intermite, M. Putignano, and C. P. Welsch, "Feasibility study of an optical fibre sensor for beam loss detection based on a SPAD array," pp. 228–230, 2009.
- [89] K. W. Jang, W. J. Yoo, J. K. Seo, J. Y. Heo, J. Moon, J. Y. Park, S. Kim, B. G. Park, and B. Lee, "Measurements and removal of Cerenkov light generated in scintillating fiber-optic sensor induced by high-energy electron beams using a spectrometer," *Opt. Rev.*, vol. 18, no. 1, pp. 176–179, 2011.
- [90] P. Z. Y. Liu, N. Suchowerska, J. Lambert, P. Abolfathi, and D. R. McKenzie,

- “Plastic scintillation dosimetry: comparison of three solutions for the Cerenkov challenge.” *Phys. Med. Biol.*, vol. 56, no. 18, pp. 5805–5821, 2011.
- [91] M. Guillot, L. Gingras, L. Archambault, S. Beddar, and L. Beaulieu, “Spectral method for the correction of the Cerenkov light effect in plastic scintillation detectors: a comparison study of calibration procedures and validation in Cerenkov light-dominated situations.” *Med. Phys.*, vol. 38, no. 4, pp. 2140–2150, 2011.
- [92] A. S. Beddar, T. M. Briere, F. A. Mourtada, O. N. Vassiliev, H. H. Liu, and R. Mohan, “Monte Carlo calculations of the absorbed dose and energy dependence of plastic scintillators,” *Med. Phys.*, vol. 32, no. 5, p. 1265, 2005.
- [93] L. L. W. Wang, D. Klein, and a S. Beddar, “Monte Carlo study of the energy and angular dependence of the response of plastic scintillation detectors in photon beams,” *Med. Phys.*, vol. 37, no. 10, pp. 5279–5286, 2010.
- [94] A. Teymurazyan and G. Pang, “Monte Carlo simulation of a novel water-equivalent electronic portal imaging device using plastic scintillating fibers,” *Med. Phys.*, vol. 39, no. 3, pp. 1518–1529, 2012.
- [95] J. Boivin, S. Beddar, C. Bonde, D. Schmidt, W. Culberson, M. Guillemette, and L. Beaulieu, “A systematic characterization of the low-energy photon response of plastic scintillation detectors,” *Phys. Med. Biol.*, vol. 61, no. 15, pp. 5569–5586, 2016.
- [96] H. P. Chan and K. Doi, “The validity of Monte Carlo simulation in studies of scattered radiation in diagnostic radiology,” *Phys. Med. Biol.*, vol. 28, no. 2, p. 109, 1983.
- [97] B. Nielsen and C. A. Carlsson, “Energy imparted to fluorescent screens from primary and scattered radiation . Variations with atomic composition and screen thickness,” *Phys. Med. Biol.*, vol. 29, no. 4, pp. 315–328, 1984.
- [98] H. P. Chan and K. Doi, “Physical characteristics of scattered radiation in diagnostic radiology: Monte Carlo simulation studies,” *Med. Phys.*, vol. 12, no. 2, pp. 152–165, 1985.
- [99] G. E. Giakoumakis, M. C. Katsarioti, I. E. Lagaris, and G. S. Panayiotakis, “A theoretical model for the x-ray luminescence of granular phosphor screens,” *J.*

- Appl. Phys.*, vol. 69, no. 9, pp. 6607–6611, 1991.
- [100] D. a Jaffray, J. J. Battista, a Fenster, and P. Munro, “Monte Carlo studies of x-ray energy absorption and quantum noise in megavoltage transmission radiography,” *Med. Phys.*, vol. 22, no. 7, pp. 1077–1088, 1995.
- [101] P. F. Liaparinos, I. S. Kandarakis, D. a Cavouras, H. B. Delis, and G. S. Panayiotakis, “Modeling granular phosphor screens by Monte Carlo methods.,” *Med. Phys.*, vol. 33, no. 12, pp. 4502–4514, 2006.
- [102] P. F. Liaparinos, I. S. Kandarakis, D. a Cavouras, H. B. Delis, and G. S. Panayiotakis, “Monte Carlo study on the imaging performance of powder  $\text{Lu}_2\text{SiO}_5\text{:Ce}$  phosphor screens under x-ray excitation: comparison with  $\text{Gd}_2\text{O}_2\text{S:Tb}$  screens.,” *Med. Phys.*, vol. 34, no. 5, pp. 1724–1733, 2007.
- [103] F. Biggs, L. B. Mendelsohn, and J. . Mann, “Hartree-Fock Compton profiles for the elements,” *At. Data Nucl. Data Tables*, vol. 16, no. 3, pp. 201–309, 1975.
- [104] Hubbell, J. H., W. J. Veigele, E. A. Briggs, and R. T. Brown, “Atomic form factors incoherent scattering functions and photon scattering cross sections,” *J. Phys. Chem. Ref. data*, vol. 4, no. 3, pp. 471–538, 1975.
- [105] J. H. Hubbell and W. J. Veigele, “Comparison of Theoretical and Experimental Photoeffect Data,” 1976.
- [106] J. H. Hubbell and H. A. Gimm, “Pair, Triplet, and Total Atomic Cross Sections (and Mass Attenuation Coefficients) for 1 MeV-100 GeV Photons in Elements  $Z= 1$  to 100,” *J. Phys. Chem. Ref. Data*, vol. 9, no. 4, pp. 1023–1048, 1980.
- [107] J. H. Hubbell and I. Overbo, “Relativistic atomic form factors and photon coherent scattering cross sections,” *Journal of Physical and Chemical Reference Data*, vol. 8, no. 1, pp. 69–106, 1979.
- [108] J. Baró, M. Roteta, J. M. Fernández-Varea, and F. Salvat, “Analytical cross sections for Monte Carlo simulation of photon transport,” *Radiat. Phys. Chem.*, vol. 44, no. 5, pp. 531–552, 1994.
- [109] J. H. Hubbell, P. N. Trehan, N. Singh, B. Chand, D. Mehta, M. L. Garg, R. R. Garg, S. Singh, and S. Puri, “A Review, Bibliography, and Tabulation of K, L, and Higher Atomic Shell X-Ray Fluorescence Yields,” *Journal of Physical and*

- Chemical Reference Data*, vol. 23, no. 2. pp. 339–364, 1994.
- [110] D. Brusa, G. Stutz, J. A. Riveros, J. M. Fernández-Varea, and F. Salvat, “Fast sampling algorithm for the simulation of photon Compton scattering,” *Nucl. Instruments Methods Phys. Res. Sect. A Accel. Spectrometers, Detect. Assoc. Equip.*, vol. 379, no. 1, pp. 167–175, 1996.
- [111] H. Zaidi, “Comparative evaluation of photon cross section libraries for materials of interest in PET Monte Carlo simulations,” *IEEE Trans Nucl Sci*, vol. 47, no. 6, pp. 2722–2735, 2000.
- [112] H.-P. Chan and K. Doi, “Studies of x-ray energy absorption and quantum noise properties of x-ray screens by use of Monte Carlo simulation,” *Med. Phys.*, vol. 11, no. 1, pp. 37–46, 1984.
- [113] B. D. Gallas, J. S. Boswell, A. Badano, R. M. Gagne, and K. J. Myers, “An energy- and depth-dependent model for x-ray imaging,” *Med. Phys.*, vol. 31, no. 11, pp. 3132–3149, 2004.
- [114] S. L. Issler and C. C. Torardi, “Solid state chemistry and luminescence of X-ray phosphors,” *J. Alloys Compd.*, vol. 229, no. 1, pp. 54–65, Oct. 1995.
- [115] S. T. Perkins, D. E. Cullen, M. H. Chen, J. Rathkopf, J. Scofield, and J. H. Hubbell, “Tables and graphs of atomic subshell and relaxation data derived from the LLNL Evaluated Atomic Data Library (EADL), Z= 1--100,” Lawrence Livermore National Lab., CA (United States), 1991.
- [116] G. F. Knoll, *Radiation Detection and Measurement*, 3rd ed. John Wiley & Sons, 2000.
- [117] J. H. Hubbell, “Review of photon interaction cross section data in the medical and biological context,” *Phys. Med. Biol.*, vol. 44, no. 1, pp. R1–R22, 1999.
- [118] “XCOM: Photon Cross Sections Database.” [Online]. Available: <https://www.nist.gov/pml/xcom-photon-cross-sections-database>.
- [119] H. P. Chan and K. Doi, “Energy and angular dependence of x-ray absorption and its effect on radiographic response in screen--film systems,” *Phys. Med. Biol.*, vol. 28, no. 5, pp. 565–79, 1983.
- [120] S. N. Ahmed, “Interaction of radiation with matter,” in *Physics and Engineering*

- of Radiation Detection*, 2nd ed., vol. 20, Academic Press, 2015, pp. 27–29.
- [121] I. Kawrakow, E. Mainegra-Hing, D. W. O. Rogers, F. Tessier, and B. R. B. Walters, “NRCC Report PIRS-701: The EGSnrc Code System: Monte Carlo Simulation of Electron and Photon Transport,” 2017.
- [122] F. Salvat, J. Fernández-Varea, and J. Sempau, *PENELOPE-2008: A code system for Monte Carlo simulation of electron and photon transport*, no. 6416. 2008.
- [123] J. Sempau, E. Acosta, J. Baro, J. M. Fernández-Varea, and F. Salvat, “An algorithm for Monte Carlo simulation of coupled electron-photon transport,” *Nucl. Instruments Methods Phys. Res. Sect. B Beam Interact. with Mater. Atoms*, vol. 132, no. 3, pp. 377–390, 1997.
- [124] D. E. Cullen, J. H. Hubbell, L. Kissel, and L. L. N. Laboratory, “EPDL97: the evaluated photo data library `97 version,” *Uclr--50400*, vol. Vol.6-Rev., pp. 1–35, 1997.
- [125] R. Ribberfors and K.-F. Berggren, “Incoherent-x-ray-scattering functions and cross sections ( $d\sigma/d\Omega$ ) incoh by means of a pocket calculator.,” *Phys. Rev. A*, vol. 26, no. 6, pp. 3325–3333, 1982.
- [126] F. Salvat and J. M. M. Fernández-Varea, “Semiempirical cross sections for the simulation of the energy loss of electrons and positrons in matter,” *Nucl. Inst. Methods Phys. Res. B*, vol. 63, no. 3, pp. 255–269, 1992.
- [127] J. Motz, A. Haakon, and H. Koch, “Pair Production by Photons,” *Rev. Mod. Phys.*, vol. 41, no. 4, p. 581, 1969.
- [128] “EpoFix Kit, 1 l resin, 130 ml hardener and required consumables (40200029),” 2017. [Online]. Available: [https://e-shop.struers.com/NO/EN/products/Mounting/Cold\\_mounting\\_resin](https://e-shop.struers.com/NO/EN/products/Mounting/Cold_mounting_resin).
- [129] C. C. Chang, R.-L. Chern, C. C. Chang, C.-C. Chu, J. Y. Chi, J.-C. Su, I.-M. Chan, and J.-F. T. Wang, “Monte Carlo Simulation of Optical Properties of Phosphor-Screened Ultraviolet Light in a White Light-Emitting Device,” *Jpn. J. Appl. Phys.*, vol. 44, no. 8, pp. 6056–6061, 2005.
- [130] J. P. Moy, A. Koch, and M. B. Nielsen, “Conversion efficiency and time response of phosphors for fast X-ray imaging with synchrotron radiation,” *Nucl.*

- Inst. Methods Phys. Res. A*, vol. 326, no. 3, pp. 581–586, 1993.
- [131] R. Morlotti, M. Nikl, M. Piazza, and C. Boragno, “Intrinsic conversion efficiency of X-rays to light in  $\text{Gd}_2\text{O}_2\text{S}:\text{Tb}^{3+}$  powder phosphors,” *J. Lumin.*, vol. 72–74, no. 96, pp. 772–774, 1997.
- [132] G. Blasse and B. C. Grabmaier, *Luminescent materials*. Springer Science & Business Media, 2012.
- [133] V. V. Nagarkar, S. R. Miller, S. V. Tipnis, A. Lempicki, C. Brecher, and H. Lingertat, “A new large area scintillator screen for X-ray imaging,” *Nucl. Instruments Methods Phys. Res. Sect. B Beam Interact. with Mater. Atoms*, vol. 213, pp. 250–254, 2004.
- [134] I. Seferis, C. Michail, I. Valais, J. Zeler, P. Liaparinos, G. Fountos, N. Kalyvas, S. David, F. Stromatia, E. Zych, I. Kandarakis, and G. Panayiotakis, “Light emission efficiency and imaging performance of  $\text{Lu}_2\text{O}_3:\text{Eu}$  nanophosphor under X-ray radiography conditions: Comparison with  $\text{Gd}_2\text{O}_2\text{S}:\text{Eu}$ ,” *J. Lumin.*, vol. 151, pp. 229–234, 2014.
- [135] G. E. Giakoumakis, C. D. Nomicos, and P. X. Sandilos, “Absolute efficiency of  $\text{Gd}_2\text{O}_2\text{S}:\text{Tb}$  screens under fluoroscopic conditions,” *Phys. Med. Biol.*, vol. 34, no. 6, pp. 673–678, 1989.
- [136] X. M. Han, J. Lin, J. Fu, R. B. Xing, M. Yu, Y. H. Zhou, and M. L. Pang, “Fabrication, patterning and luminescence properties of  $\text{X}_2\text{-Y}_2\text{SiO}_5:\text{A}$  ( $\text{A}=\text{Eu}^{3+}$ ,  $\text{Tb}^{3+}$ ,  $\text{Ce}^{3+}$ ) phosphor films via sol-gel soft lithography,” *Solid State Sci.*, vol. 6, no. 4, pp. 349–355, 2004.
- [137] G. Blasse, “The luminescence efficiency of scintillators for several applications: State-of-the-art,” *J. Lumin.*, vol. 60–61, no. C, pp. 926–929, 1994.
- [138] H. Bethe, “Molière’s Theory of Multiple Scattering,” *Phys. Rev. Lett.*, vol. 89, no. 6, pp. 1256–1266, 1953.
- [139] Y. S. Tsai, “Pair production and bremsstrahlung of charged leptons,” *Rev. Mod. Phys.*, vol. 46, no. 4, pp. 815–851, 1974.
- [140] D. Liljequist, M. Ismail, F. Salvat, R. Mayol, and J. D. Martinez, “Transport mean free path tabulated for the multiple elastic scattering of electrons and

- positrons at energies  $\leq 20$  MeV,” *J. Appl. Phys.*, vol. 68, no. 7, pp. 3061–3065, 1990.
- [141] M. J. Berger and S. M. Seltzer, “Stopping powers and ranges of electrons and positrons,” 1983.
- [142] J. Baró, J. Sempau, J. M. Fernández-Varea, and F. Salvat, “PENELOPE: An algorithm for Monte Carlo simulation of the penetration and energy loss of electrons and positrons in matter,” *Nucl. Inst. Methods Phys. Res. B*, vol. 100, no. 1, pp. 31–46, 1995.
- [143] W. R. Nelson, H. Hirayama, and D. W. Rogers, “Stanford Linear Accelerator Center Report SLAC-265,” 1985.
- [144] J. M. Fernández-Varea, R. Mayol, J. Baró, and F. Salvat, “On the theory and simulation of multiple elastic scattering of electrons,” *Nucl. Instruments Methods Phys. Res. Sect. B Beam Interact. with Mater. Atoms*, vol. 73, no. 4, pp. 447–473, 1993.
- [145] J. Baró, J. Sempau, J. M. Fernández-Varea, and F. Salvat, “Simplified Monte Carlo simulation of elastic electron scattering in limited media,” *Nucl. Inst. Methods Phys. Res. B*, vol. 84, no. 4, pp. 465–483, 1994.
- [146] J. D. Martínez, R. Mayol, and F. Salvat, “Monte Carlo simulation of kilovolt electron transport in solids,” *J. Appl. Phys.*, vol. 67, no. 6, pp. 2955–2964, 1990.
- [147] “EStar-physical measurement Laboratory.” [Online]. Available: <https://physics.nist.gov/PhysRefData/Star/Text/ESTAR.html>.
- [148] D. Liljequist, “A simple calculation of inelastic mean free path and stopping power for 50 eV–50 keV electrons in solids,” *J. Phys. D. Appl. Phys.*, vol. 16, no. 8, pp. 1567–1582, 1983.
- [149] L. Sorace and D. Gatteschi, “Electronic Structure and Magnetic Properties of Lanthanide Molecular Complexes,” in *Lanthanides and Actinides in Molecular Magnetism*, Wiley-VCH Verlag GmbH & Co. KGaA, 2015, pp. 1–26.